LUND UNIVERSITY

Search for doubly charged Higgs bosons in multi-lepton final states with the ATLAS detector

Mankinen, Katja

2020

Search for doubly charged Higgs bosons in multi-lepton final states with the ATLAS detector

KATJA MANKINEN
FACULTY OF SCIENCE | LUND UNIVERSITY

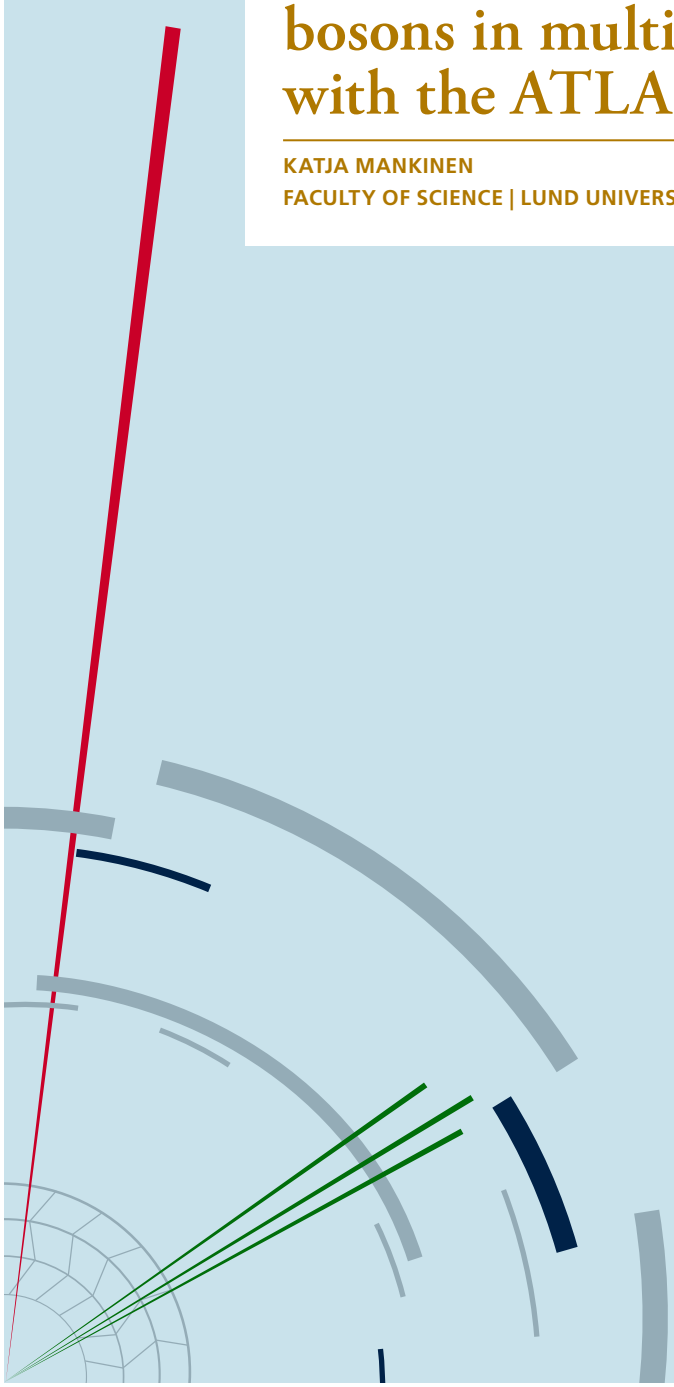

Printed by Media-Tryck, Lund 2020 NORDIC SWAN ECOLABEL 3041 0903

Department of Physics
Particle Physics Division
Faculty of Science
Lund University
ISBN 978-91-7895-384-4

Search for doubly charged Higgs bosons in multi-lepton final states with the ATLAS detector

Katja Mankinen

LUND
UNIVERSITY

Thesis submitted for the degree of
Doctor of Philosophy

Faculty opponent: Professor Paula Eerola, University of Helsinki

To be presented, with the permission of the Faculty of Science of Lund University, for public criticism in the Rydberg lecture hall (Rydbergsalen) at the Department of Physics on Friday, the 31st of January 2020 at 13:00.

Organization	Document name
LUND UNIVERSITY Department of Physics Box 118 SE–221 00 LUND Sweden	**DOCTORAL DISSERTATION** Date of disputation 2020-01-31 Sponsoring organization
Author(s) Katja Mankinen	

Title and subtitle

Search for doubly charged Higgs bosons in multi-lepton final states with the ATLAS detector

Abstract

Standard Model events with prompt, isolated, same-charge high-p_{T} leptons are rare, and therefore events with such final states provide a powerful signature towards new discoveries. This thesis presents two searches for doubly charged Higgs bosons decaying into same-charge lepton pairs using proton–proton collision data recorded by the ATLAS detector at the LHC. Observation of doubly charged Higgs bosons might provide hints about the mechanism for generating small neutrino masses. The first search uses a data sample corresponding to 36.1 fb^{-1} of integrated luminosity recorded in 2015 and 2016, focusing on the final states with electrons and muons. The second analysis extends the search with hadronically decaying taus and the full LHC Run 2 dataset recorded in 2015–2018 at $\sqrt{s} = 13\,\mathrm{TeV}$, corresponding to 139 fb^{-1}. The searches cover a wide signal mass hypothesis range from 300 GeV to 1.3 TeV, and show excellent understanding between the collision data and the Standard Model background predictions. Despite further optimization of event and physics object selection to enhance the sensitivity to new physics processes, no significant evidence of a signal is observed. Corresponding limits on the production cross-section and on the mass of the doubly charged Higgs bosons are derived for the pair production of the $H^{\pm\pm}$ bosons at 95% confidence level.

As the reconstruction of charged leptons requires excellent momentum resolution and tracking capabilities, the thesis also describes the drift time calibrations of the ATLAS Transition Radiation Tracker (TRT). By extending the lever arm of the Inner Detector, the TRT improves the momentum resolution and the track parameters of the event reconstruction. Preserving track reconstruction performance under challenging experimental conditions despite irreparable gas leaks in the detector is of the utmost importance. Precise calibrations in various gas configurations using both simulated and real data from proton–proton and heavy ion collisions are performed to achieve that goal, and overall good drift time accuracy and data quality are provided by the TRT during the full Run 2.

Keywords

ATLAS, Beyond the Standard Model, Doubly charged Higgs, Left-right symmetry, LHC, Same-charge leptons, Taus, Transition radiation tracker

Classification system and/or index terms (if any)

Supplementary bibliographical information	Language
	English
ISBN 978-91-7895-384-4 (print) 978-91-7895-385-1 (pdf)	ISSN and key title
Recipient's notes	Number of pages: 248 / Price
	Security classification

Search for doubly charged Higgs bosons in multi-lepton final states with the ATLAS detector

Katja Mankinen

LUND
UNIVERSITY

Faculty of Science, Department of Physics

ISBN: 978-91-7895-384-4 (print)
ISBN: 978-91-7895-385-1 (pdf)

Printed in Sweden by Media-Tryck, Lund University, Lund 2020

ABSTRACT

Standard Model events with prompt, isolated, same-charge high-p_{T} leptons are rare, and therefore events with such final states provide a powerful signature towards new discoveries. This thesis presents two searches for doubly charged Higgs bosons decaying into same-charge lepton pairs using proton–proton collision data recorded by the ATLAS detector at the LHC. Observation of doubly charged Higgs bosons might provide hints about the mechanism for generating small neutrino masses. The first search uses a data sample corresponding to 36.1 $\mathrm{fb}^{-1}$of integrated luminosity recorded in 2015 and 2016, focusing on the final states with electrons and muons. The second analysis extends the search with hadronically decaying taus and the full LHC Run 2 dataset recorded in 2015–2018 at $\sqrt{s} = 13\,\mathrm{TeV}$, corresponding to 139 fb^{-1}. The searches cover a wide signal mass hypothesis range from 300 GeV to 1.3 TeV, and show excellent understanding between the collision data and the Standard Model background predictions. Despite further optimization of event and physics object selection to enhance the sensitivity to new physics processes, no significant evidence of a signal is observed. Corresponding limits on the production cross-section and on the mass of the doubly charged Higgs bosons are derived for the pair production of the $H^{\pm\pm}$ bosons at 95% confidence level.

As the reconstruction of charged leptons requires excellent momentum resolution and tracking capabilities, the thesis also describes the drift time calibrations of the ATLAS Transition Radiation Tracker (TRT). By extending the lever arm of the Inner Detector, the TRT improves the momentum resolution and the track parameters of the event reconstruction. Preserving track reconstruction performance under challenging experimental conditions despite irreparable gas leaks in the detector is of the utmost importance. Precise calibrations in various gas configurations using both simulated and real data from proton–proton and heavy ion collisions are performed to achieve that goal, and overall good drift time accuracy and data quality are provided by the TRT during the full Run 2.

Keywords: *ATLAS, Beyond the Standard Model, Doubly charged Higgs, Left-right symmetry, LHC, Same-charge leptons, Taus, Transition radiation tracker*

POPULÄRVETENSKAPLIG SAMMANFATTNING

Standardmodellen är en teori som innehåller nästan allt vi vet om partikelfysik för tillfället. Den förklarar hur de grundläggande partiklarna och tre av de fundamentala krafterna interagerar med varandra. Även om den är ett av de vackraste matematiska pusslen som noggrant testats under ett halvt sekel av tusentals partikelfysiker, är den delvis ofullständigt. Det finns många problem som inte förklaras av Standardmodellen, till exempel gravitation och mörk materia - en okänd substans som står för 27% av universums materia och tros ge galaxer extra massa. Modellen förklarar inte heller den observerade obalansen mellan materia och antimateria i universum. Utan denna obalans skulle vi inte existera. Dessutom är neutrinerna i modellen masslös trots att kosmologiska observationer av neutrino-oscillationer gör det obestridligt att de verkligen har en liten massa.

Teoretiker har konstruerat flera teorier som antingen kompletterar eller omformulerar Standardmodellen för att svara på ovanstående problem. Många av dessa nya teorier förutspår att det finns andra, tyngre Higgs-partiklar än den berömda Higgs-bosonen som upptäcktes 2012, ansvariga för att ge massa till elementära partiklar. Observationen av ytterligare partiklar skulle ge en direkt inblick i teorin bortom den nuvarande Standardmodellen och öppna ett fönster mot en bättre förståelse av vårt universum.

Forskare testar om dessa nya modeller är korrekta genom att studera partiklar som skapas i partikelkollisioner och observeras av stora detektorer som ATLAS på Large Hadron Collider (LHC) vid CERN i Schweiz. Massiva elementära partiklar kan produceras i energiska partikelkollisioner, tack vare Einsteins berömda ekvation $E = mc^2$ som säger att energi i kollisioner kan omvandlas till massa hos nya partiklar. Massiva partiklar kan i sin tur sönderfalla vidare till andra partiklar som ska detekteras.

För att studera elektriskt laddade partiklar är det viktigt att rekonstruera deras spår när de färdas genom detektorn. Denna avhandling beskriver hur den yttersta spårningsdetektorn vid ATLAS, Transition Radiation Tracker, är kalibrerad. Dessa kalibreringar utförs med både simuleringar och data från partikelkollisioner för att säkerställa exakt spårning av laddade partiklar som används i nästan alla fysikanalyser.

Den här avhandlingen beskriver även jakten på ny fysik, med hjälp av speciella och ovanliga händelser där ett eller flera leptonpar (leptoner är partiklar som elektroner, myoner och tauleptoner) skapas i partikelkollisioner och där båda leptonerna i paret har samma elektriska laddning. Ett exempel på nya partiklar som producerar leptonpar är dubbelt laddade Higgsbosoner. Om de hittades, skulle det kunna ge en förklaring till neutrinomassans ursprung.För att upptäcka dubbelt laddade Higgs-bosoner, jagar vi efter ojämnheter i våra grafer. Syftet är att studera om man har observerat en statistiskt signifikant skillnad mellan Standardmodellens prognos och den experimentella datan från ATLAS-detektorn. Även om inga skillnader, dvs. ingen ny fysik hittas, kan vi begränsa eller utesluta vissa teorier.

Den här avhandlingen omfattar två sökningar efter dubbelt laddade Higgs-bosoner: den första väljer endast de två lättaste laddade leptonerna och använder data som samlats in 2015-2016. Den andra sökningen lägger till den tyngsta laddade leptonen till analysen och använder mycket mer data som samlats in mellan 2015 och 2018. Efter ett noggrant urval av partikelkollisioner med högenergetiska partiklar som produkter, stämmer bakgrundsprognoserna från Standardmodellen med observerade data väldigt bra. Detta resultat representerar utmärkt förståelse för detektorn och rekonstruktion av partiklar och partikelkollisioner. Även om ingen observation av dubbelt laddade Higgs-bosoner hittats, så kan man sätta den nedre gränsen för deras massa. Sökningarna täcker mycket intressanta signaturer med flera leptoner av samma laddning, vilket tillåter ett brett spektrum av teoretiska tolkningar och ger en bra och lovande utgångspunkt för mer optimerade studier i framtiden.

PREFACE

The studies reported in this thesis were performed at the ATLAS experiment in 2016–2019. The ATLAS experiment at the Large Hadron Collider at CERN is designed to allow a large variety of different physics analyses, ranging from testing the predictions of the Standard Model in high precision to explore rare signatures to find new physics beyond the Standard Model. This thesis focuses on the latter.

The first study of the thesis concerns the Transition Radiation Tracker (TRT), a subdetector which is used both for tracking and particle identification purposes. Tracking is essential for nearly all physics analyses, because most of the physics objects, such as charged leptons, rely on precise identification and determination of charged particle tracks. I calibrated the electron drift time, and measured position and drift time resolution both in proton–proton and heavy ion collision data. Moreover, I simulated and validated the corresponding simulated samples and studied the effects of different gas geometries. This work significantly improved the drift time accuracy and the hit position resolution, especially in cases where the TRT operates only with an argon-based gas mixture. I wrote a supporting note intended for ATLAS internal use, describing all the technical details of the work.

I actively supported the operations of the TRT as a regular and expert data quality shifter in 2016–2018. As a calibration expert, I was responsible for making sure the offline calibration procedure after each run works, and solving issues by investigating which part of the procedure or detector elements were causing problems. Apart from physics, I initiated and maintained a broad troubleshooting documentation for issues in the data quality and calibration, and maintained the version controlling of the calibration code. This work also involves training of other TRT shifters. I also contributed to modifying and validating the TRT software in new ATLAS reconstruction software release, Athena release 21, which included a comprehensive testing of tools and algorithms to make sure they are suitable for parallel computing. In parallel with the TRT work, I took multiple Inner Detector shifts at the ATLAS control room. A good understanding of the detector and tracking are vital for the next and main studies of this thesis: the searches for doubly charged Higgs bosons decaying into multi-lepton final states.

In the search for doubly charged Higgs bosons $H^{\pm\pm}$ decaying into $e^{\pm}e^{\pm}$, $e^{\pm}\mu^{\pm}$, and $\mu^{\pm}\mu^{\pm}$ final states with a data sample recorded in 2015–2016 by the ATLAS detector, I produced the simulated signal samples, and analysed especially the lepton flavour violating electron–muon channel. This task included optimizing event and object selection, validation of background predictions, and performing various cross-checks for all analysis channels. I also estimated systematic uncertainties, in particular uncertainties in the signal acceptance by varying the showering parameters in event generation. As no significant excess was found in the same-charge lepton invariant mass distributions, the limits on the mass and production cross-section of the doubly charged Higgs bosons were set. I also verified that the other decay modes of the doubly charged Higgs boson, such as $W^{\pm}W^{\pm}$, do not have a significant impact on the obtained results. The study was performed by generating a set of new signal samples and deriving the likelihood fit for each of the new hypotheses. The results were presented first as a conference note and then published in The European Physical Journal C. I participated in writing and editing of both the conference note and the main article, as well as the internal supporting documentation.

Briefly after that, the doubly charged Higgs analysis team started to search for heavy Majorana or Dirac neutrinos and right-handed W gauge bosons. The analysis framework I co-

developed for the $H^{\pm\pm}$ search was used in this search, especially in the background estimation of the same-charge lepton final states, resulting in a published article in Journal of High Energy Physics. Since there are many new physics models with similar leptonic final states, the ATLAS Multilepton cluster was formed with the idea of sharing the same analysis tools and processed datasets. For the search for type-III seesaw heavy leptons, I studied different event and kinematic cuts to improve signal efficiency and significance in the final states with light charged leptons and two jets. This work also included studying different electron and muon quality and isolation working points to maximize signal significancies, editing the supporting documentation, and developing the analysis framework. This work was published as an conference note at the Sixth Annual Conference on Large Hadron Collider Physics (LHCP2018). These searches for heavy neutrinos and new heavy leptons will be only briefly mentioned later in this thesis, and the search for doubly charged Higgs bosons will be in the spotlight instead.

Next step in my PhD journey was to extend the doubly charged Higgs boson search with hadronically decaying taus. Because sprays of hadrons called jets are easily misidentified as hadronically decaying tau leptons, I joined the ATLAS Fake-Tau Task Force aiming at understanding such fake objects better. I continued to develop an event generation filter, where the idea is to enrich simulated data sample with jets misidentified as hadronic taus. The fake-enriched samples can help in validating data-driven estimations of fake-tau background and in estimating systematic uncertainties. In addition, I compared the modelling of fake taus in full and fast ATLAS simulation to investigate if a significant improvement in fast simulation computing time can be gained with no accuracy losses, and to understand the differences observed between data and simulation. I performed the whole production chain of simulated samples from event generation to final analysis data samples.

For the search for doubly charged Higgs bosons using the full Run 2 dataset, I am the leading analyst and the senior graduate student, and I coordinate the analysis activities. I produced signal samples, and designed signal, control and validation regions for both light lepton and tau-inclusive channels. I re-optimized previous light lepton channels using improvements in reconstruction performance and event selection, and identified ways to increase signal sensitivity in all analysis channels. After ceaseless process of testing, validating, cross-checking, pushing and pulling, I derived exclusion limits on the doubly charged Higgs mass and production cross-section. Although no signal was found, the search covers a very interesting signature over a wide mass range with multiple final states, allowing many future interpretations.

I presented the results of the searches for doubly charged Higgs bosons and other ATLAS searches in two international conferences on behalf of the ATLAS Collaboration. The first talk about searches for new phenomena in leptonic final states was presented at the *Origin of Mass at the High Energy and Intensity Frontier (MASS2018)* conference, and the second talk about searches for exotic Higgs production and decays was presented at the *1st Mediterranean Conference on Higgs physics (MCHP2019)*.

To summarize, I was fortunate to get to grips with all the major aspects of the physics analysis, from generating signal samples to designing analysis regions and from understanding various signatures to performing statistical analysis in the form of setting exclusion limits. Working on the TRT and taking the control room shifts prepared me to understand where the data *really* come from and how tracking works, and studying the origin of fake taus also let me dip into the world of jets in addition to the charged leptons.

PUBLICATIONS

Some of the original work described in this thesis has appeared previously in the following publications:

[1] ATLAS Collaboration. *Search for heavy Majorana or Dirac neutrinos and right-handed W gauge bosons in final states with two charged leptons and two jets at* $\sqrt{s} = 13\,\text{TeV}$ *with the ATLAS detector*.
Journal of High Energy Physics (2019): 16.

[2] ATLAS Collaboration. *Search for doubly charged Higgs boson production in multi-lepton final states with the ATLAS detector using proton-proton collisions at* $\sqrt{s} = 13\,\text{TeV}$.
The European Physical Journal C (2018) **78**: 199.

[3] ATLAS Collaboration. *Search for type-III seesaw heavy leptons using proton-proton collisions at* $\sqrt{s} = 13\,\text{TeV}$ *with the ATLAS detector*.
ATLAS-CONF-2018-020. LHCP 2018 conference note.

[4] ATLAS Collaboration. *Search for doubly-charged Higgs boson production in multi-lepton final states with the ATLAS detector using proton-proton collisions at* $\sqrt{s} = 13\,\text{TeV}$.
ATLAS-CONF-2017-053. EPS-HEP 2017 conference note. These preliminary results are superseded by [2].

Manuscript in preparation:

Search for doubly charged Higgs boson production in multi-lepton final states with the ATLAS detector using 139 fb^{-1} *of proton-proton collisions at* $\sqrt{s} = 13\,\text{TeV}$.
Results with the full Run 2 dataset, including all charged lepton flavours.

THESIS OUTLINE

The Standard Model of particle physics describes elementary particles and their interactions, as outlined in Chapter 1. Despite its remarkable success, crowned by the discovery of the Higgs boson in 2012 by the ATLAS and CMS experiments, it is incomplete in part. There are a number of observations left unexplained by the Standard Model, such as non-zero neutrino masses, dark matter, and asymmetry of matter and antimatter in the Universe. Various models and theories have been proposed to extend or re-write the Standard Model in order to address some or all of the shortcomings of the Standard Model. Many well-motivated models beyond the Standard Model extend the Higgs spectrum to contain new doubly charged Higgs bosons. Such particles could decay into same-charge lepton final states, which provide a clean signature to be observed thanks to precise tracking and low background from the Standard Model processes. If found, doubly charged Higgs bosons could reveal the mechanism for generating small neutrino masses and open a window into new physics, as described in Chapter 2.

How the particles are searched for experimentally is explained in the following chapters. Chapter 3 introduces the Largon Hadron Collider, and one of its main experiments, the ATLAS experiment, is presented in detail in Chapter 4. Chapter 5 introduces how real and simulated data are processed, and how various physics objects are reconstructed and identified. In order to study final states involving charged leptons, their trajectories have to be precisely reconstructed. Chapter 6 shows how the ATLAS Transition Radiation Tracker (TRT) provides high-resolution tracking and how it is calibrated in various gas configurations using both

simulated and real data from proton–proton and heavy ion collisions, leading to improved hit position resolution and good data quality during the full Run 2.

The last part of the thesis presents searches for doubly charged Higgs bosons, which are hoped to manifest themselves as an excess of events in the same-charge dilepton invariant mass distribution. Chapter 7 gives an overview of the searches at ATLAS, and describes how to make these searches as sensitive to new physics as possible. Data-driven methods to model background in the same-charge lepton channels are presented, providing an excellent understanding between the collision data and Standard Model background predictions. The first search targeting electron and muon final states using a dataset collected in 2015–2016 is presented in Chapter 8, and the full Run 2 search recorded in 2015–2018 and including final states also with hadronically decaying taus is presented in Chapter 9. Finally, summary and outlook are given in Chapter 10.

AMI ATLAS metadata interface
AOD Analysis object data. Data format
ASDBLR The amplifier-shaper-discriminator baseline restorer, the first TRT front-end chip
Athena ATLAS offline software framework
ATLAS A Toroidal LHC ApparatuS
Atlfast-II The ATLAS fast simulation program
BDT Boosted decicion tree
BSM Beyond the Standard Model
B (or BR) Branching ratio
CL Confidence level
CLs Method to estimate modified frequentist confidence limits
CMS Compact Muon Solenoid
CondDB Conditions database to store the record of the detector conditions required for data analysis, for example calibration constants
COOL LCG conditions database project
CP Charge and parity symmetry
CR Control region
CSC Cathode strip chambers (Muon spectrometer)
DAOD Derived analysis object data. Data format
DAQ Data acquisition
DB Diboson
DTMROC The drift time measurement and read-out chip, the second TRT front-end chip
ECAL Electromagnetic calorimeter
ESD Event summary data. Data format
Geant4 A toolkit for simulation of the passage of particles through matter
HCAL Hadronic calorimeter
HLT High level trigger
ID Inner Detector
IOV Interval of validity
IP Impact parameter, or interaction point
LEP Large Electron Positron Collider
LFV Lepton flavour violation
LHC Large Hadron Collider
LO Leading order
LRSM Left-right symmetric model
MC Monte Carlo simulation
MDT Monitored drift tube (Muon spectrometer)
MIP Minimum ionizing particle
MS Muon spectrometer
NLO Next-to-leading order
NNLO Next-to-next-to-leading order
OC (or OS) Opposite-charge leptons
PDF Parton density function
POOL Pool of persisent objects for LHC

PV Primary vertex
QCD Quantum chromodynamics
RAW Raw data format
ROB Read-out buffer
ROD Read-out driver, the back-end electronics card
ROI Region of Interest, a sub-zone of the ATLAS detector used for Level-2 triggering
RPC Resistive plate chambers (Muon spectrometer)
SC (or SS) Same-charge leptons
SM Standard Model
SR Signal region
to TRT $t0$ time offset
TGC Thin gap chambers (Muon spectrometer)
ToF Time of flight
ToT Time over threshold
TRT Transition Radiation Tracker
TTC The trigger, timing, and control
vev Vacuum expectation value
VR Validation region

SYMBOLS

ΔR	Angular distance between two objects. $\Delta R = \sqrt{(\Delta\eta)^2 + (\Delta\phi)^2}$
ϕ	Azimuthal angle
ℓ	Charged lepton (electron, muon, or tau)
σ	Cross-section, or signal significance, or a width of a distribution
τ_{had}	Hadronically decaying tau
$\mathcal{L}$	Integrated luminosity, Lagrangian (density), or likelihood function
τ_{lep}	Leptonically decaying tau
γ	Lorentz factor, or photon
η	Pseudorapidity
β	Ratio of velocity (v) to the speed of light (c): $\beta = v/c$
c	The speed of light
M_{T}	Transverse mass
p_{T}	Transverse momentum
$\tau_{\text{had}-\text{vis}}$	Visible part of a hadronic decay of a tau lepton (without the neutrino)

CONVENTIONS

Natural units are used throughout the thesis. In natural units, the reduced Planck constant is set to $\hbar = \frac{h}{2\pi} = 1$ and the speed of light is set to $c = 1$. Therefore, the equation $E^2 = p^2c^2 + m^2c^4$ becomes $E^2 = p^2 + m^2$, where all quantities are usually measured in GeV ($1\,\text{GeV} = 1 \cdot 10^9\,\text{eV}$, where 1 eV is the energy that an electron gains when it passes through an electric potential difference of 1 V).

Electric charges are expressed in units of the elementary charge e. Charges of particles may be omitted, and the charge-conjugate decay modes are implied. For example $W^{\pm}$ may be denoted W, and the process $Z^0 \to \ell^+\ell^-$ may be referred to as $Z \to \ell\ell$. Similarly, leptonic ($\tau \to \ell\nu\bar{\nu}$) and hadronic ($\tau \to$ hadrons ν) tau decays include both τ^- and τ^+, such as in the decay $\tau^- \to e^-\bar{\nu}_e\nu_\tau$.

ACKNOWLEDGMENTS

It was a huge step to take from a cosmic ray experiment to the particle collider world: suddenly I got access to billions of data events and got 3000 new colleagues. To work as a PhD in a large collaboration like ATLAS is therefore a good piece of teamwork. This thesis would not have been possible without the support, exchange of ideas, and help of a great deal of people, too numerous to be named here. Thank you all!

I would like to thank my supervisor Else Lytken for her endless help and support during my PhD project, for letting me do things in my own way and for always being online. A very special gratitude goes out to Torsten Åkesson, my co-supervisor, for challenging me with difficult questions. He always encouraged me to take time to *think* and reflect - very important lesson. I would also like to thank Anders Oskarsson for reading this thesis draft and giving valuable feedback. In addition to boosting my morning energy with fresh coffee, he always gives me new insights into the detector world.

I am grateful to Ruth Pöttgen and Caterina Doglioni for giving priceless advice for presentations and applications from a successful early career researcher perspective. I would also like to thank Melissa Franklin for insightful and inspirational discussions, chalkboard talks, and seminars. Bozena Wlosinska: stort tack för din hjälp och stöd! Thanks to everyone at the particle physics division in Lund for Christmas parties, division excursions and fredagsfika. It was great to have such a positive working environment here!

It was fantastic to have the opportunity to work at the ATLAS experiment with so many great and talented people.

I wish to thank the whole TRT group, especially Peter Hansen, Anatoli Romaniuk, and Fred Luehring, the TRT godfather, for endless support and constructive feedback in the early parts of my PhD. Thanks to Alejandro Alonso for helping me through the calibration code jungle, and to Christian Grefe and Philippe Calfayan for guidance, explanations and discussions.

The main part of this thesis was performed within the ATLAS same-sign lepton and multilepton cluster, where Antonio Sidoti, Max Sioli and Borut Kersevan provided very generous support. Thank you for sharing your expertise! I appreciate everything that Miha Muskinja, Giulia Ucchielli, Federico Scutti, Tadej Novak, Giuseppe Carratta, and Matteo Franchini have done to keep the analysis running smoothly. Much of our team's success is due to your extraordinary skills and hard work. I've really enjoyed working with you. Simon Arnling Bååth and Shi Qiu also made enormous contribution to the doubly charged Higgs searches with hadronically decaying taus during their master's projects in Lund. Thank you for all the important work and cross-checks!

It has been great to work with, learn from, and get to know many physicists from across the world at schools, conferences and CERN. Especially the rooftop gang, thank you so much for *whatever happened* in Quy Nhon and later at CERN. I've had many extremely memorable and great moments with you.

I would also like to thank all LU-ATLAS post docs. Thanks to Will Kalderon for explaining triggers and jets over and over again (I still hope you discover a dark matter particle and

it will be named after you). Thanks to Geoffrey Mullier for challenging my views on the European strategy for particle physics, and for describing the peculiarities of the new Inner Tracker. Thanks to Jannik Geisen for running tips and moral support when I was finalizing this thesis. Thanks also to the LU-ALICE people next doors for all the afterwork evenings in Lund and at CERN.

I couldn't have reached this far without my friends at the A408 office. Thanks to all of you for so many things:

To Trine for saving the world, for listening my last-minute panics, and for excellent Danish delicacies at fika and dinner parties. To Eric for post it notes, mysig resa till kusten, gifs, theory help, and Swedish support. To Eva for pause boogie and running tips as well as promising to me and Trine that there will be a dark matter discovery by 2040. Also, thank you for all the calibrated jets. Thanks to Edgar for music recommendations, board game nights, and fun times in Belgium. To Eleni for providing a supporting shoulder, fixing bugs and memory leaks, and hosting wonderful parties. To Caterina for CPU time optimizations, finding ATLAS approved plots, and Sunday fikas. To Nathan for helping me choose the colours for the Higgs potential figure, and for continuing the triumph of the TRT. To Alex for borrowing the HDMI cable and for taking care of our Hallandslax.

Last but not least, I wish express my gratitude to my entire family: To my extended family in Kajaani and Juusonniemi for relaxing vacations and for supporting me in the good as well as the troubling times. To my sister Piia, a great travel buddy, who also let me know when she learned how to solve integrals and who suddenly asked what 2HDM means. To my parents Kaija and Matti for always supporting me wherever I end up going, for helping me reach my goals, and for saying one can become whatever she wants to be. Most importantly, to Tuukka. From the atomic physics 1 exercise sessions to the other side of the world and back, thank you for everything and more.

CONTENTS

Part I

THEORETICAL BACKGROUND

1 THE STANDARD MODEL

"And now, my dear companions," said Michel Ardan, "let us make ourselves at home; I am a domesticated man and strong in housekeeping. We are bound to make the best of our new lodgings, and make ourselves comfortable. And first let us try and see a little. Gas was not invented for moles."
— From the Earth to the Moon by Jules Verne

It is only fair to say that we may live a meaningful life without knowing what our Universe is made of, what the smallest building blocks are, and how they gain their masses. An understanding of the peculiar nature of neutrinos won't help us sleep better or make us good chefs.[1]. However, to the realm of modern wizards we call particle physicists, these questions form the most interesting puzzles. Particle physics is at the heart of understanding nature from the scales as huge as the Universe to the smallest, point-like particles and interactions between them.

A theory of elementary particles, called the Standard Model, covers more or less everything we know about particle physics at the moment. It explains how the elementary (or fundamental) particles and three of the fundamental forces of nature are related to each other. This first chapter will offer you a world of insight into the building blocks of our universe by giving an overview of the Standard Model of particle physics together with a brief summary of the elementary particles and their fundamental interactions.

1.1 ELEMENTARY PARTICLES

Ordinary matter we encounter each day is made up of atoms, which are themselves made up of particles distinguished by their electrical charge. Positively charged protons and neutral neutrons form an atom nucleus, which is surrounded by a cloud of negatively charged electrons. Protons and neutrons have inner structure: they are made up of quarks. The *elementary* or *fundamental particles*, such as electrons and quarks, are point-like and cannot be broken down into smaller constituents at least at the wavelengths we have been able to use. Yet they have measurable properties.

Each elementary particle carries many labels, such as mass, electric charge and *spin*, which represents an intrinsic angular momentum of a particle. Based on the spin, the elementary constituents of matter can be grouped in two big families, *fermions* and *bosons*, that obey different laws of statistics. In general, fermions are responsible for matter, and bosons for the forces of nature. All the elementary particles included in the Standard Model together with some of their properties are shown in Figure 1.

Fermions form the constituents of the known matter in the Universe and have a half-integer spin ($\frac{1}{2}, \frac{3}{2}, \frac{5}{2}, ...$). They obey Fermi-Dirac statistics and the Pauli exclusion principle which states that two identical fermions cannot occupy the same quantum state. Elementary fermions are further divided into two groups, *leptons* and *quarks*[2].

1 Or, as Thom Whyntie put it: "You don't need to know the difference between a muon and a gluon to order and enjoy a pint of beer, a glass of wine or an ice-cold soft drink" [5].

2 There are also composite fermions, such as baryons, which contain three quarks. Protons and neutrons are famous baryons.

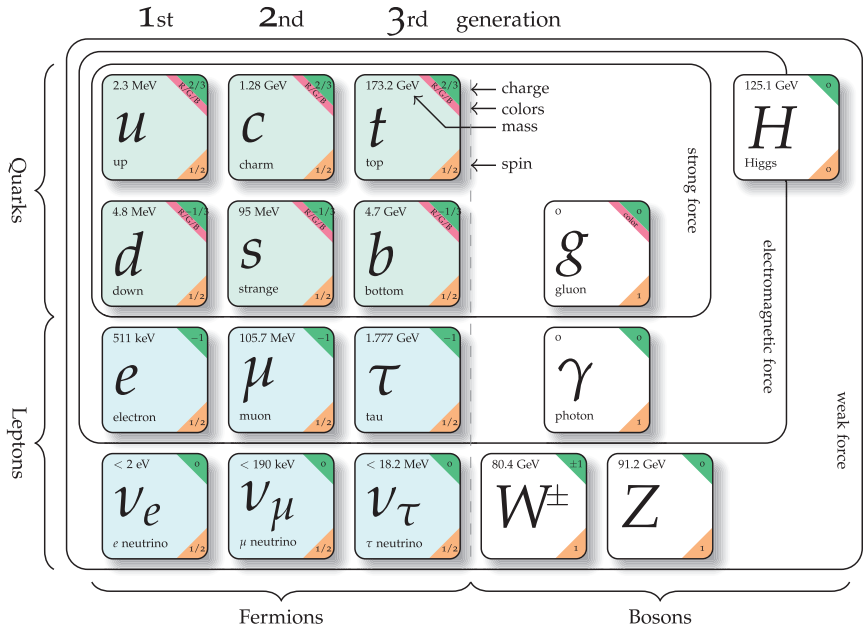

Figure 1: Elementary particles included in the Standard Model: 6 quarks, 6 leptons, 12 fermions, and 5 bosons. Masses of fermions increase from left to right. Modified from [6].

Leptons come in six flavours - unfortunately not in vanilla, chocolate, and strawberry - and they occur in pairs, called families or generations. For each family, there is a charged lepton carrying an electric charge, and a neutral neutrino. The three charged leptons are the electron e^-, the muon μ^-, and the tau τ^- with their associated neutrinos called the electron neutrino ν_e, muon neutrino ν_μ, and tau neutrino ν_τ, respectively. Based on their families, leptons are assigned a lepton number. The electron lepton number L_e (which is 1 for electrons and electron neutrinos but 0 for all other leptons), the muon lepton number L_μ and the tau lepton number L_τ are conserved in any interaction in the Standard Model.

All charged leptons have similar properties apart from the differences in their masses[3]. The muon is a heavier cousin of the electron with a mass $m_\mu \approx 207 m_e$. Therefore, it can decay into the electron, neutrinos, and photons, with dominant decay mode being $\mu^- \rightarrow e^- + \nu_\mu + \bar{\nu}_e$. Tau lepton is special: with a mass of 1.777 GeV [7] ($m_\tau \approx 3477 m_e$) and a short mean lifetime of $2.9 \cdot 10^{-13}$ s ($c\tau = 87\,\mu$m), it travels only a very short distance and it is the only lepton heavy enough to decay into both hadrons (h)[4] and leptons. Hadronic tau decays are characterized by one or three charged pions ($\pi^\pm$) or kaons ($K^\pm$), one neutrino (ν_τ) and up to two neutral pions (π^0). The hadronic decays proceed mainly through the intermediate $\rho(770\,\text{MeV})$ and $a_1(1260\,\text{MeV})$ resonances. The neutral pions decay almost exclusively to two photons. The hadronic decays account for about 65% of total tau decay modes. In the remaining 35% of the cases, taus decay purely leptonically into an electron or a muon and two neutrinos. The tau decay modes and branching fractions are summarized in Table 1.

3 Neutrinos are considered to be massless in the Standard Model, but in reality they have been observed to have tiny, non-zero masses. This will be discussed further in Section 2.1.1.

4 *Hadron* is again a classification term for bound states of quarks, such as protons and pions

Table 1: Approximate branching fractions B of different τ decay modes. [7]

Decay mode	B [%]
$\tau^- \to e^- \bar{\nu}_e \nu_\tau$	17.8
$\tau^- \to \mu^- \bar{\nu}_\mu \nu_\tau$	17.4
All pure leptonic modes	35.2
$\tau^- \to h^- \pi^0 \nu_\tau$	26.0
$\tau^- \to h^- \nu_\tau$	11.5
$\tau^- \to h^- \pi^0 \pi^0 \nu_\tau$	9.5
$\tau^- \to h^- h^+ h^- \nu_\tau$	9.8
$\tau^- \to h^- h^+ h^- \pi^0 \nu_\tau$	4.8
Other modes with hadrons	3.2
All modes with hadrons	64.8

Just as leptons, the six quarks are also divided into three generations. Up-type quarks called up u, charm c, and top t carry an electric charge of $2/3$ while down-type quarks down d, strange s and bottom b have an electric charge of $-1/3$. The quark masses also increase in higher generations: the top quark is the heaviest of all known elementary particles with a mass of $m_t \approx 173\,\text{GeV}$.

In addition to these particles, there are also corresponding *antiparticles* that are particles with identical masses but carry quantum numbers and electric charge of an opposite sign: for electron e^- there is a positron e^+, for its neutrino ν_e there is an antineutrino $\bar{\nu}_e$, and for an up quark u there is an up antiquark $\bar{u}$.

Another big family in the particle zoo consists of bosons. Bosons have an integer spin $(0, 1, 2, ...)$, and obey Bose-Einstein statistics. Almost all bosons are spin-1 particles (*vector* bosons) with the exception of the famous Higgs boson that has spin 0 (and is therefore a *scalar* boson). Bosons can be elementary, such as the Standard Model *force carriers* gluon g, photon γ, Z, W^- and W^+ bosons and the Higgs boson; or composite such as mesons that are composed of a quark and an antiquark.[5] The role of the bosons will become visible in the next section, where the interactions between all elementary particles are described.

1.2 PARTICLE INTERACTIONS

The aforementioned elementary particles interact via four forces of nature. *Strong* force, mediated by gluons, binds the quarks together into hadrons. The *electromagnetic* force, mediated by photons, is responsible for all electro-magnetic processes such as light. The *weak* force is responsible for nuclear processes like the beta decay, and it is mediated by the $W^\pm$ or Z bosons. The last one is *gravity*, probably the most known but the weakest of the four forces, which is not covered in the Standard Model and will be neglected for now[6].

1.2.1 *Electromagnetic interaction*

Both electricity and magnetism are familiar phenomena in our everyday life from light bulbs to X-ray scans and from wireless internet connection to souvenir magnets on the fridge. The

5 "If I could remember the names of all these particles I'd be a botanist." -Enrico Fermi [8]

6 Furthermore, an elementary particle that could mediate the force of gravity - graviton - has not been observed.

electromagnetic force keeps atoms together: positive protons in the nucleus attract negative electrons surrounding them.

These phenomena are fundamentally portrayed by the theory of quantum electrodynamics (QED), which describes interactions between electrically charged fermions and the mediator of electromagnetic force, photon γ. As photons are massless and travel with the speed of light, the range of the force is infinite.

1.2.2 *Strong interaction*

Quantum chromodynamics (QCD) describes strong interactions between quarks and gluons. When the quarks interact, they interact strongly by exchanging gluons that *glue* the quarks together in hadrons, and hadrons to nuclei. Strong interactions also hold protons and neutrons together in atomic nuclei, which sets the range of the interaction to 10^{-15} m, about the size of a nucleus.

The strong interaction is based on *colour* charge, just as electromagnetic interaction is based on electric charge. However, colour in this sense is completely unrelated to the everyday meaning of colour. Colour charge comes in three different types, red, blue, and green, and corresponding anticolours antired, antiblue, and antigreen. If a composite hadron contains all three colour states (like a proton), or a colour and an anticolour, it is colourless i.e. it has a zero net colour charge. Each quark has a colour, and each antiquark has an anticolour. The gluon - the mediator of strong interaction - exists in eight different states and carries a combination of colour and anti-colour. Since gluons have colour, they can interact not only with quarks but also with themselves[7].

Due to the colour force, quarks are *confined* and must combine into colourless hadrons. The closer the quarks are to each other, the *weaker* the colour force and therefore the weaker the interaction. In fact, if the interaction length scale is small enough, the force is so weak that the quarks behave almost as free particles[8]. This principle is known as *asymptotic freedom*. Accordingly, if one tries to separate two quarks in a hadron, more and more energy is needed, until the energy becomes so large that it exceeds the threshold for the creation of a new quark-antiquark pair. In this process, called *hadronization*, two colourless hadrons are produced instead of a single isolated colour charge[9]. This is an important property of coloured particles - they have never been observed free and alone. In particle accelerator experiments we observe a spray of hadrons, called *jets*, instead of single quarks or gluons.

The strength of the strong interaction therefore depends on the energy scale. The coupling strength α_s is not constant but it instead depends on the energy scale: it is a *running* coupling constant. For the scale of the momentum transfer (Q), the $\alpha_s(Q^2)$ indicates the strength of the strong interaction in the process, and to first order accuracy can be expressed as [10]

$$\alpha_s(Q^2) = \frac{4\pi}{b_0 \ln(Q^2/\Lambda_{QCD}^2)} \tag{1}$$

where $b_0 = (11C_A - 4n_f T_R)/(12\pi) = (33 - 2n_f)/(12\pi)$ is the leading order β-function coefficient, C_A and T_R are the colour factors associated to QCD processes, n_f is the number

7 This differs from the electromagnetic case where photons do not themselves have any electric charge and therefore cannot self-interact. Similarly, leptons do not have colour, preventing them to interact strongly.

8 Just as Rutherford revealed the nucleus of an atom by deflecting alpha particles passing through a thin gold foil, we can use Deep Inelastic Scattering to learn about the structure of protons.

9 A nice analogy to a hadron is a rubber band or a string like in the famous Lund string model [9]. Quarks are like the ends of a rubber band that stretches, but eventually pulls quarks back together again - or snaps into two pieces.

of fermions, and $\Lambda_{QCD} \approx 250\,\text{MeV}$. Experimentally measured the world average value of α_s at the Z mass scale is of $\alpha_s(m_Z^2) = 0.1181(11)$ [7]. At low energy scales, the coupling constant is large, $\alpha_s \approx \mathcal{O}(1)$, while in the limit $Q \to \infty, \alpha_s \to 0$.

1.2.3 *The electroweak interaction*

The weak interaction couples to all the fermions in the Standard Model. It is mediated by charged $W^\pm$ bosons and a neutral Z boson that, unlike gluons and photons, have masses ($m_W = 80.4\,\text{GeV}, m_Z = 91.2\,\text{GeV}$) and thus the interaction has a short range. Despite being much weaker than electromagnetic and strong interactions, it plays a key role in variety of physical processes: in radioactive decays such as the β decay, in changing the flavour of particles and in the violation of parity and charge-parity symmetries to be discussed shortly. In fact, without weak interaction even the Sun would not shine as it gets its energy from fusion reactions.

The $W^\pm$ bosons carry the weak *charged* current. Interestingly, they are involved in the *violation* of parity conservation. Parity transformation means simultaneously inverting the sign of spatial coordinates: a left-handed coordinate system is flipped into a right-handed coordinate system, and vice versa, like a mirror. For a long time it was believed that parity is conserved in nature. However, the Wu experiment discovered that $W^\pm$ bosons couple only to left-chiral particles (*left-handed*) and right-chiral (*right-handed*) antiparticles. Chirality is an intrinsic property of the particles with non-integer spin. For massless particles, the chirality is the same as (perhaps more intuitive) helicity, which is the dot product between the spin and momentum of the particle: particle travelling in the same direction as its spin is said to be right-handed, whereas a left-handed particle travels in the opposite direction to its spin. Antiparticles have opposite-sign helicities to those of corresponding particles. However, the helicity depends on the reference frame and is not Lorentz invariant, and therefore the chirality of massive particles is a more useful property. It is related to the *weak isospin* I, a charge of the weak interaction that all fundamental fermions carry. The weak isospin differentiates left-handed ($I = \frac{1}{2}$) fermions from right-handed ($I = 0$) fermions. In other words, only left-handed particles interact via the weak force. The weak interaction also violates the charge-parity (CP) conservation, where a particle is interchanged with its antiparticle and left-handed particles with right-handed particles.

The *electroweak* (EW) interaction is a unified description of the electromagnetic and weak force of the Standard Model. Although the two interactions appear to be distinct at low energies, the electroweak theory unifies them into one force beyond the unification energy of roughly 100 GeV. In the unified electroweak force, the charge in question is the *hyperchage*, defined as $Y = 2(Q - I_3)$ where Q is the electric charge and I_3 is the third component of the weak isospin. Hypercharge is only carried by left-handed particles, and is $I_3 = +\frac{1}{2}$ for up-type quarks and neutrinos, and $I_3 = -\frac{1}{2}$ for down-type quarks and negatively-charged leptons. The corresponding antifermions have reversed chirality and opposite-sign I_3.

The exchange of a $W^\pm$ boson changes both the flavour and the charge of the fermions: for instance, up-type quarks with $I_3 = +\frac{1}{2}$ transform via the weak interaction to down-type quarks with $I_3 = -\frac{1}{2}$. However, the electroweak eigenstates of down-type quarks (labelled as d', s', b') are not the actual quark mass eigenstates (d, s, b). This allows a transition between generations for quarks according to the unitary Cabibbo-Kobayashi-Maskawa (CKM) matrix:

$$\begin{pmatrix} d' \\ s' \\ b' \end{pmatrix} = \begin{pmatrix} V_{ud} & V_{us} & V_{ub} \\ V_{cd} & V_{cs} & V_{cb} \\ V_{td} & V_{ts} & V_{tb} \end{pmatrix} \begin{pmatrix} d \\ s \\ b \end{pmatrix} \tag{2}$$

The diagonal elements of the CKM are close to unity, which means that the transitions within one generation are favoured whereas the transition between families are strongly suppressed in the SM.

The weak interactions are also mediated by a Z^0 boson carrying the weak *neutral* current. It couples to fermions but does not change their flavour nor charge. The Z^0 boson has different coupling strength to left-handed and right-handed fermions, so these interactions also violate parity.

1.2.4 *Standard Model Lagrangian*

While the detailed mathematical expressions and derivations are outside the scope of this thesis, a brief summary of the Lagrangian formalism and quantum field theory is necessary for the understanding of the Higgs mechanism and models beyond the Standard Model. This section follows notations and examples from Refs. [11–13].

The Standard Model incorporates relativity and quantum mechanics[10] and therefore it is based on quantum field theory (QFT) where particles are excitations (or quanta) of *fields*. The dynamics of the fields are described by the *Lagrangian* formalism and symmetries. [11] Just as in classical mechanics, the equations of motion can be obtained from the Lagrangian $L = T - V$, where T is the kinetic energy and V is the potential energy of the system. In continuous system, L can be replaced with the Lagrangian density $\mathcal{L}(\phi_i, \partial_\mu \phi_i)$ where ϕ_i are *fields* and $\partial_\mu \phi_i$ are the derivatives of the fields with respect to the space-time coordinates. In the following, the Lagrangian density will be simply referred to as Lagrangian. The single-particle wave functions introduced in quantum mechanics can be replaced by excitations of a quantum field, defined at all points in space-time and satisfying the appropriate field equations. For example, spin-0 scalar particles are described by excitations of the scalar field ϕ.

Every well-known conservation law of classical physics (such as conservation of energy, momentum, and angular momentum) reveals a corresponding symmetry in nature. Similarly, every symmetry is related to a conserved quantity. This is the Noether's theorem proven by mathematician Emmy Noether, and it allows us to derive conservation laws from symmetries in the Lagrangian. When a given transformation leaves the equations of motion invariant, we call that transformation a symmetry. Symmetries can be *local*, meaning that they depend on the particular points in space and time, or *global*, meaning that they hold at all points in the space-time. In terms of particles, local symmetries are found to be related to forces, while global symmetries are found to be related to the properties of particles. Symmetries are therefore important for labelling and classifying particles as well as determining the interactions between them.

10 Particles move close to the speed of light, calling for relativity, and very short distance scales are considered, calling for quantum mechanics.

11 Symmetry is defined as a concept that does not change under a set of transformations - it is *invariant*. For example a ball looks the same if it is rotated back and forth, and therefore it has a rotational symmetry. Very good book about symmetries and their relation to particle physics can be found in Ref. [13].

For each interaction, there is a corresponding field, and the gauge[12] bosons mediating the interaction are the excitations of that field. The number of gauge bosons is equal to the number of generators of the field; the generators, in turn, come from the unitary group[13] which describe the symmetries of the field. The Standard Model has three symmetry groups: U(1), SU(2), and SU(3).

The symmetry group of the electromagnetic field is U(1), where U stands for unitarity with the condition $U^\dagger U = 1$. Since there is only one generator for the field, the associated electromagnetic force is mediated by a single, massless particle, the photon. Using Noether's theorem, we can also derive a conserved quantity from this symmetry, which can be interpreted as electric charge.

The gauge group of the weak field is SU(2), which has three generators, i.e. three gauge bosons that mediate the weak force: W^+, W^-, and Z bosons. The electro-weak interactions are therefore described by a gauge theory with the gauge group $\mathrm{SU}(2) \times \mathrm{U}(1)$. Last, the gauge group of the strong field is SU(3) corresponding to three fermion fields, giving 8 massless gluons that act on the colour charge. The left-handed fermions are paired in doublets under SU(2) because they can interact via the weak force and therefore can transform into each other, whereas the right-handed fermions are singlets because they do not interact via the weak force. It is worth emphasizing that there is no right-handed neutrino nor left-handed anti-neutrino. The lepton doublets and singlets can therefore be denoted as

$$\begin{pmatrix} \nu_e \\ e \end{pmatrix}_L , \begin{pmatrix} \nu_\mu \\ \mu \end{pmatrix}_L , \begin{pmatrix} \nu_\tau \\ \tau \end{pmatrix}_L , \; e_R, \; \mu_R, \; \tau_R \tag{3}$$

and the quark doublet and singlets are of the form

$$\begin{pmatrix} u \\ d' \end{pmatrix}_L , \begin{pmatrix} c \\ s' \end{pmatrix}_L , \begin{pmatrix} t \\ b' \end{pmatrix}_L , \; u_R, \; d_R, \; c_R \; s_R \; t_R \; b_R. \tag{4}$$

Finally, we can summarize the mathematical formulation of the Standard Model. Its symmetry group is

$$\mathrm{SU}(3)_C \times \mathrm{SU}(2)_L \times \mathrm{U}(1)_Y \tag{5}$$

where $\mathrm{SU}(3)_C$ is the unbroken colour (C) symmetry representing the strong interactions described by QCD, and $\mathrm{SU}(2)_L \times \mathrm{U}(1)_Y$ is the symmetry of the isospin and hypercharge gauge groups accounting for the unified electroweak interactions.

The Standard Model Lagrangian can be written using two components: the QCD Lagrangian and the EW Lagrangian:

$$\begin{aligned} \mathcal{L} &= \mathcal{L}^{QCD}_{SU(3)} + \mathcal{L}^{EW}_{SU(2)\times U(1)} \\ &= [\mathcal{L}^{\text{gauge}}_{SU(3)} + \mathcal{L}^{\text{matter}}_{SU(3)}]^{QCD} + [\mathcal{L}^{\text{gauge}}_{SU(2)\times U(1)} + \mathcal{L}^{\text{matter}}_{SU(2)\times U(1)} + \mathcal{L}^{\text{Higgs}}_{SU(2)\times U(1)} \\ &\quad + \mathcal{L}^{\text{Yukawa}}_{SU(2)\times U(1)}]^{EW}. \end{aligned} \tag{6}$$

The $\mathcal{L}^{\text{gauge}}$ term describes the dynamics of the gauge fields, i.e. gluons in the QCD and γ, Z and $W^\pm$ in the EW theories. The $\mathcal{L}^{\text{matter}}$ term covers interaction of the particles with the gauge

12 A nice explanation for "gauge" is the following from [13]: a bar that defines a standard meter (and which was used to measure length) can be arbitrarily changed without changing physics. Similarly, we can have different gauge fields, and transforming from one of the field to another field still describes the same physics.

13 *Group theory* is a branch of mathematics that deals with symmetries, and a *group* is a collection of transformations. Unitary groups $\mathrm{U}(N)$ have N^2 generators, while Special Unitary groups $\mathrm{SU}(N)$ have an extra restriction of an unit determinant (det(U)=1), which reduces the number of generators to $N^2 - 1$.

fields. However, there is one problem left. The Lagrangians described by these symmetry groups do not allow for any of the particles to have mass: in particular, gauge bosons $W^{\pm}$ and Z are predicted to be massless in order to preserve local gauge symmetry, yet clearly they have masses. However, mass terms can be added to the Lagrangian, if one breaks the SU(2) symmetry. After this *spontaneous symmetry breaking*, $\mathrm{SU}(2) \times \mathrm{U}(1)$ becomes $\mathrm{U}(1)_{\mathrm{EM}}$ and gives rise to the terms $\mathcal{L}^{\mathrm{Higgs}}$ and $\mathcal{L}^{\mathrm{Yukawa}}$ which are responsible for the interaction of the Higgs field with other particles and for generating their masses. The mechanism for spontaneous symmetry breaking will be covered in more detail in next section. In addition, the famous Higgs particle that has been left unattended will be finally introduced.

1.2.5 *Brout–Englert–Higgs mechanism: elementary particles get their masses*

The Brout–Englert–Higgs mechanism (or Higgs mechanism for short) is required to generate the masses of three electroweak gauge bosons, a neutral Z and charged $W^{\pm}$. For this reason, two complex scalar fields placed in a weak isospin doublet are introduced to the Lagrangian:

$$\phi = \begin{pmatrix} \phi_+ \\ \phi_0 \end{pmatrix} = \begin{pmatrix} \phi_1 + i\phi_2 \\ \phi_3 + i\phi_4 \end{pmatrix}, \mathcal{L}_\phi = (\partial^\mu \phi)^\dagger (\partial_\mu \phi) - V(\phi), V(\phi) = \mu^2 \phi^\dagger \phi + \lambda(\phi^\dagger \phi)^2. \tag{7}$$

As can be seen from Eq. 7, the potential V depends on the parameters μ^2 and λ. The parameter λ must be positive for the potential to have a finite minimum, while μ^2 can be either positive or negative. Depending on the sign, the minimum of the potential is

$$\mu^2 \geq 0 : \frac{\delta V}{\delta \phi} = 0 \rightarrow \phi_{min} = 0 \tag{8}$$

$$\mu^2 < 0 : \frac{\delta V}{\delta \phi} = 0 \rightarrow \phi_{min} = \pm\sqrt{\frac{-\mu^2}{2\lambda}} = v \tag{9}$$

where v is the vacuum expectation value of ϕ. The vacuum expectation value $\langle 0|\phi|0\rangle$ vanishes in the first case (Eq. 8) and the potential preserves the symmetry of the Lagrangian. However, if $\mu^2 < 0$, the vacuum expectation value differs from 0 (Eq. 9). This form results in the symmetrical, so-called Mexican hat potential with a local maximum at the origin as illustrated in Figure 2. The distribution falls to the minimum potential before rising again, creating an infinite set of degenerate minima that satisfy $\sqrt{\phi_1^2 + \phi_2^2} = \frac{-\mu^2}{\lambda} = v$. Choosing a particular ground state breaks the symmetry, i.e. the *symmetry is spontaneously broken*.[14] The ground state can be written as

$$\phi_0 = \langle 0|\phi_0|0\rangle = \frac{1}{\sqrt{2}} \begin{pmatrix} 0 \\ v \end{pmatrix} \tag{10}$$

By considering a small excitation and expanding $\phi(x)$ around its minimum results in

$$\phi(x) = \frac{1}{\sqrt{2}} \begin{pmatrix} 0 \\ v + h(x) \end{pmatrix} \tag{11}$$

14 In layman terms: consider the bottom of a wine bottle, or a Mexican hat. If a ball is put at the top of the hat, the whole system is symmetrical with respect to rotating the hat: no matter how much the hat is rotated around the vertical axis, it will look the same. However, if the ball falls down into the brim, the hat continues to have symmetry, but the whole system no longer does. In this case we can say that the ball will spontaneously break the symmetry.

where the quantum of the field $h(x)$, the Higgs boson, is a scalar particle with a mass

$$m_h = \sqrt{2}\mu = \sqrt{2\lambda}v. \tag{12}$$

The theory does not predict values for μ or m_h, and therefore the mass of the Higgs had to be determined experimentally. Indeed, the discovery of the Higgs boson in 2012 by ATLAS and CMS [14, 15] marked the triumph of the Standard Model of particle physics: finally a new boson at a mass of 125 GeV was found. So far the properties of the Higgs boson have been measured to agree excellently with the Standard Model predictions. However, there are still predictions to be confirmed. For instance, the Higgs self-coupling parameters determine the shape of the Higgs potential. The probability for producing two Higgs bosons simultaneously and the kinematics of such events depend on self-coupling strength, but due to low event rates the parameters have not been experimentally measured yet.

Calculating the interaction terms between the Higgs field and the $W^{\pm}, Z$ and γ bosons after the spontaneous symmetry breaking gives mass terms for these other bosons as well. While the photon remains massless, the W boson obtains mass given by $m_W = g\frac{v}{2}$ and the Z boson by $m_Z = \frac{v}{2}\sqrt{g^2 + g'^2}$, where g and g' are the coupling strengths to $\mathrm{SU}(2)_L$ and $\mathrm{U}(1)_Y$, respectively. This also gives the relation between the W and Z boson masses and the weak mixing angle, the Weinberg angle: $m_W = m_Z \cdot \cos\theta_W$.

The masses of the fermions can also be generated by *Yukawa couplings* to the Higgs field. This is achieved by adding another term, $\mathcal{L}^{\text{Yukawa}}$, to the Lagrangian. In a simple case with one real scalar ϕ and one Dirac fermion ψ, the Yukawa potential is given by $V \sim g\phi\bar{\psi}\psi$. The mass of a fermion f is given by

$$m_f = \frac{1}{\sqrt{2}} h_f v \tag{13}$$

where h_f is the coupling proportional to the fermion mass, implying that the strength of the Yukawa interactions is propotional to the mass of the fermion.

It is important to note that neutrinos remain massless in the Standard Model. The Higgs interaction couples left-handed particles to right-handed particles. As right-handed neutrinos have not been observed, they are not included in the Standard Model. Left-handed neutrinos cannot interact with the Higgs and therefore do not acquire any mass. However, there is compelling experimental evidence for small neutrino masses, as will be discussed later in Section 2.1.1.

As has now been briefly summarized, the Higgs mechanism gives mass to various fundamental particles: the more strongly a particle interacts with the Higgs field, the more massive it is. At this step, I cannot resist to introduce another analogy to the Higgs mechanism as an alternative to the popular one with a famous person entering a room [16]: namely the snowdrift analogy. Imagine a flat, snowy landscape - that is the Higgs field - and a group of elementary particles that are planning to spend time outdoors on a nice, cold winter day. An electron would have fast skis and would glide on the snowdrift without any trouble. The cousin of the electron, the muon, would have snowshoes and would be slower to follow, but would not sink into the snow. On the other hand, the heaviest elementary particle, the top quark, would have left unprepared and forgot to bring any equipment. It would drag far behind every step of the way, dipping deep into the snow. Depending on the equipment (bare feet, snowshoes, or even skis), particles sink into the snow at different ease. And of course when they sink, the harder the movement gets because the snow makes them slower: the top quark feels itself very heavy. This mechanism makes electrons light and top quarks massive. However, there's a small flaw in this analogy: the real Higgs field also resists stopping. Once moving, a particle is harder to stop, and once stopped it is harder to get moving again.

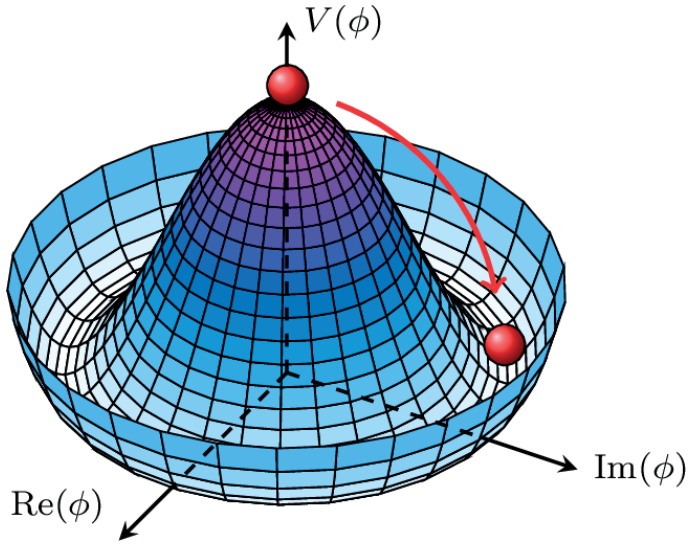

Figure 2: The Mexican hat representing the shape of the Higgs potential.

1.2.6 *Particle interactions with Feynman diagrams*

The Higgs boson cannot be observed directly in particle physics experiments. Instead, once the Higgs boson is formed, it will decay into other elementary particles that experimentalists can identify and measure in a detector.

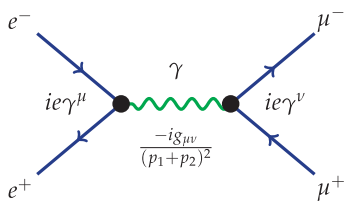

Figure 3: Example of a Feynman diagram: $e^-e^+ \to \mu^-\mu^+$ process together with expressions corresponding to each line and vertex.

Particle interactions such as the Higgs decay can be described by the pictorial language of particle physics, called *Feynman diagrams*, which include - although hidden - a precise mathematical content. An example can be seen in Figure 3, which shows the electron-muon scattering $e^-e^+ \to \mu^-\mu^+$. Particles are represented by lines: fermions with straight ones, photons, W and Z bosons with wavy ones, and gluons with spiral ones. Arrows in fermion lines denote the difference between particles and antiparticles, the latter having their arrows reversed. Each point at which lines come together is called a vertex (now emphasized with a black dot) and it represents an interaction between particles. Each vertex has a vertex factor, which describes the coupling strength of the interaction between the incoming and outgoing particles.

In this example, initial state particles are to the left, while final state particles are to the right. It is worth noting that a line describes only a particle's progress, not its trajectory. The usual conservation laws of nature hold: quantum numbers, such as charge and lepton number, must have the same total values in both initial and final states and in each vertex.

The beauty of the Feynman diagrams is that these diagrams can be turned into probabilities for a process by a set of mathematical rules of the quantum field theory, called the Feynman rules. Just by drawing a diagram it is possible to write down the probability amplitude for the transition from an initial state to a final state using the relevant Feynman rules, without calculating each process from the beginning in QFT.

According to Heisenberg's uncertainty principle of quantum mechanics, the conservation of energy can be violated for a short period of time $\Delta t < \frac{\hbar}{\Delta E}$. Thanks to this principle and the famous relation $E = mc^2$, energy can be borrowed to create short-lived particles that appear from the vacuum and then disappear again. The larger the mass and the greater the ΔE, the shorter is the time the particle can exist. Such particles are called *virtual* particles, because they cannot be directly observed. Since they do not satisfy the energy-momentum relation, they are said to be *off-shell*, whereas real particles are said to be *on-shell* (or on mass shell).

2 BEYOND THE STANDARD MODEL

Even though the Standard Model is one of the most beautiful mathematical jigsaws that has been carefully assembled and tested over 50 years by thousands of particle physicists, it is incomplete in part. There are a number of known open problems which remain unaddressed by the Standard Model, for example what is dark matter that covers up to 85% of the matter in the Universe, and why there is more matter than antimatter. In addition, the mechanism for generating neutrino masses is currently unknown in the Standard Model although observations of neutrino oscillations made it apparent that neutrinos indeed have a small mass.

Theorists have constructed several models which either extend or re-write the Standard Model in order to address some or all of the above questions. In general, those models and theories are known as *Beyond the Standard Model* (BSM) theories. To find out whether the models are correct or to rule them out if possible, particle physics experiments, such as the ones at the Large Hadron Collider (LHC) in Geneva, Switzerland, analyse particles produced by collisions in the accelerator. As the work for this thesis was done in the ATLAS experiment, I will from now on focus only on the BSM research program in the ATLAS experiment, and more precisely on the models leading to new heavy charged bosons or same-charge lepton final states.

This section summarizes a few of the most interesting problems remaining to be unsolved so far, and introduces promising suggestions to answer to some of them, which usually require introducing new particles or extended gauge structures. Experimentalists search for new physics by looking at various signatures. One of the powerful signatures for BSM searches is *pairs of same-charge leptons*, and it is indeed in the scope for the rest of this thesis.

2.1 KNOWN UNKNOWNS

2.1.1 *Nature of neutrinos*

The tiniest members of the lepton family, namely neutrinos, are mysterious neutral creatures: there is much that we know about them, but even more that we don't. The SM predicts massless, left-handed neutrinos. However, the observation of neutrino oscillations[1] by measurements of neutrinos from the Sun and experiments with reactor and accelerator neutrinos made it clear that neutrinos have masses and that they mix. In these oscillations, neutrinos change their flavour from one type into a different type. Such oscillations would not be possible if neutrinos were massless like in the Standard Model and therefore either a new conservation law or new phenomena beyond the Standard Model have to be incorporated.

In fact, the actual values of neutrino masses are still unknown. Neutrino oscillation experiments have measured only differences in mass squared, Δm^2, and therefore there are three possible arrangements for different mass levels [7]:

- Normal hierarchy with $m_1 \ll m_2 < m_3$, with $m_2 \simeq 0.0086\,\text{eV}$ and $m_3 \simeq 0.03 - 0.05\,\text{eV}$
- Inverted hierarchy with $m_3 \ll m_1 < m_2$ with $m_{1,2} \simeq 0.05\,\text{eV}$
- Degenerate neutrinos, i.e. $m_1 \simeq m_2 \simeq m_3 \simeq m_0, m_0 \gtrapprox 0.10\,\text{eV}$.

1 The experimental discovery of neutrino oscillations led to the 2015 Nobel Prize for Physics awarded to Takaaki Kajita from the SuperKamiokande Collaboration and Arthur McDonald from the SNO Collaboration.

The tightest constraint on the sum of neutrino masses by combining measurements from Planck, WMAP, highL and BAO data at 95% CL gives $\sum_{i=1}^{3} m_1 < 0.230\,\text{eV}$ [17].

However, having massive neutrinos leads to two problems: we have to solve the issue of the left-handed neutrinos and their mass since there are no right-handed neutrinos in the SM, and we have to understand why the neutrino mass is so much smaller than the masses of other particles. There are a various ways to account for neutrino masses, as has been summarised e.g. in Refs. [7, 18] and will be discussed later in Section 2.2.2. Many of them are linked into discussions on whether neutrinos are *Dirac* or *Majorana* neutrinos. Since neutrinos do not have electric charge, they can be Majorana (where neutrinos are their own antiparticles), or Dirac particles (where neutrinos and antineutrinos are different objects[2].). The Majorana nature of neutrinos would allow processes in which the total lepton number is not conserved, such as the neutrinoless double-beta decay. Such processes are not permitted for Dirac neutrinos. The so-called seesaw mechanism to generate neutrino masses will be discussed in Section 2.2.3.

2.1.2 *Dark matter*

Astrophysical data indicate that there is non-baryonic, non-luminous, weakly interacting, cold (non-relativistic) and neutral matter called Dark Matter, which forms 85% of the matter in the Universe. In other words, it does not interact via the strong nor the electromagnetic force. Evidence for dark matter arises from multiple sources on galactic scales. The rotation curve of a galaxy shows how the orbital velocity of stars around the galaxy centre changes as the distance from the centre increases. In a galaxy in which most of the mass is concentrated at the centre, the velocity should decrease with increasing distance. However, a flat rotation curve has been observed in many galaxies, implying the existence of non-luminous gravitationally interacting matter. Further proof for dark matter comes from gravitational lensing, where the gravity of massive galaxy bends and distorts the light of the distant galaxies behind the concentration of matter. It can be measured that the observed luminous mass from stars in the galaxy is not enough to produce the observed lensing effect, therefore implying the existence of dark matter. The estimate for the total amount of the dark matter in the Universe can be obtained from the cosmic microwave background (CMB).

It is likely, but not certain, that the dark matter is formed of elementary particles. The only SM particles that are non-baryonic, weakly interacting and neutral are neutrinos, making them promising dark matter candidates. However, they cannot be the only or dominant dark matter component, because they are relativistic and such would be considered as hot dark matter, which in turn cannot explain the formation of large-scale structures such as galaxy clusters.

There are various hypothetical particles that could be responsible for dark matter, with masses from sub-eV range to multiple solar masses. New types of neutrinos, called *sterile* neutrinos because they interact only via gravity, are one solution. Other examples are axions or Weakly-Interacting Massive Particles (WIMPs). Such candidates can also arise in Left-right symmetric models, which will be discussed later in Section 2.2.3.

2.1.3 *Matter-antimatter asymmetry*

Why are we and our Universe made of matter and not antimatter? After all, it is strange as the properties of matter and antimatter are very similar except the opposite charge and spin. Ac-

2 This is clear if we look at electrons that are not Majorana particles: electron has charge -1 whereas its antiparticle positron has charge +1, which make them distinct from each other.

cording to theory, the Big Bang should have created equal amounts of matter and antimatter, yet our Universe is almost entirely made of matter (otherwise, matter and antimatter would have annihilated leaving nothing but energy behind). The question is what happened to the antimatter, and why do we have this asymmetry between matter and antimatter. The problem requires CP violation by an amount that cannot be predicted by the SM alone.

2.1.4 *Three families*

The Standard Model has three fermion families, where the second and the third families are essentially copies of the first family. Based on precision measurements of the total width of the Z boson, it is revealed that there are indeed three families but no more: each neutrino contributes to the total width $\Gamma(Z \to \nu_i \bar{\nu}_i) = 167\,\text{MeV}$, and any additional neutrino would both increase the width of the resonance and decrease the peak height. Despite this precision measurement, the Standard Model does not offer a clear, convincing explanation *why* this happens. The so-called 3-3-1 model may shed light on the question, and will be discussed further in Section 2.2.4.

2.1.5 *Theoretical hints*

In addition to the above mentioned experimental hints, there are several theoretical arguments motivating searches for beyond Standard Model physics: the hierarchy problem, the potential unification of forces, and the large number of parameters in the SM lacking a fundamental explanation, just to name a few.

First, let's introduce the problem of scales. The electroweak scale at a few hundred GeV is much lower than the Plank scale at $\sim 10^{19}\,\text{GeV}$, where the gravitational force is expected to become non-negligible. Nothing restricts the SM to survive up to this scale. However, the Higgs mechanism does not come without difficulties since the mass of the Higgs boson depends quadratically on the cutoff scale Λ, the energy scale beyond which the theory may not be valid anymore. If the cutoff scale is very high, the Higgs boson mass must be severely fine-tuned with higher-order corrections, which seems *unnatural*.

Unification of all the SM interactions is theoretically very appealing as it would minimize the number of free parameters present in the SM. It leads to the formulation of Grand Unification Theories (GUT) which would elegantly link the three forces together at some large energy scale. Unfortunately, GUTs need a higher energy scale ($\mathcal{O}(10^{12} - 10^{16}\,\text{GeV})$) than the electroweak scale currently accessible at the LHC.

2.2 BSM AND SAME-CHARGE LEPTON FINAL STATES

In the experimental searches for new physics at the LHC, the solutions for above mentioned problems typically call for introducing new particles or extended gauge structures. As there is a plethora of new models explaining every detail and missing piece of the Standard Model, I will only mention a few theoretically well-motivated ones leading to new heavy charged bosons and same-charge lepton final states.

The same-charge lepton final state is a powerful signature for BSM searches as there are only a few SM processes producing pairs of such leptons[3], making it a clean signal and yielding in high signal/background ratio. In fact, rather than relying only on specific models and probing tuned parameters, the analyses presented in this thesis try to stay as *inclusive* as

3 These SM processes are a *background* for our searches, and will be discussed later in Section 7.4

possible with minimal selection cuts. This way the searches are less restricted and open more possibilities for finding new physics.

2.2.1 *Supersymmetry*

An elegant and largely tested model to explain BSM phenomena is *supersymmetry* (SUSY), on which high hopes of discovery were built before and during the LHC runs. It predicts that for each particle in the Standard Model there is a superpartner particle (*sparticle*) with the spin which differs by a half-integer - in other words, it predicts a new bosonic partner for each SM fermion, and a new fermionic partner for each SM boson. SUSY is a theoretically well-motivated solution to the Higgs naturalness problem, and it includes the lightest supersymmetric particle (LSP) as a candidate for dark matter. Furthermore, it gives a framework to unify electromagnetic, weak and strong forces at a high energy.

An important symmetry to consider is the R-parity, defined as $(-1)^{3(B-L)+2s}$, where s is the spin, B is the baryon number, and L is the lepton number [19]. All SM particles have even R-parity ($R = +1$) while SUSY particles have odd R-parity ($R = -1$). If R-parity is conserved, the SUSY particles can only be produced in pairs and the lightest SUSY particle (LSP) can be a stable neutralino $\tilde{\chi}_1^0$, which is also a candidate for dark matter. The R-parity can also be violated. Both of these scenarios can produce final states with two same-charge leptons to be observed at the LHC. To illustrate such processes, Figure 4 shows gluino, stop and sbottom production [20]. Same-charge final states result from decays of squarks and neutralinos via intermediate neutralinos and charginos that in turn lead to SM bosons.

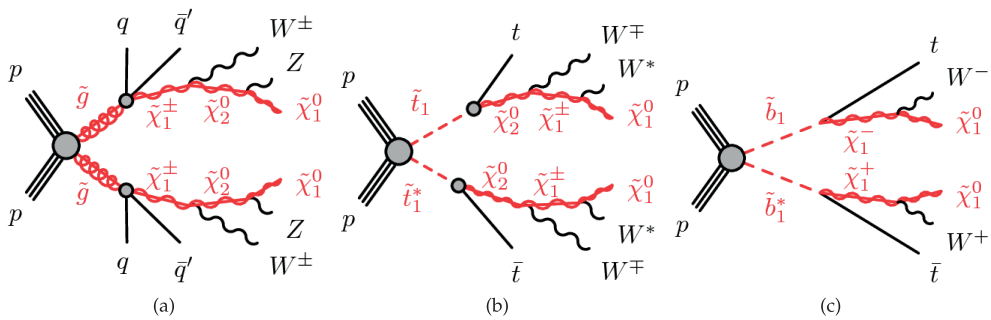

Figure 4: R-parity conserving SUSY processes featuring for (a) gluino, (b) stop, and (c) sbottom pair production. [20]

The minimal supersymmetric extensions to the SM require at least two complex doublets of scalar fields. The two-Higgs doublet model (2HDM) introduces, as it name suggests, two doublets Φ_1, Φ_2 and five physical Higgs bosons: two CP-even neutral scalars h and H, a CP-odd neutral scalar A, and two charged scalars $H^\pm$. The light neutral Higgs boson h could have similar properties to the observed 125 GeV Higgs boson, while the other Higgs bosons could be more massive. However, despite being constantly tested by scanning a very wide parameter space (such as $(\tan\beta, m_A)$ where $\tan\beta$ is the ratio of the two vacuum expectation values, and m_A the mass of the neutral CP-odd scalar boson), no sign of SUSY nor 2HDM has been seen at the LHC. Furthermore, the 2HDM is not a unique example of the extended Higgs sector, as it will turn out later in this chapter. Many other SM extensions, beyond adding a singlet scalar, imply the existence of new charged scalars.

2.2.2 *Heavy neutrinos*

As described in Section 2.1.1, neutrinos have tiny masses that are not explained by the SM. Since neutrinos are chirally left-handed and no right-handed neutrinos ν_R nor left-handed antineutrinos $\bar{\nu_L}$ have been observed, a non-zero Dirac mass term is not allowed in the SM as it requires both chiral states. In other words, a Dirac nature requires the existence of new right-handed neutrinos. In a simple extension of the SM, the neutrino mass can be generated by the Yukawa couplings of left- and right-handed neutrinos to the SM Higgs boson, in exactly the same way as charged leptons and quarks. Moreover, the total lepton number is conserved: Dirac neutrinos are given lepton number $L = +1$ and antineutrinos $L = -1$. However, since neutrinos are electrically neutral, they could be their own antiparticles i.e. be Majorana neutrinos without violating charge conservation. As neutrino oscillations indicate lepton flavour violation in the neutral sector, it is proposed that charged lepton flavour could also be violated in the SM extensions. Interactions involving Majorana neutrinos would indeed violate lepton number conservation by $\Delta L = \pm 2$, which is not allowed in the SM.

One of the common ways to explain the smallness of neutrino mass is to introduce the *seesaw mechanism*, which predicts that there are both light, left-handed neutrinos on one end of the seesaw, and heavy, right-handed neutrinos on the other end. The seesaw is then a ratio: the heavier the right-handed neutrino, the lighter the left-handed neutrino. It is important to note that both left-handed and right-handed neutrinos are needed while right-handed neutrinos have not been yet observed. In general, there are three separate seesaw mechanisms that add a few new particles into the SM and allow $B - L$ violation[4] [21]:

- **Type-I seesaw**: three heavy right-handed neutrinos are added to the SM, creating a structural symmetry between quarks and leptons. The lepton number is violated by their Majorana mass term.
- **Type-II seesaw**: a triplet scalar field with the hypercharge $Y = +2$ is added to the SM. The neutral component of the triplet acquires a vacuum expectation value and generates Majoran neutrino masses through the Yukawa interactions. Such seesaw mechanism arises naturally in the left-right symmetric models to be discussed further in Section 2.2.3. The triplet extends the Higgs sector with singly and doubly charged Higgs bosons, where the latter plays the main role in the searches presented in this thesis.
- **Type-III seesaw**: the SM is extended with heavy fermionic triplets with $Y = 0$, and the lepton number is violated by their Majorana mass term. The neutrino masses are given by $M_\nu^{\text{III}} \propto \Gamma^2 v^2 / M_\Sigma$, where M_Σ stands for the mass of the fermionic $SU(2)_L$ triplets, Γ is the Dirac Yukawa coupling and v is the EW vacuum expectation value. The new fermionic triplet components are labelled as $(\Sigma^+, \Sigma^-, \Sigma^0)$.

All of the mechanisms above are expected to be probed at observable rate in pp collisions at the LHC. As will be discussed in Section 2.2.3, the left-right symmetric models introduce the right-handed counterparts to the W and Z bosons, denoted W_R and Z_R, as well as right-handed heavy neutrinos (N_R). The production of a W_R boson and N_R neutrino could lead to a final state with two charged leptons and two jets ($\ell\ell jj$). An example of such a process is the lepton-number-violating (LNV) Keung–Senjanović (KS) process [22], shown in Figure 5. The left-right-symmetric model containing the type-I seesaw mechanism assumes heavy neutrinos N_R to be Majorana particles, allowing the LNV KS process to occur. However, in other left-right-symmetric model variants, neutrinos can be Dirac particles and lepton-number-violating

4 $B - L$ is the difference between the baryon number (B) and the lepton number (L).

processes are not expected. Whether N_R neutrinos are Majorana or Dirac neutrinos can be established by comparing the charges of the two leptons in the final state: leptons will always have opposite-charge for Dirac particles, whereas Majorana particles will give rise to lepton pairs of both opposite- and same-charge.

The author contributed to such search for right-handed W bosons and heavy right-handed Majorana or Dirac neutrinos in final states with two leptons and two jets using a 36.1 fb^{-1}sample of pp collisions recorded by the ATLAS detector at $\sqrt{s} = 13\,\text{TeV}$ at LHC [1]. No evidence of W_R bosons or Majorana or Dirac heavy neutrinos, N_R, was found assuming the KS production. These results improve upon previous ATLAS searches [23] and extend the exclusion limits on $\text{m}(W_R)$ by $1 - 2\,\text{TeV}$. Moreover, the scenario in which the N_R neutrino is heavier than the W_R boson was explored for the first time. This search will not be discussed further, and all the details can be found in Ref. [1].

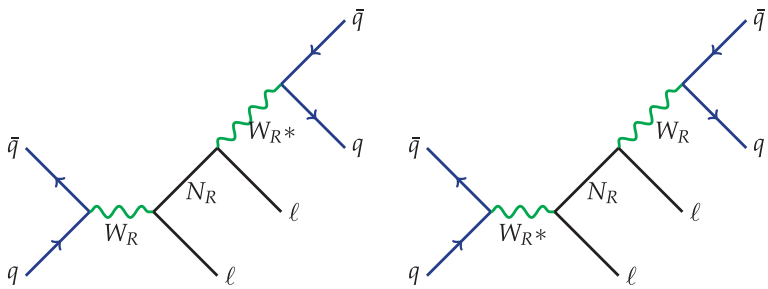

Figure 5: The Keung–Senjanović process for (a) the $\text{m}(W_R) > \text{m}(N_R)$ case and (b) the $\text{m}(N_R) > \text{m}(W_R)$ case. Leptons ℓ can be either same- or opposite-charge. [1]

As for type-III seesaw, the new charged and neutral heavy leptons could be produced in electroweak processes and be observed at the LHC. Figure 6 shows a production and decay process of new heavy leptons, where heavy charged leptons are denoted as $L^{\pm}$ and a heavy neutral particle N^0 is its own antiparticle (i.e.a Majorana particle). The final state contains two charged leptons, two jets, and large missing transverse energy. The leptons can have opposite or same charge (as shown in Figure 6), and can have either same or different flavour. The author contributed to the search for the pair production of heavy leptons using 79.8 fb^{-1} data recored in 2015-2017 by the ATLAS detector [3]. No significant excess above the SM prediction was found. Limits were set on the type-III seesaw heavy lepton masses, assuming branching fractions to all lepton flavors to be equal. Heavy leptons with masses below 560 GeV are excluded at the 95% confidence level. This search will also not be discussed further, and all the details can be found in Ref. [1].

For the rest of the thesis, the focus is on heavy doubly charged scalars that appear in many models and that could result in new resonances within the LHC reach.

2.2.3 *Doubly charged scalars in left-right symmetric models*

The left-right symmetric models (LRSM) are motivated by the odd phenomena of parity violation in the weak interactions. As parity is not violated by any of the other fundamental forces, it is suggested that the observed parity non-consevation is only a low-energy problem, and the full parity between left- and right-handed fermions could be restored at higher energies.

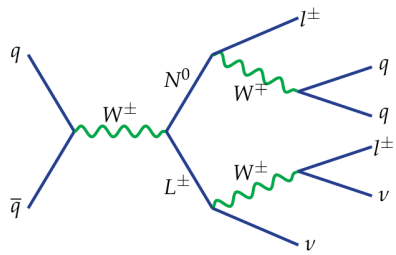

Figure 6: Feynman diagram for the production and decay process of heavy leptons predicted by the type-III seesaw model. [3]

The LRS models could explain the small neutrino masses via the seesaw mechanism, and promisingly, they include the possibility to generate both Dirac and Majorana neutrino mass terms. Furthermore, LRS models have viable dark matter candidates [24]. The scale at which the symmetry breaks is not predicted, but is potentially accessible at the LHC. The LRSM is discussed and summarized well in Refs. [25–29], including the dark matter phenomenology in Ref. [24]. In the following, a brief overview is given in order to motivate the searches incorporating doubly charged scalars and same-charge leptons.

The minimal left-right symmetric model is based on the gauge symmetry group $\mathrm{SU}(2)_L \times SU(2)_R \times U(1)_{B-L}$, where $B-L$ is the difference between baryon and lepton number, $\mathrm{SU}(2)_L$ is the usual SM SU(2) symmetry, and $\mathrm{SU}(2)_R$ is the newly-added right-handed counterpart which is a broken symmetry at low energies[5]. The gauge fields corresponding to this symmetry group couple only to right-handed fermions. In LRSM, both left-handed and right-handed fields are treated in the same way, and fermions can be assigned to doublets of the gauge groups $\mathrm{SU}(2)_L$ and $\mathrm{SU}(2)_R$ according to their chirality:

$$\ell_L = \begin{pmatrix} \nu_L \\ e_L \end{pmatrix} \sim (\vec{2}, \vec{1}, -1) \qquad \ell_R = \begin{pmatrix} \nu_R \\ e_R \end{pmatrix} \sim (\vec{1}, \vec{2}, -1) \tag{14}$$

$$q_L = \begin{pmatrix} u_L \\ d_L \end{pmatrix} \sim (\vec{2}, \vec{1}, 1/3) \qquad q_R = \begin{pmatrix} u_R \\ d_R \end{pmatrix} \sim (\vec{1}, \vec{2}, 1/3) \tag{15}$$

where the numbers (d_L, d_R, Y) denote dimensions of the $\mathrm{SU}(2)_L$ and $\mathrm{SU}(2)_R$ representations, and $Y = B - L$. Note that right-handed neutrinos ν_R are now implemented, and quarks and leptons are completely left-right symmetric.

In order to produce fermion masses, the scalar Higgs bi-doublet ϕ is added to the model:

$$\phi = \begin{pmatrix} \phi_1^0 & \phi_1^+ \\ \phi_2^- & \phi_2^0 \end{pmatrix} \tag{16}$$

However, the bi-doublet ϕ is not sufficient for breaking $\mathrm{SU}(2)_L \times SU(2)_R \times U(1)_{B-L}$ to $\mathrm{U}(1)_{\mathrm{EM}}$, and additional scalars are necessary. The electric charge operator is given by

$$Q = T_L^3 + T_R^3 + \tfrac{1}{2}(B - L) \tag{17}$$

where T_L^3 and T_R^3 are the generators of left- and right-handed isospin. This equations clearly shows how the LR symmetry is connected with $B-L$ symmetry. Therefore a scalar that carries

5 Omitting the $\mathrm{SU}(3)_C$ for simplicity.

$B - L$ charge is required, and a common choice is to extend the Higgs sector with two scalar Higgs triplets $\Delta_{L,R}$ [30] in addition to the bi-doublet:

$$\Delta_L = \begin{pmatrix} \Delta_L^+/\sqrt{2} & \Delta_L^{++} \\ \Delta_L^0 & -\Delta_L^+/\sqrt{2} \end{pmatrix} \sim (\vec{3}, \vec{1}, 2)\,, \quad \Delta_R = \begin{pmatrix} \Delta_R^+/\sqrt{2} & \Delta_R^{++} \\ \Delta_R^0 & -\Delta_R^+/\sqrt{2} \end{pmatrix} \sim (\vec{1}, \vec{3}, 2)\,. \tag{18}$$

The neutral right-handed component, acquiring a non-vanishing vacuum expectation value (vev) of $\langle \delta_R^0 \rangle \equiv v_R/\sqrt{2}$, breaks the $\mathrm{SU}(2)_L \times SU(2)_R \times U(1)_{B-L}$ symmetry at higher energy. Furthermore, it generates Majorana masses for the right-handed neutrinos and masses for the new heavy right-handed gauge bosons W_R and Z_R. The bi-doublet vacuum expectation value becomes

$$\langle \phi \rangle = \begin{pmatrix} \kappa_1/\sqrt{2} & 0 \\ 0 & \kappa_2/\sqrt{2} \end{pmatrix} \tag{19}$$

where $\kappa \equiv \sqrt{\kappa_1^2 + \kappa_2^2} \simeq 246\,\mathrm{GeV}$. This vacuum expectation value induces a mixing between left- and right-handed gauge bosons and gives masses to W_L, Z_L, and charged SM fermions. Moreover, the left-handed triplet Δ_L acquires a small vacuum expectation value, $\langle \delta_L^0 \rangle \propto v^2/v_R$, where $v^2 = \kappa_1^2 + \kappa_2^2$.

What is the most noteworthy in terms of this thesis is that a new neutral scalar together with a singly and a doubly charged scalar are introduced in Eq. 18. In LRSM, the doubly charged scalars $\Delta_{L,R}^{\pm\pm}$ are from now on referred to as *doubly charged Higgs bosons* or $H_{L,R}^{\pm\pm}$. Their production mechanisms and decays will be discussed in Section 2.2.5, and the last part of the thesis is dedicated on searching for them with the ATLAS detector at the LHC.

2.2.4 *Doubly charged scalar and vector bileptons in 3-3-1 models*

The 3-3-1 model, or the bilepton model, is a simple extension to the SM and is based on the gauge group $\mathrm{SU}(3)_C \times \mathrm{SU}(3)_L \times \mathrm{U}(1)_X$, hence the name [31]. It aims to explain *why* there are three families of quarks and leptons in the Standard Model: in particular, why the second and the third families appear as the first family alone accounts for the majority of the baryonic matter. The probed model and its mathematical formulation is discussed in detail in Refs. [31], [32] and [33], and therefore only a brief summary is given below.

In the 3-3-1 model, the occurrence of three families is provided by cancellation of the gauge anomalies. In the SM, the anomaly cancellation [34] is guaranteed family by family, and thus it can work with an arbitrary number of quark and lepton families. Unlike the SM, the main idea in the 3-3-1 model is that all three families, each having a non-zero anomaly, must be combined together for anomaly cancellation. The overall anomaly vanishes only for a multiplet of three (3, 6, 9...) families. On the other hand, in order to ensure that the QCD is an asymptotic free theory, the number of families has to be strictly smaller than six. Therefore the SM has to have three generations.

The model considered here adds three types of new particles: gauge bosons, exotic quarks, and additional scalars. In particular, it adds two *bileptons*, i.e. gauge bosons $Y^{\pm\pm}$ of charge $Q = \pm 2$ and lepton number $L = \pm 2$. Furthermore, a Higgs scalar sector, which is a sextet of $\mathrm{SU}(3)_L$, is added in order to account for the lepton masses. As a result, the model incorporates both new doubly charged scalar states $H^{\pm\pm}$ and the vector bileptons $Y^{\pm\pm}$, which can lead to the production of two same-charge lepton pairs.

The charge operator becomes $Q = T^3 + \bar{\beta} T^8 + X$, where T^3 and T^8 are the Gell-Mann matrices of $\mathrm{SU}(3)_L$, and $\bar{\beta} = \pm\sqrt{3}$. As mentioned, the gauge structure is $\mathrm{SU}(3)_C \times \mathrm{SU}(3)_L \times$

$\mathrm{U}(1)_X$, where the fermions in the fundamental of $SU(3)_c$ are accommodated in triplets of $\mathrm{SU}(3)_L$.

The three families of quarks are treated asymmetrically. The first two families can be expressed as

$$Q_1 = \begin{pmatrix} u_L \\ d_L \\ D_L \end{pmatrix}, \quad Q_2 = \begin{pmatrix} c_L \\ s_L \\ S_L \end{pmatrix}, \quad Q_{1,2} \in (3, 3, -1/3) \tag{20}$$

whereas the third family is

$$Q_3 = \begin{pmatrix} b_L \\ t_L \\ T_L \end{pmatrix}, \quad Q_3 \in (3, \bar{3}, 2/3) \tag{21}$$

where D, S and T are exotic extra quarks. The right-handed quarks $\bar{q}$ are singlets under $SU(3)_L$, just as in the Standard Model. In order to cancel all anomalies, three lepton families are arranged into triplets of $SU(3)_L$:

$$l = \begin{pmatrix} l_L \\ \nu_l \\ \bar{l}_R \end{pmatrix}, \quad l \in (1, \bar{3}, 0), \quad l = e,\ \mu,\ \tau. \tag{22}$$

In order to break the electroweak symmetry, three scalar triplets of $SU(3)_L$ are introduced:

$$\rho = \begin{pmatrix} \rho^{++} \\ \rho^{+} \\ \rho^{0} \end{pmatrix} \in (1, 3, 1), \quad \eta = \begin{pmatrix} \eta^{+} \\ \eta^{0} \\ \eta^{-} \end{pmatrix} \in (1, 3, 0), \quad \chi = \begin{pmatrix} \chi^{0} \\ \chi^{-} \\ \chi^{--} \end{pmatrix} \in (1, 3, -1). \tag{23}$$

The breaking from $\mathrm{SU}(3)_L \times \mathrm{U}(1)_X$ to $\mathrm{U}(1)_{\mathrm{EM}}$ is done in two steps. First, the breaking from the $\mathrm{SU}(3)_L \times \mathrm{U}(1)_X$ to $\mathrm{SU}(3)_L \times \mathrm{U}(1)_Y$ is achieved by the vacuum expectation value of the neutral component of ρ which gives masses to the extra gauge bosons, $Z', Y^{\pm}$ and $Y^{\pm\pm}$, and the exotic quarks D, S and T. After that, the spontaneous symmetry breaking mechanism from $\mathrm{SU}(3)_L \times \mathrm{U}(1)_Y$ to $\mathrm{U}(1)_{\mathrm{EM}}$ is acquired from the vacuum expectation values of the neutral components.

As can be seen, the phenomenology of this model is very rich as it accomodates a variety of new particles and both vector and scalar bosons. In the experimental searches for BSM, the model could be probed in the final states of two same-charge leptons [33] or two-same charge leptons and two jets [32]. Figure 7 shows Feynman diagrams for the pair-production of bilepton $Y^{\pm\pm}$ leading to the same-charge lepton final states without additional jets.

2.2.5 *Production mechanisms of the doubly charged Higgs*

As shown, doubly charged Higgs bosons are theoretically well motivated and appear in many new physics models. In addition to left-right symmetric models (LRSM) [24–29] and type-II see-saw models [35–39], they arise also from Higgs triplet models [40, 41], the little Higgs model [42], the Georgi–Machacek model [43], scalar singlet dark matter [44], and the Zee–Babu neutrino mass model [45–47]. Experimentally doubly charged Higgs boson provides a powerful signature towards new discoveries, as it decays into energetic, isolated leptons with the same electrical charge.

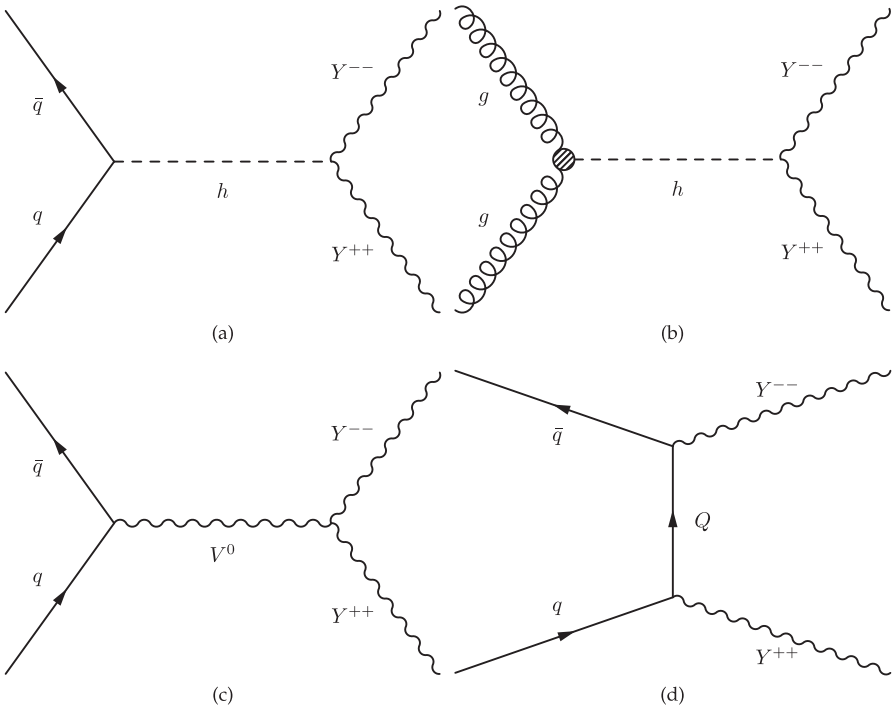

Figure 7: Example Feynman diagrams for production of two bileptons $Y^{\pm\pm}$: (a) Drell-Yan like production via a SM-like Higgs h, (b) gluon-gluon-fusion production, (c) Drell-Yan like production via a photon or a Z boson V^0, and (d) production via the exchange of an exotic quark Q. [32]

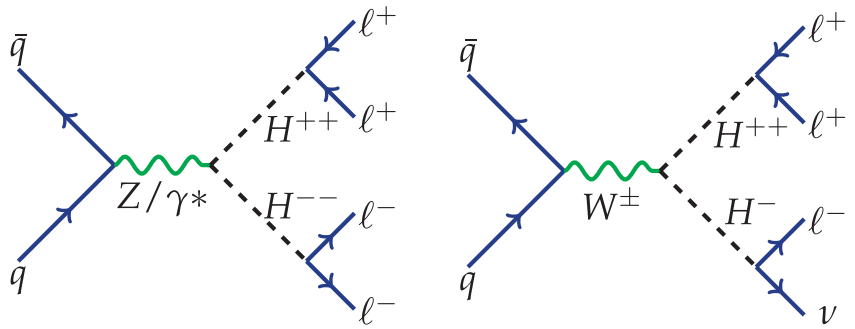

Figure 8: (a) Pair-production $pp \to \gamma^*/Z^* \to H^{\pm\pm}H^{\mp\mp}$ and (b) associated production $pp \to W^{\mp *} \to H^{\pm}H^{\mp\mp}$.

The main production mechanism for the doubly charged Higgs at the LHC is expected to be the Drell–Yan process through an s-channel photon or a Z boson exchange [48–50], as illustrated in Figure 8a, and therefore it is the mechanism we focus on in this thesis work. In terms of LRSM, doubly charged Higgs particles can couple to both left-handed and right-handed leptons, and are referred to as $H_L^{\pm\pm}$ and $H_R^{\pm\pm}$. For the searches presented in this thesis work, the cross-sections of the process are computed according to the model in Ref. [35]. The cross-section for $H_L^{\pm\pm}H_L^{\mp\mp}$ production is about 2.3 times larger than for $H_R^{\pm\pm}H_R^{\mp\mp}$ due to different couplings to the Z boson [51]. As the kinematic properties of both left- and right-handed particles are expected to be similar, they are commonly denoted as $H^{\pm\pm}$. Section 7.1 will be dedicated on discussing the signal characteristics in more detail in the experimental point of view.

Despite the pair-production of $H^{\pm\pm}$ is expected to be the dominant production mechanism, it is not a unique process. The $H^{\pm\pm}$ bosons could also be produced in association with a singly charged Higgs in a process $pp \to W^{\mp *} \to H^{\pm}H^{\mp\mp}$ (illustrated in Figure 8b). The cross-sections for this mechanism are expected to be comparable to the pair production assuming that masses of both singly and doubly charged Higgs are similar [52]. Furthermore, two photon fusion process could contribute the pair-production of the doubly charged Higgs, whereas the vector-boson-fusion mechanism is expected to be either absent or small due to weak couplings [53].

2.2.6 *Decay modes*

The doubly charged Higgs can decay either leptonically into a pair of same-charge leptons or into a pair of W bosons. The branching ratio for the $H^{\pm\pm}$ to decay into a pair of same-charge leptons or W bosons depends on the vacuum expectation value v_Δ of the Higgs triplet [35, 38]. For low values of v_Δ, $H^{\pm\pm}$ decays almost exclusively to leptons, while for high values of v_Δ it decays mostly to a pair of W bosons. This is illustrated in Figure 9. Analyses presented in this thesis consider only the case where the $H^{\pm\pm}$ particle decays into same-charge leptons, allowing lepton flavour violation, and the coupling to W bosons is assumed to be negligible. In such case, the partial decay width is given by

$$\Gamma(H^{\pm\pm} \to \ell^{\pm}\ell'^{\pm}) = k\frac{h^2_{\ell\ell'}}{16\pi}m(H^{\pm\pm}) \tag{24}$$

where $k = 2$ if both leptons have the same flavour ($\ell = \ell'$) and $k = 1$ if they have a different flavour. The factor $h_{\ell\ell'}$ has upper bounds that depend on the flavour combination. The various constraints and the sources are discussed in detail in Refs. [53, 54] and summarized in Section 2.3. In general, there is no preference for decays into τ leptons, as the coupling is not typically proportional to the lepton mass unlike it is for the SM Higgs boson. Moreover, only prompt decays of the doubly charged Higgs bosons ($c\tau < 10\,\mu\text{m}$) are considered in this analysis, corresponding to $h_{\ell\ell'} \gtrsim 1.5 \cdot 10^{-6}$ for $\text{m}(H^{\pm\pm}) = 200\,\text{GeV}$.

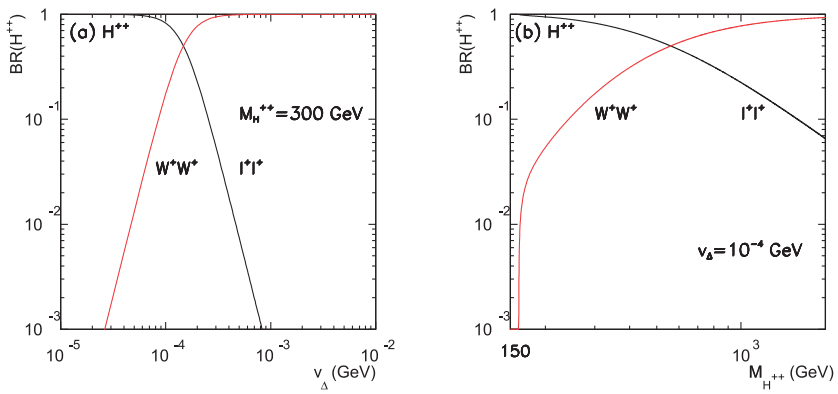

(a) (b)

Figure 9: Branching fractions of the doubly charged Higgs boson decays as a function of (a) the vacuum expectation value for $\text{m}(H^{\pm\pm}) = 300\,\text{GeV}$, and (b) the $\text{m}(H^{\pm\pm})$ for the vacuum expectation value of $v_\Delta = 1 \cdot 10^{-4}\,\text{GeV}$. [55]

2.3 EXPERIMENTAL CONSTRAINTS

The history of direct $H^{\pm\pm}$ searches reaches back to the LEP era and earlier. The first experiments to set limits on the $H^{\pm\pm}$ mass were HRS and MAC located at the Positron Electron Project (PEP) collider at SLAC and CELLO, PLUTO and TASSO at the Positron-Electron Tandem Ring Accelerator (PETRA) at DESY, as summarized in Ref. [56]. The L3 detector at the e^-e^+ collider LEP searched for the pair-production of doubly charged Higgs bosons in four-lepton final states at $\sqrt{s} = 130\text{-}209\,\text{GeV}$, setting the lower limit from 95.5 GeV to 100.2 GeV at 95% confidence level [57].

The D0 and CDF experiments at the Fermilab Tevatron Collider searched for the pair production of $H^{\pm\pm}$ in $p\bar{p}$ collisions at $\sqrt{s} = 1.96\,\text{TeV}$ in various leptonic final states, setting lower limits for the $H^{\pm\pm}$ mass from 112 GeV to 150 GeV at 95% confidence level [58, 59]. The H1 experiment at the ep collider HERA at DESY also searched for $H^{\pm\pm}$ in $e^{\pm}\mu^{\pm}$ and $e^{\pm}\tau^{\pm}$ pairs. This search set the lower limit of the $H^{\pm\pm}$ mass to 141 GeV assuming doubly charged Higgs couples only to electron-muon pairs, and 112 GeV assuming couplings only to electron-tau pairs [60].

Both CMS and ATLAS have performed similar searches at the LHC. In Run 1 with the centre-of-mass energy of $\sqrt{s} = 7\,\text{TeV}$ and $\sqrt{s} = 8\,\text{TeV}$, the ATLAS collaboration studied dilepton [61] and multi-lepton ($ee, e\mu, \mu\mu, e\tau$ and $\mu\tau$) final states [62, 63] and excluded $H^{\pm\pm}$ masses below $370 - 550\,\text{GeV}$. Similarly, CMS considered leptonic final states with three or four light leptons to probe both the Drell-Yan pair production of $H^{\pm\pm}H^{\mp\mp}$ and the associated production with a singly charged Higgs $H^{\pm\pm}H^{\mp}$, which resulted in a lower mass bounds of $368 - 621\,\text{GeV}$ for different lepton flavour combinations in a same-charge pair [64]. During the LHC Run 2, similar searches have been performed. CMS extended the $H^{\pm\pm}$ mass range to $800 - 820\,\text{GeV}$ for final states with only light leptons, to 714 GeV for decays into $e\tau$ and to 643 GeV for decays into $\mu\tau$, respectively [65].

As mentioned, $H^{\pm\pm}$ can also decay to W bosons: $H^{\pm\pm} \to W^{\pm}W^{\pm}$. The CMS collaboration searched for such decays in the context of single $H^{\pm\pm}$ production through vector-boson fusion at large triplet vacuum expectation values v_t (assuming $v_t \approx \mathcal{O}(10)$ GeV) for the Georgi–Machacek model of Higgs triplets [66]. The ATLAS Collaboration searched for $H^{\pm\pm} \to W^{\pm}W^{\pm}$ assuming pair production of $H^{\pm\pm}$ and smaller values of $v_t = 0.1\,\text{GeV}$, setting lower limit on the mass of the $H^{\pm\pm}$ to 220 GeV at 95% CL [67].

Furthermore, there are *indirect* experimental constraints from various experiments that set limits on the $H^{\pm\pm}$ mass correlated with the size of the coupling. There are four types of processes involving virtual exchange of doubly charged Higgs, which could lead to large deviations from the SM predictions [53]:

- Bhabha scattering $e^+e^- \to e^+e^-$, where $H^{\pm\pm}$ contributes via a t-channel process as illustrated in Figure 10a. The OPAL and H1 collaborations studied the Bhabha scattering $e^+e^- \to e^+e^-$ to constrain the Yukawa couplings to electrons h_{ee} of the $H^{\pm\pm}$ boson [57, 68], deriving limits of $0.15 - 1.5$ for $\text{m}(H^{\pm\pm})$ $80\,\text{GeV} - 2\,\text{TeV}$.
- Rare, lepton-flavour-violating decays of μ and τ mediated by $H^{\pm\pm}$, such as the tree-level decay process through off-shell $H^{\pm\pm}$: $\ell_i^- \to \ell_j^-\ell_k^+\ell_l^-$ and a loop induced decay $\ell_i^- \to \ell_j^-\gamma$ (Figure 10b and 10c). Given the current upper limits on the rare decay branching ratios of such processes, the bounds on the ratio of couplings to $H^{\pm\pm}$, $(h_{ee}h_{e\mu})/(m^2_{H^{\pm\pm}}/(100\,\text{GeV})^2)$, can be constructed and are $10^{-7} - 10^{-4}$.
- The muonium-antimuonium conversion (Figure 10d) gives constraints on $(h_{ee}h_{\mu\mu})/(m^2_{H^{\pm\pm}}/(100\,\text{GeV})^2) < 1.98 \cdot 10^{-3}$.
- The muon anomalous magnetic moment $g - 2$ can be both measured and computed to a very high precision, and any large deviations from the SM predictions could indicate new physics. The Brookhaven E821 experiment indeed found a 3σ discrepancy between the SM prediction and experimental result [69]. Doubly charged Higgs could contribute to $a_\mu = (g-2)/2$ as shown in Figure 10e. Requiring theory and experiment to be consistent within 4σ gives constraints on $(h^2_{\mu\mu} + \frac{1}{4}h^2_{e\mu} + \frac{1}{4}h^2_{\mu\tau})/(m^2_{H^{\pm\pm}}/(100\,\text{GeV})^2)$ $< 3.4 \cdot 10^{-2}$.

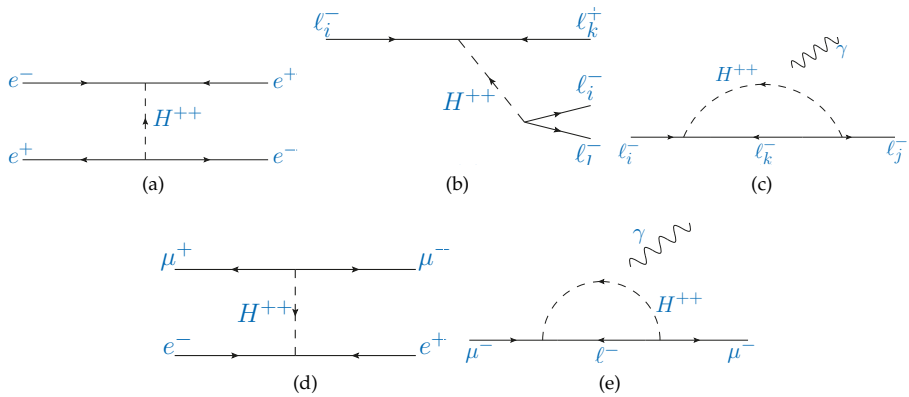

Figure 10: Feynman diagrams for $H^{\pm\pm}$ contributions to (a) Bhabha scattering, (b) lepton-flavour-violating decays $\ell_i^- \to \ell_j^- \ell_k^+ \ell_l^-$ and (c) $\ell_i^- \to \ell_j^- \gamma$, (d) muonium-anti-muonion conversion, and (e) muon $g-2$. Diagrams taken from [53].

Part II

THE EXPERIMENTAL SETUP

3 THE LARGE HADRON COLLIDER

We need the world's largest machine to examine the tiniest particles in the Universe and to search for new physics that could manifest itself in pairs of same-charge leptons. Such a machine is the Large Hadron Collider (LHC), a circular accelerator at CERN, which forms a 27-km-long ring under the French-Swiss border near Geneva, utilizing the same tunnel that was used for the Large Electron-Positron (LEP) collider.

The LHC was designed to make discoveries. This goal was achieved with the discovery of the Higgs boson in 2012 [14, 15]. The LHC provides enough energy for the experiments to explore physics at the TeV scale to look for evidence for a wide range of new physics from new heavy vector bosons to supersymmetry and extended Higgs sector. The high collision rate allows high precision measurements of QCD, electroweak interactions, and flavour physics. In addition, the LHC can accelerate heavy ions to study specific phenomena, such as quark-gluon plasma, in conditions similar to the very early Universe.

The LHC accelerates two counter-rotating beams of protons and heavy ions at a velocity approaching the speed of light and makes the beams collide at four interaction points. Very high energies are needed in order to produce massive particles: how massive the produced particles can be is dictated by the total centre-of-mass energy ($\sqrt{s}$ [1]) available. In the first period of proton–proton (pp) data taking, the so-called LHC Run 1, the LHC operated at $\sqrt{s}$=7 TeV in 2010-2011, and $\sqrt{s}$=8 TeV in 2012. Run 1 consolidated the SM and complemented it with the Higgs boson discovery. The LHC Run 2 in 2015-2018 operated at $\sqrt{s}$=13 TeV and the Run 3 starting in 2021 is foreseen to operate at $\sqrt{s}$=14 TeV.[2] In addition to protons, the LHC can also collide heavy ions (such as lead $^{208}\mathrm{Pb}^{82+}$). During Run 2, proton–lead and lead–lead beams collided at the centre-of-mass energy of 5.02-8.16 TeV per nucleon pair. There was also a special Xe–Xe run at the energy 5.44 TeV per nucleon pair in 2017. [70]

This chapter starts by explaining *how* protons and heavy ions are accelerated and set on a collision course. They collide at four major LHC experiments introduced in Section 3.2. Each of those experiments has a purpose of understanding Nature better and finding new physics, and the accelerator has to deliver as many events as possible in order to help the experiments to reach that goal. How likely it is to produce such events can be characterized by the accelerator's ability to produce the required number of interesting interactions. Quantitative measures for doing so are explained in the last part of this Chapter in Section 3.3.

3.1 ACCELERATING HADRONS

Accelerating protons is a complicated process at CERN and it requires many participating machines in the accelerator chain. Each machine boosts the energy of the proton beam before injecting the beam into the next machine.

Every observed pp event at the LHC has their origin in a simple bottle of hydrogen gas. The protons, obtained from hydrogen atoms by stripping the electrons away, begin their journey

1 $s = (p_1 + p_2)^2$ where p_1 and p_2 are the four-momenta of the colliding protons. In collider experiments, the centre-of-mass energy is $2E_{\mathrm{beam}}$ whereas in fixed-target experiments it is $\sqrt{E_{\mathrm{beam}}}$. Therefore larger energies are easier to reach with colliders.

2 As a former cosmic ray experimentalist, I must emphasize that nature is still far more powerful than any machine: the highest energies of the cosmic ray particles observed are up to 10^{20} eV.

in a linear accelerator called Linac2. It accelerates the protons to the energy of 50 MeV. After that, the protons are sent to the Proton Synchrotron Booster (PSB), which accelerates them to 1.4 GeV. Next in line is the Super Proton Synchrotron (SPS) - the birthplace of Z and W boson discoveries in the 1980s - where the protons are accelerated to 450 GeV. Only the final step is the Large Hadron Collider, which accelerates protons to their final energy up to 6.5 TeV in two beam pipes.

Very strong magnets are needed to direct and focus the beams around the accelerator ring. The LHC has 1232 dipole magnets which bend the beams. Each magnet weighs 35 tonnes and is 15 m long, producing a total magnetic field of 8.3 T by using a 11 kA current flowing through superconducting coils cooled to -271.3 °C. In addition, 392 quadrupole magnets are used to focus the particles in a tight beam. In each beam, protons are organized in *bunches* spaced by 25 ns. Each proton beam can contain up to 2808 bunches at full intensity, and each bunch can contain $1.15 \cdot 10^{11}$ protons at the start of nominal fill. [70].

The name of the accelerator is not Large Proton Collider - protons are not the only particles accelerated at the LHC. Heavy lead ions are obtained from a source of vaporised lead. Unique to ions is that they travel to Linac3, from where they are accumulated and accelerated to 72 MeV per nucleon in the Low Energy Ion Ring (LEIR). Then they share the rest of their path with protons to PS and SPS. PS can accelerate them to 5.9 GeV per nucleon, and SPS even further up to 117 GeV per nucleon. The accelerator chain together with experiments around accelerators is shown in Figure 11.

Under normal operating conditions, the beams can circulate for many hours before dumping. These periods of stable operation are called stable runs, and during them the beams from the two separate beam lines cross at four interaction points (IP) inside the four experiments across the LHC.

3.2 EXPERIMENTS

The LHC hosts four major experiments:

- ATLAS (A Toroidal LHC ApparatuS) is a general-purpose experiment designed to exploit a huge range of new physics searches and the SM measurements. [72]
- CMS (Compact Muon Solenoid), similarly to ATLAS, is a general-purpose experiment. However, it has a different magnet system and other technical solutions than ATLAS on the other side of the LHC ring. In this way, both experiments can extend and support each other, providing cross-confirmation of any new discoveries. The CMS detector is built around a huge superconducting solenoid magnet producing a 4 T magnetic field, which is enclosed in a 12000-tonne steel return yoke. The CMS inner tracking consists of all silicon detectors. [73]
- ALICE (A Large Ion Collider Experiment) is optimized to study the physics of strongly interacting matter using heavy ion collisions. At these extreme energy densities and temperatures, a phase of matter called quark-gluon plasma can be formed. [74]
- LHCb (Large Hadron Collider beauty) studies heavy flavour physics. It searches for evidence of new physics in CP violation, and rare decays of beauty and charm hadrons. Its design differs from other big experiments: it is a *forward* spectrometer as its goal is to study B mesons produced close to the beam pipe. LHCb has a very successful physics programme with the observation of pentaquarks, the discovery of CP violation in charm particle decays, and observations of new baryon particles. [75, 76].

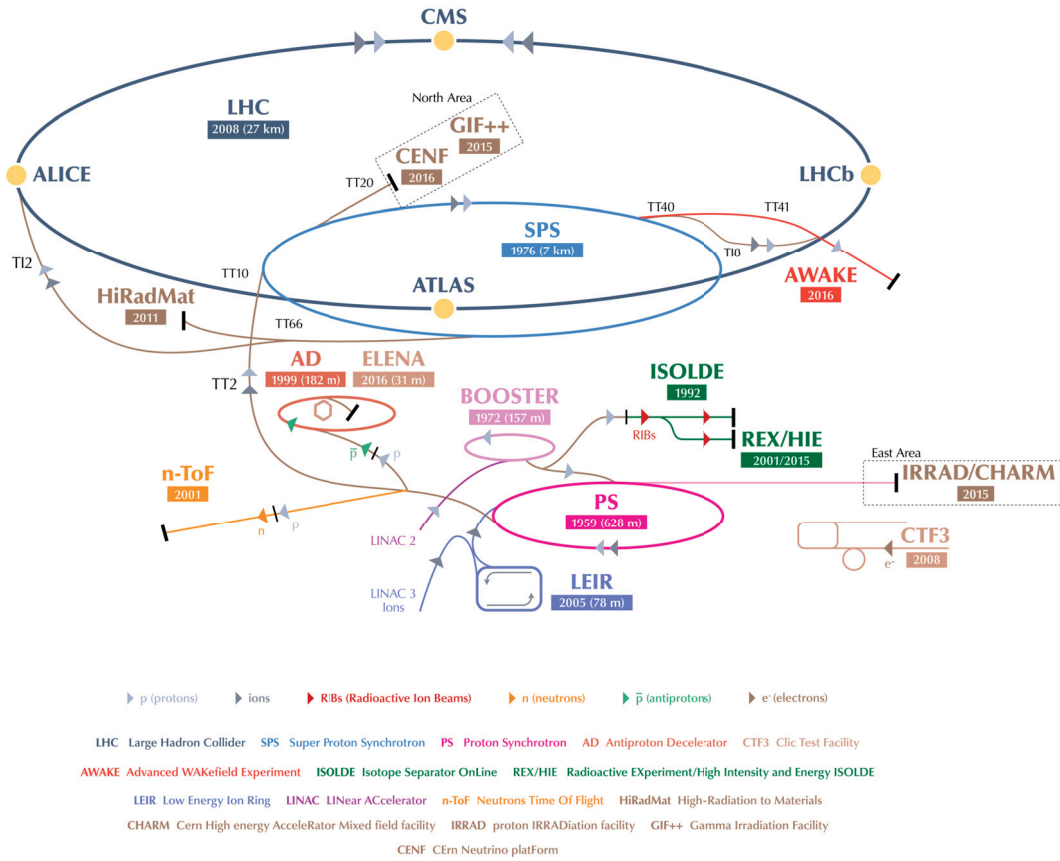

Figure 11: The accelerator chain leading to the LHC (dark blue line) and the experiments around it. Figure taken from [71].

In addition to these four giants, there are also three smaller experiments around the LHC: TOTEM (TOTal cross-section, Elastic scattering and diffraction dissociation Measurement), LHCf (The Large Hadron Collider forward) and MoEDAL (the Monopole and Exotics Detector at the LHC). TOTEM, located on the sides of the CMS interaction point, and LHCf, on the sides of the ATLAS collision point, study properties of forward particles - those that swoosh past each other rather than colliding head-on when the proton beams collide. MoEDAL searches for a hypothetical particle called the magnetic monopole, and is located near LHCb.

3.3 LUMINOSITY AND CROSS-SECTION

One of the main measures of the LHC performance is the luminosity L, which describes the ability of an accelerator to produce the required number of interactions. It can be calculated using beam parameters as

$$L = \frac{N_p^2 n_b f_{\text{rev}} \gamma_r}{4\pi\epsilon_n \beta*} F \tag{25}$$

where N_b is the number of particles per bunch ($\approx 10^{11}$), n_b the number of bunches per beam (2808), f_{rev} the revolution frequency ($\approx$ 11 kHz), γ_r the relativistic gamma factor ($\approx$ 7000), ϵ_n the normalized transverse beam emittance (3.75 µm), $\beta*$ the beam squeezability at the collision point (0.55 m), and finally F the geometric luminosity reduction factor due to the crossing angle at the IP. Both ATLAS and CMS experiments aim at the peak luminosity of $L = 10^{34}$ cm^{-2}s^{-1}. [77]

Luminosity drives our ability to produce rare processes with a low *cross-section* σ, which is a measure of how likely it is that a given process happens under certain conditions. Cross-sections are usually quoted in barns, where 1 barn = 10^{-28} m^2, often expressed in picobarns (pb) 1 pb = 10^{-12} barn and 1 fb = 10^{-15} barn. The *integrated* luminosity $\mathcal{L}$ ($\mathcal{L} = \int L dt$) is measured in inverse cross-section units (fb^{-1}, pb^{-1},...) and is related to number of events N_{event}:

$$N_{\text{event}} = \mathcal{L} \cdot \sigma \cdot \epsilon \cdot A \tag{26}$$

where σ is the cross-section for the physics process, ϵ is the efficiency and A is the geometrical acceptance of the detector.

The cross-section depends on the process and on the collision energy, as shown in Figure 12. Events with new and heavy particles are rare when two protons collide at the LHC, i.e. they have a low cross-section. Therefore a high collision rate is needed to have a statistically significant amount of new particles such as the Higgs boson, the discovery of which was one of the main goals of the ATLAS experiment. As can be seen, there are many orders of magnitude difference between the total pp cross-section and the Higgs production cross-section: $\sigma_{pp}/\sigma_H \approx 10^{11}$! New, exotics particles have even smaller cross-sections and will be produced even less often than the Higgs boson. Out of the recorded signal events, only a fraction will be found amongst the large backgrounds, which come to a great extent from events with jets. Therefore experimentalists develop more and more accurate analysis methods to identify signal events from the increasing backgrounds. Figure 12 not only shows the impressive amount of data and luminosity we expect to have every second, but also that the very rare processes can be reached with the current energies, hopefully revealing something beyond the Standard Model.

Given the need to maximize the sensitivity to new physics, it is important to have as high luminosity as possible. There are a couple of ways to do it: the number of proton bunches can be increased, or the cross-sectional area of the proton beams can be reduced. To ensure stable operating conditions for the experiments, the luminosity can be levelled, i.e. reduced with respect to the nominal and maintained at this constant level as long as possible. High luminosity comes at a cost: it leads to multiple pp interactions in each bunch crossing, called *pile-up* μ.

Pile-up comes in two forms. *In-time* pile-up refers to multiple simultaneous pp interactions in a single bunch crossing, and *out-of-time* pile-up refers to the effect of seeing multiple interactions outside of the current bunch crossing due to the long read-out and processing times of various detector parts. High pile-up complicates physics analyses, as interesting physics events are accompanied by a number of pile-up events. Therefore, a lot of effort is put into detector design, event reconstruction and analysis to mitigate the pile-up effects.

Total integrated luminosity recorded by ATLAS during full LHC Run 2 is shown in Figure 13a. ATLAS recorded about 150 fb^{-1}of pp collision data which significantly exceeds the Run 1

data of roughly 25 fb^{-1}. The difference in delivered luminosity and recorded luminosity is caused by data acquisition inefficiencies. Only a part of the recorded data satisfies strict data quality requirements, as will be discussed in more details in Section 6.6 in terms of one of the ATLAS subdetectors.

Figure 13b shows the mean number of interactions per crossing $\langle\mu\rangle$ for the proton-proton collisions recorded in 2015-2018 at 13 TeV centre-of-mass energy. The mean of the full Run 2 is $\langle\mu\rangle = 33.7$. The small peak at low-μ corresponds to data recorded for studying high precision W physics.

3.4 WHY A HADRON COLLIDER?

To look for physics beyond the Standard Model, we need to have high enough energies to maximize sensitivity to new heavy particles, and enormous amount of collisions, i.e. high luminosity, to see very rare processes. The LHC can provide both.

But why do we collide hadrons instead of light leptons? Lepton colliders, such as electron-positron or muon-muon colliders, offer a clean event and a well-defined value of the collision energy, because the collision happens between two point-like particles rather than two partons of a composite particle. With such clean initial states, it would be possible to perform very precise measurements of the SM particles to determine their exact parameters and find possible deviations leaving room for new physics discoveries. However, it is challenging to reach high collision energies with circular e^+e^- colliders due to large energy losses of electrons by synchrotron radiation[3]. Muons are heavier than electrons and for that reason loose less energy by synchrotron radiation, but there are challenges arising from the short muon lifetime, and from the production of large numbers of muons in bunches with small emittance [80].

A hadron-hadron collider could also collide protons against anti-protons as at Tevatron. While proton–anti-proton colliders have an advantage that both counter-rotating beams can rotate in the same magnetic field, packing enough antiprotons into a single beam and storing them would be really challenging at high energies needed.

3 A solution would be to reduce the curvature either by increasing the radius of the circular collider, or by having a linear collider instead.

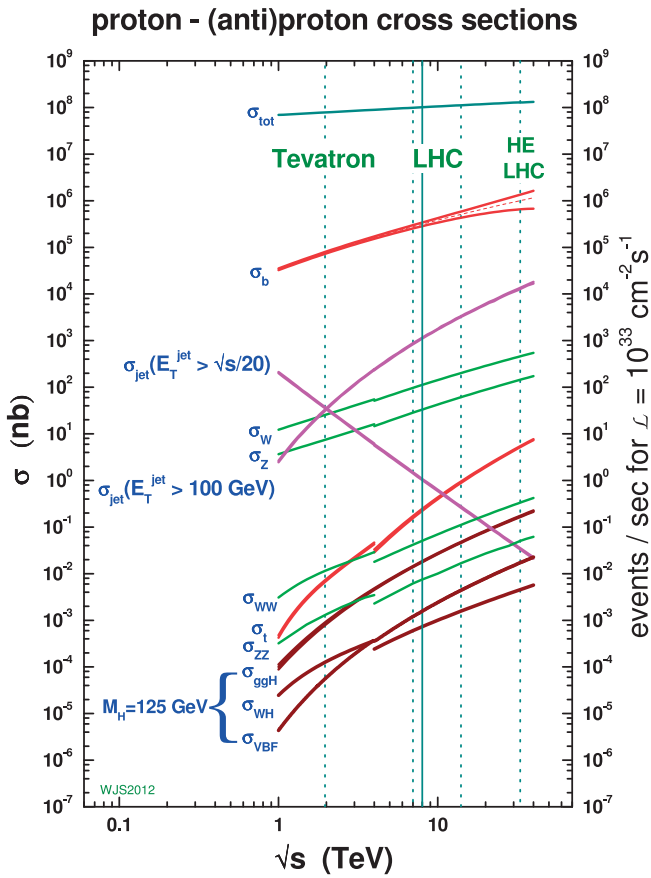

Figure 12: Standard Model cross-sections as a function of centre-of-mass energy. Vertical lines represent various colliders: Tevatron with $\sqrt{s} = 1.96\,\text{TeV}$, the LHC with $\sqrt{s} = 7\,\text{TeV}$ (2011), $\sqrt{s} = 8\,\text{TeV}$ (2012) and $\sqrt{s} = 14\,\text{TeV}$ (as designed), and the possible High Energy LHC (HE-LHC) upgrade with $\sqrt{s} = 33\,\text{TeV}$. [78]

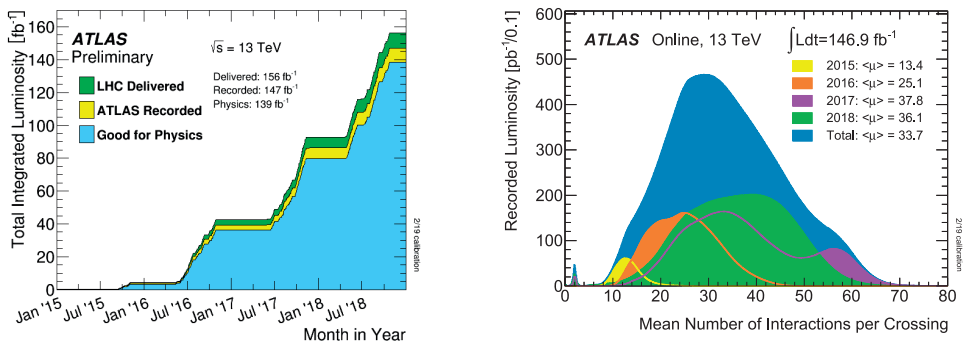

(a) (b)

Figure 13: (a) Total integrated luminosity versus time delivered to ATLAS (green), recorded by ATLAS (yellow), and analysed and marked as good for physics analysis (blue), and (b) mean number of interactions per bunch crossing, $\langle\mu\rangle$, for the proton-proton collisions at 13 TeV recorded in 2015-2018 during the LHC Run 2. [79]

4 THE ATLAS EXPERIMENT

ATLAS (A Toroidal LHC ApparatuS) is a general-purpose detector which is designed to exploit the full discovery potential of the LHC from discovering the Higgs boson to searches for new heavy W- and Z-like gauge bosons, supersymmetry, and exotic heavy Higgs bosons. ATLAS also contributes to high precision measurements of QCD and electroweak interactions. Therefore, ATLAS has to cope well with a broad variety of possible physics processes and signatures covering electron, photon, muon, jet, tau, and missing transverse energy measurements as well as heavy flavour tagging.

The ATLAS design choices were driven by the benchmark physics goals that set the required thresholds for detection efficiencies and resolutions at high luminosity and extreme radiation doses. High collision rate causes high radiation levels requiring fast, radiation-hard electronics and sensor elements. These challenges are answered by having a cylindrical detector consisting of several subsystems and covering the full solid angle (4π) with a total length of 42 m and a radius of 11 m, making ATLAS a big friendly giant. ATLAS uses a large variety of technologies for reconstructing and identifying nearly all particles produced in the event. It has an efficient tracking system for charged particle momentum measurements, b-quark tagging, and electron and photon identification, as well as tau and heavy-flavour vertexing. Tracking is complemented by calorimeters that provide accurate energy measurements of particles undergoing either electromagnetic or hadronic interaction. Finally, muons are measured with a muon spectrometer system. The ATLAS detector layout is shown in Figure 14. With over 100 million electronic channels and 3000 km of cables, ATLAS is one of the most complex and impressive machines ever built.

This chapter describes the ATLAS detector and its subsystems, following closely the technical design report [72] and the phase-II upgrade note [81]. The coordinate system and common kinematic variables are defined in Section 4.1, after which the ATLAS detector subsystems are described.

4.1 COORDINATE SYSTEM AND COMMON KINEMATIC VARIABLES

ATLAS uses a right-handed coordinate system, where the nominal interaction point (IP) is defined as the origin, and the z-axis along the beam pipe. The $x-y$ plane is *transverse* to the beam direction: the x-axis points from the IP to the centre of the LHC ring, and the y-axis points upwards. Cylindrical coordinates (r, ϕ) are used in the transverse plane, ϕ being the azimuthal angle around the z-axis. The pseudorapidity is defined in terms of the polar angle θ as $\eta = -\ln\tan(\theta/2)$.[1] Pseudorapidity is zero for particle trajectories perpendicular to the beam ($\theta = 90°$), and when the polar ange θ approaches zero, pseudorapidity approaches infinity. Hard interactions with high momentum transfer produce particles at small η far off the beam pipe direction. Angular separation between particles is expressed in terms of $\Delta R = \sqrt{\Delta\eta^2 + \Delta\phi^2}$, where $\Delta\eta$ and $\Delta\phi$ are differences in pseudorapidity and azimuthal angle, respectively.

1 This is a convenient definition: η depends only on θ, and not on the energy of the particle, unlike rapidity defined as $y = 1/2\ln[(E + p_z)/(E - p_z)]$. For massless particles and particles with $p_T \gg m$, the rapidity and pseudorapidity are the same.

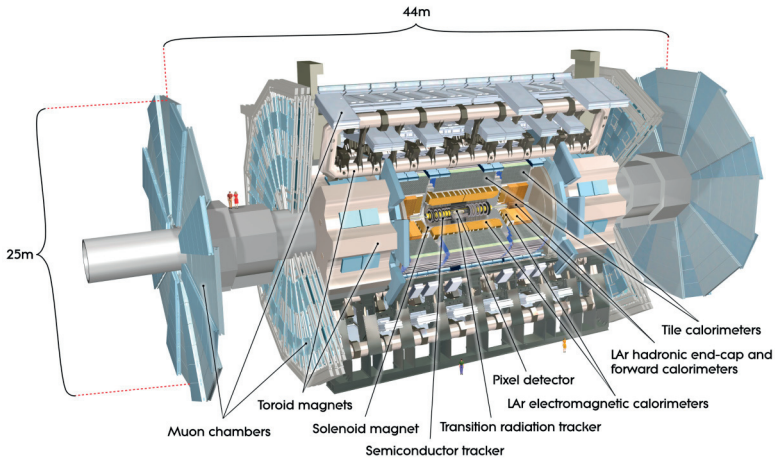

Figure 14: The ATLAS detector. [72]

It is often convenient to use transverse components in the $x-y$ plane, such as transverse momentum $p_T = \sqrt{p_x^2 + p_y^2}$ defined as the momentum perpendicular to the beam axis, and transverse energy E_T. The reason comes from the momentum conservation in the $x-y$ plane, which implies that the vectorial sum of the transverse momentum of all the collision products must be zero; any imbalance is referred to as missing transverse energy.

Missing transverse energy, E_T^{miss}, comes either from non- or weakly interacting particles such as neutrinos that are invisible to detectors, or from limited detector acceptance, dead regions in the detector, or other problems in the detectors. It can also indicate a presence of a new particle, such as dark matter particle or neutralinos from supersymmetry, which makes E_T^{miss} an important variable for BSM searches. It is not a simple object: a good understanding of all objects in an event is needed from electrons to jets. Any missed muon, mismeasured jet and dead area of the detector can affect to missing transverse energy. Generally it can be expressed using its x- and y-components

$$E_T^{miss} = \sqrt{(E_x^{miss})^2 + (E_y^{miss})^2}, \quad \phi^{miss} = \arctan(E_y^{miss}/E_x^{miss}) \tag{27}$$

where ϕ^{miss} is its direction.

4.1.1 *Tracking parameters*

In ATLAS, the commonly used track parametrization is the set of perigee parameters (z_0, d_0, θ, ϕ, q/p), where the perigee is the closest approach of the track to the beam-axis z. The distance to the origin in the z direction is the longitudinal impact parameter z_0. The distance in the $x-y$ plane to the beam axis, d_0, is called the transverse impact parameter. The impact parameter is given a positive sign if the direction of the track is clockwise with respect to the origin, and negative otherwise. The polar angle θ is the angle of the track to the z axis. The azimuthal angle ϕ is the angle in the $x-y$ plane. Finally, q/p where q is the charge and p is the momentum of the particle can be deduced from the measured track curvature. If the magnetic field is not applied, the curvature parameter is set to 0. The track parameters are illustrated in Figure 15.

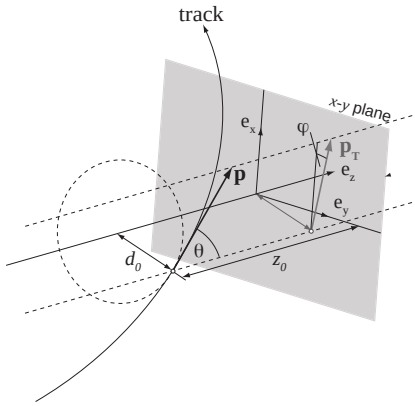

Figure 15: Track parameters used in ATLAS. [82]

4.1.2 *Momentum measurement*

The path of a charged particle moving in a magnetic field is described by a helix, i.e. the path is bent by a magnetic field. The radius of curvature R of the track depends on the momentum of the particle and the strength of the magnetic field. The motion of a charged particle in a uniform field B can be determined by the Lorentz force, and one can obtain the transverse momentum $p_T = qBR$ where q is the charge of the particle [83]. The particle's transverse momentum can be measured from the *sagitta* of the track, defined after a bit of algebra as

$$s \approx \frac{0.3BL^2}{8p_T} \tag{28}$$

where L is the length of the track measured on the transverse plane and defined by the outer radius of the tracking system. As Eq. 28 shows, particles with higher p_T have smaller sagitta and therefore straighter tracks. The relative momentum resolution can be determined by

$$p_T = \frac{0.3L^2B}{8s} \Rightarrow \frac{\delta p_T}{p_T} = \frac{\delta s}{s} = \frac{8}{0.3}\frac{1}{L^2B}p_T\delta s \tag{29}$$

which tells that the measurement uncertainty can be minimized by maximizing L (large lever arm, large tracking systems) and having strong magnetic fields. It can be noted that the inverse of transverse momentum $1/p_T$, not p_T, can be measured with Gaussian uncertainties.

Track curvature in a magnetic field can be measured using a minimum three measurements. For large number of equally spaced detectors with the same position accuracy σ in a uniform magnetic field of strength B, the expression for momentum resolution can be generalized according to [84]

$$\frac{\delta p_t}{p_t} = \frac{p_t\sigma}{0.3BL^2}\sqrt{(A_N)} \tag{30}$$

where

$$A_N = \frac{720N^3}{(N-1)(N+1)(N+2)(N+3)} \tag{31}$$

in the units of GeV, tesla and meter, and p_T is the component of the momentum perpendicular to the magnetic field. Eqs. 29-30 illustrate that the momentum resolution degrades

linearly with momentum, and improves linearly with the magnetic field. However, the most important parameter is the lever arm L which improves quadratically with radial extension of the detector.

4.2 PARTICLE IDENTIFICATION

Particle identification is achieved by comparing the energy deposits in different parts of the detector system. When a particle emerging from the collision[2] travels outwards from the interaction point, it will first encounter the Inner Detector, which is responsible for tracking and momentum measurements of the charged particles such as electrons. Neutral particles such as photons and neutrons do not leave any track to the Inner Detector. The energies of particles will then be measured in electromagnetic and hadronic calorimeters forming the next two layers of ATLAS. Electrons and photons will lose their energies in the electromagnetic calorimeter. Collimated bundles of charged hadrons (jets) leave a small energy deposit in the electromagnetic calorimeter due to ionization energy loss, and a larger energy deposit in the hadronic calorimeters. Only muons and neutrinos will survive beyond the hadronic calorimeter. Because muons have relatively long lifetimes and interact only minimally with other detector parts, muons will be tracked further in dedicated muon chambers and their momenta are measured from their tracks bended in a magnetic field. Neutrinos are invisible to ATLAS: they do not leave any signature to any layer of the detector. However, we can reconstruct them by calculating how much energy and momentum there is "missing" due to energy and momentum conservation laws as explained in 4.1. As shown in Figure 16, all these layers together allow us to identify particles produced in collisions and measure precisely their energies and directions.

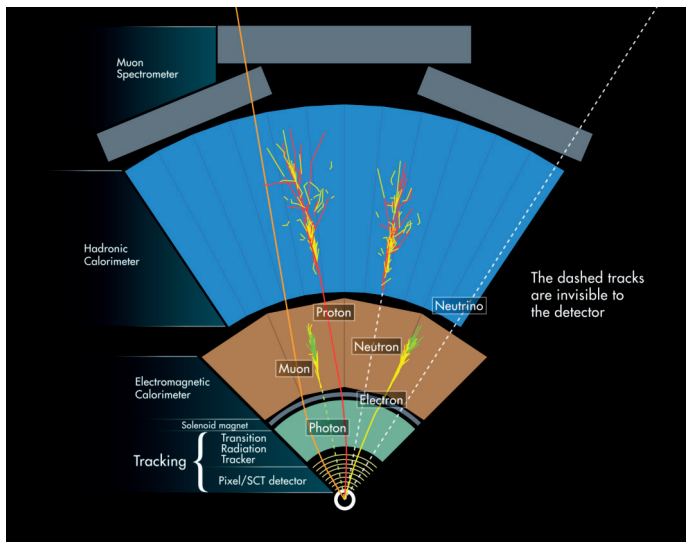

Figure 16: Interactions of particles with different parts of the ATLAS detector. [72]

2 Not all the particles live long enough to travel through the whole detector, in which case we can reconstruct their decay products such as electrons, muons, photons, taus and hadrons.

4.3 INNER DETECTOR

The main goal of the Inner Detector (ID) is to provide reliable and accurate tracking of charged particles of $p_T > 0.5\,\text{GeV}$, and to determine their charge, momentum, direction and origin (*vertex*) with high reconstruction efficiency up to $|\eta| < 2.5$. Together with calorimeters and muon systems, the ID contributes to particle identification. Electrons can be separated from pions by measuring transition radiation or ionization energy loss (dE/dx). The ID is also important for electron reconstruction by matching isolated tracks to calorimeter energy deposits. These goals call for high-granularity and high-resolution detectors given the large track density close to the interaction point (IP). The ID consists of three complementary subdetectors: semiconductor pixel and strip detectors, providing 3-dimensional space points ($|\eta| < 2.5$), and a straw-tube tracking detector generating and detecting transition radiation and providing both tracking information and particle identification ($|\eta| < 2.0$). All subsystems are composed of a barrel with cylindrical layers, and two end-caps placed symmetrically around the IP. Sitting in a 2 T solenoidal magnetic field, the ID can precisely measure the curvature of tracks of charged particles and therefore provide excellent momentum measurements. The layout of the Inner Detector is illustrated in Figure 17.

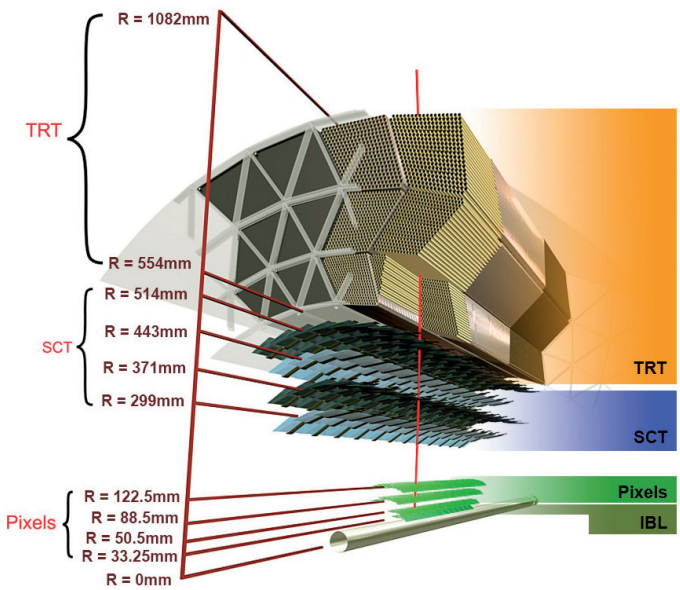

Figure 17: Inner Detector of the ATLAS detector with the new Insertable B-layer. [85]

The ID utilizes different technologies at different radii.

A silicon pixel detector (Pixel) forms the innermost part of the ID and provides a very high granularity to cope with high particle density close to the interaction point. Therefore it improves the impact parameter reconstruction and vertexing. Precise impact parameter measurements are essential for associating tracks with the origin where the initial pp collision took place (primary vertex) and for reconstructing secondary vertices from the decays of primary particles (e.g. B decays, or long-lived particles) or through their interaction with detector material. It is also required for heavy flavour tagging and lifetime measurements. In particular, the b-tagging (i.e. ability to distinguish b-jets from jets originating from light

quarks) relies on accurate measurements of the impact parameter and displaced secondary vertices due to the long lifetime of b-hadrons.

The Pixel detector was originally made of three barrel layers and three disks on each side, resulting in total 1744 pixel sensors and about 80 million individual pixels. Silicon semiconductor pixel sensors measure the energy deposited by ionizing particles and locate spatial hits with a hit resolution of 10 µm in the transverse ($r - \phi$) plane, and 115 µm along z and r. During the first long shutdown of the LHC in 2013-2014, a new innermost pixel detector, the Insertable B-layer (IBL) was inserted between the first pixel layer and a new thinner beam pipe at the radius of 33 mm [86]. It gives additional 8 million pixels, each pixel providing a spatial hit resolution of 8 µm in the $r - \phi$ plane and 40 µm along the z axis. It improves the impact parameter and vertex resolution, and maintains the performance at the higher luminosities despite radiaton damage effects in the pixel B-layer. Furthermore, it improves the b-tagging performance by about 10% [87].

The Semiconducting Tracker (SCT) is essential for the precise momentum measurement. The SCT, located outside the Pixel detector, consists of 4088 modules of silicon-strip detectors. The detectors are arranged in four barrel layers and two endcaps of nine disks each. Each barrel layer and endcap disk gives two strip measurements at a small (40 mrad) stereo angle to provide two-dimensional space-points. A hit position resolution of the SCT is 17 µm in the transverse ($r - \phi$) plane, and 580 µm along z and r. The SCT and Pixel detectors together are often referred to as the Silicon detector.

The Transition Radiation Tracker (TRT) forms the outermost part of the Inner Detector and extends track reconstruction radially up to a radius of 1082 mm. It provides charged particle tracking based on the use of almost 300000 straw detectors, each of which is a proportional drift tube with a diameter of 4 mm. Furthermore, it is used for particle identification through transition radiation measurements. Particle identification is based on distinguishing between two energy deposit thresholds for the signal readout: a low threshold is optimized to detect ionization from particles traversing the straws, while a high threshold is sensitive to transition radiation photons. The TRT will be discussed in more detail in Chapter 6.

The momentum and vertex measurements require fine-granularity detectors close to the interaction point. However, the influence of the detector on the particle, i.e. photon conversion and secondary interactions with the detector material, has to be limited. This can be achieved by minimizing the material budget of both detectors and supporting structures, and therefore the number of precision layers must be limited. Furthermore, covering large areas with silicon detectors would be too expensive at larger radii. The gaseous straw tube detector TRT gives large number of tracking points with much less material per point and at lower cost. The TRT extends the lever arm of the track measurements and improves the momentum measurement especially for high-p_{T} particles.

4.4 CALORIMETERS

After particles travel through the Inner Detector, they arrive to the ATLAS calorimeters. The calorimeters, presented in Figure 18, aim to measure the energy of charged and neutral particles and jets. They are also used to estimate missing transverse energy. The calorimeters cover the range $|\eta| < 4.9$ in order to measure transverse energy accurately and to minimize the presence of uninstrumented regions. There are two calorimeters in ATLAS: an electromagnetic targeting particles interacting via the electromagnetic force, and a hadronic calorimeter

absorbing strongly interacting particles. This distinction is useful: this way different interaction behaviour between the hadrons[3] and electrons or photons can be distinguished.

All ATLAS calorimeters are *sampling* calorimeters with alternating layers of passive absorbing and active material. The absorbing material causes the incoming particle to initiate an electromagnetic or a hadronic shower of secondary particles. Particles created in the showers are detected and their energy is accurately measured in the active layers. This sandwich design allows compact detectors with very dense and usually cheap absorber material, but on the other hand only a part of the particle's energy is deposited in the active layer and can be measured. A great benefit of using calorimeters for energy measurements is that the energy resolution increases with increasing energy. Calorimeters can also measure the energy of neutral particles, such as neutrons and neutral pions.

ATLAS uses two types of active material: Liquid argon (LAr) and scintillating plastic. The measured signal in a calorimeter is proportional to the deposited energy and energy of the primary particle. This measurement can be done by detecting the light produced in a scintillating plastic, or by measuring deposited charge left by ionization in a liquid. When a charged particle passes through a scintillator, it excites the valence electrons, which then re-emit the absorbed energy as light, i.e. *scintillate*. The scintillation light is detected and amplified by photomultiplier tubes. Particles that traverse the liquid argon medium create charge by ionization, inducing an electrical signal to be read out.

The passive absorber material (such as lead) interacts with charged and neutral particles, but does not measure the deposited energy. Electrons lose energy by emitting bremsstrahlung, and photons convert to e^+e^- pairs, forming an electromagnetic shower. Muons emit less bremsstrahlung thanks to their high mass, hence passing the calorimeter system as minimum-ionizing particles. Particles interacting via strong force typically lose their energy through nuclear interactions, creating secondaries that form a cascade of hadrons. If a neutral pion is produced, it decays into two photons, adding an electromagnetic component to the hadronic shower.

4.4.1 *Electromagnetic calorimeter*

The fine-granularity EM calorimeter is divided into a barrel ($|\eta| < 1.475$) and two endcaps ($1.375 < |\eta| < 3.2$), matching the η region of the Inner Detector and therefore suited for measuring electrons and photons precisely.

The electromagnetic calorimeter uses a liquid argon detector with accordion-shaped electrodes as active material, and lead plates absorbers given the short radiation length $X_0 = 0.56\,\text{cm}$ in lead. The total depth of the EM calorimeter is 22 radiation lengths in the barrel and 24 in the endcap region.

In the region $|\eta| < 2.5$, the EM calorimeter is segmented in three layers in depth. The first layer with very high segmentation in η allows precise measurements of the shower position. Furthermore, it is used to reject fake photons from π^0 decays, and to separate electrons from charged pions. The second layer collects the largest fraction of the EM shower. Only the highest energy electrons will reach the last layer which collects the tail of the EM shower, and is therefore less segmented in η. In addition, a thin presampler layer of argon covers $|\eta| < 1.8$ region. It is used to correct for energy losses of particles, caused by the Inner Detector, the solenoid, and the cryostats, before they reach the calorimeters.

3 Note that hadronic showers can come from many different sources. For example, they can come from the hadrons from the fragmentation of quarks and gluons produced in the collision, or from hadronic tau decays.

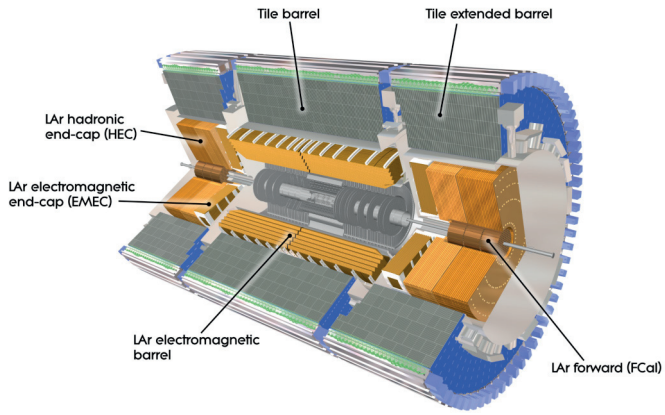

Figure 18: ATLAS calorimeters. [72]

4.4.2 *Hadronic calorimeter*

The coarser-granularity hadronic calorimeter (HCAL) surrounds the EM calorimeter, and it is responsible for identifying the energy and direction of jets and hadronically decaying τ leptons, as well as for measuring the missing transverse energy. The HCAL is divided into three hadronic calorimeters that use different techniques and materials at different regions: the Tile Calorimeter (TileCal), the Hadronic Endcap Calorimeters (HEC), and the Forward Calorimeter (FCal).

The Tile Calorimeter is a non-compensating sampling calorimeter and uses plastic scintillation plates (tiles) as active material, and steel as absorbing material. It covers the central region of $|\eta| < 1.7$ and is longitudinally segmented into three layers, which are used for triggering and reconstructing jets. The Hadronic Endcap Calorimeter consists of two independent wheels per endcap and covers a region $1.5 < |\eta| < 3.2$. It uses liquid argon as active medium and copper plates as absorbers. In the forward region up to $|\eta| < 4.9$, the liquid argon Forward Calorimeter is used to improve reconstruction of missing transverse energy and to identify forward jets. It is divided in three modules per endcap: the first one using copper as absorbing material and designed for electromagnetic measurements, and the other two using tungsten to measure hadronic energy deposits.

4.5 MUON SPECTROMETER

Particles that travel through the full depth of calorimeters are either non- or weakly-interacting particles such as neutrinos, or minimum ionizing particles (MIP) which deposit only ionization energy in the calorimeters[4]. Ideally, only muons should be observed in the muon system that forms the outermost part of the ATLAS detector.

The muon spectrometer (Figure 19) consists of four sub-systems complementing each other: two in the barrel ($|\eta| < 1.05$) and two in the endcaps ($1.05 < |\eta| < 1.05$). One sub-system for each region provides a precise measurement of the particle momentum in the region $|\eta| < 2.7$, while the second sub-system with fast response is used to trigger on events with

4 Rarely, they can also come from a shower that was not fully absorbed in the calorimeter material.

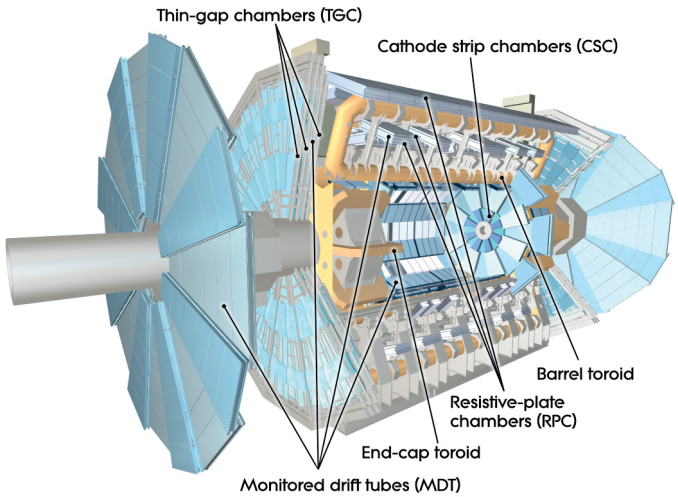

Figure 19: ATLAS muon system. [72]

muon candidates in the region $|\eta| < 2.4$. The full muon system is immersed in a toroidal magnetic field of roughly 0.5 T in the barrel and 1 T in the endcap regions. This setting allows for precise tracking and momentum measurement of charged particles with momenta down to about 3 GeV, which is constrained by the energy loss in the calorimeters, and up to 3 TeV.

The high-precision tracking is performed by three layers of Monitored Drift Tubes (MDTs) covering $|\eta| < 2.7$. Each chamber gives $6 - 8$ pseudorapidity measurements along the muon track. The MDTs can achieve an average resolution of 35 µm per chamber and 80 µm per tube. For $2 < |\eta| < 2.7$, multi-wire proportional Cathode Strip Chambers (CSCs) are used to measure precision coordinates, providing a single-hit resolution of 60 µm. To achieve the high resolution, the muon chambers are aligned with a precision of 30-60 µm.

To have a fast system to trigger on muons, the precision-tracking chambers have been complemented by Resistive Plate Chambers (RPC) in the barrel region ($|\eta| < 1.05$) and Thin Gap Chambers (TGC) in the endcap region ($1.05 < |\eta| < 2.4$). These trigger chambers produce a signal within 15-25 ns, which allows to trigger and to identify the beam-crossing. Furthermore, the trigger chambers measure the track coordinate in the bending plane η and in the non-bending plane ϕ with a spatial resolution of 5-10 mm.

4.6 MAGNETS

A strong magnetic field is necessary to have a strong bending power needed for determining the momenta and charge of charged particles, which can be measured from the curvature and direction of the tracks. The magnet system in the ATLAS detector consists of four superconducting magnets: a central solenoid generating the magnetic field for the Inner Detector, and three large air-core toroids surrounding the calorimeters and generating the magnetic field for the muon system. The overall magnet system is about 26 m long and has a diameter of 22 m, and it is illustrated in Figure 20.

The central solenoid creates a central field of 2 T along the beam line, bending particle trajectories in the ϕ direction. Since the solenoid is placed in front of the electromagnetic calorimeter, the material budget has to be minimal in order to not degrade the calorimeter

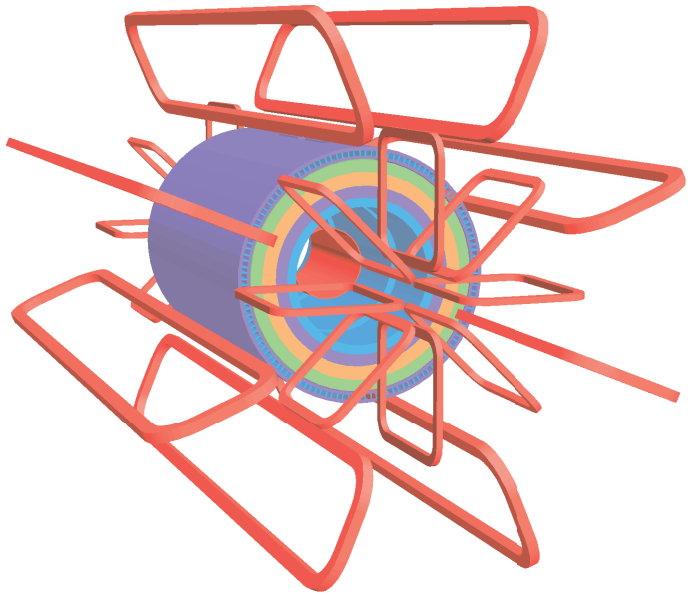

Figure 20: ATLAS magnet system showing both the central solenoid and endcaps. [72]

performance: particles should not start showering before they arrive to the active layers of the calorimeter.

The toroids produce magnetic field for the muon spectrometer, and bend muons in the η direction. This magnet configuration provides a field with a strong bending power that is perpendicular to the muon tracks even at high pseudorapidities. Forward-going particles carry high momenta but low *transverse* momenta perpendicular to the beam, and therefore the toroids allow constant momentum resolution independently of the production angle within the η acceptance.

The toroid magnetic system is divided into two parts: one barrel and two endcap systems. The barrel toroid system consists of eight coils generating a magnetic field of 3.9 T. The endcap toroids produce a magnetic field of 4.1 T and are rotated by 22.5° with respect to the barrel toroid system in order to have radial overlap and to optimize the bending power in the transition region between the two systems. Furthermore, the open structure of toroids minimizes the amount of material in front of the muon spectrometer. Therefore, it reduces multiple scattering, which is limiting the muon momentum resolution.

4.7 FORWARD DETECTORS: BEAM MONITORING AND LUMINOSITY

A large fraction of the produced particles at the LHC are produced with small angles relative to the beam line, i.e. in the forward direction. These events can be used to determine the total cross-section (which describes the overall interaction probability) by estimating the luminosity delivered by the LHC. The ATLAS forward detectors are designed to study such events in the very high η region.

- LUCID (LUminosity measurement using Cherenkov Integrating Detector) is the main relative luminosity detector. It is designed to detect inelastic pp scattering in the forward

direction in order to measure and monitor luminosity and beam conditions. It consists of several small Cherenkov detectors and is located at ± 17 m from the interaction point.

- ZDCs (Zero-Degree Calorimeters) are used in heavy-ion collisions to detect forward neutrons with $|\eta| > 8.3$, to determine the centrality of collisions, and to work as a trigger for ultra-peripheral ion-ion interactions. The ZDCs are located at ± 140 m from the IP.
- ALFA (Absolute Luminosity For ATLAS) provides alternative measurements of luminosity. It measures the absolute luminosity and total cross-section via elastic scattering at small angles. It consists of scintillating-fibre trackers located inside Roman pots at a distance of ± 240 m from the IP. The detectors can be moved vertically and may approach the beam as close as few millimetres.
- AFP (ATLAS Forward Proton) measures the momentum and emission angle of forward protons that remain intact from the interaction. The corresponding physics processes are associated with elastic and diffractive scattering such as pomeron (QCD) and photon (QED) exchange. AFP is a silicon tracker located inside Roman pots at 220 m from the IP.

The luminosity calibration relies on various detectors and algorithms. LUCID provides the primary bunch-by-bunch luminosity measurement, which is complemented by bunch-by-bunch measurements from the ATLAS Beam Conditions Monitor (BCM) diamond detectors and offline measurements of the multiplicity of reconstructed charged particles [88]. BCM also monitors the stability of the LHC beam. The luminosity scale is calibrated using special van der Meer (vdM) scans, where the beams are separated vertically and horizontally so that the beam overlap varies. Increasing overlap leads to more interactions.

5 FROM SIGNALS TO DIGITS, FROM PARTICLES TO NTUPLES

Recording electrical signals from the detector initiates a long and complicated processing of data, which includes many aspects from triggering to physics object reconstruction and to data quality estimations. However, it is also necessary to compare the recorded data with theoretical expectations. Therefore, complex simulations of both various physics processes and the ATLAS detector itself are required to model the expected contributions.

This chapter starts by reviewing how real data from particle collisions are taken (Section 5.1) and triggered (Section 5.2) at ATLAS. As we need to understand the ATLAS data from the first principles, the simulation of the physics processes and the interactions of particles with the detector material are discussed in Section 5.3. After obtaining both real and simulated data, they are processed in a similar way using the same methods as explained in Section 5.4. Finally in Section 5.5, physics objects such as electrons, muons, taus, and jets can be reconstructed and identified among other processes.

5.1 DATA TAKING

The first long period of data taking, LHC Run 1 at $\sqrt{s} = 7\text{-}8\,\text{TeV}$ in 2009-2012, completed the SM with the Higgs boson discovery and consolidated the SM with detailed precision measurements. After the first long shutdown, the LHC Run 2 at $\sqrt{s} = 13\,\text{TeV}$ in 2015-2018 delivered almost $160\,\text{fb}^{-1}$ of data. These data are further divided up to periods and runs in ATLAS. A run is a continuous period of data recording, usually corresponding to a single LHC fill recording data for many hours. Each run can be further divided into luminosity blocks which correspond approximately to a minute of data taking each, and therefore each run has usually a few hundred luminosity blocks. The Good Runs List (GRL) is a list of good luminosity blocks within the data runs forming a set of good-quality data that can be used for physics analyses. A group of runs taken with similar conditions is called a data taking period.

The Run Control (RC) system [89] steers the data acquisition by controlling the detector, the trigger and data acquisition (TDAQ) system and communicating between the two. During a run, the record of the state of the detector is continuously stored to an online conditions database, which will be also mentioned in Section 6.7.

5.2 TRIGGERS

The ATLAS experiment is designed to study the collisions at a very high collision rate of 40 MHz with reading data from 100 million channels, leading to a size of 1.5 MB per event and resulting in a data volume of more than 60 TB/s. Even if this kind of data flow could be handled technically, no experiment can afford the disk space to store that much data. As mentioned, only a part of these data contain events with interesting physics and is reasonable to store and analyse. The trigger and DAQ (TDAQ) system reduces the initial data rate to about 200 interesting events per second based on a multi-step selection process.

First, a hardware based Level-1 trigger filters the event rate from 40 MHz to about 75 kHz by utilizing signals from the calorimeters and the muon chambers. It has 2.5 µs to decide which events to keep and which events to discard. The Level-1 trigger consists of the Calorimeter

Trigger (L1Calo), the Muon Trigger (L1Muon) and the event-decision part implemented in the Central Trigger Processor (CTP). It defines regions-of-interest (RoIs) which have muon tracks in the muon system or calorimeter clusters with high transverse energy for electron/photon and jet reconstruction.

If the Level-1 trigger decides an event was interesting, the information is sent to the next trigger levels in the sequence, Level-2 trigger and Event Filter, which form the software-based High Level Trigger (HLT) system. Level-2 trigger reduces the data rate to about 3.5 kHz. The HLT uses information from calorimeters, precision measurements from the muon system, and tracking information from the Inner Detector. Finally, the Event Filter selects the remaining 200 events per second to be stored at a permanent mass storage.

A sequence of both L1 and HLT trigger algorithms is collectively called a trigger. It can rapidly identify signatures of a given type and a given transverse momentum or energy threshold. Such signatures can be particles such as muon, electron, tau, photon, tau, and (*b*-)jets, or characterize global event, such as missing transverse energy. For example, in this thesis we make use of both single- and dilepton triggers with specific transverse momentum thresholds. The full list of the possible Level-1 and HLT triggers and their configurations that are optimized for the LHC running conditions are encoded in the *trigger menu*. The trigger menu consists of a) primary triggers used for physics analyses, b) support triggers used for performance measurements and monitoring, c) alternative triggers, using experimental or new reconstruction algorithms, d) back-up triggers with tighter selections, and finally e) calibration triggers which are used for detector calibration.

As discussed in Section 3.3, the probability for a given process to occur can vary a lot between different processes. The QCD dijet and multijet production dominates over rare, exotic processes at the LHC. If the trigger chooses all events passing a certain transverse momentum threshold, a resulting dataset will consist mainly of dijet events. For this reason, some triggers can be *prescaled* to reduce the trigger rate especially at lower transverse momenta. Prescale of N means that every N events are kept by the trigger, and the rest are thrown away. However, the majority of ATLAS analyses use unprescaled triggers for the best sensitivity.

5.3 DETECTOR AND EVENT SIMULATION

5.3.1 *Modelling of physics processes*

The main goal of the Monte Carlo simulation of events is to understand the underlying physics of the observed data and the performance of detectors. Simulations are used for several purposes: to predict event rates and topologies of physics processes, and to study experimental signatures that can be compared to measurements. In addition, simulations are useful when optimizing tools and analysis strategies from event selection to background estimation. In data analysis, simulation can be used to calculate efficiencies of a detector or a specific algorithm, such as physics object reconstruction efficiencies and acceptance corrections. Simulations play also a crucial role when systematic uncertainties are evaluated and set. Last but not least, no new experiments or detectors could be designed without relying heavily on simulations.

The simulation of physics events in ATLAS is performed in multiple steps. First step is *event generation*, in which particles from hard processes and their immediate decays in the event are generated. The resulting particles are passed to the *detector simulation*, where their interactions with the detector material are simulated using GEANT4 simulation toolkit [90]. However, such events with particles from only hard processes do not correspond the real collision events due to a lack of pile-up. This issue is addressed by overlaying soft *minimum*

bias events to simulate the interactions between the other particles in the bunch crossing. All of the particles, either from the original hard process or from the pile-up, are passed through the detector simulation and their energy deposits in sensitive elements of the detector are estimated. These first two steps will be further discussed below in Section 5.3.2.

Next step is *digitization*, where the simulated energy deposits are turned into a digitized detector responses. Each subdetector has a model of how the hit in the detector element is translated into a digital output of the readout electronics. These models include various effects such as the noise modelling and masking inefficient or dead channels. At this point, triggers are also simulated. After digitization, simulated data looks like raw data observed in the actual detector, with the exception that the *truth information* is still stored for simulated events. The truth information includes a record of interactions from the generator for every particle. The rest of the analysis procedure is performed in a similar manner as for real data: digitized signals are turned into tracks in the ID and MS and into energy deposits in the calorimeters, as will be described in Section 5.5.1.

5.3.2 *Event generators*

Generating simulated Monte Carlo (MC) datasets is a complex process involving several steps from calculating the matrix elements for each process to simulating the interactions of particles with matter to finally reconstructing the objects as if they were really recorded in the detector. There are multiple computer programs, so-called event generators, which generate physics events with a wide range of physics processes using Monte Carlo techniques.

In general, the first step is to look what happens initially when two hadrons come in on a collision course. Since the partons in the initial state are only constituents of hadrons, they have just a momentum fraction x of the proton momentum. The calculation of production cross-sections relies on knowing the distribution of the momentum fraction and flavour composition of the partons, called Parton Distribution Function (PDF). The PDFs are determined by global fits to data by many collaborations such as CTEQ [91], MSTW [92], and NNPDF [93].

A hard subprocess results from partons interacting at high momentum scale (at the LHC typically $\mathcal{O}$(100-1000 GeV)) and producing outgoing "resonances" such as the top or Z, W or Higgs bosons. Such event can usually be characterized by large momentum transfers and large angles with respect to the beam pipe. It can be described by the relevant matrix elements (MEs), usually calculated to leading order (LO), next-to-leading order (NLO), or even next-to-NLO (NNLO).

The partons can also radiate virtual gluons, which can further emit gluons or produce quark-antiquark pairs. Such a process starting from a hard process and continuing downwards to lower and lower momentum scales leads to the development of Parton Showers (PS). The Initial-State Radiation (ISR) happens before the hard interaction takes place, while Final-State Radiation (FSR) occurs when any parton in the final state radiates.

In hadron-hadron collisions, the energy carried by the remaining constituent partons is mostly directed into the forward direction of the detector and remains in the beam-beam remnants. However, these partons can also undergo interactions forming an underlying event. Multiple parton interactions (or MultiParton Interactions, MPIs) may occur within a single hadron-hadron collision between the remaining partons. The underlying event is challenging to model, because the interactions of the partons likely depend on the energy of the partons, and therefore it is necessary to have accurate PDFs. The pile-up, as defined earlier, corresponds to the number of simultaneous, overlapping particle interactions that are recorded during one bunch crossing. In soft interactions around few GeV, most of the collision energy is lost along the beam pipe and momentum transfer of the interaction is small, suppress-

ing particle scattering at large angles. Events with such interactions are called *minimum bias* events, and account for the majority of the interactions observed in ATLAS.

As quarks and gluons have a colour charge and cannot exist individually due to colour confinement, they recombine into colourless hadrons in a hadronization process after showering. This process leads to a collimated spray of hadrons called a jet which can be detected in the detector. There are different approaches to model hadronization, such as the Lund model of jet fragmentation where hadrons are formed via the string fragmentation model [9]. In the scluster hadronization model, gluons are split into $q\bar{q}$ pairs, creating colour singlets that then can form clusters and decay into hadrons [94, 95].

Figure 21 illustrates a hard interaction and secondary interactions in a pp event.

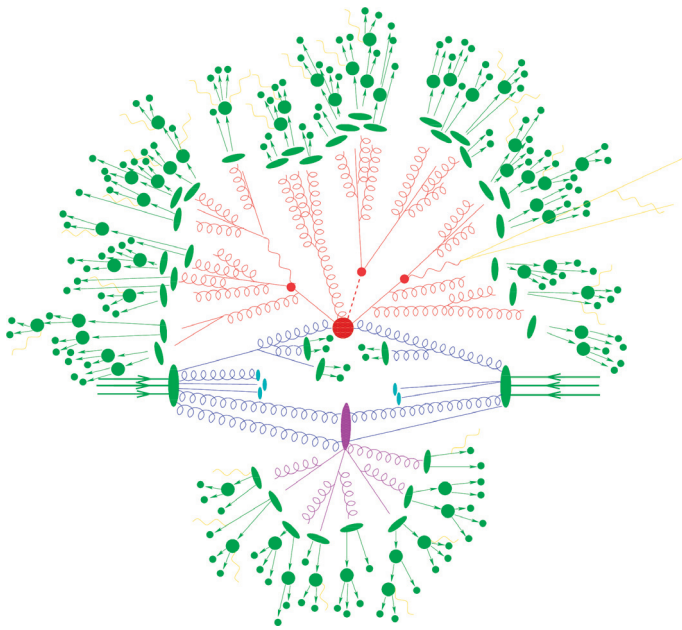

Figure 21: Illustration of a pp event showing the hard interaction (big red circle) of two partons (blue lines) from incoming protons (large green ellipses). Parton showers (red) emerge from the decay products of the hard interaction. The resulting final-state partons hadronize (light green ellipses) and hadrons decay into other particles (dark green cicles). A secondary interaction (purple ellipse) between proton remnants creates again parton showers, which hadronize into colourless states followed by decays into stable particles. In addition, beam remnants (light blue ellipses) are shown. Electromagnetic radiation can occur at any stage (yellow lines). [96]

Event generators provide detailed simulations of the physics of hard processes, ISR and FSR, multiple interactions, hadronization and how all these pieces are combined together. Such generators can often be categorized in parton shower generators and matrix element generators, where the former models all steps mentioned above using leading order matrix elements, whereas the latter calculates only the hard scatter cross-section using exact higher-order matrix elements. Parton shower approach works well when simulating new physics and developing tools for distinguishing signal from background. For high-precision measurements, the matrix element generators are often more suitable [97]. A brief summary of the

generators relevant to this thesis work is given below, following a more detailed overview of different generators given in Refs. [98] and [99].

General purpose generators provide a full event simulation including the hard process generation, parton showering and hadronization with subsequent decays.

- PYTHIA [100] is one of the most used MC event generators in $pp/p\bar{p}$ and e^+e^- physics. Pythia has focused on soft physics such as hadronization based on the Lund string fragmentation model, minimum bias physics and the underlying event, but it contains the whole machinery from ISR and FSR parton showers (which can be either virtuality-ordered or mass-ordered in older versions, or p_T ordered in newer) to analysis tools, together with many BSM processes.
- HERWIG (Hadron Emission Reactions With Interfering Gluons) [101] uses angular-ordered parton showers, and a cluster hadronization model. The choice of angular ordering stems from the colour coherence studies: assume a colour charge, like a quark, emitting a first gluon under an angle θ_1 and a second gluon under an angle θ_2. The second gluon would resolve the individual colour charges of the quark and the first gluon only if $\theta_2 < \theta_1$; otherwise, the second gluon would only feel the combined colour charge of the quark and the first gluon (which is the colour charge of the quark only). Therefore, colour coherence yields in an angular ordering in this emission pattern. [10]
- SHERPA (Simulation of High-Energy Reactions of PArticles) [102] originated in merging a matrix element calculator into a parton shower program. As both approaches essentially describe the same physics, they must be combined consistently in a process called matching and merging, which has been emphasized by SHERPA. SHERPA uses a hadronization model similar to the cluster model used in HERWIG. Furthermore, SHERPA is the only of these three generators that was originally written in C++: both PYTHIA and HERWIG were originally written in Fortran. It was the first major generator to combine processes at NNLO with parton showers for $W^{\pm}$, γ^*/Z and Higgs production.

There is also a variety of specialized programs that can perform higher-order calculations at parton level, but which have to be complemented with parton showers from aforementioned general purpose generators. Practically, matrix-element generators such as MADGRAPH5_aMC@NLO [103], POWHEG (Positive Weight Hardest Emission Generator) [104], and ALPGEN [105] can provide only parton level output and generate Les Houches Event (LHE) files to be used as inputs to PYTHIA or HERWIG for the parton showering and hadronization.

5.3.3 *ATLAS tunes*

As shown, various event generators use parton showers, hadronization, and multiple interaction models to produce simulated events that have as similar properties as possible to real collider data. However, the predictions from MC event generators do not always match data recorded in ATLAS accurately enough. As high-multiplicity perturbative QCD calculations can rely on approximations and non-perturbative physics may not be fully understood from first principles, each model includes several free parameters to be optimized to describe observed phenomena. In order to provide a more accurate description of simulated data, the showering model and underlying event model used by the generator can be *tuned* by fitting parameters to data. The resulting parameter sets are called MC generator tunes.

ATLAS has introduced several sets of tuned parameters in PYTHIA, obtained by adjusting MPI and initial and final state parton shower parameters and typically derived with respect to a given PDF set such as CTEQ6L1, MSTW2008LO, and NNPDF23LO. Such tunes series

include the AU2 tune series for simulation of underlying event and the A2 tune for minimum bias and pile-up event simulation used in Run 1 modelling. The AZ/AZNLO tunes for the low-end of the Z-boson p_{T} and general-purpose high-p_{T} A14 tune series are used in Run 2 modelling. A detailed description of the tuned parameters can be found in Refs. [106] and [107].

In order to estimate the doubly charged Higgs signal uncertainty, the impact of varying different tunes and PDFs set was studied and found to be negligible within experimental resolution. The details and results are presented in Appendix A.

5.3.4 *Event generation filters*

Sometimes it is useful to generate only events that pass a certain selection criteria in order to increase statistics of a particular types of events. A good example of such a filter is the one applied on PYTHIA QCD dijet samples, which are split into several filtered subsamples based on the leading jet p_{T}. As the dijet production cross-section falls steeply with increasing leading jet p_{T}, requesting even millions of events will lead to a very few events with energetic jets. To be able to study such large-p_{T} jets, the filter is applied and it increases sample statistics with events exceeding certain p_{T} thresholds.

Another way to increase statistics in a particular phase space is to filter events based on the final state. For example a sample of a $t\bar{t}$ process can be divided into subsamples: first including only hadronic final states, and the second including semi-leptonic or di-leptonic top decays depending on what the W decays into. Filter weights must be taken into account in the physics analyses by weighting events as the filter does not generate the full cross-section of each process.

Apart from using and generating filtered samples in this thesis work, I developed an event generation filter to enrich samples with jets that are misidentified as taus. The filter could help in validating data-driven estimation of such backgrounds and in estimating related systematic uncertainties. More details on the filter design and results are shown in Appendix D.

5.3.5 *Fast and full simulation*

The full simulation of ATLAS is done using the GEANT4 [90] simulation toolkit, which incorporates the passage of particles and particle interactions through the complete model of the ATLAS detector. This calls for accurate geometrical description and correct composition of all the materials used in the subdetectors. In the Inner Detector, it is important to model multiple scattering, energy losses, bremsstrahlung, photon conversions, and nuclear interactions accurately. In the calorimeters, both electromagnetic and hadronic cascades are created from the particles and their interactions within the different detector materials. As the electromagnetic component involving pair production and bremsstrahlung is generally well understood, GEANT4 models it properly with implementations for $\gamma, e^{\pm}, \mu^{\pm}, \tau^{\pm}$ and all stable charged hadrons and ions. However, the nuclear processes involved in hadronic showers are more complicated. GEANT4 includes several models to simulate these processes. Different physics models, physics processes assigned to each individual particle, and cross-sections required for a particular simulation application with their respective energy ranges are collected in *physics lists*.

Depending on the energy range, different physics lists are used. At high energies, typical models are Quark-Gluon String (`QGS`) and Fritiof (`FTF`), whereas in the intermediate energy region Binary (`BIC`) and Bertini (`BERT`) cascade models are used instead, leaving the Precom-

pound (P) model to be used at low energies. ATLAS uses FTFP_BERT_ATL as a default physics list: as its name reveals, it is a combination of the FTF, P and BERT, where the Bertini model is responsible for a variety of hadronic interactions from 0 to 12 GeV and the Fritiof model over the range 3 GeV-100 TeV. When these two overlap, the Bertini model is invoked with a linearly decreasing probability and the Fritiof model with the complementary probability. The list ATLAS uses is identical to the standard FTFP_BERT, except the transition between the FTF model and the Bertini cascade is changed. The FTFP_BERT list provides a good agreement with data, including shower shape, energy response and resolution. [108]

Despite the very detailed simulation of ATLAS, there are still some differences between real collision data and simulate data. The differences can be caused by mismodelling of the detectors or different data-taking conditions that were not included in the simulation. Indeed, simulations serve as the best-guess only: we do not have *perfect* knowledge on all run conditions such as μ and instantaneous luminosity. For this reason, analyses can correct mismodelling effects by *scale factors* that modify some properties of physics objects or the whole event, such as particle momentum or the total event weight.

The full GEANT4 simulation is widely used for MC production in ATLAS as a very detailed simulation of the detector response is necessary for many parts of the analyses. As the LHC luminosity increases, leading to increasing amount of data, larger simulated datasets for estimating systematics and for studying rare signatures among huge backgrounds are needed. However, it is a computationally expensive task to simulate such large and precise datasets, especially when computing the particle interactions with the active and passive detector material. In particular, it is slow to model showers in the calorimeters due to the high number of secondary particles being generated. Therefore, a fast simulation parametrization called Atlfast-II (AFII) is often used in parts where the highest precision is not necessary.[1]

Atlfast-II uses the FastCaloSim package in the calorimeter simulation [109], and GEANT4 in the Inner Detector and Muon Spectrometer simulation. The simulation begins with the simulation of the initial particles from the event generator using GEANT4. After each particle leaves the ID volume, its type is checked: only muons are further processed with GEANT4 in the calorimeter, and other particles leaving energy deposits in the calorimeters will be computed by FastCaloSim. FastCaloSim saves computing time as it considers only a simplified detector geometry and replaces the full simulation of the detector response by parametrizations. FastCaloSim parametrizes the longitudinal and lateral energy profiles, which are based on the GEANT4 simulation of single particles: electrons and photons for electromagnetic showers, and charged pions for both neutral and charged hadronic showers. The single particles are generated in small bins of the particle energy and pseudorapidity to account for the distribution of active and passive material in the calorimeters. As the energy deposits depend on the origin of the shower, all parametrizations are also binned in the longitudinal depth of the shower centre. The fast calorimeter simulation reproduces the longitudinal shower properties, including fluctuations and correlations, but takes only the average lateral shower properties and uncorrelated lateral energy fluctuations into account. All the parametrizations can also be tuned against data to get more accurate descriptions. With this approach, the average shower shape is well described; however, the accuracy is worse when describing the jet substructure and boosted objects. With this approach, the overall simulation time is reduced by roughly one order of magnitude. The time gain becomes more evident when measuring the simulation time for different processes using both GEANT4 and Atlfast-II, as shown in Table 2 [110].

In this thesis work, datasets from both full and fast simulation were used. As hadronically decaying taus use calorimeter information in the reconstruction, it is crucial to prove that

1 There are also other simulation techniques and combinations of them used in ATLAS, such as Fatras (Fast ATLAS Track Simulation) and Atlfast-IIF which combines FastCaloSim with Fatras.

Process	GEANT4	Atlfast-II
Minimum bias	551	31.2
$t\bar{t}$	1990	101
Jets	2640	93.6
Photon and jets	2850	71.4
$W^{\pm} \to e^{\pm}\nu_e$	1150	57.0
$W^{\pm} \to \mu^{\pm}\nu_\mu$	1030	55.1
Heavy ion	56 000	3050

Table 2: Simulation times per event, in kSI2K normalized CPU time, for various processes in the full simulation (GEANT4) and the fast simulation (Atlfast-II). [110]

there are no differences in the performance between fast and full simulation. While such work was done for *real* taus, it was important to confirm that the same behaviour is true for *fake* taus as well. Jets misidentified as taus were compared in full and fast simulation, and the results and discussions are presented in Appendix C.

5.4 DATA PROCESSING

ATLAS uses the LHC Computing Grid (LCG), which is a global computing infrastructure providing computing resources to store, distribute and analyse the data from the LHC [111]. It consists of three classes of computing centres: Tier-0, Tier-1 and Tier-2. The Tier-0 centre at CERN is responsible for recording raw data from the ATLAS detector onto tape, performing calibration processing and first physics data processing. The Tier-1 centres are large computing centres around the world, storing replicas of the raw data on tape. The existing raw data can be *reprocessed* at Tier-1 as the knowledge of detector conditions improve. The reprocessing takes the advantage of improved reconstruction performance and bug fixes as well as improved software and algorithms. Group and user analysis jobs are mainly run in regional Tier-2 centres that provide disk and CPU resources. The MC simulation production is run both on Tier-1 and Tier-2. The tiered structure adds redundancy by securing data with replicas, and increases the accessibility as there are more replicas for frequently used and popular datasets.

ATLAS has to bookkeep *conditions metadata* to store non-event data, including subdetector hardware and software configurations, information on misalignments and masked or dead channels, and parameters describing run conditions [112]. These data are stored in two separate database systems, which will be further discussed in terms of the TRT in Section 6.7.

The simulated samples have to correspond to the conditions during data taking. Various Monte Carlo campaigns have been run, the relevant for this thesis being the MC16 production campaign. In this campaign, simulated datasets were produced to follow the pile-up profile and run conditions of data taking periods: `MC16a` corresponds to 2015+2016, `MC16d` to 2017, and `MC16e` to 2018 data $\langle\mu\rangle$ and conditions, respectively.

5.4.0.1 *Data formats and tools*

The recorded collision data are huge: there is no way eager physicists with their personal laptops could analyse these raw data events to discover new physics. Furthermore, these data cannot easily be read by the common analysis tools such as ROOT [113], and they do not

necessarily contain the analysis objects such as jets that are reconstructed from particles. The recorded collision data and simulated events are therefore processed through reconstruction into more streamlined formats suitable for analysis. In order to compare simulated data with recorded data, common data formats are used from the reconstruction onwards [111].

As described, simulation starts by generating events where the output is - very creatively - called the EVNT data format in the form of HepMC event records. After simulating the interactions with the detector, the output format is called HITS, and it contains simulated energy deposits. As these two steps are purely based on simulation, there are no counterparts for EVNT nor HITS in the data stream from the actual detector. Accordingly, these formats contain truth information

From the real detector side, the RAW data are events as delivered by the Event Filter, and contain all the hits from the detector in byte-stream format, leading to a size of roughly 1.5 MB per event. In simulation, the corresponding format is Raw Digital Object (RDO), i.e. simulated digitized detector output, which differs from the RAW format simply by including additional *truth* information from the event generation level.

The final step is to convert digitized output into actual physics quantities such as particle energies and positions. Both RDO and RAW data need to be further reconstructed in order to find tracks, to identify particles, and to measure their properties such as momenta and energy based on track curvature and calorimeter measurements. Details on the reconstruction of various physics objects is given in Section 5.5. The reconstructed data are stored in the Event Summary Data (ESD) format with a size of $\mathcal{O}$(1 MB/event). It contains the detailed output of the detector reconstruction from track collections to physics objects and subdetector specific data collections. Both measured data and simulated data share the same ESD data format, with the exception of simulated data additionally containing Monte Carlo truth information about the simulated event.

Analysis Object Data (AOD), derived from ESD, contains a summary of the reconstructed event such as individual collections for various particle types as well as the pile-up conditions and run number. It is a format that is suitable for data analysis with a target size of roughly 200 kB per event. Data can be further reduced to select only targeted events and store only the necessary information for each analysis. The data reduction can be done in several steps via *skimming*, *thinning*, and *slimming* of the sample. Skimming means that whole events are removed from a sample based on a preset criteria. In thinning, whole objects (such as tracks or jets) are removed within events, while slimming means that only some variables within objects are removed. After selecting only targeted events, Derived AODs (DAOD) are being produced using specific derivation frameworks. Each physics group has designed suitable derivations to suit their analysis needs. For example, in this thesis work we will be using derivations from the ATLAS Exotics searches (EXOT) as well as Supersymmetry (SUSY) searches.

The whole procedure from event generation to simulation and from processing all data coming from the trigger to reconstruction and final data analysis can be done using ATLAS Athena software [111, 114]. Most importantly, it is used for processing a bulk of data through the steps mentioned above. Moreover, many analyses develop additional analysis tools to suit their own needs.

5.5 PHYSICS OBJECT RECONSTRUCTION AND IDENTIFICATION

We have previously described how proton–proton collisions result in electronic signals measured by different detectors in ATLAS, and how events can be simulated using Monte Carlo techniques. Now we want to go back and understand which Feynman diagrams correspond to the recorded event we see in the detector data. High reconstruction and identification ef-

ficiency of all physics objects is important for all analyses in order to analyse data enriched with real objects of interest. This requirement goes hand in hand with a high rejection of background events that have a similar signature in the detector.

Correct reconstruction of trajectories of the particles, or tracks in short, is essential for reconstructing and identifying higher-level objects - i.e. *electrons, muons, taus, and jets*. Therefore, tracking and vertex reconstruction in ATLAS is discussed first. Since doubly charged Higgs boson decays into light leptons, the reconstruction and identification of electrons and muons is summarized. However, it can also decay into hadronically decaying taus, which have a peculiar signature that looks similar to the one of jets. Therefore, both jet and tau identification will also be discussed. Last, as neutrinos are formed as a side product of the tau decays, their presence must be inferred from the missing transverse energy.

5.5.1 *Tracks*

The aim of the tracking is to reconstruct the trajectory of a charged particle as accurately as possible. In other words, the aim is to find the collection of hits created by the charged particle crossing the detector elements - this is *pattern recognition* - and estimate a set of track parameters by performing a *track fit*. The trajectory of a particle cannot itself be directly measured, but instead we have to rely on measurements of several discrete points in the detector.

The reconstructed tracks are in a solenoidal field and can be described by a set of five parameters $(z_0, d_0, \theta, \phi, q/p)$, as explained in Section 4.1. The pattern recognition and track fitting can be done in various different ways in ATLAS. Track fitting can be done globally or locally using methods such as the global χ^2 and Kalman filter. In global methods, hits in all detector layers are treated simultaneously, whereas in local methods, or in so-called track following, the algorithm starts by constructing track seeds and adds hits by following seed through detector layers. [115]

In the global χ^2 fitting, the χ^2 function to be minimized is

$$\chi^2 = \sum_{i=1}^{N} \frac{r_i^2}{\sigma_i^2} \tag{32}$$

where r_i are residuals, i.e. the difference between the measured hit position and the position predicted by the track, and σ_i are their uncertainties. The advantage of this strategy is that given the track model is linear and the measurement uncertainties are Gaussian, this estimate has the smallest variance. [116]

The Kalman filter is an iterative algorithm that combines both pattern recognition and track fitting. It starts by estimating track parameters on the first layer. Tracks are then extrapolated from this layer to the next layer. On the next layer, new tracks are constructed with updated parameters and uncertainties, and this measurement is further extrapolated to the next layer. Once the last hit is added to the track, the Kalman filter is repeated backwards using all the measurements. Finally, if the track satisfies certain quality criteria based on total number of hits, number of holes (a "missing hit" on a track), and total χ^2, it is included in the final list of reconstructed tracks. The Kalman filter algorithm is widely used for track fitting, because it can take material effects such as multiple scattering and energy loss into account.

The Combinatorial Kalman filter explores all the possibilities by building all candidates in parallel in order to avoid bias. If the first layer contains several hits that are compatible with the track, several branches of the filter are created. These branches are propagated in parallel to the next layer, where they can each split again. If a branch has multiple holes, the branch is dropped. Finally, the branch with the highest quality track, again in terms of number of holes and total number of hits, is included in the list of reconstructed tracks. [116]

In the ATLAS ID, the main way to find tracks is referred to as inside-out track finding where the track finding starts from the seeds in the inner layer of the pixel detector and continues by finding hits towards the outer layers of the ID. The algorithm is especially designed for the efficient reconstruction of primary particles, and the main steps are [117, 118]:

- Space point formation: the drift circles in the TRT and the clusters of neighbouring hits in the pixel and SCT detectors are created, and transformed into 3D space points.
- Track finding seeded by space points: a set three of space points form a seed; a seed can be built using space points from the pixel only, SCT only, or from a combination of both detectors. Seeds passing initial requirements of p_{T} and d_0 cuts are then input to a track finding algorithm. A combinatorial Kalman filter technique is used to complete the track candidates within the silicon detector.
- Ambiguity solving: to eliminate misidentified hits or track duplicates, track candidates are ranked based on a scoring function applying positive scores for unique measurements and good-quality fits, while penalising missing or shared measurements with other track candidates.
- TRT extension: the tracks are extended into the TRT. TRT extensions can significantly increase the momentum resolution by exploiting the longer lever arm for the measurement.

Another way, in the outside-in algorithms, a track search starts from segments reconstructed in the TRT and continues inwards by adding hits recorded in the silicon detectors. This algorithm is designed and used mainly to reconstruct secondary particles. Tracks that have a segment in the TRT but no extension into the silicon detector are called TRT-standalone tracks. [115]

The ATLAS Tracking combined performance (CP) group defines two track selection working points for general use, called `Loose` and `Tight Primary`, based on transverse momenta, pseudorapidity and the number of hits in each ID subdetector. `Loose` represents the track quality requirements applied during reconstruction. `Tight Primary` adds an additional set of criteria to be applied to the reconstructed track collection, with the aim of keeping high efficiency for prompt tracks while reducing fakes significantly.

`Loose` selection selects tracks with the following requirements:

- $p_{\mathrm{T}} > 500\,\mathrm{MeV}$
- $|\eta| < 2.5$
- Number of Pixel and SCT clusters on track ("silicon hits") ≥ 7
- Number of shared modules ≤ 1
- Number of silicon holes ≤ 2
- Number of pixel holes ≤ 1

`Tight primary` selection, in addition to the `Loose` selection requirements, selects tracks that satisfy the following criteria:

- Number of Pixel and SCT clusters on track ≥ 9 if $|\eta| \leq 1.65$ and ≥ 11 if $|\eta| > 1.65$
- At least one hit on one of the two innermost pixel layers (IBL and B-layer)
- No missing hits in the pixel detector

A shared hit means that a hit is assigned to multiple tracks. A pixel module is shared if it has at least one shared hit, and a SCT module is shared if it has at least two shared hits. Holes are missing hits on a reconstructed track; however, inactive modules or regions are excluded from the definition. Both `Loose` and `Tight primary` tracks can have extensions into the TRT, but no criteria are applied on the number of TRT hits. [119]

5.5.2 *Vertices*

An event can have multiple interaction vertices due to large number of pp collisions per bunch crossing. Primary vertices, i.e. the reconstructed positions of the hard interactions, are reconstructed using an iterative vertex finding algorithm. A set of reconstructed tracks satisfying specific track selection criteria are defined, and form a seed for a vertex. The centre of the beam spot is taken as the transverse position of the first seed. Then an iterative fit to estimate the best vertex position is made using the seed and nearby tracks. In each iteration, tracks with worse agreement in the fit are down-weighted and the vertex position is recomputed. After the vertex position is defined, tracks that do not match with the vertex are removed and can be used for the determination of another vertex. The procedure is then repeated until no additional vertices are found.

Among all the vertices in the event, the one with the highest sum of squared transverse momenta of the associated tracks is chosen as the primary vertex.

5.5.3 *Electrons*

5.5.3.1 *Reconstruction*

Electrons are light, charged particles that interact highly with material. Therefore, electrons are triggered [120] by and reconstructed from energy deposits in the electromagnetic calorimeter that are matched to a reconstructed track in the Inner Detector. Since this thesis work uses prompt, isolated and central ($|\eta| < 2.47$) electrons, only they are discussed in this section.

An electron reconstruction starts by building clusters from the energy deposits in the electromagnetic calorimeter. The EM calorimeter is divided into a grid of towers of size $\Delta\eta \times \Delta\phi = 0.025 \times 0.025$ in the $\eta - \phi$ space. A sliding window algorithm with a window of size 3×5 towers in $\eta \times \phi$ is used to find seed clusters with total cluster transverse energy above 2.5 GeV. If two seed-cluster candidates are found very close to each other, the candidate with the higher transverse energy is retained. These seeds are then used to build EM clusters by iterating over every element in the calorimeter. After that, the reconstructed tracks in the Inner Detector are matched to the EM clusters [121]. Figure 22 shows schematically the path of an electron through the ATLAS subdetectors.

5.5.3.2 *Identification*

Prompt electrons (from the hard scattering, or from the decay of heavy resonances such as Higgs, W and Z bosons) in the central region ($|\eta| < 2.47$) are distinguished from other particles using a set of selection criteria in a multivariate likelihood-based (LH) identification method. Electron identification relies on the quality of the charged-particle tracks, longitudinal and lateral shower development in the calorimeter, and the track-to-cluster matching. The input variables are selected so that they can discriminate prompt electrons from hadronic jets

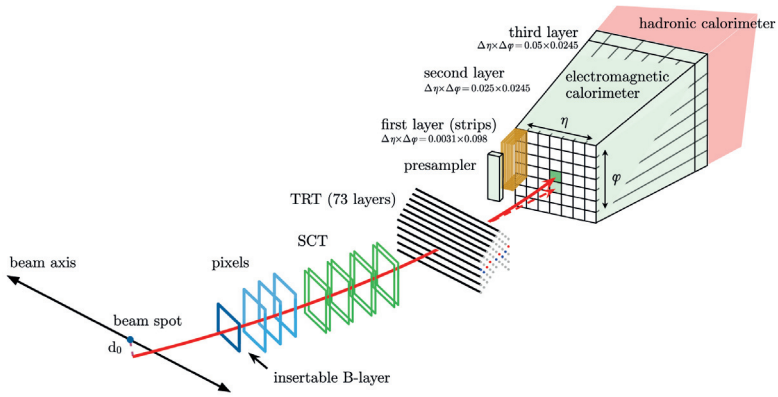

Figure 22: The path of an electron through ATLAS. The trajectory of an electron is shown in red. The dashed red line shows a photon produced by the interaction of the electron with the detector material. Figure taken from [122]

that have a similar signature, electrons from photon conversions[2], and non-prompt electrons from the decay of hadrons containing heavy flavours. The full list of input variables can be found in Ref. [122].

The LH identification method uses probability density functions (pdfs) for signal and background. The advantage of this method over the cut-based identification is that a prompt electron can still satisfy the identification criteria even if it fails to pass the selection criterion for a single quantity. Using the pdfs, the electron likelihood for the electron candidate to pass the signal hypothesis is built. It is based on the LHs for signal, L_S, and for background, L_B, which are products of n input pdfs P [122]:

$$L_{S(B)}(\mathbf{x}) = \prod_{i=1}^{n} P_{S(B),i}(x_i) \tag{33}$$

where $\mathbf{x}$ is the vector of the discriminating variable values, $P_{S,i}(x_i)$ is the value of the signal pdf for quantity i at value x_i and $P_{B,i}(x_i)$ is the corresponding value of the background pdf.

For each electron candidate, a discriminant d_L can then be formed:

$$d_L = \frac{L_S}{L_S + L_B} \tag{34}$$

where the discriminant d_L has a sharp peak at unity for signal and zero for background.

Four LH-based identification discriminants, optimized in bins of η and E_T, are used to define identification working points for electrons targeting specific efficiencies and background rejection factors: `VeryLoose`, `Loose`, `Medium`, and `Tight`. They correspond to increasing thresholds for the LH discriminant. The efficiencies for identifying a prompt electron with $E_T = 40\,\text{GeV}$ are 93%, 88%, and 80% for the `Loose`, `Medium`, and `Tight` working points, respectively.

All the working points have requirements on the tracking criteria. The `VeryLoose` working point requires only one hit in the pixel detector, and provides loose identification requirements suitable for background studies. The `Loose`, `Medium`, and `Tight` working points require

2 An electron can lose a large amount of its energy due to bremsstrahlung. These photons caused by the interaction with detector material can convert into an electron-positron pair, which again can interact with the detector material.

at least two hits in the pixel detector and seven hits total in the silicon detectors. In addition, in order to reduce the background from photon conversions, one of the pixel hits must be in the innermost pixel layer (B-layer) for the `Medium`, and `Tight` working points. For the same reason, `LooseBL` working point acts as a variant of the `Loose` working point but also requires one pixel hit in the B-layer. The `Loose` working point provides very good identification efficiency but less background rejection. `Medium` working point improves the electron quality, whereas `Tight` working point provides the highest electron identification and rejection against background at a cost of selection efficiency.

5.5.3.3 *Isolation*

A characteristic prompt lepton has only a little activity in the calorimeter and in the ID in an area of ΔR surrounding it. However, some prompt decays, such as $t\bar{t}$ production, complicate this matter as prompt leptons are produced together with jets originating from the same primary vertex. For this reason, further selection criteria based on the activity around the electron candidate can be added in order to better distinguish electrons from backgrounds arising from hadronic jets, photon conversions and semi-leptonic decays of heavy quarks. Such criteria are called *isolation* criteria, and again various working points are derived to target specific efficiencies of selecting electrons with excellent background rejection.

The activity near electrons, i.e. isolation, can be quantified by using the tracks of nearby charged particles and energy deposits in the calorimeters, resulting in the calorimeter isolation variable $E_{\mathrm{T}}^{\mathrm{coneXX}}$ and the track isolation variable $p_{\mathrm{T}}^{\mathrm{coneXX}}$.

The raw calorimeter isolation ($E_{\mathrm{T,raw}}^{\mathrm{isol}}$) [123] is built by summing the transverse energy of topological clusters whose barycentre falls within a cone centred around the electron cluster barycentre, as illustrated in Figure 23.

The raw calorimeter isolation still includes the electron energy, called the core energy $E_{\mathrm{T,core}}$, which is subtracted by removing the energy of the EM calorimeter cells contained in a $\Delta\eta \times \Delta\phi = 5 \times 7$ rectangular cluster (shown in yellow in Figure 23) around the candidate electron's direction. This way, both real, fake and non-prompt electrons are subtracted for any transverse momentum and pile-up. However, the method does not subtract all the electron energy that may have been deposited outside of the fixed rectangular area, and an additional leakage correction is needed. This leakage is parametrized as a function of E_{T} and $|\eta|$ using simulated samples of single electrons without pile-up. The pile-up and underlying-event contribution to the isolation cone is also estimated.

The fully corrected calorimeter isolation variable $E_{\mathrm{T}}^{\mathrm{coneXX}}$ is defined as

$$E_{\mathrm{T}}^{\mathrm{coneXX}} = E_{\mathrm{T,raw}}^{\mathrm{isolXX}} - E_{\mathrm{T,core}} - E_{\mathrm{T,leakage}}(E_{\mathrm{T}}, \eta, \Delta R) - E_{\mathrm{T,pile\text{-}up}}(\eta, \Delta R)$$

where XX is the size of the employed cone, $\Delta R = \mathrm{XX}/100$, which is $\Delta R = 0.2$ for the electron working points.

The track isolation variable $p_{\mathrm{T}}^{\mathrm{coneXX}}$ is obtained from the sum of the transverse momenta of selected tracks within a cone around the electron track direction. The computation uses tracks with $p_{\mathrm{T}} > 1\,\mathrm{GeV}$ and $|\eta| < 2.5$, and that have at least seven silicon hits, at most one shared hit, at most two silicon holes (i.e. missing hits in the pixel and SCT detectors) and at most one pixel hole. In addition, the tracks are required to have a loose vertex association: the track was either used in the primary vertex fit, or it satisfies $|\Delta z_0| \sin\theta < 3\,\mathrm{mm}$. By such selection, the aim is to suppress the impact of pile-up, select tracks that originate from the vertex that is chosen to be relevant for the process, and reject the background from conversions and secondary particles. The track-p_{T} contribution of the candidate electron and converted photons is subtracted from the cone.

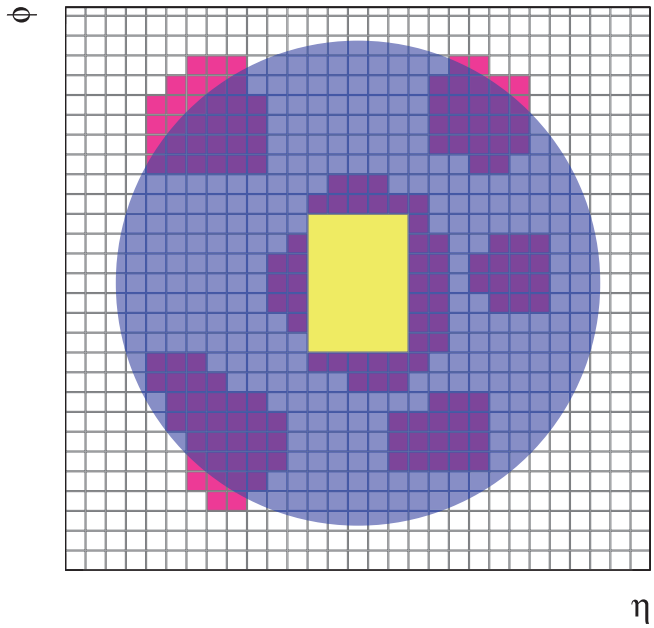

Figure 23: Illustration of a calorimeter isolation, where the grid represents the second-layer calorimeter cells in the η and ϕ directions. The blue circle represents the isolation cone of the candidate electron. Topological clusters, represented in red, for which the barycentres fall within the isolation cone are included in the computation of the isolation variable. The yellow rectangle represents the 5×7 cells covering an area of $\Delta\eta \times \Delta\phi = 0.125 \times 0.175$ corresponding to the subtracted cells in the core subtraction method. [122]

Small cones with radius much less than $\Delta R = 0.2$ are difficult to build in the calorimeter isolation due to the finite granularity of the calorimeter. The ID allows much narrower cone sizes thanks to finer granularity. Smaller cone sizes become useful in boosted decay signatures or busy environments, where other decay products can be very close to the electron direction. For such cases, a variable-cone-size track isolation $p_{\mathrm{T}}^{\mathrm{varconeXX}}$ can be used, where the cone size decreases for electrons with larger p_{T}:

$$\Delta R = \min\left(\frac{10}{p_{\mathrm{T}}[\,\mathrm{GeV}]}, \Delta R_{\mathrm{max}}\right)$$

where ΔR_{max} is the maximum cone size. The value of 10 GeV comes from a simulated $t\bar{t}$ sample, and is designed to maximize the rejection of background.

Various working points are derived centrally in ATLAS to suit specific needs of physics analyses. Precision measurements may prefer to use tight isolation requirements with the best rejection of background processes, whereas searches for new physics often prefer to have looser criteria to ensure high signal efficiency. In the searches for doubly charged Higgs boson, the latter approach is used, and the optimized and chosen working points will be discussed in Chapters 8-9.

The electron isolation working points (WP) are divided into categories, and are presented in Table 3. `Gradient` isolation WP targets at a fixed value of the isolation efficiency, for example efficiency of 90% for electrons with $p_{\mathrm{T}} = 25\,\mathrm{GeV}$ and 99% for electrons with $p_{\mathrm{T}} = 60\,\mathrm{GeV}$.

Table 3: Electron isolation working points and isolation efficiency ϵ_{iso}. [122]

Working point	$E_{\text{T,cone}}^{\text{isol}}$ ($\Delta R = 0.2$)	$p_{\text{T,var}}^{\text{isol}}$ ($R_{\text{max}} = 0.2$)	Total ϵ_{iso}
`Loose_TrackOnly`	-	$\epsilon_{\text{iso}} = 99\%$	99%
`Loose`	$\epsilon_{\text{iso}} = 99\%$	$\epsilon_{\text{iso}} = 99\%$	98%
`Tight`	$\epsilon_{\text{iso}} = 96\%$	$\epsilon_{\text{iso}} = 99\%$	95%
`Gradient`	$\epsilon_{\text{iso}} = 0.1143 \times p_{\text{T}}[\text{GeV}] + 92.14\%$	$\epsilon_{\text{iso}} = 0.1143 \times p_{\text{T}}[\text{GeV}] + 92.14\%$	90(99)% at 25(60) GeV
`FCLoose`	$E_{\text{T,cone}}^{\text{isol}}/p_{\text{T}} < 0.20$	$p_{\text{T,var}}^{\text{isol}}/p_{\text{T}} < 0.15$	-
`FCTight`	$E_{\text{T,cone}}^{\text{isol}}/p_{\text{T}} < 0.06$	$p_{\text{T,var}}^{\text{isol}}/p_{\text{T}} < 0.06$	-
`FCTight_TrackOnly`	-	$p_{\text{T,var}}^{\text{isol}}/p_{\text{T}} < 0.06$	-
`FCHighPtCaloOnly`	$E_{\text{T,cone}}^{\text{isol}} < 3.5$ GeV	-	-

`FixedCut` (FC) isolation WP implements fixed requirement criteria on the value of the isolation variable.

5.5.4 *Muons*

5.5.4.1 *Reconstruction*

Muons are the only charged particles that can travel through ATLAS, and therefore they can be measured both in the Inner Detector and the Muon Spectrometer (MS). Muon reconstruction is first performed independently in both systems, and then the information is combined to reconstruct muons for physics analyses. In the ID, muon tracks are reconstructed as described in Section 5.5.1. In the MS (see Section 4.5), the reconstruction starts by searching for hit patterns inside each muon chamber to form segments. In the MDT chambers and nearby trigger chambers (RPC, TGC), a Hough transform [124] is used to search for hits on a track in the bending plane. The MDT segments are reconstructed by performing a straight-line fit to the hits found in layers, and the RPC or TGC hits measure the coordinate orthogonal to the bending plane. The CSC segments are formed using a combinatorial search in the η and ϕ planes. Muon tracks are then reconstructed by fitting hits from segments in different layers. A detailed description of the muon reconstruction is given in Ref. [125], and the main points are summarized below.

The information from the ID, MS and calorimeters is then combined to form the muon tracks for physics analyses. About 96% of muons are reconstructed by fitting hits from the ID and MS tracks, and the rest are formed by tagging tracks from ID with the muon signature in calorimeter or the MS. In total, four types of muons can be defined depending on the subdetectors used in reconstruction:

- Combined (CB) muons are formed from tracks that are first reconstructed independently both in the ID and the MS, and then refitted globally to a combined track. They are the default muon candidates to be used in the analysis as they have the highest purity.
- Segment-tagged (ST) muons: if an extrapolated track from the ID is associated with at least one local track segment in the MDT or CSC chambers, it is classified as a muon track. The ST muons are used when muons cross only one layer of MS chambers because they either fall outside of the MS acceptance or have too low transverse momentum.

- Calorimeter-tagged (CT) muons: if a track in the ID can be matched to an energy deposit in the calorimeter compatible with a minimum-ionizing particle, the track is identified as a muon. These muon candidates have the lowest purity, but they compensate for the regions where the MS is only partially instrumented to allow for cabling and services. The CT muons are optimized for the very central region $|\eta| < 0.1$ and for $15\,\text{GeV} < p_{\text{T}} < 100\,\text{GeV}$.
- Extrapolated (ME) muons: the muon track is reconstructed based only on the track in the muon spectrometer, and requiring that the track could originate from the IP. The track parameters are defined at the IP, and take into account the estimated energy loss in the calorimeters. The muon is required to traverse at least three layers of the MS chambers in the forward region, and at least two layers otherwise. The ME muons are used to extend the acceptance into the region $2.5 < |\eta| < 2.7$ which is outside the ID geometrical coverage.

In order to avoid double-counting, overlaps between different muon types are resolved by the following priorities: when two muon types share the same track in the ID, preference is given first to CB, then to ST, and finally to CT muons. Overlap in the MS is resolved by selecting the track with better fit quality and larger number of hits.

5.5.4.2 *Identification*

Muons from the hard scattering, the decay of heavy resonances such as Higgs, W and Z bosons, are identified based on applying a set of quality requirements aiming to reject non-prompt muons coming mainly from pion and kaon decays.

Various variables are used in muon identification, including the q/p significance defined as the absolute value of the difference between charge/momentum ratio of the muons measured in the ID and MS divided by the sum in quadrature of the corresponding uncertainties. It is a powerful variable to suppress the contamination from fake hadrons. Furthermore, the normalized χ^2 of the combined track fit is used. Similarly to electrons, specific track requirements are also applied. These sets of criteria are organized in centrally derived *muon identification working points* and provided together with scale factors (SF) to account for mismodelling in the simulation. Available working points are [125]:

- `Loose`, which is designed to obtain maximal reconstruction efficiency and uses all muon types. It comes at the cost of larger fake rate from hadrons and larger systematic uncertainties on the SFs when compared to `Medium`.
- `Medium`, which provides high efficiency ($p_{\text{T}} > 5\,\text{GeV}$, $0.1 < |\eta| < 2.7$) with a small fake rate and small systematic uncertainties associated with muon reconstruction and calibration. Only CB and ME muon tracks are used. A loose selection on the compatibility between ID and MS momentum measurements is applied, in particular the q/p significance is required to be less than seven in order to eliminate the fake muons originating from hadrons. It is the default working point for muons in ATLAS.
- `Tight`, which minimizes the fake rate to reach high purity at the cost of some efficiency loss. Only CB muons with hits in at least two stations of the MS and satisfying the `Medium` criteria are used. The normalized χ^2 of the combined track fit is required to be less than 8 to remove bad tracks, and requirements on the compatibility between ID and MS momentum measurements are added to improve the background rejection especially for muons with $p_{\text{T}} < 20\,\text{GeV}$, where the misidentification probability is higher.

Table 4: Muon isolation working points. [125]

Isolation WP	Definition
`LooseTrackOnly`	99% efficiency constant in η and p_{T}
`Loose`	99% efficiency constant in η and p_{T}
`Tight`	96% efficiency constant in η and p_{T}
`Gradient`	$\geq 90(99)\%$ efficiency at 25 (60) GeV
`FixedCutTightTrackOnly`	$p_{\mathrm{T}}^{\mathrm{varcone30}}/p_{\mathrm{T}}^{\mu} < 0.06$
`FixedCutTightTrackOnly_FixedRad`	$p_{\mathrm{T}}^{\mathrm{varcone30}}/p_{\mathrm{T}}^{\mu} < 0.06$
`FixedCutLoose`	$p_{\mathrm{T}}^{\mathrm{varcone30}}/p_{\mathrm{T}}^{\mu} < 0.15$, $E_{\mathrm{T}}^{\mathrm{topocone20}}/p_{\mathrm{T}}^{\mu} < 0.30$

- `LowPt` to maximize the efficiency for muons down to $p_{\mathrm{T}} = 3\,\mathrm{GeV}$ maintaining a reasonable fake rate. Muons with lower momenta than 3 GeV are challenging to reconstruct because they do not reach the muon spectrometer or they lose too much energy in the calorimeter, leaving no significant signal over noise in the MS.
- `HighPt`, which is designed to give the best possible momentum resolution for the high p_{T} range above 100 GeV, and optimized for searches for high-mass Z' and W' resonances. Only CB muons with at least three hits in the three MS stations satisfying the `Medium` selection criteria are considered. While this selection reduces the reconstruction efficiency by about 20%, it improves the p_{T} resolution of muons above 1.5 TeV by approximately 30%.

5.5.4.3 *Isolation*

Just as electrons, muons originating from the decay of heavy particles are often produced isolated from other particles. The measurement of the detector activity around a muon candidate, i.e. muon isolation, is used to further reject background from semi-leptonic decays, which are embedded in jets.

The two muon isolation variables, a track-based isolation variable $p_{\mathrm{T}}^{\mathrm{varcone30}}$ and a calorimeter-based isolation variable $E_{\mathrm{T}}^{\mathrm{cone20}}$, are defined similarly to the electron isolation variables as explained in Section 5.5.3.3. The various working points for muon isolation are shown in Table 4. Each analysis can choose a suitable combination of identification and isolation working points. For example `FCTightTrack_FixedRad`, works very well for reducing the fake lepton background but may have a poor isolation efficiency in boosted regions where the leptons and jets are close-by. Working points for the doubly charged Higgs boson search are described and optimized in Chapters 8-9.

5.5.5 *Jets*

The majority of the pp collisions at the LHC lead to the production of quarks and gluons, which carry colour charge and cannot exist individually due to colour confinement as discussed in Section 1.2.2. Indeed, the quarks and gluons hadronize and form collimated sprays of particles leaving energy deposits in the calorimeters. These energy deposits can be reconstructed as jets. It is important to reconstruct a jet as accurately as possible, because they work as a link to the underlying unobserved partons.

5.5.5.1 *Reconstruction*

The inputs for jet reconstruction are either topologically clustered calorimeter cells, the so-called *topo-clusters*, or particle flow objects. In particle flow [126], jets are formed using tracks matched to the primary hard-scatter or pile-up vertex and remaining calorimeter clusters. A specific cell-based energy subtraction algorithm is applied in order to remove overlaps between the momentum and energy measurements made in the ID and calorimeters [127]. In the context of this thesis work, only topo-clusters are used.

Topo-clusters are formed from calorimeter cells with large energy deposits exceeding the expected noise. The topo-clusters are corrected such that their direction points back to the hard-scatter primary vertex rather than the detector origin, improving the angular resolution. These topo-clusters can be calibrated at the electromagnetic (EM) scale, which corrects the jet energy to the energy deposited by an electromagnetic shower, or at the Local Cell Weighting (LCW) scale to correctly reconstruct the response of the calorimeter to hadrons [127].

A jet can be reconstructed in many ways using various jet clustering algorithms such as k_t, anti-k_t and Cambridge/Aachen. All of the three algorithms mentioned are based on a similar sequential clustering method, and assume that particles within jets will have small differences in transverse momenta.

The sequential clustering method relies on calculating the distance variable d_{ij} defined as [128]

$$d_{ij} = min(p^a_{Ti}, p^a_{Tj}) \times \frac{R^2_{ij}}{R} \tag{35}$$

where a corresponds to a particular clustering algorithm, $R^2ij = (\eta_i - \eta_j)^2 + (\phi_i - \phi_j)^2$ is the $(\eta - \phi)$ space distance between the two particles i and j, and R is the radius parameter defining the final size of the jet. Another important distance variable is $d_{iB} = p^a_{ti}$ corresponding to the momentum space distance between the beam axis B and the detected particle i.

The algorithm is rather simple. First, the minimum of $\{d_{ij}, d_{iB}\}$ is found. If d_{ij} is the minimum, particles i and j are combined into one particle and removed from the list of particles. If d_{iB} is the minimum, i is labelled as the final jet. The procedure is repeated until all particles are part of a jet with $R_{ij} > R$.

The variants of this method differ by their values a: $a = 2$ in the k_t algorithm, $a = -2$ in the anti-k_t and $a = 0$ in the Cambridge/Aachen algorithm. The k_t algorithm prefers to cluster soft particles first and is good at resolving subjets. The anti-k_t algorithm instead prefers to cluster hard particles first, which makes it good at resolving jets but worse for studying jet substructure, the task in which the Cambridge/Aachen algorithm works well. These algorithms satisfy an important requirement for jet reconstruction algorithms: they are *infrared and collinear* (IRC) safe. Collinear safety means that a single large-p_{T} jet definition should not radically change if it is divided into two collinear (i.e. close-by) particles. A soft emission arising from hadronization process, an underlying event or pile-up should not change a jet definition either (infrared safety). In IRC unsafe jet algorithms, the leading order splittings may lead to one set of jets, while the next-to-leading order diagrams may lead to a different set, leading to meaningless infinite cross-sections in perturbation theory. [129]

ATLAS uses various jet definitions. In general, jets are reconstructed using the anti-k_t algorithm. Jets representing quarks (except top) and gluons are typically reconstructed with $R = 0.4$ and called small-R jets. Large-R jets with $R = 1.0$ contain hadronically decaying massive particles, such as W and Z bosons and top quarks.

After building jets, they are calibrated in different steps to account for several effects. Different corrections are applied for jets reconstructed using the EM and LCW topo-clusters. For

EM-scale small-R jets, the jet energy scale (JES) calibration includes many stages: a) pile-up correction to account for the energy offset caused by pile-up, b) correction of the detector response based on Monte Carlo simulation, c) global sequential correction to reduce the jet response dependence on the flavour of the initiated jet, and d) *in situ* calibration to account for the differences between MC and data.

The aim of the procedure is to correct the jet four-momentum at the EM scale to the jet four-momentum at the particle level. Similar steps are applied for LCW-scale large-R jets. Because of the large radius parameter, a jet volume can be contamined with initial state radiation, multiple parton interactions and event pile-up. Jet *grooming* aims to remove soft components and rebuild the final jet from the remaining constituents. ATLAS typically uses the *trimming* procedure [130], where the constituents of the original anti-k_t jet are reclustered using the k_t algorithm and thrown away if the sub-jet p_{T} is less than a certain value of the original large-R jet p_{T}.

5.5.5.2 *Jet tagging*

After calibration, the jets can be *tagged* to identify their likely originating particle and to separate boosted, massive hadronic decays from QCD multijet production. In ATLAS, there are multiple taggers from variable taggers to boosted decision trees and deep neural networks to perform such tasks. For variable taggers, the jet mass is a powerful substructure variable for distinguishing QCD jets from massive particles, but it is not suitable for separating quarks from gluons. The track multiplicity and jet width are useful instead. Such discriminating variables are discussed more in Appendix C, where ways to identify jets misidentified as taus are covered.

In particular, identification of b-jets is important in ATLAS both for precision measurements and the search for new physics, as b-jets may characterize the final state (such as $H \to b\bar{b}$) or form a significant part of the backgrounds due to top decays ($t \to Wb$). The b-tagging algorithms rely on the special features of b-hadrons: a relatively long lifetime, a displaced secondary vertex and a large impact parameter d_0. A multivariate b-tagging algorithm called MV2c10 was developed for Run 2. It utilizes a boosted decision tree and is optimized for Run 2 to exploit the IBL and improved tracking software [131]. In the analyses presented in this thesis, events b-jets are usually vetoed i.e. only events with exactly zero b-jets are taken into account to suppress top background.

5.5.6 *Taus*

5.5.6.1 *Reconstruction*

The lifetime of a τ lepton is $2.9 \cdot 10^{-13}$ s, and therefore a typical 50 GeV tau lepton travels only roughly 2 mm before decaying[3]. Therefore the tau leptons have to be identified from their decay products. Taus decay either hadronically or leptonically (via $\tau \to \ell\nu_\ell\nu_\tau$, where ℓ is an electron or muon). Leptonic decays will yield isolated electrons or muons that can also be directly produced, which makes it experimentally challenging to discriminate their origin. Therefore, leptonic tau decays are reconstructed as electrons and muons, and the presence of neutrino is inferred from the missing momentum in the event. In the following we will only consider hadronic taus unless otherwise stated. The tau reconstruction in ATLAS is covered in detail in Ref. [132].

3 The first layer of the ATLAS detector is the Insertable B-layer at radii of 33 mm, so taus decay before they reach it.

The hadronic τ decay (mostly to pions and kaons) is characterized by a narrow collimated jet with a low track multiplicity, and a presence of missing energy in the event. Therefore, the reconstruction of the visible decay products of hadronic tau decays starts with a jet reconstruction. Jets constructed using the anti-k_t algorithm [133, 134] with a distance parameter $R = 0.4$ and three-dimensional clusters of calorimeter cells (*topo-clusters*), calibrated using a local hadronic calibration (LC) as inputs, are used as seeds of the hadronic tau candidates. Jets are additionally required to have $p_{\mathrm{T}} > 10\,\mathrm{GeV}$ and $|\eta| < 2.5$. Any tau candidate in the crack region between the barrel and forward calorimeters, $1.37 < |\eta| < 1.52$ is vetoed.

The primary vertex (PV) in the event is not necessarily the same as the tau vertex (TV) at which the tau is produced. The p_{T} of all tau candidates in the region $\Delta R < 0.2$ from the jet seed direction is summed. The tau vertex then corresponds to the vertex to which the largest fraction of the p_{T} sum is matched. Tracks associated to the $\tau_{\mathrm{had-vis}}$ candidate are required to have $p_{\mathrm{T}} > 1\,\mathrm{GeV}$ and at least two hits in the pixel layers (including the IBL), and at least seven hits in total in the pixel and SCT detectors. In addition, requirements on the distance of closest approach of the tracks to the tau primary vertex must be passed: $|d_0| < 1.0\,\mathrm{mm}$, and $|z_0 \sin\theta| < 1.5\,\mathrm{mm}$. This information can be used to suppress the background contribution from QCD jets. The charge of the $\tau_{\mathrm{had-vis}}$ candidate is reconstructed from the sum of the track charges. Tracks passing these requirements are then associated to *core* ($0 < \Delta R < 0.2$) and *isolation* cones ($\Delta R < 0.4$) around the $\tau_{\mathrm{had-vis}}$ direction. The mass of the tau candidate is defined to be zero. Consequently, the p_{T} and E_{T} are identical, and the energy of the tau is obtained from a separate tau energy calibration procedure using information about the associated tracks and calorimeter clusters [132].

5.5.6.2 *Identification*

Tau reconstruction alone does not identify tau candidates reliably enough, as the detector signature mimics the signature of jets. As discussed in Section 3.3, multijet events occur at a very high rate at the LHC and form a major background to the identification of hadronically decaying taus. As hadronic tau decays typically lead to 1 or 3 charged tracks (referred to as 1- and 3-prong taus, respectively), the number of tracks is a good discriminating variable against jets. Furthermore, the tau decay cone is often narrower than a typical jet cone, which makes the cone size another such variable.

To make maximal use of all the discriminating variables available, tau identification relies on Boosted Decision Tree (BDT) methods with the main aim of rejecting backgrounds arising from quark- and gluon-initiated jets. The BDTs for tau candidates with one and three tracks are trained separately using simulated $Z/\gamma^* \to \tau\tau$ for signal and dijet events for background. The BDT input variables are based on the track and TopoCluster information: the calorimeter measurements reveal information about the shower shape, and the electromagnetic calorimeter is sensitive to the neutral pion content due to photons coming from the decay of neutral pions. A correction depending linearly on the $\langle\mu\rangle$ is applied to each variable to avoid dependence on the pile-up conditions. Full list of the input variables can be found from Ref. [135].

Three identification working points are defined: `Loose` with target efficiency of 0.6 and 0.5 for 1- and 3-prong taus; `Medium` with efficiency of 0.55 and 0.4 for 1- and 3-prong taus; and `Tight` with efficiency of 0.45 and 0.3 for 1-prong and 3-prong taus, respectively. The tau identification efficiencies are shown in Figure 24 for 1-prong $\tau_{\mathrm{had-vis}}$ candidates as a function of the transverse momentum of the tau and as a function of the average number of interactions per event, showing that identification efficiency is less dependent on those quantities.

Jets are not only objects that have signature similar to hadronic taus. In fact, electrons fullfill most of the requirements of the tau identification and cause a large fake rate. Overlap

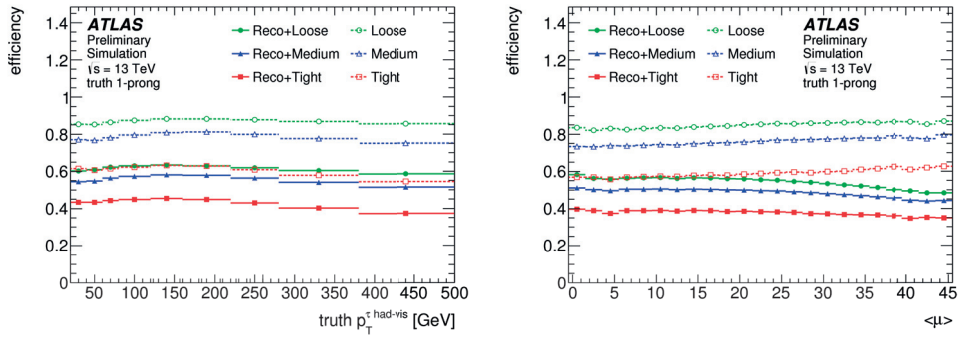

(a) (b)

Figure 24: Efficiency for 1-prong $\tau_{\text{had-vis}}$ identification (open symbols) and combined reconstruction and identification efficiency (full symbols) as a function of (a) $\tau_{\text{had-vis}}$ p_{T} and (b) the average number of interactions per event. [135]

removal procedure already reduces the fake rate from electrons, but there is an additional dedicated multivariate likelihood method approach to distinguish taus from electrons. If a reconstructed tau candidate associated with a single track is within a distance of $\Delta R < 0.4$ of a reconstructed electron, it will be rejected if the electron has a high likelihood score of being an electron [135]. The fake taus will be discussed further in Section 9.3.4.3, as they form a major background in the search for the doubly charged Higgs boson decaying into final states involving taus.

5.5.7 *Missing Transverse Energy*

Missing transverse energy, $E_{\text{T}}^{\text{miss}}$, arises from non- or weakly interacting particles such as neutrinos - or even dark matter particles - that are invisible to detectors. However, their presence can be indirectly determined by momentum conservation: the vectorial sum of the transverse momenta of all the particles should be zero, and any imbalance in the total measured momenta in the $x-y$ plane is defined as the missing transverse energy. Both neutrinos and hypothetical particles particles account for *real* missing transverse energy. However, $E_{\text{T}}^{\text{miss}}$ can also come from limited detector acceptance, dead regions, or other problems in the detectors. Any missed muon, misreconstructed or miscalibrated jet, and dead area of the detector can contribute to the missing transverse energy, in which case this contribution is called *fake* $E_{\text{T}}^{\text{miss}}$. Therefore all objects in an event have to be properly measured and understood as outlined above. Generally, $E_{\text{T}}^{\text{miss}}$ is calculated using information from both the Inner Detector and the calorimeters.

The $E_{\text{T}}^{\text{miss}}$ is defined as a negative vectorial sum of various objects [136]:

$$E_{\text{T}}^{\text{miss}} = -\left(\sum \boldsymbol{p}_{\text{T}}{}^{\mu} + \sum \boldsymbol{p}_{\text{T}}{}^{e} + \sum \boldsymbol{p}_{\text{T}}{}^{\gamma} + \sum \boldsymbol{p}_{\text{T}}{}^{\tau} + \sum \boldsymbol{p}_{\text{T}}{}^{\text{jets}} + \sum \boldsymbol{p}_{\text{T}}{}^{\text{soft}}\right) \tag{36}$$

where $\boldsymbol{p}_{\text{T}}{}^{i}$ is the transverse momentum of each object i, and the soft term refers to calorimeter clusters or ID tracks not associated with any hard object. The so-called overlap-removal procedure is applied to remove duplicates if the same object is reconstructed as two separate objects, such as an electron and a jet.

Another commonly used quantity to estimate the event activity is the scalar sum of the transverse momenta $\sum p_{\mathrm{T}}$:

$$\sum p_{\mathrm{T}} = \sum p_{\mathrm{T}}^{\mu} + \sum p_{\mathrm{T}}^{e} + \sum p_{\mathrm{T}}^{\gamma} + \sum p_{\mathrm{T}}^{\tau} + \sum p_{\mathrm{T}}^{\mathrm{jets}} + \sum p_{\mathrm{T}}^{\mathrm{soft}}. \tag{37}$$

Taking into account the scalar sum of transverse momenta from only from reconstructed hard objects, this quantity can be referred to as H_{T}:

$$H_{\mathrm{T}} = \sum p_{\mathrm{T}}^{\mu} + \sum p_{\mathrm{T}}^{e} + \sum p_{\mathrm{T}}^{\gamma} + \sum p_{\mathrm{T}}^{\tau} + \sum p_{\mathrm{T}}^{\mathrm{jets}}. \tag{38}$$

In essence, the $E_{\mathrm{T}}^{\mathrm{miss}}$ exists in the transverse plane $x - y$. As such, it can be written directly using its components on that plane:

$$E_{\mathrm{T}}^{\mathrm{miss}} = \sqrt{(E_x^{\mathrm{miss}})^2 + (E_y^{\mathrm{miss}})^2}. \tag{39}$$

To account for estimated resolutions and efficiencies of objects contributing to $E_{\mathrm{T}}^{\mathrm{miss}}$ and to reject backgrounds where mismeasured objects cause fake $E_{\mathrm{T}}^{\mathrm{miss}}$, another variable called object-based $E_{\mathrm{T}}^{\mathrm{miss}}$ significance $\mathcal{S}$ can be defined:

$$\mathcal{S} = \frac{\left|E_{\mathrm{T}}^{\mathrm{miss}}\right|}{\sqrt{\sigma_{\mathrm{L}}^2\left(1 - \rho_{\mathrm{LT}}^2\right)}} \tag{40}$$

where σ_L^2 is the total variance in the longitudinal directions to the $E_{\mathrm{T}}^{\mathrm{miss}}$, and ρ_{LT} is the correlation factor of the longitudinal and transverse measurements. A high value of $\mathcal{S}$ indicates that $E_{\mathrm{T}}^{\mathrm{miss}}$ is not well explained by the resolution smearing alone, and suggests that the event is likely to contain unseen objects [136].

6 TRANSITION RADIATION TRACKER

6.1 INTRODUCTION

The ATLAS Transition Radiation Tracker (TRT) is the outermost part of the ATLAS Inner Detector consisting of nearly 300 000 straws, each of which is a proportional drift tube with a diameter of 4 mm. When a charged particle hits a straw tube, it ionizes gas atoms inside the straw and creates ionization clusters. Then the electrons drift towards the anode wire, and their cascade in the strong electric field produces a detectable signal. The *beauty* of the TRT is in its ability to help both in tracking and particle identification. Each charged particle crosses on average 30-40 TRT straws, leaving a set of track position measurements that can considerably improve momentum resolution. Particle identification can be achieved by measuring transition radiation emitted by particles on their way through the radiator material.

The spatial position of charged-particle tracks is determined from the drift time measurements. The drift time measurements start by measuring the leading-edge time of a signal, which depends on various effects, such as the time of flight of the particle from the collision point through the straws, the signal propagation from the anode wire to the read-out electronics and the actual drift time. To take into account different propagation effects of a signal, a correction known as the calibration constant t_0 is applied. Once the drift time is accurately measured and corrected, it can be translated into a drift radius, i.e. the distance of closest approach of the charged particle to each anode wire, making use of the relation between drift time and drift distance, called the *r-t* relation. Both the t_0 constant and the *r-t* relation have to be calibrated every time data taking conditions change in order to ensure the best possible momentum reconstruction and position resolution in the TRT.

The TRT is operated mainly with a gas mixture of 70% Xe, 27% CO_2, and 3% O_2 in Run 2. During the 2012 data taking period, several leaks developed in the gas supply tubes. Many of them occurred in inaccessible areas and therefore the repair of the leaks is not possible. Because of the high cost of losing the xenon-based mixture, some parts of the TRT were switched to operate with an argon-based gas mixture instead. While argon has lower efficiency to absorb transition radiation photons leading to lower electron identification capabilities, it is suitable for tracking. Since the gas properties affect the drift time, it is crucial to have accurate t_0 and *r-t* calibrations for each of the gas mixtures.

Before calibrations, the TRT design and choices for gas mixtures are described in Section 6.2. Section 6.3 gives an overview of different track and hit parameters needed for evaluating the tracking performance. As promised, calibrations will form the major part of this chapter: Section 6.4 starts by calibrating simulated data in various gas geometries, and Section 6.6 does the same with real data, showing that the TRT tracking performs well despite gas leaks, high occupancy and pile-up.

6.2 DETECTOR DESIGN

As discussed in Section 4.3, the primary goal of the Inner Detector is to reconstruct tracks and vertices with high efficiency, and contribute to electron, muon, and photon recognition together with the calorimeter and muon systems. The TRT contributes to particle momentum measurements and pattern recognition by providing a large number of hit measurements at

the outer radius of the ID. The radial extent of the TRT is an essential element for the tracking performance: longer lever arm improves momentum resolution significantly with less material per point [1] and at lower cost compared to silicon detectors, compensating its lower precision per point. In addition, the TRT provides particle identification based on transition radiation. In particular, it is able to distinguish between electrons and pions up to roughly 100 GeV. The detailed description of the TRT detector can be found in Refs. [137], [138], and [139], and an overview is given below.

The basic detecting elements of the TRT are the straw tubes, or just straws in short, which can operate at high interaction rates. Straws are made of two layers of polyimide film (Kapton), strengthened by thin carbon fibres to improve mechanical properties such as tolerance towards tension, humidity and temperature. However, the straw walls must be thin enough in order to let transition radiation photons go through and be absorbed in the gas. These walls act as cathodes, held at a negative potential at a voltage of -1.5 kV, corresponding to a gas gain of 2.5×10^4 for the xenon-based gas mixture. A gold-plated tungsten wire of 31 µm diameter at ground potential forms the anode inside each tube. The straw radius of 4 mm is a compromise between response time, number of ionization clusters, and operational stability. Larger straw radius would give higher hit efficiency, but it leads to longer drift times in the straw which is an issue in short bunch crossings of 25 ns at the LHC. The spaces between the straws are filled with a radiator material, polymer fibres in the barrel and foils in the endcaps, to create transition radiation. [137]

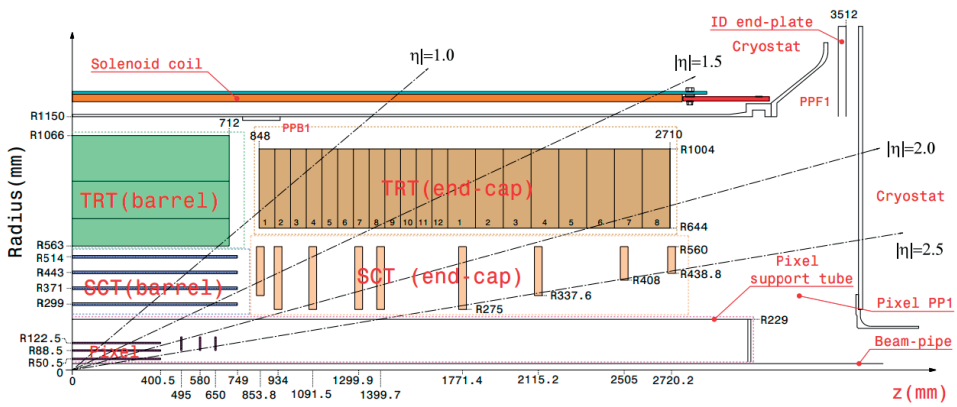

Figure 25: The Inner Detector during Run 1 in the $r - z$ plane, where r is the radial distance from the z-axis, showing only positive z side. [140].

The TRT consists of three parts: a cylindrical barrel with 52544 straws in the center for $|\eta| < 0.625$, and two endcaps, with 122880 straws each, consisting of multi-plane wheels at higher $\eta < 2.0$. In the barrel, straws are aligned along the beam direction whereas in the endcaps they are aligned perpendicular to the beam axis and point outwards in the radial direction. These orientations were chosen to maximize the number of straws passed. Each detector part is further divided into two sides according to their z location: side A with a positive global z coordinate and side C with a negative z coordinate. In the barrel, the same straw goes from side A to side C but the wire is divided in two by an insulating glass joint, in order to reduce the occupancy of the innermost straws at high luminosities. Each side is read

1 Less material leads to less multiple scattering, which is a major source of uncertainty of the track transverse momentum measurements

out separately at each end. Wires in the innermost 9 straw layers are split into three parts, with the central part not being read out, and these straws are referred to as "short straws". Each endcap is also further divided into type A and type B in z, where type A has 6 wheels per side at $848 < z < 1710\,\text{mm}$, and type B has 8 wheels per side at $1740 < z < 2710\,\text{mm}$ [139, 141]. This geometry provides continuous tracking at large radius in the ID. All charged particles with $|\eta| < 2.5$ and $p_T > 0.5\,\text{GeV}$ cross about 40 TRT straws. To illustrate the geometry and dimensions of the ID, it is shown in Figure 25 as it was during Run 1 (that is, without the IBL).

6.2.1 *Transition radiation*

Transition radiation (TR) photons are emitted when a highly relativistic particle traverses the boundary between two materials of different dielectric properties. The total transition radiation energy emitted by a relativistic particle is [142]

$$E = \frac{\alpha}{3}\gamma\hbar\omega_p \tag{41}$$

where $\gamma = E/m$ is the Lorentz gamma factor, and ω_p is the plasma frequency depending on the materials at the boundaries, typically around 20 eV. The TR photons are typically produced with energies of 5-15 keV [2] and emitted at small angles ($\theta \approx 1/\gamma$) to the track direction.

However, many transition regions (such as plastic foils) are needed to increase the number of TR photons. It is interesting to note that the energy deposit in the straw is not only proportional to the velocity of the particle, but also increases with γ (energy!)[3]. As electrons are much lighter than pions, their γ factor is significantly larger. Consequently, electrons have larger probability for emitting transition radiation. Transition radiation hence offers the possibility of electron identification for relativistic particles.

A detector suitable for detecting transition radiation consists of a radiator followed by a layer made of proportional counters filled with a gas mixture, i.e. straws in the context of the TRT. The TR photons have to be recorded using a gas that can absorb them efficiently at the relevant photon energies. The gas choice is driven by the photoelectric absorption cross-section, which depends strongly on atomic number Z ($Z(\sigma_{\text{photo}} \propto Z^5)$ [7]. Therefore high-Z gases such as xenon (Z=54) are favoured. For the same reason, when designing radiator foils, atomic number Z should be as low as possible. Otherwise, the TR photons would not be able to escape from the radiator [143]. The other reason to prefer noble gases (such as xenon) over complex molecules is that the deposited energy leads to ionization instead of leading to excitation of molecules.

6.2.2 *Gas mixtures*

The choice of the straw gas mixture in the TRT is restricted by few requirements. First, for the most efficient particle identification determined by efficient X-ray absorption, the gas must be a xenon-based mixture as described above. The drift velocity in the gas must also be as fast as possible in order to minimize the pile-up effects that arise from particles produced in interactions before or after the bunch crossing of interest. A small fraction of the gas has to be

2 On average, a minimum ionizing particle deposits an energy of roughly 2 keV in a straw.

3 This is a huge advantage for the particle identification, which in many other cases (energy loss by ionization, time of flight, Cherenkov radiation which is emitted when a charged particle crosses a dielectric medium at a speed greater than the phase velocity of light in that medium) depends on the velocity: $\beta = \frac{v^2}{c^2} \to 1$. [142].

a quenching gas, absorbing any secondary photons emitted by excited gas atoms that could lead to fake signals and sparks. Most of the quenching gases can burn in air, representing a security risk; however, a gas mixture containing some oxygen is inflammable [83]. Last, stable operation over long periods of time without sparking must be guaranteed. Therefore it was decided to use a ternary mixture of Xe (70%), CO_2 (27%) and O_2 (3%). Higher concentrations of xenon could lead to unstable operations [137].

At the beginning of the LHC and ATLAS operations, the TRT detector was operated using only xenon-based gas mixture, which allowed the TRT to combine its tracking capabilities with electron identification based on transition radiation photon detection. However, several gas leaks in gas supply tubes developed in the TRT gas system during Run 1 and Run 2 operations due to corrosion caused mainly by ozone [4]. In many cases, the leaks occurred in locations that are inaccessible [5], and therefore their repair is not possible.

As the leaks continued, it was decided to change the gas mixture from xenon to a cheaper gas mixture in parts of the TRT where the xenon losses were too high and therefore unaffordable. In order to keep the particle identification capability based on transition radiation, a gas with a relatively high Z and therefore sizeable cross-section for the photoelectric effect had to be found. Such gases are for example krypton (Z=36) and argon (Z=18). However, as krypton has radioactive isotopes that can be produced when exposing it to ionizing radiation, it was rejected [144] and an argon-based gas mixture of $Ar(70\%)/CO_2(27\%)/O_2(3\%)$ was chosen instead. While argon has lower efficiency to absorb TR photons leading to decreased electron identification capabilities, it works well for tracking purposes. The most important tracking characteristics to be focused on are the drift time measurement accuracy and efficiency.

Some differences in the tracking performance are expected when comparing argon-based mixture to xenon, mainly because the electron drift time depends on the type of gas used. The measured time of drift determines the position of the track relative to the wire. From many time measurements transformed to hit positions, the track of the charged particle can be completely reconstructed. Argon-based gas results in larger drift velocity leading to shorter drift time and even to a reduction of the straw occupancy from adjacent bunches [145]. A straw signal will differ significantly when comparing these two gas mixtures. Because of the signal shape from the straw in argon-based mixture, the TRT read-out electronics can integrate more charge during the signal processing than for a xenon-based mixture (about 15% instead of 5% [140]) and therefore can operate at a lower threshold, as we will see later in this chapter. In principle a lower threshold should result in better drift time measurement accuracy. On the other hand, the argon-based gas mixture has a lower density than xenon, and electrons have a longer mean free path (the distance between two electron ionization clusters in a gas) in argon. These properties result in fewer primary ionization clusters (8-9 clusters created by a particle travelling 2 mm in argon [146]), which also reduces the spatial resolution of the hit. Furthermore, the cluster energy loss $\mathrm{d}E/\mathrm{d}x$ is lower in the argon-based gas mixture than in the xenon-based gas mixture [147, 148]. In the following, saying only argon or xenon straws works as a shorthand for straws filled with a argon or xenon-based gas mixture.

When Run 2 started in 2015, the innermost barrel layer and two endcap wheels (endcap side C wheel 3 and endcap side A wheel 5) were switched to operate with argon, and xenon was kept in other parts of the detector. In 2016, barrel layers 0 and 1 as well as endcap wheels 3 and 5 on side A and wheels 3, 5, and 8 on side C were filled with argon. During 2017 and 2018, a wheel on endcap side C was swapped: wheel 3 filled with argon was switched

4 The gas mixture is exposed to continuous ionizing radiation, splitting the O_2 molecules that can regroup again to form O_3.

5 Remember, ATLAS is like an onion. Total peeling of it would be required in order to reach all the affected parts.

to wheel 2, keeping the setup otherwise the same. All of these different gas *geometries*[6] are shown in Figure 26.

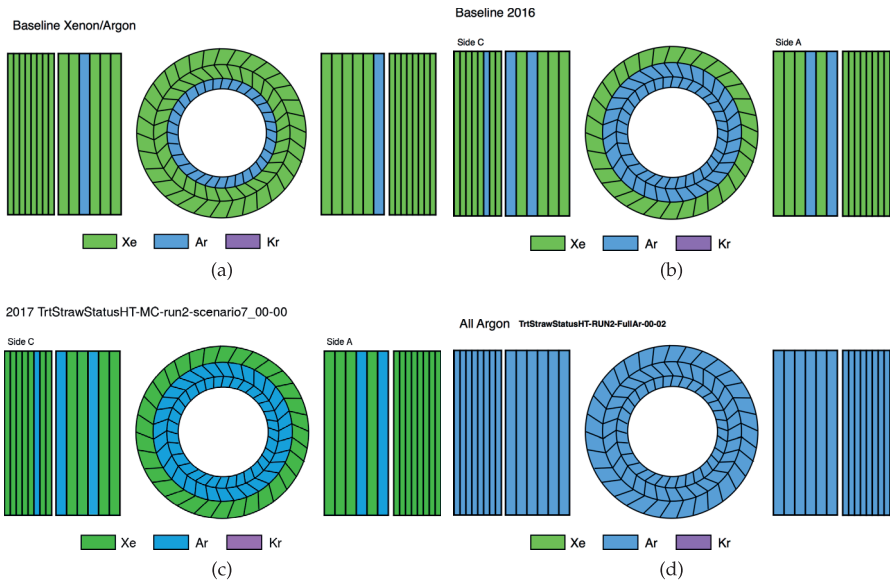

Figure 26: Gas geometry in the TRT during different data taking periods during the LHC Run 2: (a) in 2015, (b) in 2016, (c) in 2017, and (d) in 2015-2018 during heavy ion collisions.

The impact of operating the TRT with argon-based gas mixture has been evaluated in terms of ATLAS performance and physics analyses [149]. The major effect is that the number of fake electrons and photons rises at low-p_{T} and high η, which affects various physics analyses that suffer from increasing backgrounds. Tracking performance is, however, expected to be similar both with argon and xenon mixtures, and further studies are needed.

6.2.3 *Signal processing*

When a charged particle crosses a straw tube filled with gas, it deposits on the average 2 keV of energy in the gas and produces primary ionization clusters. The electrons drift towards the anode wire, and as they get closer, the strong electric field allows them to ionize more of the gas, inducing a cascade or avalanche of electrons. This avalanche produces a detectable signal with a gas gain of approximately $2 \cdot 10^4$. The straw signal has a fast sharp pulse corresponding to the avalanche electrons reaching the anode, and a slowly falling ion tail due to the positive ions created in the avalanche process drifting towards the cathode walls. These ion tails are cancelled in the front-end electronics by analogue signal processing. A characteristic signal can be seen in Figure 27.

The signal is then amplified, shaped and discriminated by the first front-end chip, the Amplitude Shaper Discriminator Baseline Restorer (ASDBLR). This analog readout by ASDBLR is implemented as a custom-designed Application Specific Integrated Circuit (ASIC). The chips are connected directly to the straw wires: each ASDBLR has 8 channels, each corresponding to a single straw. As the energy loss by ionization is typically around 2 keV as opposed to the

6 Changing the gas mixture does obviously not change the physical geometry of the TRT.

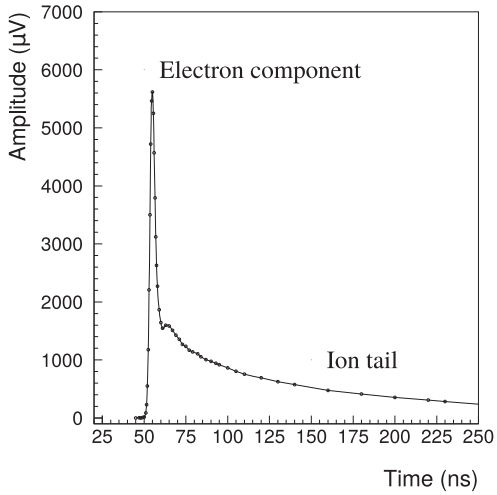

Figure 27: The signal in a TRT straw, showing the electron component and the ion tail. [150]

typical TR photon energy of 5-15 keV, the signal can be discriminated and it can contribute to electron identification. The signal is discriminated against two adjustable thresholds by the ASDBLR to separate hits from minimum ionizing particles from those arising from transition radiation: the low threshold (LT) and the high threshold (HT), and are quite uniform across the detector. These thresholds are also referred to as Low Level threshold (LL) and High Level threshold (HL). The LT of 100-300 eV is used to measure an electron drift time for tracking, and the HT of about 5-7 keV is used for detecting the larger currents from TR photons providing the electron-pion separation.

The signal in argon mixture is smaller due to a lower number of primary electron clusters and a lower number of electrons in each cluster. However, the performance of both gas mixtures has to be kept at the same level. In other words, the hit efficiency describing the probability of a hit if a particle passes a straw has to be similar for straw filled with argon and xenon. This can be achieved by tuning the thresholds of the argon gas mixture, increasing the sensitivity of the read-out electronics to ionization clusters. The low threshold was tuned to match the straw hit efficiency, while the the high threshold was tuned to agree with the probability for a hit from a minimum ionizing particle to pass the high threshold [151]. The output of each channel is a ternary signal, and it indicates whether none, one or both of the discriminators fired. The discriminator thresholds are shared by all channels in the ASDBLR. [152]

The signals are then sampled by the second ASIC, a digital front-end chip called the Drift Time Measurement and Read-Out Chip (DTMROC), which measures the timing of the signals, buffers it and transmits data to the TRT readout drivers (ROD) when a Level-1 trigger accept occurs [152]. The digital signal for each 25 ns bunch period at the LHC consists of eight bits 3.125 ns wide. The bit is set to one if the energy exceeds the low threshold, and set to zero otherwise. The 9th bit indicates whether the energy exceeds the high threshold. In total, 27 bits are transmitted from the DTMROCs, corresponding to 24 bits associated with the LT and 3 bits with the HT.

During Run 2, the bunches of protons were colliding every 25 ns. This collision rate is challenging for the TRT as its readout time is 75 ns, or three bunch crossings. Figure 28 shows the signal pulse in a 75 ns readout window, its bit pattern and how it is related to different

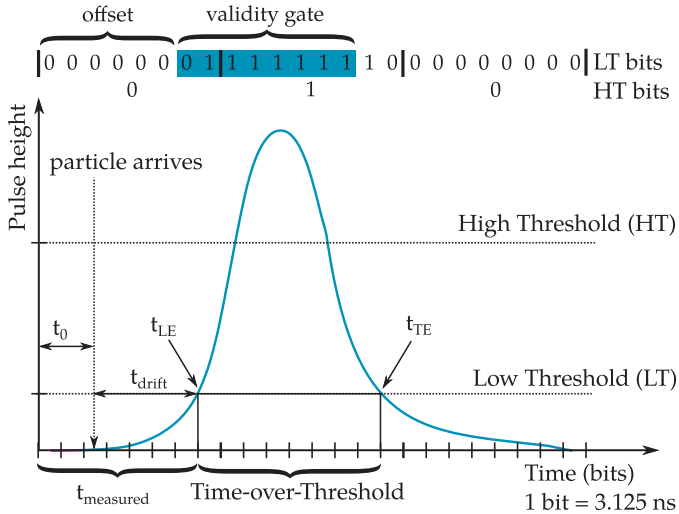

Figure 28: A schematic view of the TRT straw signal pulse and the 75 ns readout window. The drift time t_{drift} , time offset t_0 , leading edge time t_{LE} and trailing edge time t_{TE} as well as the validity gate (in blue) are shown. Modified from Ref. [153].

time parameters. The choice of the window size was driven by the maximum drift time in the magnetic field: it can be up to 50 ns, and the full signal has to be contained in the readout. As explained, each signal is digitized into 24 bins of 3.125 ns. First, the time at which the ionization signal first rises over a low threshold is called the Leading Edge time t_{LE} . In a bit pattern it is seen as the first transition from 0 to 1. The second transition from 1 to 0, i.e. the time bin of the last bit that fired, is known as the Trailing Edge time t_{TE} . If the furthest electrons were always produced exactly at the straw wall, they would drift the full straw radius of 2 mm and the t_{TE} would be independent of the track-to-wire distance. However, because of the finite number of primary ionization clusters and signal shape effects, this is not the case in reality [154]. Examples of the leading edge and trailing edge time distributions are presented in Figure 29.

The time between leading and trailing edge is the measured time-over-threshold t_{ToT} . It is related to the perpendicular distance between the track and the centre of the straw, as illustrated in Figure 30. If a particle crosses a straw near the wire, the signal pulse will be broader and t_{ToT} will be larger. Furthermore, a particle that deposits more energy inside the straw will on average result in higher signal, exceed the low threshold sooner, and have signal above threshold for longer. Accordingly, larger energy deposits lead to an earlier t_{LE} , later t_{TE} and longer t_{ToT} on average [154]. The measured t_{ToT} is therefore also related to the energy loss $\mathrm{d}E/\mathrm{d}x$ of the charged particle and can also be used to separate electrons from pions. To minimize straw hit occupancy (the fraction of straws with hits) from out-of-time pile-up caused by interference between adjacent bunch crossings, a validity gate is introduced. A validity gate restricts the portion of the TRT readout where the signal appears within a certain time window: it suppresses the number of hits that come from tracks originating from neighbouring bunch crossings, which have the same distribution but are shifted by 25 ns.

The straw signal processed by the front-end electronics is transmitted to the TRT back-end electronics. The communication between the TRT front-end electronics and the data acquisition (DAQ) system consists of custom 9U VME64x modules: the Timing, Trigger, and Control

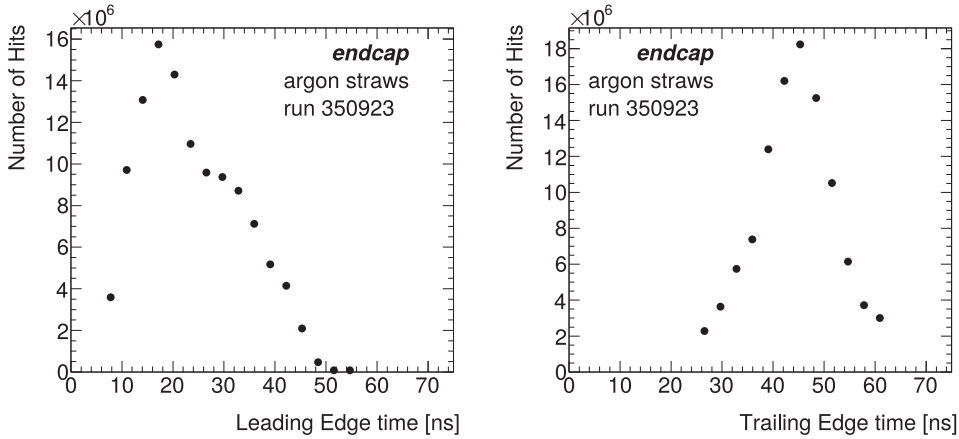

(a) (b)

Figure 29: Examples of the (a) Leading Edge and (b) Trailing Edge time distributions for proton-proton collision run 350923 in endcap argon straws, requiring at least 12 TRT hits on a track with $p_T > 2\,\text{GeV}$.

(TTC) modules and Read-Out Driver (ROD) modules. There are 10 VME crates filled with 96 RODs and 48 TTCs in total, each crate being controlled by a Single Board Computer (SBC).

A ROD receives data from the front-end, packages them, and sends its buffer to a Read-Out Buffer (ROB) module that keeps the data until a Level-2 trigger is ready to process data from several RODs for a defined trigger region of interest (ROI). A TTC is responsible for delivering timing and control signals to the front-end through intermediate patch panels, which are physically located in the midst of the ATLAS muon system. In total, there are 350000 electronic channels (two channels per barrel straw), each channel providing a drift time measurement and two independent thresholds.

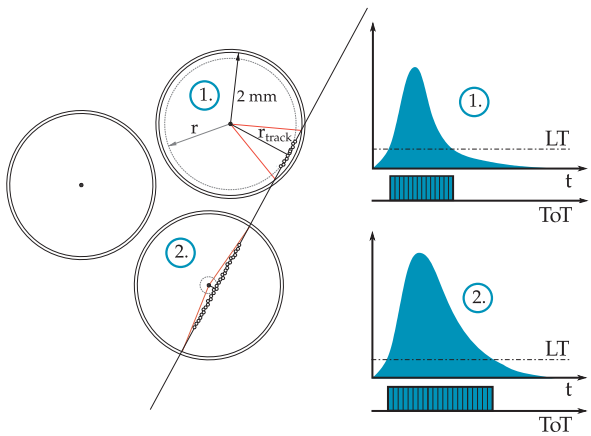

Figure 30: Time-over-threshold illustrated. Modified from Ref. [155].

6.3 TRACKING WITH THE TRT

"The proof of the pudding is in the eating, and the proof of the drift chamber is in the track parameters." [83]

As described in Section 5.5.1, the track reconstruction relies on measurements of several discrete spatial hits in the detector. However, the TRT measures the drift *time* rather than a position point at which a particle crossed the straw and therefore the drift time has to be translated into drift circle radius to be used in the track reconstruction. This is done by determining the relation between drift time and drift radius, the so-called *r-t* relation will be covered in detail in Section 6.4.2. The distance of the closest approach of the track to anode wire is called the track-to-wire distance. Determining the side of the anode wire at which a particle crossed the straw remains ambiguous, and is resolved by the tracking algorithm.

For any tracking detector at the LHC, measuring tracks in the dense environment with high pile-up is challenging but extremely important. Many signatures occurring in potential new physics scenarios include heavy resonances decaying into highly boosted objects, such as hadronic jets and τ leptons. In such signatures, the separation between highly collimated charged particles is comparable to the granularity of individual sensors in the ID. To prevent losses in efficiency, to increase the possibility of discovering new phenomena and to allow more detailed measurements, the tracking detectors must be able to provide good-quality tracking even in a high occupancy environment [117]. To quantify the TRT tracking performance, few parameters can be used, such as the straw efficiency, the track position measurement accuracy, and the number of precision hits which will be defined shortly. The difference between the drift radius (r) and the track-to-wire distance (r_{track}) is called the position residual (see Figure 31), and the width of the residual distribution obtained from all hits and tracks describes the position resolution of the TRT. The resolution determines how accurately the drift time can be measured, and how well the position of the anode wire is known.

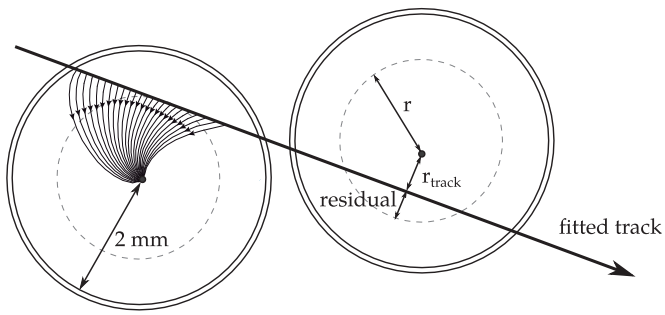

Figure 31: The particle traversing the tube ionizes the gas and causes an electron shower towards the central anode wire. The bending of the electron trajectories is caused by the magnetic field. Here two TRT straws (solid circles) and their drift circles (dashed circles) are shown with the fitted track (solid line), the track-to-wire distance r_{track} and the residual r - r_{track} . Figure is modified from Ref. [156] and inspired by Ref. [157].

There are different types of the TRT hits, i.e. straws that are fired when a particle crossed them, as shown in Figure 32. *Holes* are straws that are crossed by a fitted track but did not fire, i.e. there is no hit. *Outlier* is a hit on track for which the fitted track passes at least 100 µm of the straw wall. Outlier hits are only used in pattern recognition, and for them a drift radius of $r = 0\,\text{mm}$ and an uncertainty of $d/\sqrt{12} = 4\,\text{mm}/\sqrt{12} = 1.15\,\text{mm}$ are assigned. The uncertainty comes from the standard deviation of a flat probability distribution for a hit. *Tube*

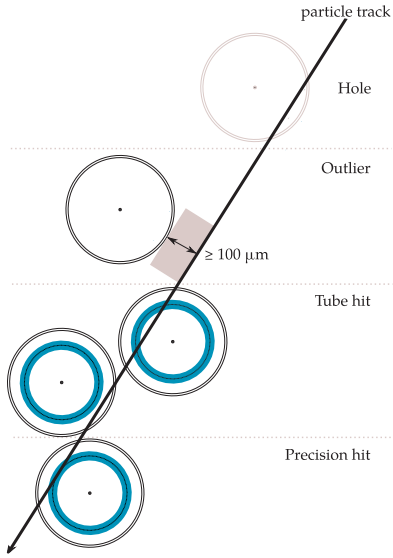

Figure 32: Different hit type definitions in the TRT straws. A fitted particle track crosses multiple straws (solid circles), and can have outlier hits, tube hits, precision hits, or holes, as defined in detail in the text. An outlier is a hit on track for which the fitted track passes at least 100 μm of the straw wall (grey box). Hole (grey circle) is a straw which is crossed by a fitted track but not fired: there is no hit. Drift circles (dashed circles) and error on drift radius (blue circles) are also illustrated. Figure is modified from an original sketch by Narei Lorenzo Martinez and Ref. [158]

hits are used in pattern recognition and in track fitting, and come in two different types: either they are unprecise hits inside the straw wall with a measured residual value larger than 2.5 of the hit uncertainty, or they are hits on a track with no valid leading edge. Finally, *precision hits* are hits with a residual within 2.5 of the hit uncertainty. There are around 30-40 TRT hits per track, except in the transition region between barrel and endcaps where the number of hits is reduced to approximately 25 hits.

The ATLAS ID track-finding algorithm first forms tracks in the silicon detectors, and uses the TRT hits to extend the number of hits on the track at larger radii. The TRT track extension fraction is the fraction of tracks reconstructed in the silicon detectors which use a TRT extension. If the TRT hits are not found to reconstruct the track extension (for example because of interactions with the detector material), only silicon detectors are used to reconstruct the track. Figure 33a shows the TRT track extension as a function of the TRT occupancy.

As was shown in Section 4.1.2, the spatial resolution and the number of hits are important parameters for the momentum measurement. The TRT contributes significantly to the particle momentum reconstruction accuracy, for which an example of heavy-ion simulations is shown in Figure 33b. The tracks with and without including the TRT measurements are compared in a low momentum range $2\,\text{GeV} < p_{\text{T}} < 2.5\,\text{GeV}$ because the occupancy effects are expected to be the most noticeable in this range. As can be seen, including the TRT hits in the particle momentum measurement improves the momentum resolution by about 25%. Even at extreme occupancies of 90%, the TRT improves the ID momentum resolution by about 10%, which applies to about 70% of the tracks in such high-occupancy conditions in heavy-ion collisions. In both figures, several requirements have to be satisfied in order to include the TRT extension to the track: number of TRT hits, fraction of precision hits, and overall goodness of the fit [140].

6.4 CALIBRATION PRINCIPLES

In the TRT, the spatial position of the tracks is determined from the drift time measurements. The TRT indeed measures the drift time, and therefore the drift time calibration is essential to have the best resolution and the best momentum reconstruction in the TRT. The main goal

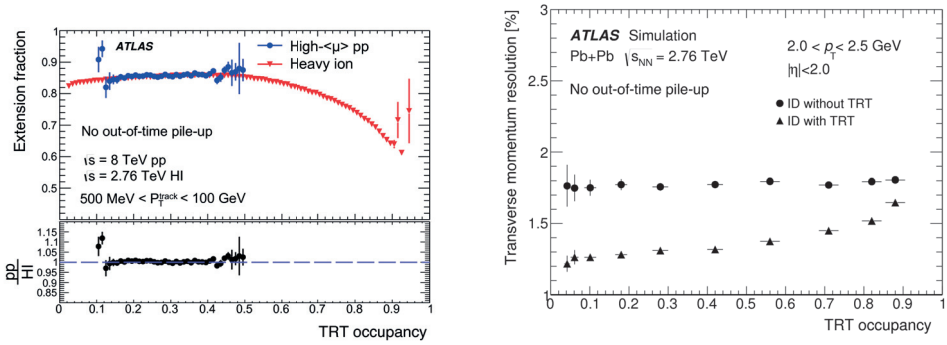

(a) (b)

Figure 33: (a) The TRT track extension fraction as a function of the TRT occupancy for $40 \leq \langle\mu\rangle \leq 70$ in pp and heavy ion collisions recorded in Run 1 with a xenon-based gas mixture. (b) The p_{T} resolution of ID tracks as a function of the TRT occupancy with and without TRT measurements for heavy ion simulations with a xenon-based gas mixture. From [140]

of the calibration is to provide a precise estimate for the distance between the track and the centre of the straw, i.e. track-to-wire distance r_{track}, based on the measured leading edge time t_{LE}. Once the drift time t is known, it can be translated to the drift radius r using the so-called r−t (radius-to-time) relation. Many parts of the following description of the calibration process are further discussed in Ref. [156].

There are several timing effects on the measured leading-edge time of the signal, and therefore the time has to be calibrated in order to reach the best possible accuracy. The measured leading edge t_{LE} depends on four parameters

$$t_{\mathrm{LE}} = \underbrace{t_{\mathrm{collision}} + t_{\mathrm{ToF}} + t_{\mathrm{SP}}}_{t_0} + t. \tag{42}$$

Parameter $t_{\mathrm{collision}}$ is the time when the collision occurs with respect to the start of the TRT read-out window, and t_{ToF} is the time-of-flight between the production of a particle and when it crosses the straw. As furthest straws are placed at a distance of 2.7 meters, it takes up to 9 ns for a relativistic particle to reach them [146]. The signal propagation time t_{SP} is the time for a signal on the wire to reach the read-out electronics. Finally, the drift time t is the quantity of interest (see Figure 28). The collision time, time-of-flight time, and the signal propagation time can be combined into one quantity called t_0 calibration constant, because they do not vary much within a small region of the detector. The methods for calibrating the t_0 constant will be discussed shortly.

Once the drift time t is known, it can be translated to the drift radius r used in the track fitter. The drift radius r is not the same as the actual distance of closest approach of the track to the wire, because the primary electrons bend in the magnetic field and there is a finite number of primary ionization clusters on the track inside the straw, as shown in Figure 31. Instead, it serves as the best estimate of the track-to-wire distance given by the measured time. The drift radius is thus defined as $r\,(t\,) = r\,(t_{\mathrm{LE}} - t_0\,)$. After the tracking of the particle is done, the distance between the track and the center of the straw, r_{track} , can be obtained. This radius can be converted again to the track drift time (t_{track}) using the inverse r-t relation:

$$t_{track} = r^{-1}(r_{track}). \tag{43}$$

The calibration is performed iteratively. For each iteration, tracks are reconstructed in the full Inner Detector using a set of calibration constants. The reconstructed tracks are then used to calculate the new calibration constants t_0 and the values for the parameters of the r−t relation, which are then used as input values to the next iteration. The t_0 and r−t constants are determined independently. These steps are repeated until the change in the calibration constants is small and the minimal residuals are achieved in all detector regions: the TRT barrel, and the TRT endcaps on side A and side C.

As mentioned, the position residual is the difference between the drift radius r and the track-to-wire distance r_{track}:

$$\Delta r = r - r_{track}. \tag{44}$$

The track position measurement accuracy, i.e. the detector resolution, is defined as the width σ_r of a Gaussian fit to the mean of the position residual distribution. The aim is to minimize the width during the iterative calibration procedure. The fit is done iteratively in the range $\pm 1.5\sigma_r$ around the mean of the distribution. Although the hit residuals do not form a perfect Gaussian, mostly because tube hits are included, the hits found in the non-Gaussian tail would not significantly improve the track reconstruction accuracy. In addition, increasing the range to $\pm 2 - 2.5\sigma_r$ would degrade the track quality at higher occupancy [148]. The residual distribution is expected to be centered at 0 mm and be symmetric if the detector is perfectly aligned; any miscalibration and misalignment would affect the position resolution. The uncertainty of the width is less than 0.1 µm in all cases presented in the following.

Accordingly, time residual Δt is defined by

$$\Delta t = \underbrace{t_{\mathrm{LE}} - t_0}_{t} - t_{track} \tag{45}$$

where t is the measured drift time, t_{LE} is the leading edge time and t_{track} is the track drift time for a given track-to-wire distance. The Δt distribution is also fitted iteratively with a Gaussian function of mean μ_t and width σ_t in the range $\mu_t \pm 1\sigma_t$. The time residual distribution is asymmetric, mainly due to ionization clusters and electron drift properties in the gas mixture. The mean of the fitted Gaussian, μ_t, is related to the quality of the detector timing.

6.4.1 *The t_0 calibration constant*

As discussed above, various timing effects from clock propagation, signal propagation, and the time of flight of the particle can be combined into one offset variable, the t_0 calibration constant. To determine the t_0 calibration constants, the distribution of time residuals is obtained for different detector elements as shown in Eq. 45. After the distributions are fitted with a Gaussian distribution, the t_0 calibration constants are then updated after iteration i as

$${t_0}^{\mathrm{i}} = {t_0}^{\mathrm{i}-1} + \mu^{\mathrm{i}} - \tilde{\mu} \tag{46}$$

where $\tilde{\mu}$ is an offset of 0.5 ns optimized to provide the best position residual for tracks with p_{T} over 2 GeV [156]. The first calibration uses the best knowledge of current calibration constants that are saved in global database, as will be discussed in Section 6.7.

6.4.2 *The r-t calibration constant*

The relation between the drift time t and the drift radius r can be obtained from a fit to a third order polynomial, the *r-t* relation:

$$f(t) = a_0 + a_1\, t + a_2\, t^2 + a_3\, t^3 \tag{47}$$

$$r(t) = \begin{cases} 0\,; & f(t) < 0 \\ f(t)\,; & 0 < f(t) < R_\circ\,; \\ R_\circ\,; & f(t) > R_\circ \end{cases} \qquad R_\circ = 2\,\text{mm}\ (\textit{straw radius}) \tag{48}$$

where a_i are the four parameters to be calibrated.

An example of the *r-t* relation fit can be seen in Figure 34. The slope of the *r-t* relation, $\frac{\partial r}{\partial t}$, is the drift velocity of the electrons. The *r-t* relation clearly shows that the electron drift velocity is slower in xenon than in argon gas mixture, and using argon mixture results in shorter drift time for a given drift radius. The regions where drift velocity is not constant correspond to the areas near the wire or the straw tube wall: electrons drift faster when they are close to the anode wire, and slower when they are near the straw wall. The "gaps" visible in number of the hits in each bin are caused by a bin width which is not a multiple of 3.125 ns, i.e. the size of actual bins that the detector is read out.

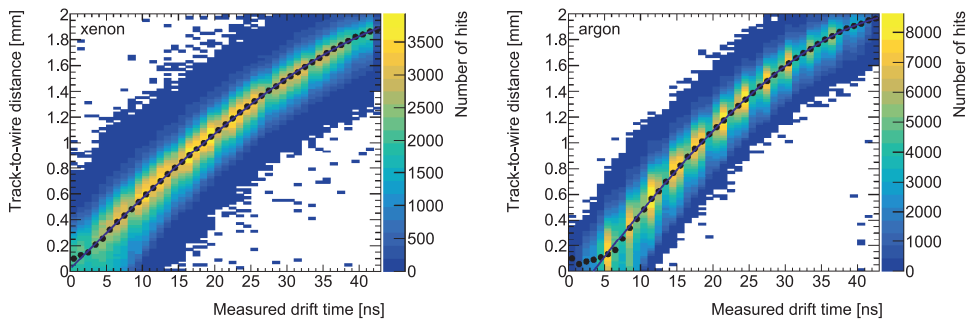

(a) (b)

Figure 34: Example of the *r-t* relation for straws filled with (a) xenon and (b) argon using a *pp* data run in 2017. The black circles represent the peak position of the Gaussian fit to the track-to-wire distributions in time slices. The blue line shows a third degree polynomial $f(t)$ fitted to the points.

To compute the calibration constants in the *r-t* relation, the track-to-wire distances r_{track} are accumulated for 1 ns wide slices of the measured drift time t . The peak of each track-to-wire distance distribution is fitted with a Gaussian function in each time slice, and the mean is extracted for every slice. Absolute track-to-wire distances for selected drift time bins are shown in Figure 35. The absolute value r_{track} is used because the *r-t* relation does not depend on the sign of the drift radius, and no difference is expected between positive and negative drift radius. The extracted mean values are shown as black circles in Figure 34. Figure 35 also clearly illustrates how the residual width decreases with increasing drift time. This behaviour is expected because the short drift time is caused by particles traversing close to the anode wire. The closer to the wire, the more increased uncertainties in timing due to the electron drift and amplification.

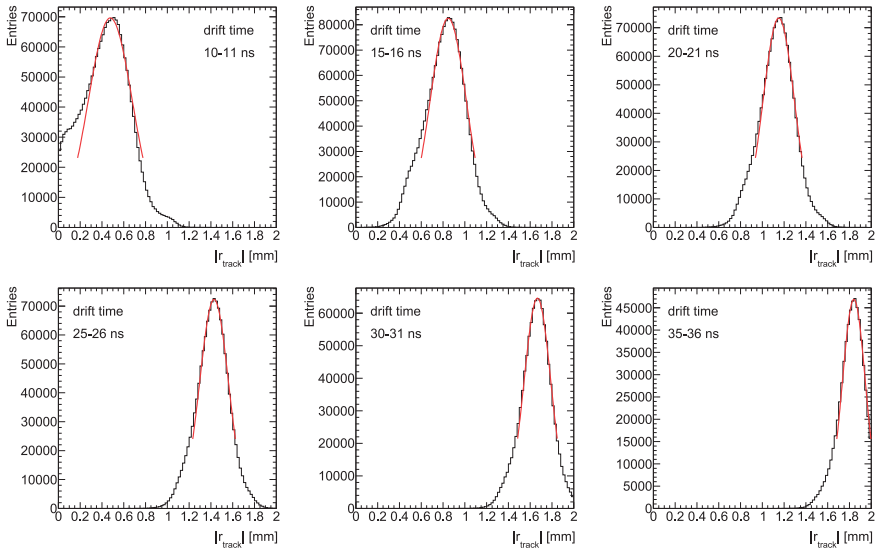

Figure 35: Absolute track-to-wire distances for selected drift time bins measured in Endcap C xenon straws during a heavy ion run in 2018. The red line corresponds to a Gaussian fit performed to extract the mean.

A third degree polynomial in the *r-t* relation is then fitted to all the peak mean points, and the fit is used to determine the drift distance depending on the measured time. The parameters a_i from the third degree polynomial fit are then used for the next iteration. The points at $t \approx 0$ ns are not well described by the fitted curve, because the track-to-wire distance is defined always positive. They also suffer from the way the charge arrives over a longer time when the track is further from the wire. The pulses caused by tracks passing near the wire are long and often the closest cluster is far from the distance of closest approach, as illustrated earlier in Figure 30.

The ID is placed inside a solenoid magnet which provides a 2 T magnetic field parallel to the beam pipe. The *r-t* relations of the barrel and the endcaps are expected to differ slightly, because the straws are oriented in a different way with respect to the magnetic field direction: the wires are parallel to field in the barrel and mostly transverse in the endcap regions. Furthermore, the field is quite uniform in the central region ($z \approx 0$), but the strength reduces when z increases, making the electron path straighter and causing the electron to arrive earlier to the wire. The *r-t* relations are also determined separately for Endcap side A and C, although they are not expected to differ if the gas configuration stays the same.

Even though the t_0 and *r-t* relation are determined independently, a shift of the *r-t* relation along the time axis causes also a shift of the t_0 constant and the offset in t_0 leads to a change in the parameters of the *r-t* relation. This is shown in another parametrization of Eq. 47:

$$f(t) = a_0 + a_1 (t - b) + a_2 (t - b)^2 + a_3 (t - b)^3 \tag{49}$$

where b is a parameter changing the t_0 constant and therefore also affecting the *r-t* relation. In order to solve this ambiguity, a point of the *r-t* relation is fixed. As a compromise between correlations of different parameters and uncertainties, the fixed point was decided to be $f(t =$

18 ns) = 1 mm because it is in the middle of the straw and gives $f(t = 0\,\text{ns}) \approx 0\,\text{mm}$ for the straws filled with xenon [156].

Both the parameters obtained from the t_0 and r-t calibrations are stable for fixed run conditions. It is necessary to get as good r-t and t_0 calibrations as possible. If a bad calibration is used, there are various severe effects: a wrong drift circle radius is assigned to a hit, hence affecting tracking that uses drift circles. The position resolution will be degraded. The number of precision hits on track will be reduced, since the precision hits associated with the track are those where the drift circle radius is well matched to the track fit. A few hits might be even totally lost because the validity gate uses the t_0 calibrated drift time.

6.4.3 *Detector granularity*

Calibrations can be performed in various granularities from the whole TRT detector down to individual straws. However, finer granularity and thus more accurate description of the TRT comes with the cost of increasing computing time. To have good quality calibrations and fits, a certain minimum number of hits is needed: approximately 5000 hits for barrel and 1500 for endcaps [159]. The possible granularities in the offline calibration software to be used in calibrations to achieve this minimum level are

- Detector level, where either the whole detector or subdetectors can be used. The whole TRT calibrations use information from all the straws, whereas at subdetector level the information from straws is divided into four parts: barrel side A ($z > 0$) and C ($z < 0$), and endcap A and C.
- Layer level, which corresponds to modules in the barrel (in range 0-2 depending on the distance to the beam axis) and wheels in the end-cap (0-13) depending on the z coordinate.
- ϕ sector, where each endcap and barrel side are segmented into 32 equal ϕ slices. The ϕ slice 0 corresponds to zero degrees when looking onto side A.
- Straw layer, range of which depends on the detector layer in question. Straws are arranged in layers at approximately constant radius in the barrel and at the same z coordinate in the endcaps.
- Straw number, which is counted within a straw layer and therefore depends on the detector part.

For the simulation studies, it is often enough to perform calibrations on the layer level to achieve stable and good quality calibrations, whereas data is calibrated on a DTMROC chip level, where 16 straws are attached for read-out.

6.5 CALIBRATION OF SIMULATED DATA

Since the gas properties affect the drift time and thus calibrations, it is crucial to have accurate calibrations for all different gas configurations used during data taking. This section summarizes the setup and results of the r-t and t_0 calibrations done for three different simulated TRT gas geometries: all detector parts filled with argon (full argon geometry), and gas geometries used during 2015 and 2016 data taking. The following calibration studies have been performed using only Monte Carlo samples. More technical details together with exact simulation data tags and corresponding intervals of validity (IoV) are reported in Ref. [160]. I

was fortunate enough to calibrate also real data during full Run 2 data taking, both in proton–proton and heavy ion collisions. The same calibration principles hold also in data calibrations, and the detailed results are shown in Section 6.6.

6.5.1 *TRT in simulations*

The TRT, together with other ATLAS subdetectors, is carefully modelled using the GEANT4 simulation toolkit as described in Section 5.3. However, the GEANT4 package does not calculate energy deposits in a thin layer of gas in straw tubes precisely enough, and for this reason it was decided to calculate them during the digitization step instead. The TRT simulation contains a detailed model of many physics processes such as ionization of the gas molecules, cluster creation, as well as the signal propagation and shaping. The Photo Absorption and Ionization (PAI) model is used to calculate the ionization deposited by charged particles traversing a straw. The model creates a small number of ionization clusters, and computes the energy loss in each cluster based on the particle charge, mass and momentum. The drift time of each cluster is calculated using electron drift velocities, which are based on Garfield simulations [161] and depend on the magnetic field orientation. The time is also corrected to take into account the time of flight and signal propagation time. The straw signal is formed by recording the signal amplitudes and arrival times. The collected signal is amplified and then sent to the front-end electronics, where it is shaped and discriminated against low and high thresholds. The track coordinates are reconstructed making use of the *r-t* relationship as described earlier. In addition, the white-noise, originating from the thermal noise of capacitors in the front-end electronics or noise from the anode wire, is modelled to reproduce noise levels in the detector. Further discussion of the simulation model falls outside the scope of this paper, and more information can be found in Refs. [141, 146, 156].

6.5.2 *Full argon geometry*

Full argon geometry has argon in every part of the TRT detector. This geometry was used during 2015-2018 heavy ion data taking, and therefore corresponding simulated samples had to be created using good calibrations. As it is only meaningful to calibrate objects that are interesting for actual physics analyses, this calibration was performed using special STARLIGHT MC samples [162]. These samples were simulated to study especially two-photon and photon-pomeron scattering in heavy ion collisions. The used tracks were required to have $p_{\mathrm{T}} > 1\,\mathrm{GeV}$.

The position and time residual widths, object to minimization after iterations, are shown in Figure 36. The residual width is obtained from a Gaussian fit to the core of the distribution, where the fit was performed within $\pm 1.5\sigma$ around the mean in position residual distributions and within $\pm 1.0\sigma$ around the mean in the time residual distributions. Corresponding *r-t* relation plots are presented for barrel and endcaps in Figure 37.

The position resolution is 100-116 µm which is smaller than the usual resolution obtained from *pp* collisions. This is explained by a special configuration of the sample with zero pile-up and very little activity. There are no large differences in the residual widths between barrel and endcaps, as can be expected due to the fully symmetric geometry. The time residual mean converges around 0.5 ns which corresponds to the best position resolution. The shift comes from the asymmetric nature of the time residual distribution, and therefore the time residual distribution has a small offset from zero [159]. The tail of large time residual hits comes from tracks which traverse close to the wire, and generate hits with long drift times.

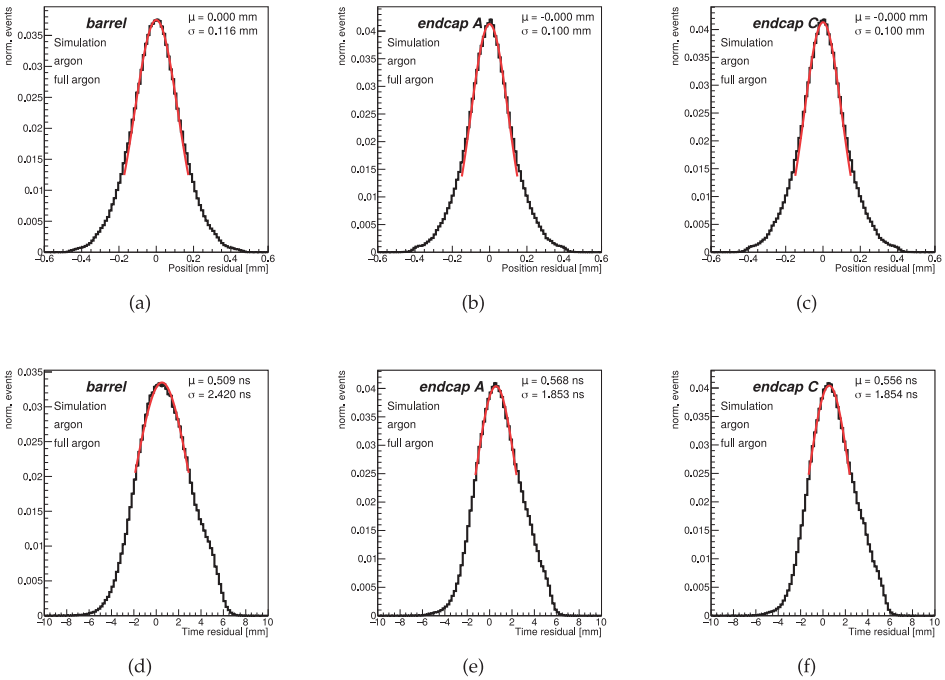

Figure 36: Resolutions obtained for the full argon gas geometry after calibration. Position resolution for (a) barrel, (b) endcap A, and (c) endcap C. Time resolution for (d) barrel, (e) endcap A, and (f) endcap C, respectively.

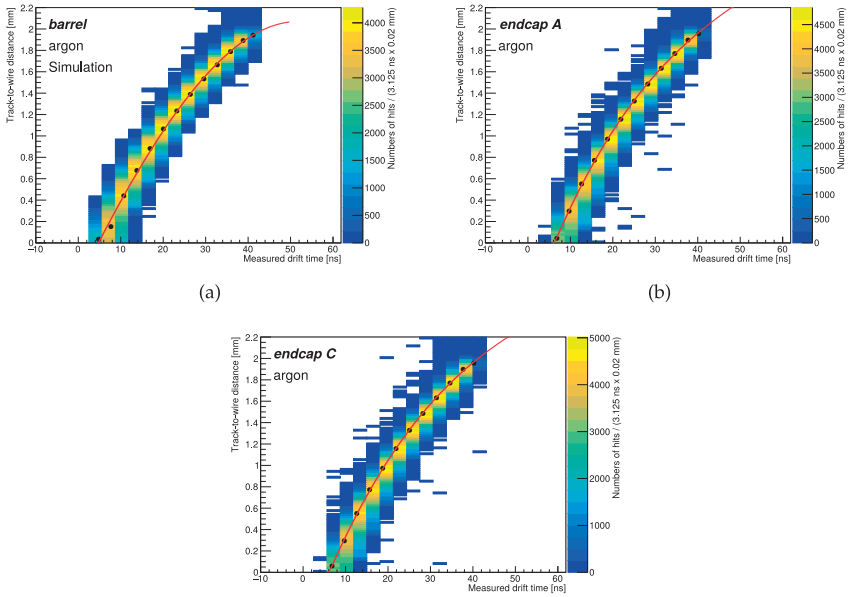

Figure 37: The *r-t* relations obtained for the full argon gas geometry for the (a) barrel, (b) endcap A, and and (c) endcap C.

As explained, the calibrations are performed in an iterative way. The first iteration was obtained with values of t_0 and *r-t* obtained from a global database, corresponding to *pp* collision runs with only xenon-based gas. The position residuals converge after a few iterations for both barrel and endcaps, as shown in Figure 38. As can be seen, the position residual widths decrease from 200-230 µm to 120 µm after only two iterations even in this extreme case where the gas geometry and therefore the calibration constants differ largely from the initial ones. To make sure the optimal resolution is obtained, more iterations were run. This demonstrates that the iterative calibration procedure works well: it converges to the optimal calibration constants leading to constant resolution.

The obtained calibration constants were uploaded to the global database (see Section 6.7 for details) and are used in all simulated heavy ion samples in Run 2.

6.5.3 *2016 geometry and tuning of low threshold*

The TRT gas geometry for 2016 has argon in barrel layers 0 and 1, endcap A layers 3 and 5, and endcap C layers 3, 5, and 8, and xenon in the rest of the layers (see Figure 26). Because five additional layers were filled with argon with respect to previous data taking year, a new set of calibrations were required in order to simulate the TRT performance accurately.

As the TRT operates now both in argon and xenon-based gas mixtures, it is important to match the simulated performance to the performance measured in real data. Section 6.2.3 described how the low and high thresholds are used to separate hits from minimum ionizing particles from those arising from transition radiation. Any change in low threshold and/or signal shaping requires a new set of t_0 and *r-t* calibrations. Indeed, the thresholds and signal

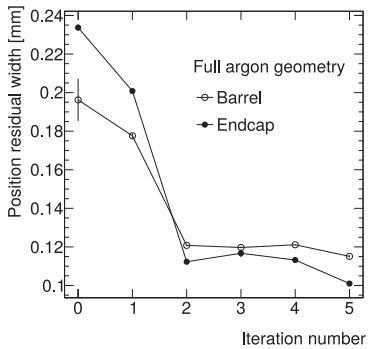

Figure 38: Improvement in position residual widths for TRT barrel and endcaps after iterations using full argon geometry in the TRT. Iteration 0 refers to the residual width obtained with the previous calibration results not optimized for the full argon geometry.

shaping in the digitization were carefully tuned within the TRT group [151] in order to have a good agreement between Monte Carlo and collision data. For this reason, in addition to obtaining the results with a new gas geometry, different argon LT settings were calibrated (70 eV, 150 eV, and 250 eV), while xenon LT remained unchanged for all studies.

The 70 eV low threshold tune for argon corresponds to the threshold in the front-end electronics set according to the noise occupancy requirements. Comparison between Monte Carlo and collision data revealed that the time-over-threshold was too large due to too early leading edge time in simulation. The leading edge time can be delayed by raising the low threshold, which decreases both the time-over-threshold and the trailing edge. However, the resolution degrades with increasing low threshold, and a compromise between MC/data agreement for the leading edge, the trailing edge, and the time-over-threshold has to be made while maintaining a satisfying position resolution. After tuning and calibrations, the low threshold was set to 150 eV so that the resolution is acceptable and a good agreement between Monte Carlo data simulated with POWHEG +PYTHIA 8 and collision data is found, as shown in Figure 39. In some cases, the simulation predicts better accuracy than observed in data, which is likely to be due to mismodelling of some parameters for the Ar-based mixture.

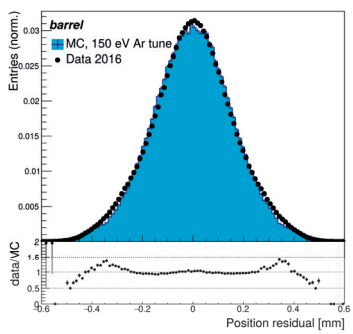

Figure 39: Position residual distribution for the Ar-based barrel straws for data and simulation using the 150 eV argon low threshold setting after t_0 and r-t calibrations. The width of the fit is $\sigma_{\text{data}} = 0.148$ mm for data and $\sigma_{\text{MC}} = 0.146$ mm for a simulated sample.

The track selection used in the calibration is very loose in order to maximize the available statistics. The track p_T is required to be larger than 2 GeV and the track must have at least 8 hits in the silicon detectors and at leat 20 hits in the TRT. The impact parameters are required to be $|z_0| < 300$ mm and $|d_0| < 300$ mm. The resulting residual distributions obtained after t_0 and *r-t* calibrations for each of the low threshold settings in 2016 geometry are shown in the following.

6.5.3.1 70 eV *argon tune*

The low threshold of 70 eV corresponds to the threshold in the front-end electronics. Results after iterations for the 70 eV LT tune and 2016 geometry are shown in Figure 40 for argon regions and in Figure 41 for xenon regions.

The position resolution varies from 115 µm in the edcaps to 128 µm in the barrel for straws filled with argon, and similar results are obtained for the straws filled with xenon: about 120 µm in the endcaps, and 128 µm in the barrel. The time residual mean is around 0.9 ns in the argon straws, which is slightly larger than the obtained value of 0.5 ns earlier and arises from the pronounced tail of large time residual hits. As the low threshold is not tuned for xenon-based gas mixtures, the position residuals do not drastically change and the results with xenon are not shown further.

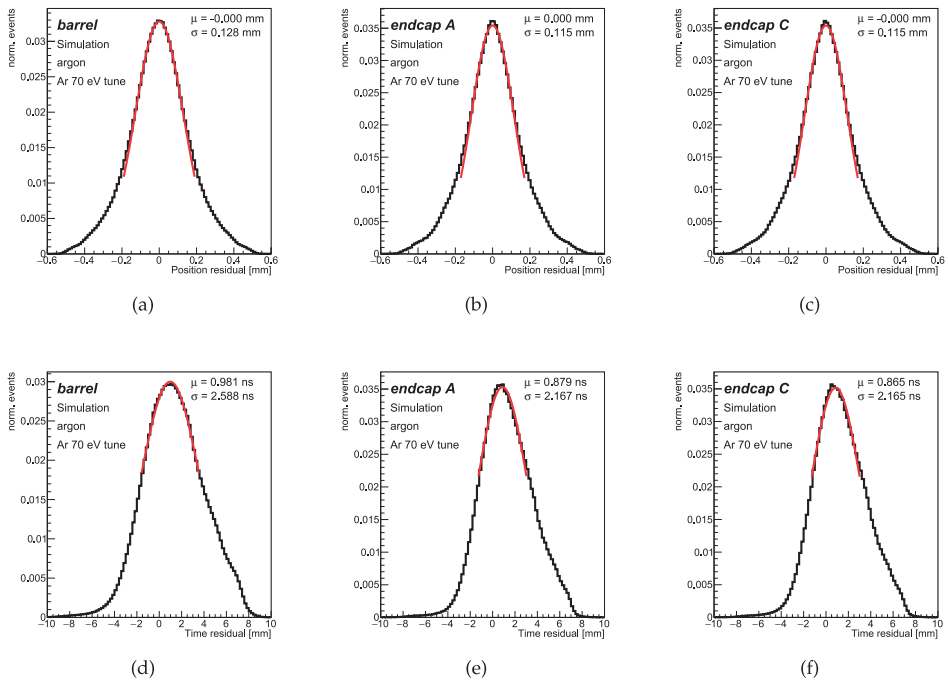

Figure 40: Position resolutions obtained in straws filled with argon in the 2016 gas geometry and the LT argon tune of 70 eV after calibration shown for (a) barrel, (b) endcap A, and (c) endcap C. Time resolution are shown for (d) barrel, (e) endcap A, and (f) endcap C, respectively.

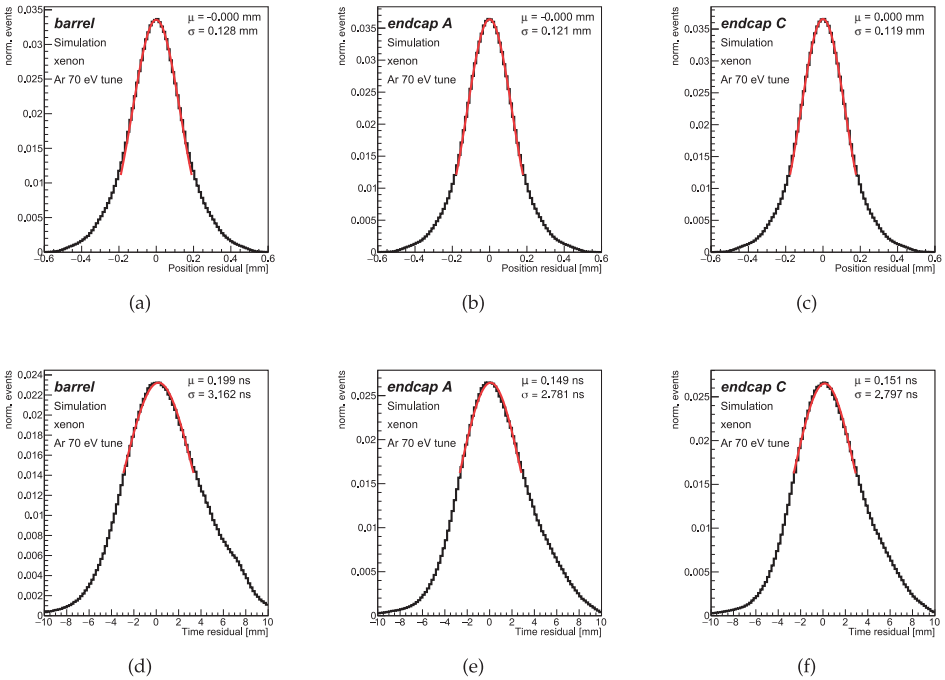

Figure 41: Position resolutions obtained in straws filled with xenon in the 2016 gas geometry and the LT argon tune of 70 eV after calibration for (a) barrel, (b) endcap A, and (c) endcap C. Time resolution are shown for (d) barrel, (e) endcap A, and (f) endcap C, respectively.

6.5.3.2 150 eV *argon tune*

The low threshold was increased to 150 eV keeping the gas geometry the same corresponding to 2016 data taking geometry. Results after iterations are shown in Figure 42 for the straws filled with the argon-based gas mixture. As can be seen, raising the threshold decreases the position resolution by roughly 20 µm to 135 µm in the endcaps and to 146 µm in the barrel region. These results generally correspond the measured position resolution in the collision data, and were also updated to the global database to be used in the simulations corresponding to data taking periods in 2016-2018.

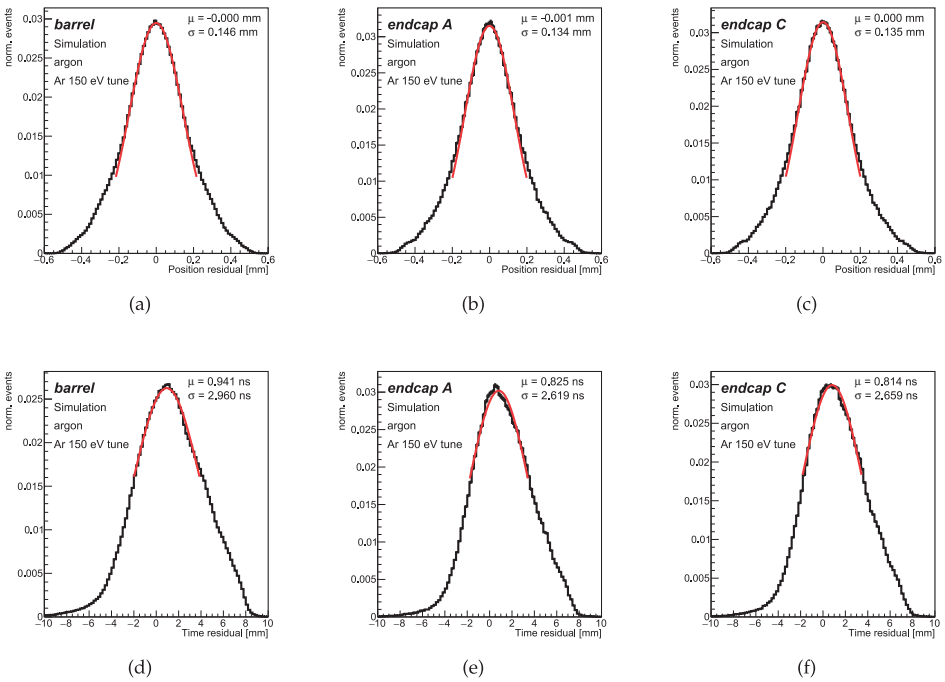

Figure 42: Position resolutions obtained in straws filled with argon in the 2016 gas geometry and the LT argon tune of 150 eV after calibration for (a) barrel, (b) endcap A, and (c) endcap C.

6.5.3.3 250 eV *argon tune*

Last, the low threshold was increased by 100 eV to 250 eV. Results after iterations are shown in Figure 43 for the straws filled with the argon-based gas mixture, and show clearly that raising the threshold further decreases the position resolution by about 10 µm to 146-148 µm in the endcaps and to 154 µm in the barrel region. These results indicate that a compromise between an excellent MC/data agreement for the leading edge, the trailing edge, and the time-over-threshold has to be made for having a satisfying position resolution. In general, the position resolution is thought to be acceptable if it is less than 150 eV in all detector parts.

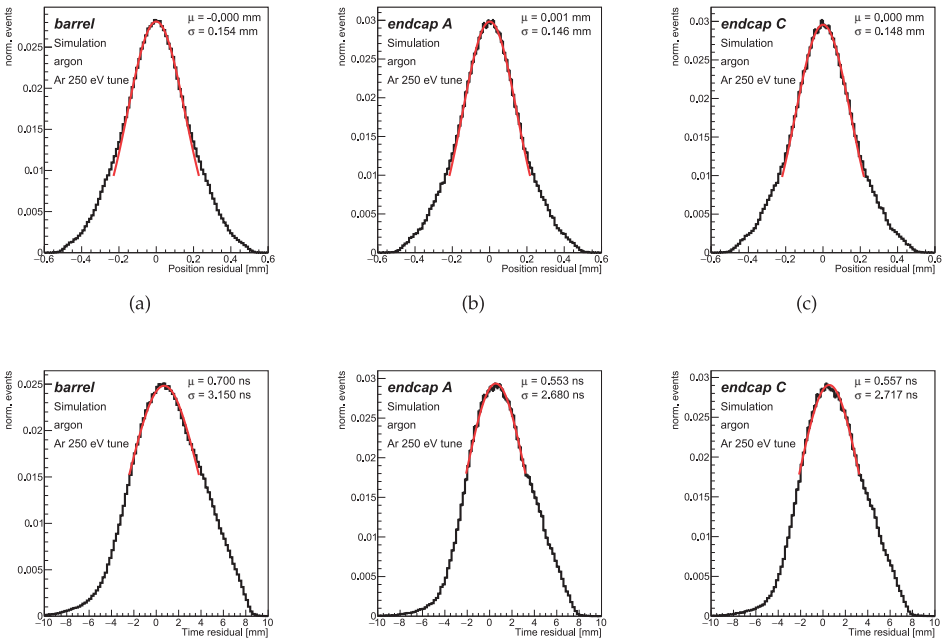

Figure 43: Position resolutions obtained in straws filled with argon in the 2016 gas geometry and the LT argon tune of 250 eV after calibration for (a) barrel, (b) endcap A, and (c) endcap C.

6.5.4 *2015 geometry*

The 2015 gas geometry was used during 2015 proton–proton data taking, and it has argon in barrel layer 0 (B0), endcap side C wheel 3 (EC3), and endcap side A wheel 5 (EA5). All other layers and wheels are filled with xenon, as illustrated in Figure 26. This calibration on simulated data was performed in 2016 to study the effect of tuning the argon Low Threshold (LT) level, where the threshold was set to 150 eV. Results of the 150 eV argon tune for 2015 geometry are shown in Figure 44 for parts of the TRT filled with the argon-based gas mixture, leading to position resolution of 140 mm in the barrel, 136 mm in the endcap side A and 132 mm in the endcap side C. Small differences in the endcap resolutions do not affect tracking quality, and can be expected due to asymmetric gas geometry in the endcaps. These results also correspond to the calibrated results for the 2016 gas geometry with the same low threshold setting of 150 eV, as presented in Section 6.5.3.2.

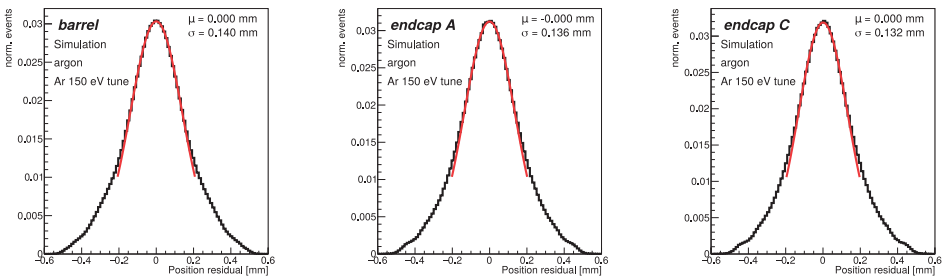

(a) (b) (c)

Figure 44: Position resolutions obtained for the 2015 gas geometry and the LT argon tune of 150 eV after calibration for (a) barrel, (b) endcap A, and (c) endcap C.

6.5.5 *Effect on the track selection*

Tracking relies on the performance of the whole Inner Detector. In order to have high reconstruction efficiency and low fake track rate, common track quality working points have been derived centrally. These working points implement different selection requirements on number of hits and holes in ID subdetectors as well as cuts on χ^2/ndof for the reconstructed tracks. Altering certain cuts, such as the number of shared hits, has been shown to affect the overall track reconstruction significantly, especially in dense environments with TeV-scale jets [163].

There is an interplay between good quality tracks and the overall available statistics in the TRT. For this reason, the impact of various track selections in the TRT calibrations was studied. Using the 2016 TRT geometry with 150 eV argon tune, two sets of simulated samples were created: loose selection with no requirements on the number of hits in the pixel and SCT detectors, and a slightly tighter selection with at least 2 hits in the pixel detector and at least 6 hits in the SCT [7]. However, there was no significant difference in obtained resolution between those two selection criteria. Tracks used in physics analyses will however usually have more stringent cuts, and especially higher transverse momenta, for which reason the study on different momentum cuts was performed.

7 Note: these do not correspond to the centrally derived working points "Loose" and "Tight"!

The selection criteria of the transverse momentum, in short p_T, can have a huge effect for both tracking and calibration. Large-p_T particles have straighter tracks whereas low-p_T particles get bent so much in the magnetic field that their tracks curl up inside the detector. The multiple scattering increases when the particles have lower momentum, which is important to take into account as the scattering of particles in the detector material deteriorates the measured results. For particles with higher momenta, the time-of-flight decreases and shorter drift times will be measured. In addition, particles with larger momentum deposit more energy and therefore create higher signals [156]. As mentioned in Section 6.2.3, the particle will exceed the low threshold sooner, producing shorter measured drift times.

To study the effect of varying the transverse momentum, different threshold requirements of p_T were applied for a simulated 2016 geometry sample using the low threshold tune of 150 eV for argon. The position residual width σ_p as a function of the p_T of the track is shown in Figure 45 for both argon and xenon straws. This study is statistically limited at higher momenta, but the residual widths decrease for high-p_T particles as expected due to a reduced amount of multiple scattering and increasing ionization.

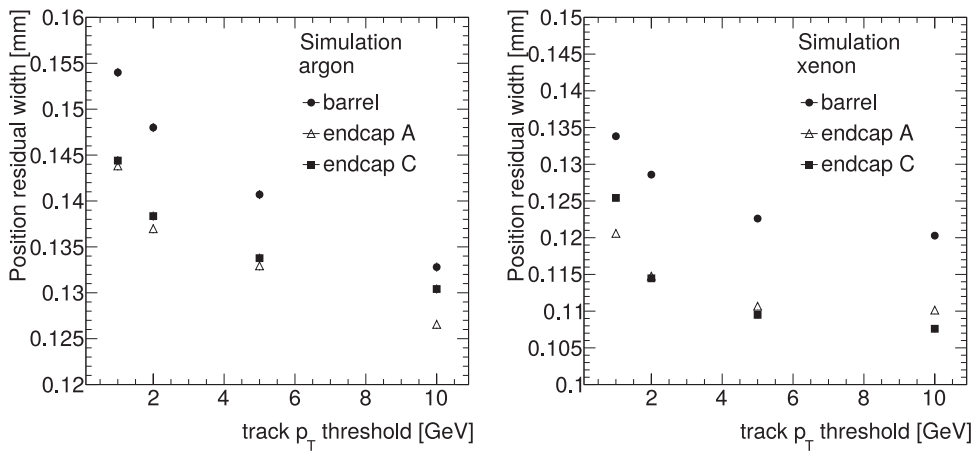

(a) (b)

Figure 45: Position residuals widths for different p_T threshold cuts in a simulated sample with the 150 eV argon tune, for (a) argon and (b) xenon straws.

6.5.6 *Accuracy of t_0 constants*

The t_0 and *r-t* calibrations form an iterative process, where the detector performance is evaluated after each round of iteration. The final aim of the calibration is to obtain the best possible detector resolution, where the calibration constants do not vary much and the fits are stable leading to the minimal residual widths. By choosing different values of t_0 calibration constants and studying which shift gives the most narrow residual widths, we can see if the calibration works in an optimal way and how much an overall time shift affects the resolution.

In order to confirm that the derived calibration indeed leads to minimum residual widths, the obtained t_0 calibration constants were systematically shifted by ± 3 ns in steps of 0.1-0.25 ns and new data samples were fully reconstructed with these shifted constants. The *r-t* values stay constant during the procedure.

Figure 46 illustrates the resulting position residual width distribution as a function of the shifted t_0 values, obtained using the 2016 gas geometry and argon 150 eV LT tune. There is a shallow minimum around the ideal values of t_0 . When t_0 values are shifted with respect to the original t_0 values from the calibration, the position residual widths change from 0.12 mm to 0.21 mm in xenon straws and from 0.13 mm up to 0.24 mm in argon straws. The width has a clear sensitivity even to small changes in t_0 of $\pm$0.1 ns. If the t_0 is shifted by 1 ns around the minimal residual, the residual width can be even 15 µm worse. Conversely, by obtaining the ideal t_0 values from calibration, the minimum position resolution can be reached.

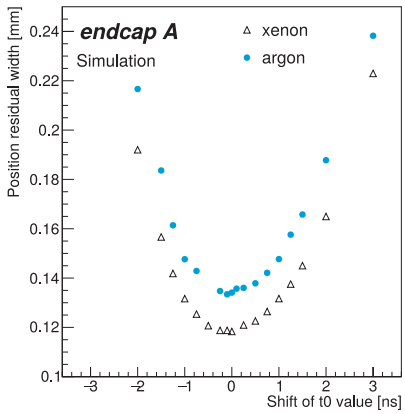

Figure 46: Position residual width as a function of shifted t_0 values, shown for endcap A.

6.5.7 *Summary and outlook*

Track reconstruction in the TRT requires knowing the track-to-wire distance for each hit. In order to get the best momentum resolution on the tracks, there are two quantities that need to be calibrated: t_0 constant and *r-t* relation. This section described the calibration procedure of t_0 constant and *r-t* relation for simulated data. The calibration was performed for different gas geometries. In the so-called full argon geometry, the whole TRT detector is filled with only the argon-based gas mixture. This geometry was used in heavy-ion runs during full Run 2, and is considered to be one option for Run 3 operations if the TRT gas leaks continue. For the first time, calibration constants for the full argon geometry were calculated, and a very good detector resolution of less than 120 µm can be reached in events with low activity also in the argon-based gas mixture, which confirms that the gas mixture is well suitable for tracking purposes. The obtained *r-t* and t_0 calibration constants were updated in the global conditions database, and are used in MC16 heavy ion simulations.

As the gas leaks continued to develop in various parts of the TRT, in total seven layers of the TRT were operated with the argon-based gas mixture during 2016-2018 *pp* collisions, which called for new calibrations to match the gas configuration. The low threshold of the argon-based gas mixture was tuned in order to have a good agreement between Monte Carlo and collision data in t_{LE} , t_{TE} , t_{ToT} and position residual width distributions. Any low threshold or signal shaping change requires a set of new t_0 and *r-t* calibrations, and therefore simulated samples with argon LT settings from 70 eV to 250 eV were calibrated using the 2016 gas

geometry. After careful tuning and calibrations, the low threshold was set to 150 eV so that the resolution is 135-146 µm in all TRT regions for low-p_T tracks, resulting in a very good MC/data agreement.

In the advent of the ATLAS software Athena Release 21, the Inner Detector conditions were frozen already in September 2016 - well before any of the actual physics analysis started with the release. Release 21 is the release used for the rest of the Run 2 data taking in all reconstruction and analysis tasks, while Release 22 will only be used during long shutdown 2 (LS2) starting in 2018. As there were no reprocessing of the data in 2017, release 21 was planned to be used at the Tier-0 in both 2017 and 2018. All detector conditions, including the best knowledge of t_0 and r-t calibrations over various scenarios, for the coming two years were required to be ready in September 2016. The presented results entered the database in time.

It is worth mentioning that in some cases, the simulation predicts better accuracy and resolution than observed in data, which is likely to be due to mismodelling of some parameters for the argon-based mixture. A lot of effort has been put in understanding if the magnetic field orientation alone can explain the differences observed between different TRT parts. Furthermore, a few bugs related to the drift circle definition have been fixed, the argon signal shape has been further tuned, and additional time-over-threshold and high threshold corrections are being studied by various people within the TRT group. These simulation studies ensure that the TRT can provide the best possible tracking performance despite the gas leaks and ever-increasing luminosity in Run 3.

Another significant aspect of the calibrations is of course the performance in real collision data. This will be the topic in the next section.

6.6 COLLISION DATA QUALITY AND CALIBRATION

During Run 2 in 2015-2018, ATLAS recorded a total integrated luminosity of 149 fb^{-1} pp collision data of which roughly 95% are good for physics analysis. The quality of the collected dataset is carefully evaluated to understand and eliminate any detector-related problems. The TRT detector performed very well despite the gas leaks and challenging environment due to pile-up and high occupancy. Overall, it significantly contributed to the ATLAS tracking and electron identification.

As motivated earlier, drift time calibrations form an important part of data preparation: if the calibrated time has an offset of even order of nanoseconds, it affects the detector resolution and therefore the whole tracking performance. This section summarizes calibrations done using real collision data during Run 2, and concentrates especially on the impact of using the argon-based gas mixture. Section 6.6.1 starts by introducing how the data quality is evaluated for the TRT before the calibration results and obtained tracking performance for pp collisions are shown in Section 6.6.2. Corresponding results obtained from heavy ion data are reported in Section 6.6.5. The best knowledge of the TRT conditions is stored in a global conditions database as outlined in Section 6.7. The databases bookkeep the status of each individual channel at all times: which detector parts are working, which are noisy or dead, and which r−t relationship they obey. Finally, Section 6.8 summary of the whole chapter is given.

6.6.1 *Data quality monitoring*

The data coming from the Event Filter see Section 5.2) is recorded in various *streams*, each of which is defined with dedicated trigger menus [164]:

- The physics streams. The main physics stream (`physics_Main`) with a rate of 1.3-1.4 kHz in 2018 is suitable for data analysis, and it focuses on specific final state objects and event topologies.
- The calibration streams contain specific events for various subdetectors, and are used for computing many alignment and calibration constants.
- The express streams are processed very rapidly and used for data quality and monitoring. They contain only a small subset of data corresponding to ~ 20 Hz with all types of events so that the data quality can be effectively monitored. In other words, they allow almost real-time assessment of how usable the data for each subdetector is. The data are reconstructed almost real time and the aim is to obtain results before the main reconstruction starts.

The TRT data quality is continuously assessed by monitoring a large set of different distributions during data taking periods. A small fraction of the data is evaluated online nearly real-time, and the final decision on the goodness of the data quality is made after full processing of the run.

The TRT data quality evaluation is based on the `express_express` and `physics_Main` streams. Since calibration and express streams are required for evaluating data quality and further reconstruction of physics data, they are processed during the express processing (ES1) launched shortly after the beginning of the run. At the same time, several monitoring histograms are produced using the Athena monitoring framework and the results are displayed on a central ATLAS monitoring website. These histograms are automatically checked by the TRT monitoring software and various algorithms, and the run data are compared with reference runs, which are being updated if run conditions change significantly. After the checks, the distributions are flagged to green, yellow and red corresponding to good, moderate and bad, depending on their quality. The most critical distributions to be monitored with the TRT are the leading and trailing edge distributions, as they can reveal problems in the gas mixture or timing. Similarly, the position and time residual widths indicate possible miscalibrations. Evaluating average detector occupancy for low and high threshold hits can help find issues with the gas mixture or front-end electronics. [164]

After each run, dedicated calibration jobs are automatically processed at Tier-0. As a result, a list of dead or inefficient straws together with position and time residual width distributions and a new set of t_0 and *r-t* curves are produced. The calibration corrects the small daily variations of the leading edge times of the signal. The TRT experts can also manually launch calibration jobs to fix large position resolutions or to correct any time offset. The t_0 and *r-t* calibration constants are updated every time when the time offset is larger than 0.3 ns, usually caused by a slow shift of the LHC clock, which happens from once a week to once a month during data taking.

If any problem affects the data quality, the TRT offline and expert shifters assign a *a defect* to the corresponding lumiblocks and save it in a dedicated conditions database. Such defects can be either intolerable, indicating a severe problem affecting the data quality, or tolerable, implying a minor problem while data are still adequately good to be used in physics analysis.

The new calibration constants and all other condition updates in ATLAS have to be updated within 48 hours in a so-called calibration loop, during which the new calibration constants can be updated for further bulk processing. The bulk processing generated with the `physics_Main` stream uses the new calibrations and contains all the physics events for each run, leading to improved resolution and higher efficiencies compared to the express stream.

The TRT data quality was very good during the whole Run 2 data taking period. In fact, in 2018 no data was flagged with intolerable defects which mean 100% efficient and good

data. Most of the problems arose with ROD patch panels, which require one or more RODs to be totally excluded from data taking causing sectors with absence of recorded data. Other problems come from the high voltage or the gas mixture that cause reduced hit efficiencies. Typically such problems affect only some parts of the detector and can be recovered.

6.6.2 *Data calibration*

Good calibrations are of the utmost importance for the tracking performance. The t_0 and *r-t* calibration principles applied in data are the same as described for simulated data in Section 6.4. However, calibrations are performed automatically after each run, and in case of problems they can also be manually calibrated just as simulated data. After calibrating the drift time for each run, it is important to evaluate how the calibrations affect the data quality. As mentioned, time and position residual distributions are used to spot problems with the calibration, and thus they are the key distributions to look at when evaluating the data quality.

Figure 47 clearly illustrates the power of calibrations. It shows the position resolution in straws filled with xenon recorded in a *pp* run in 2017 before and after t_0 and *r-t* calibrations. The resolution can be improved by up to 40 µm if the running conditions have drastically changed between runs for example due to changes in the gas properties.

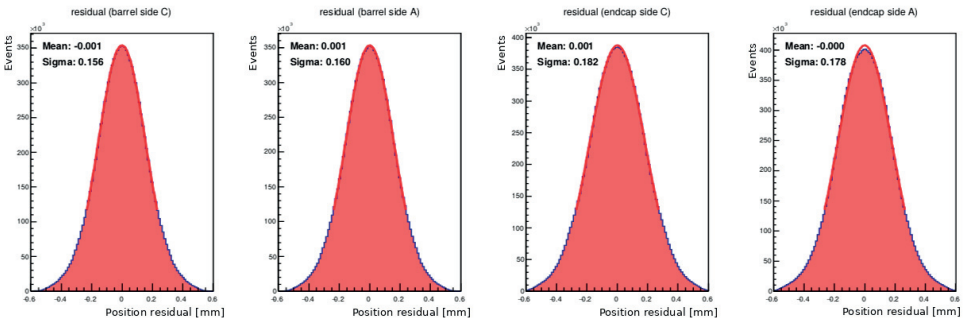

(a)

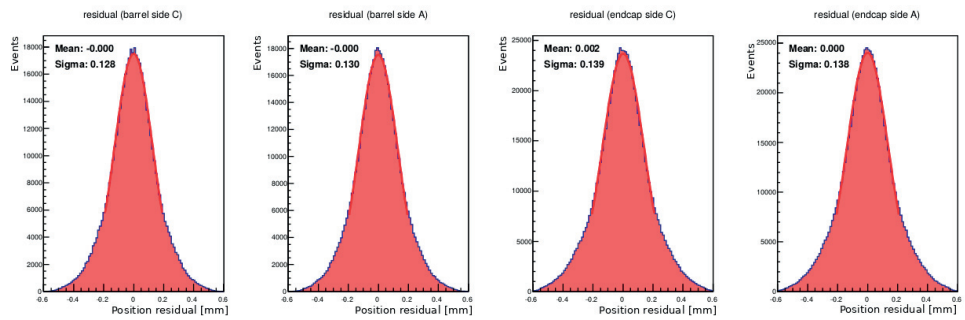

(b)

Figure 47: Example of a *pp* run recorded in 2017 (a) before and (b) after t_0 and *r-t* calibrations.

6.6.2.1 *Updating web display*

The shifter evaluates the data quality partly based on the histograms presented in a web display, where the current run to be evaluated is shown together with a good-quality reference run. In the *r-t* relation plots, the web display overlays an additional reference line showing a fixed calibration. In order to have a good reference line in such plots distinguishing barrel from endcap and argon from xenon straws, the *r-t* constants were compared in 32 data runs (357193-358985) in 2018. Figure 48 shows the *r-t* curves calibrated for those runs together with a curve obtained from the mean of the curves, and a curve using the old fixed value from the web display. Unlike the old reference line, both argon and xenon mean curves cross at the fixed point $r = 1\,\text{mm}, t = 18\,\text{ns}$ indicated with dashed lines, showing a clear difference between drift times in two gas mixtures. We can also see that the curves do not deviate significantly from run to run which implies stable calibrations. The small deviations at larger drift time values are more visible in parts filled with argon. As a conclusion, the mean value of these *r-t* relations was picked for argon and xenon separately, and updated to the web display, improving the agreement between the runs evaluated and the reference runs.

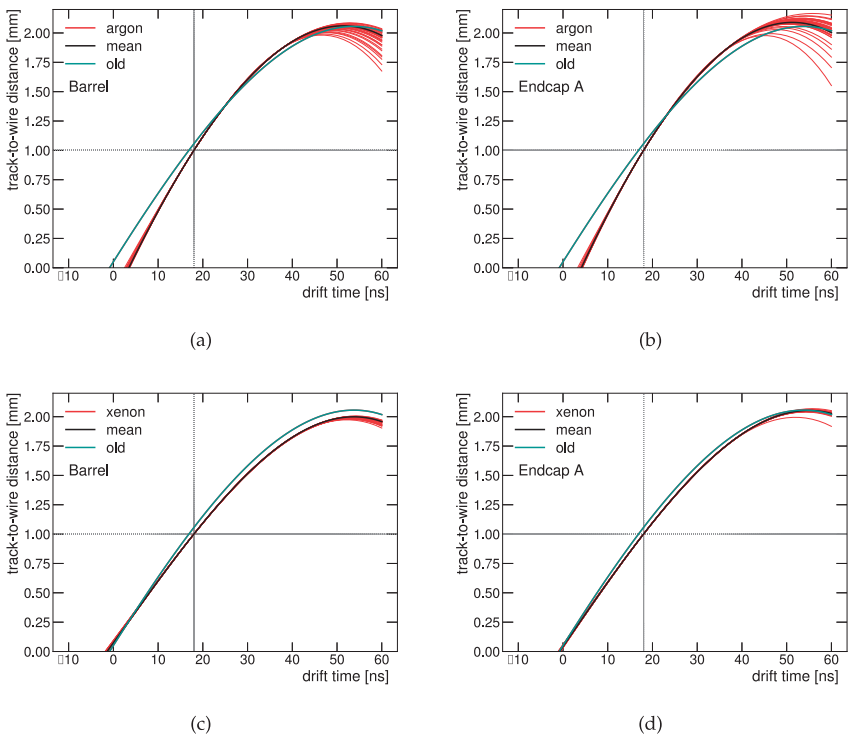

Figure 48: The *r-t* relations calibrated for runs 357193-358985 (red lines) together with a curve obtained from the mean of the curves (black line), and a curve using the old fixed value from the web display (green line). The dashed lines indicate the fixed reference point. Shown (a) argon straws in the barrel, (a) argon straws in the endcap A, (c) xenon straws in the barrel, and (c) xenon straws in the endcap A.

6.6.3 *Geometrical effects on tracking*

The TRT is divided into barrel and endcap regions, which differ by having different gas mixtures, as well as straw and magnetic field orientation. Furthermore, the occupancy (the fraction of straws with hits) varies based on the distance from the interaction point. The highest occupancies are measured with the parts of the TRT that are closest to the beam pipe where the track density is high; conversely, the outermost barrel layers have the lowest occupancy as the particle density falls with the distance from the interaction point. All these factors affect the tracking performance, which is usually quoted for a single detector part independently. To illustrate these factors, Figure 49 shows position resolution and number of hits in different detector parts with a track selection where $p_{\mathrm{T}} > 1\,\mathrm{GeV}$ and $|d_0| < 20\,\mathrm{mm}$. Figure 49a shows the position resolution in wheels filled with xenon in endcap A, represented in $z - \phi$ plane where the detector layer index increases with increasing z. The gaps indicate that the layer is filled with argon instead. It can be seen that the performance is similar over different ϕ sectors as expected from the detector geometry.

The position resolution depends strongly on the position of the endcap wheel, being better in the innermost endcap wheels closer to the interaction point. Small degradations of the position resolution may be observed in small z, because the tracks crossing the first wheels have hits both in the barrel and endcap in the region $0.625 < |\eta| < 1.070$, which reduces the number of hits on the track. Moreover, the front-end electronics of the barrels are located in this region, increasing the material the particles have to cross and therefore causing multiple scattering [156]. These effects are more visible if looked at the chip level rather than the entire layer level. With larger z, the tracks consist only of hits recorded in the endcaps, which improves the resolution. After $z > 1740\,\mathrm{mm}$ the straw distance in type B wheels is larger than in in type A wheels, which increases the material budget and therefore the risk of multiple scattering. The number of hits on track is also reduced, which increases the resolution width at the outer layers in the endcaps.

Figure 49b shows the position residual width in the outermost barrel layer in straws filled with the xenon-based gas mixture. Two lower layers are filled with argon and therefore not shown. Each dot corresponds to a DTMROC chip, presented in the $x - y$ plane. In a similar way, Figure 49c shows the number of hits in the same xenon layer in the barrel, illustrating how there are many more hits closer to the interaction point.

6.6.4 *Dependence on number of interactions per bunch crossing*

The position residual distribution depends on the occupancy, t_0 calibrations, and to some extent also on the quality of the track selection. It also depends on the number of interactions per bunch crossing which is closely related to the detector occupancy. A denser environment with higher pile-up yields to larger residual widths as tracking gets more and more challenging with increasing pile-up. An additional complication comes from the shadowing effect, where the background hits affect the leading edge time: if a background track crosses the straw closer to the wire than the particle of interest, the leading edge time becomes earlier than the real one, and the time measurement for the later real hit is not recorded. These background hits give wrong drift circle measurements, causing the total number of precision hits to decrease with increasing occupancy.

Figure 50 shows position residual width as a function of $\langle\mu\rangle$ for the TRT barrel in the proton–proton run 350923 recorded in 2018 for xenon and argon straws. A similar trend can be seen in all TRT detector parts and runs during Run 2. The position resolution increases with increasing $\langle\mu\rangle$ which is expected, and varies from 140 µm to 169 µm in straws filled with

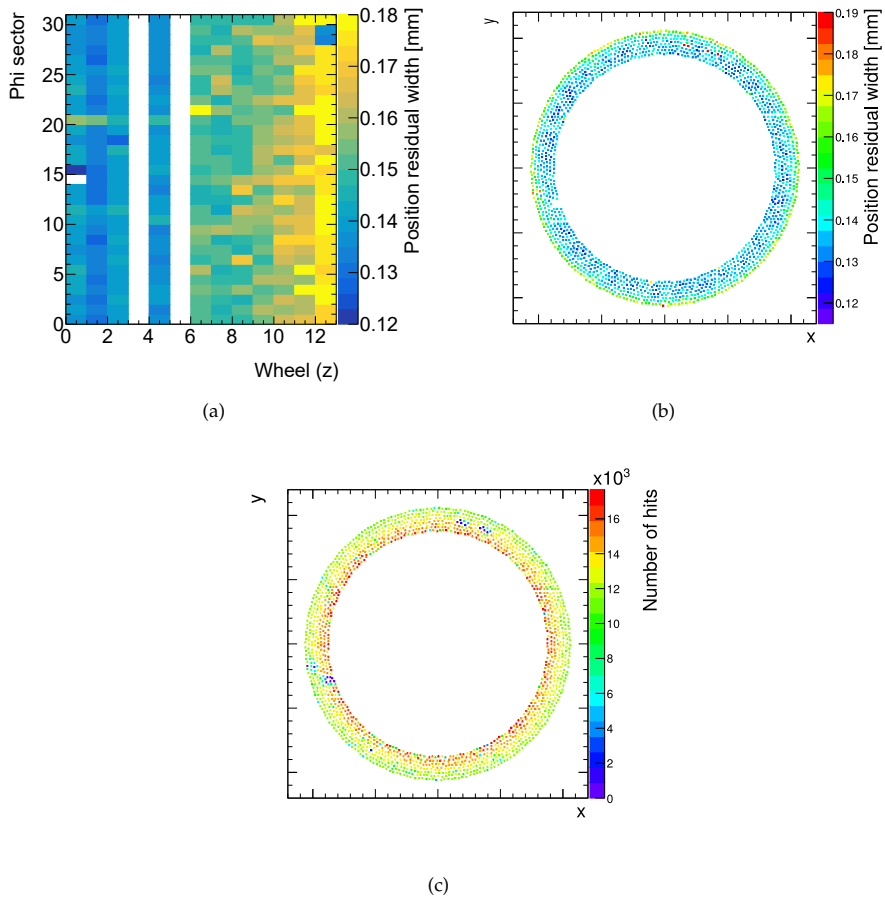

Figure 49: Example of position resolutions obtained from pp data in 2018 (a) as a function of detector layer with increasing z, shown for wheels filled with xenon in endcap A, (b) barrel layer, shown for straws filled with xenon in outer layer of the barrel. In addition, (c) number of hits shown for straws filled with xenon in outer layer of the barrel is shown. Selected tracks have $p_{\mathrm{T}} > 1\,\mathrm{GeV}$ and $|d_0| < 20\,\mathrm{mm}$.

argon, and from 132 µm up to 160 µm in straws filled with xenon. As can be seen, the position residual width is smaller in straws filled with xenon. This can be explained by the fact that the layers filled with xenon in the TRT barrel are located at the outermost layers at large R, thus expected to have less hits and less distorting occupancy from pile-up. The difference between two gas mixtures is, however, less than 10 µm over a wide range of $\langle\mu\rangle$ values. Furthermore, the width of the residual distributions are expected to be larger than the intrinsic accuracy per hit due to the loose track selection applied ($p_{\mathrm{T}} > 2\,\mathrm{GeV}$, at least 8 silicon hits, at least 15 TRT hits). As a minimum number of pixel and SCT hits is low, many of the tracks passing the criteria can be worse-quality TRT standalone tracks affecting the residuals. It should be also emphasized that Figure 50 is obtained using only one run which covers a wide $\langle\mu\rangle$ range. Individual runs at relatively small high or low $\langle\mu\rangle$ range can yield much better residuals, thanks to calibrations and other machine conditions.

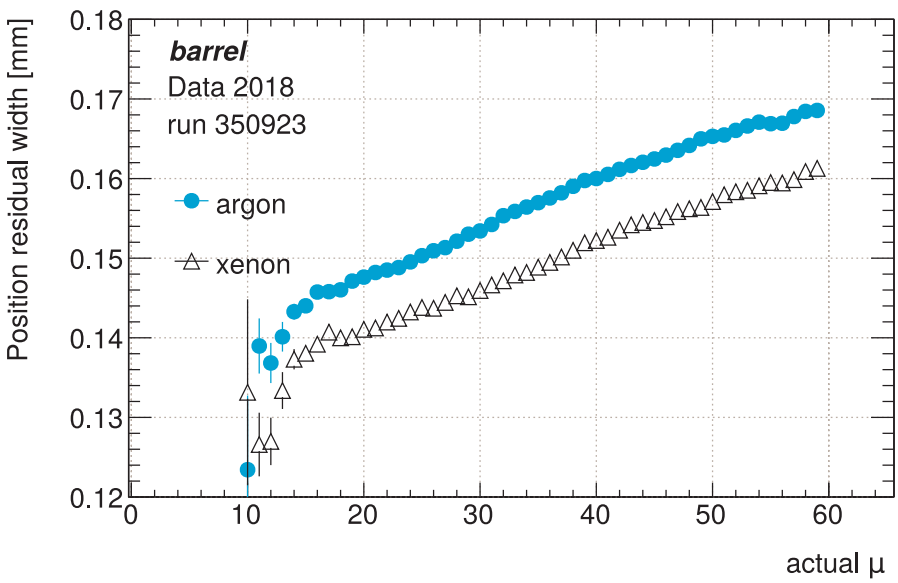

Figure 50: Position residual width in the TRT barrel as a function of actual interactions per bunch crossing in the pp run 350923.

6.6.5 *Heavy ion runs*

In addition to protons, the LHC has successfully collided heavy ions during Run 2. At the end of the each year's data taking, proton–lead and lead–lead beams collided at the centre-of-mass energy of 5.02-8.16 TeV. There was also a special Xe–Xe run at the energy 5.44 TeV per nucleon pair in 2017. For the heavy ion runs, the TRT was turned to operate only with argon-based gas mixture. The calibration works in the same way as in the proton-proton collisions, but comes with a limitation in the detector occupancy.

Centrality of the heavy ion collisions is illustrated in Figure 51: smaller the centrality, more head-on the heavy ions collide. For very central heavy ion collisions, the TRT occupancies rise up to 90%, making it very challenging to maintain good position resolution and tracking performance. The track quality of such busy events is less optimal. With such huge track density,

a lot of computing power is needed for pattern recognition. However, calibrating such events within a calibration loop is not possible with resources available, as the first accumulation step already takes more than a day. For these reasons, during the 2018 heavy ion data taking it was decided to look at the so-called `physics_UPC` stream (Ultra-Peripheral Collisions) instead of the `physics_HardProbe` stream. The stream containing hard probes includes events where the centrality is low, which means that the centers of the colliding ions do not have large offsets and the ions collide close to head on. Hard probe events are usually very busy: the multiplicity of charged tracks is higher and for this reason tracking is more difficult.

The `physics_UPC` stream contains soft collisions where the two colliding heavy ions hit with a glancing blow: in other words, they have high centrality meaning that the centers of the ions are widely offset and the collision is not head on, as can be seen in Figure 51. In this case, the multiplicity of charged tracks is low, there are more forward events, and the TRT and tracking work well giving good residual measurements. When the TRT is well calibrated, residuals in the `physics_UPC` stream are very good and resemble proton-proton events. This is shown in Figure 52, where an example of position resolution measured in a heavy ion recorded in 2018 is presented, resulting in $\sigma_p \approx 140\,\mu\text{m}$ across the detector.

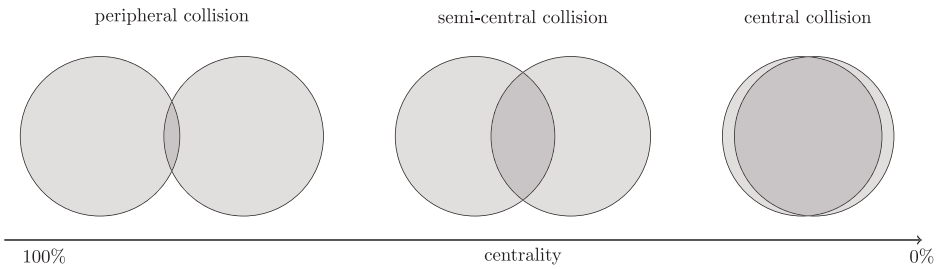

Figure 51: Centrality of the collisions

Figure 53 shows the *r-t* relation for the same run. As visible in Figure 53b, the *r-t* relation does not vary much between different detector parts in the gas configuration where all the detector parts are filled with the argon-based gas mixture. The drift time in barrel is slightly lower than in the endcaps due to the magnetic field orientation and strength, as explained in Section 6.4.2.

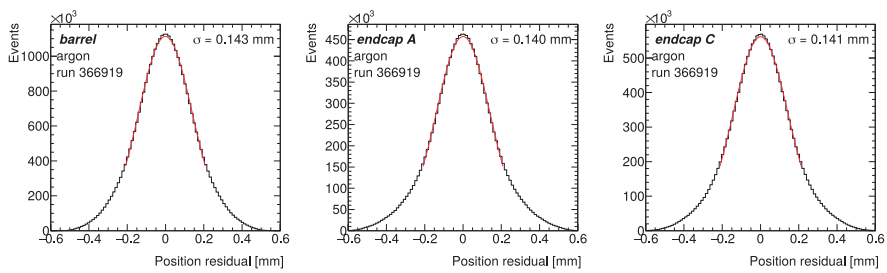

Figure 52: Position resolution in heavy ion run 366919 in various detector parts. The TRT was filled only with the argon-based gas mixture.

Despite a few technical problems related to the start of the automatic calibrations and configuring the detector to operate fully with argon on the software side, the data quality

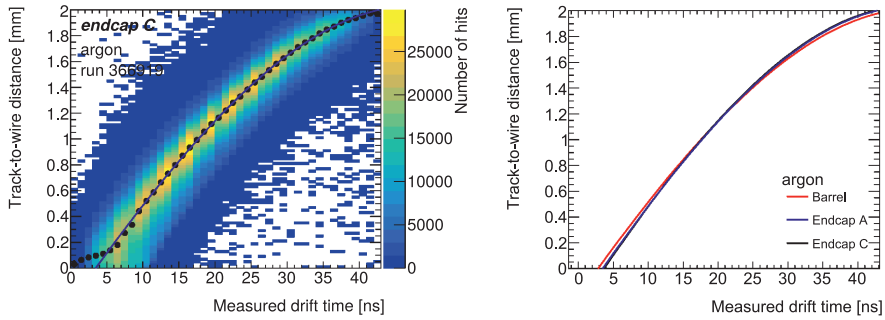

(a) (b)

Figure 53: The *r-t* relation in heavy ion run 366919, shown for (a) in endcap C only, and (b) all detector parts.

was excellent in both heavy ion and *pp* runs during Run 2. One of the highlights of the ATLAS heavy ion data taking is the observation of light-by-light scattering in ultra-peripheral Pb+Pb collisions [165], which may have remained unobserved if some parts of the detectors flagged runs with intolerable defects.

6.7 CONFIGURATION AND CONDITION DATABASE

In order to gather the best knowledge of the TRT detector, it is important to record its status straw-by-straw at all times: which detector parts are functioning and which are dead or noisy, what is the *r-t* relationship and the gas configuration, etc. The ATLAS experiment has two database systems to store such information: a configuration database and a conditions database [111]. The configuration database stores information on the detector hardware and software configurations and on detector control, trigger and data acquisition. The conditions database collects data from the detector control system (DCS) and stores information on run conditions and detector status during each run, including the states, online and offline calibrations, and alignments of each subsystem. All the data from both databases is accessible offline by the reconstruction and analysis software.

The condition database is implemented using the LHC Computing Grid COOL product, which is used to manage conditions data in time intervals called Intervals of Validity (IOV), versions and tags. COOL databases can be stored using several relational technologies such as Oracle, MySQL, and SQLite, based on the CORAL (Common Relational Abstraction Layer). Moreover, the COOL API has been implemented into the ATLAS software.

COOL data is stored in folders, which are relational database tables. Each folder stores several objects of the same type with their IOVs. In terms of the TRT, the most important folders are `StatusHT`, which contains the gas description of the TRT, and `Rt/t0`, which contains the most up-to-date t_0 and *r-t* calibrations for given gas descriptions and runs. These folders therefore include more than one version of conditions and are labelled as different *tags*. In the data processing, each of the ATLAS subsystems includes their preferred tags in a specific global conditions tag, which is used in the data processing and reprocessing (where the same runs are processed again with improved algorithms or software, as described in Section 5.4). As described in Section 6.5.7, the best calibrations of the simulated datasets were updated to

these global conditions tags. I also created several new `StatusHT` tags to support various TRT gas descriptions in different years.

6.8 CONCLUSIONS AND OUTLOOK

Being a tracker at the LHC is not easy: trackers are expected to resolve individual tracks with a high efficiency despite being exposed to very high hit density. The TRT plays an important role together with the silicon detectors in the tracking performance of the ATLAS. As the TRT measures drift time, the drift time calibration is essential to reach the optimal track position measurement accuracy. Once the drift time is known, it can be converted to the drift radius using the *r*-*t* relation.

In this chapter, multiple t_0 and *r*-*t* calibrations were performed in various gas configurations using the xenon and argon-based gas mixtures. The calibrations were done using simulated datasets as well as real data from both proton–proton and heavy ion collision events. In all of these cases, good position resolution and data quality is achieved, which shows that the argon-based gas mixture is well simulated and calibrated, hence suited for tracking studies in the TRT. The power of calibrations was also illustrated in terms of significantly improving the position resolution. Even in large occupancies resulting from multiple interactions in a bunch crossing, the TRT resolution is significantly better than the designed value at smaller pile-up [141]. All of this shows that during Run 2, the TRT operated successfully despite gas leaks and being subjected to very high rates of incoming particles.

There are still multiple items to be studied further before Run 3. This work includes argon tuning in simulations, and deriving new time-over-threshold and high threshold corrections to be applied with increasing luminosity and pile-up, among many other things. Furthermore, the calibration software has to be updated to suit future needs with upgraded computing systems.

We have now calibrated the t_0 values and *r*-*t* relations in both simulated and collision data, and obtained a large set of good quality tracks. Now it is time to do something with them: namely, let's hunt for a bump and search for doubly charged Higgs bosons!

Part III

SEARCHING FOR DOUBLY CHARGED HIGGS BOSONS

7 ANALYSIS OVERVIEW

"We need maps to orient ourselves, even when we know they're incomplete or faulty. And we need our imagination to be inspired to go beyond the familiar and narrow sights of our little village. And we need our boots and perseverance to keep walking. Safe travels!"
— Antonella De Santo on Twitter

7.1 INTRODUCTION

Needless to say, curious minds working on the ATLAS experiment are often interested either in measuring the Standard Model parameters more and more accurately, or in searching for new physics that could give some hints on the fundamental nature of our Universe. For the latter, we have to filter out interesting events that could include something new, something that we have not been able to observe before. During the data taking, ATLAS can record and store up to a few hundred events per second. However, even after triggering only interesting events during data taking, only a tiny bit out of this huge amount of data is really interesting and could potentially include something that is of our main interest.

But how to select interesting events that would potentially have their origins in new physics? A smart way is to look at rare signatures: if there are only a few similar events expected based on the Standard Model, i.e. low background, it is easier to find a signal and hunt for a bump, or an excess of events. One of such rare signatures is a final state with two same-charge (or *same-sign, SS*) leptons. As we will see, only a few Standard Model processes decay into such final states, but there are new hypothetical particles that could do so. If we then also require the leptons to have high transverse momenta and to be isolated (without a lot of jet activity around them), we can even further polish the final state. In physics jargon, we can say that the *final state has a high sensitivity to new physics*.

A theoretically well motivated hypothetical particle decaying into same-charge lepton final states is a doubly charged Higgs boson, as outlined in Chapter 2. It has the honour of playing the major role and being in the spotlight for this thesis. It arises in many new physics theories and if found, it could explain the smallness of neutrino masses. This thesis covers two searches for doubly charged Higgs boson with the ATLAS detector. The first search targets at doubly charged Higgs decays into *light* leptons (electrons and muons): $H^{\pm\pm} \to e^{\pm}e^{\pm}$, $H^{\pm\pm} \to e^{\pm}\mu^{\pm}$, and $H^{\pm\pm} \to \mu^{\pm}\mu^{\pm}$, and it was performed using a dataset collected during 2015 and 2016 corresponding to 36.1 fb^{-1}. This analysis is published in The European Physical Journal C [2] and is described in detail in Chapter 8. The second search for doubly charged Higgs bosons adds hadronically decaying taus into the analysis and uses the full Run 2 dataset corresponding to 139 fb^{-1} as described in Chapter 9. Including hadronically decaying taus in the analysis allows us to probe if there is a larger, mass-dependent coupling to the third-generation leptons (similarly to the Standard Model Higgs), which would lead to an enhancement of decays into tau leptons. In addition, it gives us the handle to utilize more of the statistical power of the available data: after all, tau-inclusive final states form a majority of all possible final state combinations.

Since both searches use similar approaches, this overview chapter highlights their common properties and methods. The sensitivity to doubly charged Higgs bosons can be maximized by increasing signal acceptance, or getting rid of more background contributions. That is

why the section begins by describing the signal characteristics and simulated signal samples, followed by an introduction to the backgrounds and how their contribution can be estimated (Sections 7.4 and 7.5). Finally, after having well understood backgrounds and hopefully a clear visible signal, the statistical analysis can be performed in order to claim a discovery or set exclusion limits as described in Section 7.6.

7.2 SIGNAL CHARACTERISTICS

As overviewed in Chapter 2.2.5, events with highly energetic, isolated same-charge lepton pairs provide a promising signature to search for doubly charged Higgs bosons. Especially the light charged leptons provide a clean signature and very good sensitivity with low, or at least well modelled, backgrounds. Furthermore, charged leptons are efficient to trigger: potential signal events are not lost due to complex and rare trigger signatures. Thanks to low expected background, the signal is expected to become visible in a form of an excess of events over the Standard Model predictions. In case no such excess is found in data, limits on the cross-section and the mass of the doubly charged Higgs boson are derived.

The main production mechanism for the doubly charged Higgs boson is expected to be the Drell–Yan process at the LHC: $pp \to Z/\gamma^* \to H^{\pm\pm}H^{\mp\mp}$. The presented searches target only leptonic decays of the $H^{\pm\pm}$ particle: $H^{\pm\pm} \to \ell^{\pm}\ell'^{\pm}$, where $\ell = e, \mu, \tau$, allowing lepton flavour violating states such as $e\mu$ and $\mu\tau$. Other final states X that are not directly selected in this analysis are taken into account by reducing the lepton multiplicity of the final state. These states X would include for instance W bosons, as well as particles which escape detection or fall outside of the detector acceptance. The total assumed branching ratio of $H^{\pm\pm}$ is therefore $B(H^{\pm\pm} \to \ell^{\pm}\ell^{\pm}) + B(H^{\pm\pm} \to X) = 100\%$. Additional motivation to study cases with $B(H^{\pm\pm} \to \ell^{\pm}\ell^{\pm}) < 100\%$ arises from the type-II see-saw models with specific neutrino mass hypotheses resulting in a fixed branching ratio combination [39, 166, 167] which does not necessarily correspond to $B(H^{\pm\pm} \to \ell^{\pm}\ell^{\pm}) = 100\%$.

The so-called truth level kinematic distributions of the same-charge lepton pairs in simulated $pp \to H^{++}H^{--}$ events are shown in Figure 54. In these distributions, lepton means only electron and muon (although a tau signature would look the same in truth level), and no additional cuts are applied. As illustrated, the $H^{\pm\pm}$ is expected to form a narrow mass resonance, and to result in a pair of high p_{T} same-charge leptons.

7.3 SIGNAL SIMULATION

7.3.1 *Light lepton samples*

The $H^{\pm\pm}$ signal samples were generated at leading order (LO) using PYTHIA 8.186, which implements the left-right-symmetry model scenario of $H^{\pm\pm}$ production described in Ref. [51]. The ATLAS A14 set of tuned parameters [106] is used together with the NNPDF23 [168] parton distribution function set.

Since the analysis with 36.1 fb^{-1} targets only the light lepton decays of the $H^{\pm\pm}$ bosons, the vacuum expectation value of the neutral component of the left-handed Higgs triplet (v_{Δ}^{L}) was set to zero to suppress decays into W bosons. Since these decays into W bosons could potentially have an impact on the expected signal strength, a study with samples with non-zero vacuum expectation values was performed as presented in Appendix B.

The decay width of the $H^{\pm\pm}$ to leptons depends on the $h_{\ell\ell'}$ couplings. The $h_{\ell\ell'}$ couplings of light lepton pairs were set to be the same: $H^{\pm\pm}$ coupling to $ee = \mu\mu = e\mu = 0.02$. This way

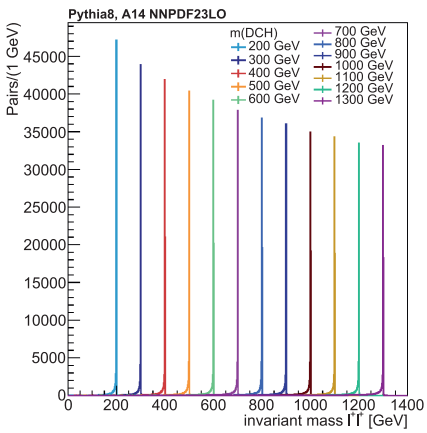

(a)

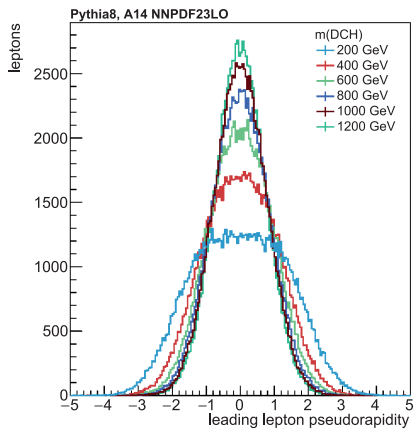

(b)

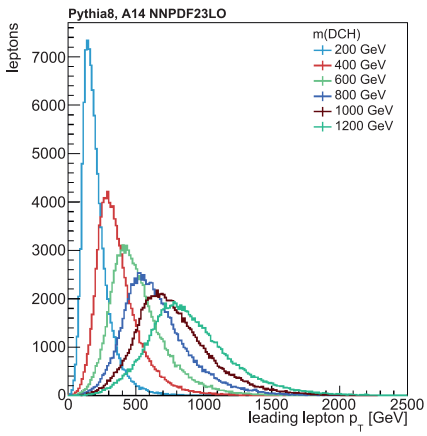

(c)

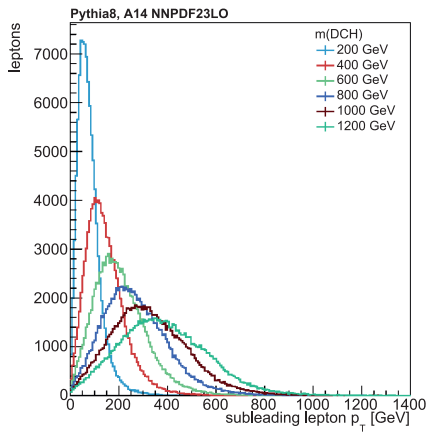

(d)

Figure 54: The truth level (a) invariant mass of the same-charge lepton pair, (b) leading lepton η, (c) leading lepton p_{T}, and (d) subleading lepton p_{T} distributions in simulated $pp \to H^{++}H^{--}$ events. In these plots, lepton means only electrons and muons.

Table 5: NLO cross-sections for the pair production of $H_L^{++}H_L^{--}$ and $H_R^{++}H_R^{--}$ in pp collisions at $\sqrt{s} = 13\,\text{TeV}$.

$m(H^{\pm\pm})$ [GeV]	$\sigma(H_L^{\pm\pm})$[fb]	K-factor ($H_L^{\pm\pm}$)	$\sigma(H_R^{\pm\pm})$[fb]	K-factor ($H_R^{\pm\pm}$)
300	13	1.25	5.6	1.25
350	7.0	1.25	3.0	1.25
400	3.9	1.24	1.7	1.24
450	2.3	1.24	0.99	1.24
500	1.4	1.24	0.61	1.24
600	0.58	1.23	0.25	1.24
700	0.26	1.23	0.11	1.23
800	0.12	1.22	0.054	1.23
900	0.062	1.22	0.027	1.23
1000	0.032	1.22	0.014	1.24
1100	0.017	1.23	0.0076	1.24
1200	0.0094	1.23	0.0042	1.25
1300	0.0052	1.24	0.0023	1.26

the decay width is negligible compared to the detector resolution. The $H^{\pm\pm}$ couplings to tau leptons were set to 0. In addition, the couplings were assumed to be equal for both $H_R^{\pm\pm}$ and $H_L^{\pm\pm}$ particles. This choice gives a good statistical coverage for all light lepton decay channels.

The production of the $H^{\pm\pm}$ was implemented via the Drell–Yan process. The cross-sections at $\sqrt{s} = 14\,\text{TeV}$ was calculated with NLO accuracy by the authors of Ref. [35], but as the LHC runs with $\sqrt{s} = 13\,\text{TeV}$, a rescaling was provided with the CTEQ6 PDF [169]. For processes where the cross-section at a next-to-leading order is non-negligible, a factor called the K-factor ($K = \sigma_{\text{NLO}}/\sigma_{\text{LO}}$) is applied to the expected cross-section of the simulated samples. The cross-sections and corresponding K-factors are summarized in Table 5. As can be seen, the cross-section for $H_L^{++}H_L^{--}$ production is approximately 2.3 times larger than that of $H_R^{++}H_R^{--}$ for all mass points due to the different couplings to the Z boson [51].

To cover a large mass range, 23 MC samples with different $H^{\pm\pm}$ particle masses from 200 GeV to 1300 GeV in steps of 50 GeV were generated. The best $H^{\pm\pm}$ mass resolution after event selection can be obtained in the electron–electron final states, with resolutions of around 30 GeV for masses of 200-500 GeV and 50 GeV to 100 GeV for higher masses. In the electron–muon final state, the mass resolution varies from 50 GeV to 150 GeV, and in muon–muon final states from 50 GeV to 200 GeV.

7.3.2 *Tau-inclusive samples*

In the full Run 2 analysis, tau leptons were added to the analysis, and therefore new signal samples were needed. The process of generating tau-inclusive signal samples followed similar steps as light lepton samples. The couplings to all lepton flavours ($H^{\pm\pm} \to \ell^{\pm}\ell^{\pm'}$, $\ell = e, \mu, \tau$) were set to 0.02, allowing also lepton-flavour violating final states $e\tau$, $\mu\tau$, and $e\mu$. In order to have enough statistics in tau-inclusive channels, an event generator filter was designed and

used to select at least one tau in a sample. In addition to these tau-inclusive samples, the previously generated light lepton samples are used in cases where there are no tau leptons in the final state. The full description of the sample generation process together with an event generation filter able to generate specific τ final states is described in a master's thesis conducted as a part of this analysis [170].

In total 11 tau-inclusive MC samples with different $H^{\pm\pm}$ particle masses from 300 GeV to 1300 GeV in steps of 100 GeV were generated. Since hadronically decaying taus were added, full GEANT4 sample of one mass point in the middle of the search range ($H^{\pm\pm} = 600$ GeV) was requested in addition to ATLAS fast simulation samples. The aim was to study if there are any differences between full and fast simulated signal samples after reconstruction. As can be seen in Appendix C, there are no differences to be seen in the kinematic distributions or tau origins, and only a small difference in the number of reconstructed taus is observed due to the full simulation step. Therefore, it is safe to use only fast simulated samples, as is already done for light leptons.

7.4 BACKGROUNDS

Although final states with the same-charge leptons are rare according to the Standard Model predictions, there are still background contributions from various processes that can lead to such signatures. These contributions can be divided into three categories:

- Prompt SM processes: mainly from diboson (WZ, ZZ, $W^{\pm}W^{\pm}$) and top-antitop ($t\bar{t}W$, $t\bar{t}Z$, $t\bar{t}H$)
- Non-prompt and fake backgrounds
- Lepton charge misidentification.

The dominant background process depends on the channel under scope: for example, regions including electron-pairs tend to have a large electron charge misidentification background. Different background components and the methods to predict them will be described in detail in this section.

7.4.1 *Prompt backgrounds*

Prompt background arises from particles which originate from or very close to the primary interaction point, and the background predictions are obtained from Monte Carlo simulations.

The majority of the prompt leptons considered in the analyses presented comes from diboson production, where two bosons decay leptonically: $ZZ \to \ell\ell\ell\ell$, $WZ \to \ell\ell\ell\nu$, as shown in Figures 55a and 55b. These background contributions are irreducible because they result in a similar final state as $H^{\pm\pm}$, same-charge dileptons, even if one of the leptons is lost. The diboson processes have relatively large cross-sections: the production cross-section measured by ATLAS are $\sigma(pp \to WZ) = 51 \pm 0.8 \pm 2.3$ pb, and $\sigma(pp \to ZZ) = 17.3 \pm 0.6 \pm 0.8$ pb [171], which makes their contribution to the same-charge final states very large. In order to distinguish diboson processes from the $H^{\pm\pm}$ signal, further selection cuts to exploit different topologies are implemented. For example, the diboson contribution can be suppressed by removing events where the dilepton invariant masses are close to that of an on-shell Z boson, i.e. by applying a Z-veto.

Another process with large cross-section leading to same-charge leptons is the $t\bar{t}$ production. Figure 55c shows an example of the $t\bar{t}$ production giving a trilepton signature. The corresponding measured production cross-sections are $\sigma(pp \to t\bar{t}) = 818 \pm 8 \pm 35$ pb, and

$\sigma(pp \to Z) = 58.43 \pm 0.03 \pm 1.66$ nb [171]. The background contribution from $t\bar{t}$ process can be suppressed by applying a b-jet veto in the event selection.

The prompt backgrounds also provide a source of reducible background due to lepton charge misidentification. For example in the process $Z \to \ell^+\ell^-$+jets, one of the charged leptons may have been reconstructed with the wrong charge. Since the analyses covered are affected by the charge misidentification, the ways to estimate it are covered in detail later in Section 7.4.3.

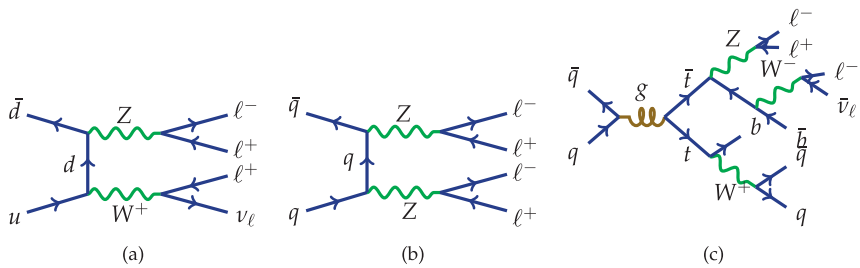

Figure 55: Feynman diagrams for the various processes leading to same-charge leptons: (a) WZ$\to \ell\ell\ell\nu$, (b) ZZ$\to \ell\ell\ell\ell$, and (c) $t\bar{t}$ production giving a trilepton signature.

7.4.2 *Non-prompt and fake backgrounds*

Same-charge lepton final states can also originate from non-prompt and *fake* backgrounds, where a physics object such as a jet is misreconstructed as a charged lepton. There are multiple sources of non-prompt and fake leptons, and their main origin depends on the lepton flavour.

Non-prompt leptons arise mainly from semileptonic decays of hadrons containing b or c quarks, for example in $t\bar{t}$, Z+jets, W+jets, and QCD multijet processes. These leptons are therefore real leptons but do not originate from the interaction point, hence they are non-prompt. Real, non-prompt electrons can also be produced in photon conversions ($\gamma^* \to e^+e^-$), as will be discussed more in Section 7.4.3.

In addition to non-prompt leptons, additional source of background arises from hadronic jets that are misidentified as prompt charged leptons. Fake electrons can be formed from an electrically charged component of a jet, which leaves a track in the Inner Detector and deposits energy in the electromagnetic calorimeter, leaving a signal which closely mimics the electron signature. A huge portion jets are misidentified as hadronically decaying taus, making background estimation particularly challenging for taus. The hadronic tau signature is very similar to that of gluon- and quark-initiated jets and the production cross-section of QCD multijet events clearly exceeds the production cross-section of tau leptons. However, the narrow shower width in the calorimeters, the number of tracks and the displaced decay vertex can be used to separate hadronic taus from misidentified jets. Illustration of both a hadronic tau and a jet is shown in Figure 56. Furthermore, electrons can also be misidentified as 1-prong hadronic taus. Fake taus arising from misidentified muons are almost entirely removed by the overlap removal procedure. Non-prompt and fake muons arise mainly from semileptonic decays or meson decays in flight.

For now on, both non-prompt and fake backgrounds form a background contribution collectively known as "fake background". This contribution is estimated in a data-driven way, as will be described in Section 7.5.

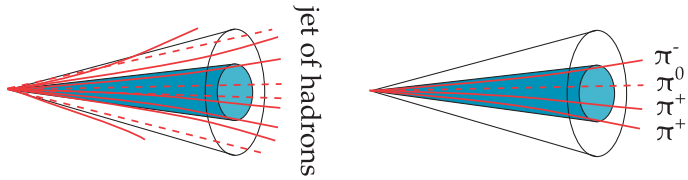

Figure 56: Schematic illustration of a jet consisting of hadrons (left) and a three-prong hadronic tau (right). The *core cone* is shown as blue together with *isolation cone*.

7.4.3 *Electron charge misidentification*

Prompt background events with two opposite-charge electrons can lead to same-charge electron final states if the charge of one electron is misidentified. The dominant process affecting the analysis is Drell-Yan ($q\bar{q} \to Z/\gamma^* \to e^+e^-$) followed by $t\bar{t}$ production. As the charge of an electron is determined from the curvature of the associated track, it can be misidentified if a wrong track is matched to the electron candidate, or if the track curvature is wrongly measured. The most likely mechanism of electron charge misidentification is *bremsstrahlung* leading to trident events and stiff tracks. Trident events arise when an electron emits bremsstrahlung, and the radiated photon converts into a electron-positron pair due to interactions with the detector material. The energy deposits in the calorimeter may then be matched to a track with an opposite charge compared to the original electron. The radiated photon can also transfer most of its energy to the opposite-charge electron and the original charge is lost. Trident events are responsible for the charge misidentification in most of the cases.

Stiff tracks arise from the photon emission without subsequent electron-positron pair production. The electron track has only very few hits in the silicon pixel layers and a short lever arm on its track curvature, which makes it very challenging to reconstruct a correct charge. However, in this case the energy of the electron is likely correctly reconstructed from the EM calorimeter information because the emitted photon deposits its energy in the calorimeter as well. For a similar reason, electrons with very high momenta or at large pseudorapidities are more likely to have charge misidentification, as their tracks are straight, and the electron charge is derived from the track curvature.

The charge misidentification is modelled in GEANT4 simulation, but not fully realiable due to the complex processes and lack of very precise descriptions of the detector material involved. The electron misidentification probability can be measured in a data-driven way, and then compared to the Monte Carlo prediction. The charge misidentification probability is obtained from a likelihood fit on a specific $Z \to ee$ data sample, where electron pairs are selected around the Z boson peak and categorised in opposite-charge (OC) and same-charge (SC) selections. The contribution from other processes than $Z \to ee$ is estimated with simulations and subtracted from the observed data. The number of opposite-charge and same-charge electron pairs in the two regions ($N^{ij} = N^{ij}_{\text{SC}} + N^{ij}_{\text{OC}}$) are used as inputs of the fit. The probability to observe N^{ij}_{SC} same-charge pairs is the Poisson probability, defined as

$$f(N^{ij}_{\text{SC}}; \lambda) = \frac{\lambda^{N^{ij}_{\text{SC}}} \mathrm{e}^{-\lambda}}{N^{ij}_{\text{SC}}!} \tag{50}$$

where N^{ij}_{SC} is the measured number of same-charge pairs, $\lambda = N^{ij}(P_i(1-P_j) + P_j(1-P_i))$ is the expected number of same-charge pairs in bin (i, j), i and j are the two electrons in the

pair, and P_i and P_j are the charge misidentification probabilities. The negative log likelihood used in the fit is defined as

$$-\log L(\mathbf{P}|\mathbf{N}_{\text{SC}}, \mathbf{N}) = \sum_{i,j} \log(N^{ij}(P_i(1-P_j) + P_j(1-P_i)))N^{ij}_{\text{SC}} - N^{ij}(P_i(1-P_j) + P_j(1-P_i)). \quad (51)$$

The charge misidentification probability is parameterized as a function of electron p_{T} and η, $P(p_{\text{T}}, \eta) = \sigma(p_{\text{T}}) \times f(\eta)$. The binned values, $\sigma(p_{\text{T}})$ and $f(\eta)$, are free parameters in the likelihood fit, and the area of the distribution describing $f(\eta)$ is set to unity in order to have a proper normalization. The charge misidentification probability is measured with the same method in a simulated $Z/\gamma^* \to ee$ sample and in data. As the simulated charge misidentification deviates from data, charge misidentification scale factors are obtained and applied to all prompt electrons in simulated events to tackle problems with simulation: scale factors are $P(p_{\text{T}}, \eta; \text{data})/P(p_{\text{T}}, \eta; \text{MC})$ if the charge is misreconstructed, and $(1 - P(p_{\text{T}}, \eta; \text{data}))\ /\ (1 - P(p_{\text{T}}, \eta; \text{MC})$ if the charge is properly reconstructed.

7.4.4 *Muon charge misidentification*

The probability of muon charge misidentification is found to be negligible in the searches presented in this thesis. Muons have much greater mass than electrons (105.7 MeV) and for this reason, they are not as strongly accelerated when encountering electromagnetic fields, and they do not lose energy to bremsstrahlung as rapidly as electrons. Therefore, the main mechanism for charge misidentification is suppressed. In addition, the muon tracks are measured also in the muon spectrometer complementary to the Inner Detector, which provides a much larger lever arm for the curvature measurement and charge reconstruction.

7.4.5 *Tau charge misidentification*

The charge of the tau candidate is determined as the sum of of the charges of associated reconstructed tracks, and the probability of tau charge misidentification is expected to be small but not zero. Single-prong tau decays can be misidentified as three-prong decays due to additional tracks from underlying event. Furthermore, the neutral pions in the tau decay products decay into a pair of photons, which can consequently convert into e^+e^- pairs leading to additional tracks. Three-prong tau decays can be misidentified as single-prong decays, if some of the tracks are lost due to detector inefficiencies, track reconstruction and track selection.

The tau charge misidentification rate was estimated to range from 0.4% to 3.8% in ATLAS, and will be further discussed in Section 9.3.3. This study was conducted as a part of the $H^{\pm\pm}$ analysis using the full Run 2 dataset, and technical details of the work can be found in Shi Qiu's master's thesis [172].

7.5 BACKGROUND ESTIMATION METHODS

Events with two hadronic jets and events with a jet and a real lepton can pass the dilepton signal event selection if these jets are misidentified as leptons, as described earlier. Simulating each process that could contribute to this kind of *fake* background is challenging for two main reasons. First, the interactions that cause the detector to misidentify jets as leptons are difficult

to simulate reliably. Secondly, this kind of interactions are relatively rare and therefore very large MC samples would be needed to make reliable, accurate predictions. For these reasons, data-driven techniques are necessary to provide a reliable estimation of events containing both non-prompt and fake leptons. A widely used approach is to use data-driven *matrix method* or *fake factor method* to estimate the contribution of fake leptons passing the signal selection. In the following, main properties of both methods are summarised.

7.5.1 *Matrix method*

The aim of the matrix method is to estimate the total amount of fake events entering a particular signal region. To do so, certain identification criteria applied in the nominal signal selection are loosened to assess the probability of looser fake objects passing the signal selection. Therefore, two selection criteria are defined: the *tight* selection which is the same as the nominal signal selection, and the less stringent *loose* selection which corresponds to the baseline selection, achieved by loosening some of the tight selection requirements such as the identification or the isolation level. The number of selected events is called N_{T} in the tight (T) selection and N_{L} in the loose (L) selection. Both samples are expected to contain events with both real and fake leptons. The following formulation is obtained from [173] where also more details can be found.

The whole idea of the matrix method relies on the real rate r and fake rate f, where the real rate is the probability that a real loose (L) lepton also passes the tight (T) criteria. Correspondingly, the fake rate is the probability that a fake lepton passing the loose selection criteria also passes the tight criteria. The fake rate can be determined in a data-driven way by measuring it in a fake-enriched region, and then extrapolating it to the signal region. A similar approach can be taken to determine the real rate in a region dominated by real objects. In such regions, the samples should have as high *purity* as possible. Purity is defined as the relative amount of fake or real leptons in a fake or real control region, respectively.

To derive the equations used in the matrix method, we start by defining the fake rate f and the real rate r:

$$r = \frac{N_{\text{tight}}^{\text{real}}}{N_{\text{loose}}^{\text{real}}}, \qquad f = \frac{N_{\text{tight}}^{\text{fake}}}{N_{\text{loose}}^{\text{fake}}} \tag{52}$$

As mentioned, these rates can be obtained by measuring the number of loose and the number of tight objects. The number of loose leptons N_L is the sum of the tight leptons N_T and *strictly loose* leptons $N_{L'}$, which are loose leptons failing the tight criteria:

$$N_L = N'_L + N_T. \tag{53}$$

The matrix method links the number of real (R) and fake (F) objects to the number of tight and loose objects. Using 52, it follows that when a sample contains both real and fake leptons, the number of tight and strictly loose leptons can be expressed as

$$N_T = N_T^R + N_T^F = r \cdot N_L^R + f \cdot N_L^F \tag{54}$$

and

$$N'_L = N_L - N_T = N_L^R + N_L^F - (N_T^R + N_T^F) = N_L^R \cdot (1 - r) + N_L^F \cdot (1 - f). \tag{55}$$

If there are two leptons, Equations 54 and 55 can be expanded to a 4×4 matrix, which gives the name to this method. All of the possible combinations of two lepton candidates are then denoted by N_{xy} with $x, y \in R, F$. Practically, one can measure four kinds of pairs: pairs with

two tight objects, pairs with two strictly loose objects, and pairs with one tight and one strictly loose object. The numbers of each of those events are then denoted by N_{xy} with $x, y \in T, L'$. The transfer matrix between the number of real and fake electrons and the number of tight and strictly loose objects can then be written as

$$\begin{pmatrix} N_{TT} \\ N_{TL'} \\ N_{L'T} \\ N_{L'L'} \end{pmatrix} = \begin{pmatrix} r_1 r_2 & r_1 f_2 & f_1 r_2 & f_1 f_2 \\ r_1(1-r_2) & r_1(1-f_2) & f_1(1-r_2) & f_1(1-f_2) \\ (1-r_1) r_2 & (1-r_1) f_2 & (1-f_1) r_2 & (1-f_1) f_2 \\ (1-r_1)(1-r_2) & (1-r_1)(1-f_2) & (1-f_1)(1-r_2) & (1-f_1)(1-f_2) \end{pmatrix} \begin{pmatrix} N_{RR} \\ N_{RF} \\ N_{FR} \\ N_{FF} \end{pmatrix} \tag{56}$$

Given the real and fake rates, the matrix shown in Eq. 56 can be inverted. By using the inverted matrix and by measuring numbers of different kinds of pairs (N_{TT}, $N_{TL'}$, ...), the number of events passing the nominal selection caused by pairs with fake objects can be obtained:

$$\begin{pmatrix} N_{RR} \\ N_{RF} \\ N_{FR} \\ N_{FF} \end{pmatrix} = \frac{1}{(r-f)^2} \begin{pmatrix} (1-f)^2 & (f-1)f & f(f-1) & f^2 \\ (f-1)(1-r) & (1-f)r & f(1-r) & -rf \\ (r-1)(1-f) & (1-r)f & r(1-f) & -rf \\ (1-r)^2 & (r-1)r & r(r-1) & r^2 \end{pmatrix} \begin{pmatrix} N_{TT} \\ N_{TL'} \\ N_{L'T} \\ N_{L'L'} \end{pmatrix} \tag{57}$$

The combined contribution of fake leptons to the nominal di-lepton selection is then given by

$$\begin{aligned} N_{TT}^{\text{fakes}} = \; & \alpha[2rf(f-1)(1-r) + f^2(1-r)^2] N_{TT} \\ & + \alpha(1-f) f r^2 (N_{TL'} + N_{L'T}) \\ & - \alpha r^2 f^2 N_{L'L'} \end{aligned} \tag{58}$$

where $\alpha = 1/(r-f)^2$.

7.5.2 *Fake factor method*

The fake factor is derived from the matrix method by assuming that no prompt leptons appear in the fake-enriched samples, and the real rate $r = 1$. However, this assumption is not fully correct as there is a small contamination of such prompt leptons. Therefore, the number of prompt leptons is estimated using simulation and subtracted from the number of tight and loose leptons used to measure the fake factors in the fake-enriched regions. Following again the formulation derived in Ref. [173], we can define the *fake factor* F as

$$F = \frac{f}{1-f}. \tag{59}$$

The total contribution of fake leptons to the nominal selection can then be expressed as

$$N_{TT}^{\text{fakes(FF)}} = F(N_{TL'} + N_{L'T}) - F^2 N_{L'L'}. \tag{60}$$

Using the fake factor formula, replacing $N_{TL'}$, $N_{L'T}$, and $N_{L'L'}$ with the exact expressions from Eq. 56, and by further simplifying the equation one obtainsW

$$N_{TT}^{\text{fakes(FF)}} = \frac{f(1-r)}{(1-f)} \frac{2r - fr - f}{1-f} N_{RR} + rf(N_{RF} + N_{FR}) + f^2 N_{FF}. \tag{61}$$

As mentioned, two real leptons should not contribute to the fake background, and therefore number of such events has to be estimated and subtracted:

$$N_{TT}^{\text{fakes}} = \left(F(N_{TL'} + N_{L'T}) - F^2 N_{L'L'}\right)_{\text{data}} - \left(F(N_{TL'} + N_{L'T}) - F^2 N_{L'L'}\right)_{N_{RR}\text{fromMC}} \quad (62)$$

The fake factor should be evaluated for each lepton candidate separately, and therefore Eq. 62 can be generalised to account for two different fake factors F_1 and F_2 for the first and second lepton candidate, respectively. This formulation yields to more representative form of the fake factor, expressed as a sum over all the lepton pairs:

$$N_{TT}^{\text{fakes}} = \left[\sum_{N_{TL'}} F_2 + \sum_{N_{L'T}} F_1 - \sum_{N_{L'L'}} F_1 F_2\right]_{\text{data}} - \left[\sum_{N_{TL'}} F_2 + \sum_{N_{L'T}} F_1 - \sum_{N_{L'L'}} F_1 F_2\right]_{N_{RR}\text{fromMC}} \quad (63)$$

The fake factor can be obtained by measuring the ratio of tight and strictly loose objects in a fake-enriched sample:

$$F = \frac{f}{1-f} = \frac{N_{\text{tight}}^{\text{fake}}}{N_{\text{loose}-\text{tight}}^{\text{fake}}} = \frac{N_{\text{num}}^{\text{fake}}}{N_{\text{den}}^{\text{fake}}}. \quad (64)$$

The strictly loose and the tight regions are often called the *denominator* and the *numerator* region in the fake factor method.

7.5.3 *Template method*

Contributions from different processes can also be estimated using the so-called *template method*. This method makes use of shape differences in the distributions of variables that are sensitive to the observable of interest. These distributions are called templates, and are usually obtained from simulations. Model parameters of the background templates are fitted to the data by optimizing the agreement between the data and the sum of templates. [174]

The template fit is traditionally used for example in the measurements of the top quark mass. In the context of this thesis work, the template fit method is used for estimating the tau charge misidentification probability and the centrally derived fake tau background estimations (see Appendix C).

7.6 STATISTICAL ANALYSIS

"One operation alone remained to be accomplished to bring all to a happy termination; an operation delicate and perilous, requiring infinite precautions, and against the success of which Captain Nicholl had laid his third bet."

— From the Earth to the Moon by Jules Verne

After carefully selecting the events, and estimating and validating backgrounds, the last fun parts of the analysis are about to begin: we approach the final results and get to know if we have found some excesses above the predictions. Until this step the analysis has been *blinded*: we have not yet looked the actual data events in the regions where the signal is expected to be in order to avoid any experimental biases.

The aim of the statistical analysis is to tell what information can be extracted from the measurement. A discovery of a new particle would need several significant observations in

different channels. However, recently nature has not been kind enough to leave us any hints of new physics to be seen at the LHC experiments. In the case when a searched and dearly wished-for new particle does not show up, we can set *exclusion limits* on the cross-section and mass of the hypothetical particle, or some parameters of the theory.

This chapter starts by describing how to evaluate whether the measured dataset is consistent with what we expect from theory. If it is, a certain region of a phase-space where a new particle did not show up can be exluded using the so-called the CL_s method, which is introduced in Section 7.6.2.

7.6.1 *Hypothesis test*

The goal of the analysis is to draw conclusions based on data and estimated backgrounds and to evaluate if they are consistent with a given hypothesis. A null hypothesis H_0 is often taken as a general statement that there is nothing new: in the searches for new physics, H_0 is usually the Standard Model stating that the observed data originate only from the SM background processes. In such case, the H_0 can also be referred to as the *background-only* (b) hypothesis. A *signal+background* ($s + b$) hypothesis H_1 serves as an alternative, complementary hypothesis in which an additional new physics signal process takes place. In the context of this thesis, it corresponds to a doubly charged Higgs with a mass m on top of the SM background processes.

Once signal and signal+background hypotheses are defined, the hypothesis testing aims to answer whether the null hypothesis can be rejected based on the experimental measurements, or whether the measurements are compatible with it. The *p-value* is a measure of how consistent (or inconsistent) the observed data is with the background-only hypothesis. It describes the probability of obtaining data that is equally or more incompatible with the predictions of H_0, assuming the null hypothesis is true. A small p-value suggests that the observed data is unlikely to be explained by the null hypothesis, i.e. it indicates large fluctuations of the background or a presence of a signal. [174]

In particle physics, *significance* σ is often quoted instead of the p-value. It is the number of standard deviations that correspond to an area p under the tail of a Gaussian distribution [175]. For example, a 3σ significance corresponds to a p-value of 1.35×10^{-3}. For a discovery, a significance of 5σ has been agreed to, corresponding to a p-value of 2.87×10^{-7} for the null hypothesis. Of course, before claiming a new discovery, the reliability of the statistical model and associated uncertainties must be carefully addressed. Accordingly, a p-value of 0.05 (corresponding to 95% *confidence level* (CL)) is often used to exclude the existence of a new signal.

In case no significant excess is observed, exclusion limits on the model parameters (such as a $H^{\pm\pm}$ mass or a production cross-section) can be estimated. For setting exclusion limits, a parameter of interest (POI) is varied and the exlusion hypothesis test is repeated until a POI value with 95% exclusion is found. That is why setting exclusion limits is also called a hypothesis test inversion. In the search for doubly charged Higgs bosons, the parameter of interest is the *signal strength* μ.

In addition to the parameters of interest, there may be additional uncertain parameters that model for example the effect of systematic uncertainties. Such parameters are called *nuisance parameters* θ. For several systematic uncertainties the set of several nuisance parameters is written as $\boldsymbol{\theta}$. Each nuisance parameter can alter the expected signal and background yield by changing the normalization and/or shape of the input distribution. Based on the parameters of interest μ and nuisance parameters θ, a likelihood function can be constructed to describe the probability to observe the data given the parameter values:

$$\mathcal{L}(\mu, \boldsymbol{\theta}) = \prod_{i}^{\text{bins}} \mathcal{L}_{\text{poiss}}(N^{i}_{\text{data}} \mid \mu s^{i}(\boldsymbol{\theta}) + b^{i}(\boldsymbol{\theta})) \times \mathcal{L}_{\text{gauss}}(\boldsymbol{\theta}) \tag{65}$$

where the Poissonian term describes the statistical fluctuations of the data, and a Gaussian term models the effect of auxiliary measurements to constrain the systematic uncertainties such as those arising from luminosity, cross-sections or experimental systematic uncertainties. N_{data} is the number of data events in the i-th bin, $s^{i}(\boldsymbol{\theta})$ is the expected signal yield, and $b^{i}(\boldsymbol{\theta})$ is the expected background yield.

The level of agreement between the observed data and a hypothesis can be evaluated by defining a *test statistic* q_{μ} for a given signal strength μ. The searches for new physics often use a *profile likelihood ratio* as a test statistic. The profile likelihood ratio is constructed from two maximum likelihoods: the unconditional maximum likelihood $\mathcal{L}(\hat{\mu}, \hat{\boldsymbol{\theta}})$ with the best fit values $\hat{\mu}$ and $\hat{\boldsymbol{\theta}}$, and the conditional maximum likelihood $\mathcal{L}(\mu, \hat{\hat{\boldsymbol{\theta}}}_{\mu})$ which maximizes the likelihood function for a given μ.[1] The profile likelihood ratio is therefore defined as [176]

$$q_{\mu} = -2 \ln \left(\frac{\mathcal{L}(\mu, \hat{\hat{\boldsymbol{\theta}}}_{\mu})}{\mathcal{L}(\hat{\mu}, \hat{\boldsymbol{\theta}})} \right). \tag{66}$$

The profiled likelihood ratio is defined as a positive quantity, $0 \leq q_{\mu} \leq 1$, where larger q_{μ} close to 1 indicate background-like data and lower q_{μ} signal-like data.

7.6.2 CL_s method

The p-value for an observed value of the test statistic $q_{\mu,\text{obs}}$ is defined as

$$p = \int_{q_{\mu,\text{obs}}}^{\infty} f(q_{\mu} \mid \mu, \boldsymbol{\theta}) dq_{\mu}. \tag{67}$$

In order to derive the 95% CL limits, the probability density functions (PDFs) of the test-statistic ($f(q_{\mu} \mid \mu)$) are determined by running a set of toy experiments based on both b and the $s + b$ hypotheses. The corresponding p-values p_b and p_{s+b} are obtained separately for these hypotheses using the same test statistic q_{μ}, and the consistency of the data with the hypothesis to a certain confidence level[2] is tested using the CL_s method [177], defined as

$$CL_s = \frac{p_{\text{s+b}}}{1 - p_{\text{b}}} = \frac{CL_{s+b}}{CL_b}. \tag{68}$$

If it is less than 5%, the hypothesis is said to be exluded at 95% CL. The CL_s method aims to avoid excluding hypotheses that the experiment does not have sensitivity to. Furthermore, the CL_s limits correspond to the frequentist limits when the experiment is fully sensitive [177]. In the searches for doubly charged Higgs boson, the CL_s method is implemented via the statistical framework HistFitter [178] to perform a maximum-likelihood fit of the invariant mass distribution of the same-charge leptons. The main goal is to derive an upper limit on the signal production cross-section as a function of the $H^{\pm\pm}$ mass and branching ratios.

1 In other words, a hat indicates MLE (Maximum Likelihood Estimator), and a double hat means a constrained MLE with a fixed μ.

2 Note: not *confidence interval*. If we run an ensemble of experiments, each of them will yield a different confidence interval. Having a 95% confidence interval would mean that out of that ensamble of experiments, 95% of the obtained confidence intervals will contain the true value

8 SEARCH FOR DOUBLY CHARGED HIGGS BOSONS WITH 36.1 FB^{-1}

The first of the two searches covered in this thesis uses a dataset collected during 2015 and 2016 corresponding to the integrated luminosity of 36.1 fb^{-1} [2]. This search for doubly charged Higgs boson targets only decays of the $H^{\pm\pm}$ into light leptons (electrons and muons), denoted by ℓ. Other final states X that fall outside of the scope of this search, such as τ leptons or W bosons together with other particles escaping detection, are taken into account by reducing the lepton multiplicity of the final state. The total assumed branching ratio of $H^{\pm\pm}$ is therefore $B(H^{\pm\pm} \to e^{\pm}e^{\pm}) + B(H^{\pm\pm} \to e^{\pm}\mu^{\pm}) + B(H^{\pm\pm} \to \mu^{\pm}\mu^{\pm}) + B(H^{\pm\pm} \to X) = B(H^{\pm\pm} \to \ell^{\pm}\ell^{\pm}) + B(H^{\pm\pm} \to X) = 100\%$. In the absence of evidence for a signal, lower limits on the mass of the $H^{\pm\pm}$ particle are set at the 95% confidence level.

The chapter is divided as follows. Section 8.1 describes the used datasets in detail, and all the peculiarities exploited to define event selection and a set of criteria for analysis objects are explained in Section 8.2. Section 8.3 describes how different backgrounds are estimated. After showing the representative distributions in various analysis regions in Section 8.4, the systematic uncertainties are discussed in Section 8.5. Finally, statistical analysis and results together with systematic uncertainties are covered in Section 8.6.

8.1 DATASET AND SIMULATED EVENT SAMPLES

8.1.1 *Data sample*

The data were collected at $\sqrt{s} = 13\,\text{TeV}$ during 2015 and 2016, corresponding to an integrated luminosity of 3.2 fb^{-1} in 2015 and 32.9 fb^{-1} in 2016. The average number of pp interactions per bunch crossing in the dataset is 24.

The uncertainty on the combined 2015+2016 integrated luminosity is 3.2%. Following a methodology similar to the one described in Ref. [179], this uncertainty is derived from a preliminary calibration of the luminosity scale using x–y beam-separation scans performed in August 2015 and May 2016.

8.1.2 *Triggers*

Different triggers were used in different channels: dielectron triggers in the electron channel, combined electron-muon trigger in the mixed channel containing both electrons and muons, and single-muon triggers in the muon channel.

Events in the electron channel are required to pass a dielectron trigger `2e17_lhloose`. This is a High Level Trigger (HLT) with a threshold on the transverse energy $E_{\text{T}} = 17\,\text{GeV}$ of each electron. It requires that electrons pass at least likelihood loose offline reconstruction level but they do not have to satisfy any isolation requirements.

Events in the muon channel are selected with a single muon HLT trigger chain `mu50 OR mu26_ivarmedium`. This chain includes two triggers with p_{T} thresholds of 26 GeV and 50 GeV, respectively. The first trigger applies a p_{T} threshold of 26 GeV and a track-based isolation requirement according to a medium working point of the muon reconstruction algorithm at trigger level [180]: $p_{\text{T}}\text{varcone30}/p_{\text{T}}(\mu) < 0.07$, where $p_{\text{T}}\text{varcone30}$ is the scalar sum of the

transverse momenta of the tracks with $p_T > 1$ GeV in a cone of size $\Delta R = \sqrt{(\Delta\eta)^2 + (\Delta\phi)^2} = \min(10\,\text{GeV}/p_T(\mu), 0.3)$ around the muon, excluding the muon track itself. This additional requirement gives discrimination power between isolated, signal-like leptons and non-isolated, background-like leptons. The second trigger only applies a 50 GeV p_T threshold requirements and no isolation requirements.

Finally, the events in the mixed channel are required to pass any of the triggers used for the muon channel or the electron channel, or a combined trigger `HLT_e17_lhloose_nod0_mu14` selecting one electron with a E_T threshold of 17 GeV and one muon with a p_T threshold of 14 GeV. Electron must have at least likelihood loose identification level, but no d_0 requirement is applied. Events with four leptons are selected using a combination of dilepton triggers.

All of these triggers are unprescaled in 2015 and 2016 data taking periods. Although single electron triggers might provide higher acceptance, they were discarded in order to avoid tighter online than offline selection, which would interfere with the data-driven background estimation. The background estimation needs both loose and tight identification working point for leptons. The electron identification used is `LHLoose`, but given there was no unprescaled single-electron trigger with low momentum and with `LHLoose` identification in 2015-2016, di-electron triggers were used instead.

8.1.3 *Simulated samples*

Prompt, irreducible background, as described earlier in Section 7.4, originates from the SM processes resulting in same-charge leptons. These cover mainly diboson ($W^{\pm}W^{\pm}$ / ZZ / WZ) and $t\bar{t}X$ processes ($t\bar{t}W$, $t\bar{t}Z$, and $t\bar{t}H$). Prompt background predictions were obtained from MC simulated events, summarized in Table 6 together with their theoretical cross-sections. In general, these MC samples are normalized using theoretical cross-sections. However, yields of some MC samples are considered as free parameters in the final likelihood fit, as described in Section 7.6.

Reducible background arises from the electron charge misidentification and from events with non-prompt leptons or other objects misidentified as light leptons, collectively called fakes. The electron charge mis-identification arises mainly from the Drell–Yan ($q\bar{q} \to Z/\gamma^* \to \ell^+\ell^-$) process, followed by $t\bar{t}$ production. However, the charge misidentification rate in simulation deviates from observations in data, and therefore scale factors are derived in a data-driven way and applied to simulated events as explained in Section 7.4.3. The lepton fakes originate mainly from decays of light- or heavy-flavour hadrons into light leptons in production of W+jets, $t\bar{t}$ and multi-jet events. Simulated samples are not used to estimate the fake background contribution due to large uncertainties in the simulation of jets and hadronization. Instead, a data-driven fake factor method is utilized and validated in special validation regions, as explained in Section 7.5.2.

The **signal** samples were generated at LO using Pythia 8.186, which uses the left-right-symmetry model scenario of $H^{\pm\pm}$ production. ATLAS A14 set of tuned parameters [106] is used together with the NNPDF23 [168] parton distribution function set. The sample generation is described in detail in Section 7.3.

The SM **Drell–Yan process** was modelled using Powheg-Box v2 [104, 181, 182] and utilizing Pythia 8.186 [100] for parton showering. The CT10 PDF set [183] was used to calculate the hard scattering process. The AZNLO tune [185] was used in combination with the CTEQ6L1 PDF set [192] to model non-perturbative effects. Photos++ version 3.52 [193] was used for photon emissions from electroweak vertices and charged leptons. The dataset was divided into 19 subsamples with subsequent invariant mass intervals to have enough statistics over the whole mass range. The cross-sections computed at NLO with the CT10 PDF set in the Drell–

Table 6: Simulated signal and background event samples: the corresponding event generator, parton shower, cross-section normalization, PDF set used for the matrix element and set of tuned parameters are shown for each sample. The cross-section in the event generator that produces the sample is used where not specifically stated otherwise.

Physics process	Event generator	ME PDF set	Cross-section normalization	Parton shower	Parton shower tune
Signal					
$H^{\pm\pm}$	Pythia 8.186 [100]	NNPDF2.3NLO [168]	NLO (see Table 5)	Pythia 8.186	A14 [106]
Drell–Yan					
$Z/\gamma^* \to ee/\mu\mu/\tau\tau$	Powheg-Box v2 [104, 181, 182]	CT10 [183]	NNLO [184]	Pythia 8.186	AZNLO [185]
Top					
$t\bar{t}$	Powheg-Box v2	NNPDF3.0NLO [93]	NNLO [186]	Pythia 8.186	A14
Single top	Powheg-Box v2	CT10	NLO [187]	Pythia 6.428 [188]	Perugia 2012 [189]
$t\bar{t}W$, $t\bar{t}Z/\gamma^*$	MG5_aMC@NLO 2.2.2 [190]	NNPDF2.3NLO	NLO [191]	Pythia 8.186	A14
$t\bar{t}H$	MG5_aMC@NLO 2.3.2	NNPDF2.3NLO	NLO [191]	Pythia 8.186	A14
Diboson					
ZZ, WZ	Sherpa 2.2.1 [102]	NNPDF3.0NLO	NLO	Sherpa	Sherpa default
Other (inc. $W^{\pm}W^{\pm}$)	Sherpa 2.1.1	CT10	NLO	Sherpa	Sherpa default
Diboson Sys.					
ZZ, WZ	Powheg-Box v2	CT10NLO	NLO	Pythia 8.186	AZNLO

Yan simulated events were scaled to NNLO with the CT14NNLO PDF set [184]. VRAP [194] was used to calculate corrections for QCD effects and Mcsanc [195] for electroweak effects from LO to NLO.

Another sample of $Z \to ee$ events was generated with Sherpa 2.2.1 [102] to measure the probability of electron charge misidentification, as explained in Section 7.4.3. The electron p_{T} spectrum is essential for measuring the charge misidentification probability, and was found to be better modelled by Sherpa than by Powheg, in particular when invariant masses of the electron pair are close to the Z boson mass. Sherpa uses Comix [196] and OpenLoops [197] to calculate the matrix elements up to two partons at NLO and up to four partons at LO in the strong coupling constant. The merging with the Sherpa parton shower [198] follows the ME+PS@NLO prescription in [199].

The **$\mathbf{t\bar{t}}$ process** was generated with Powheg-Box v2 using Pythia 8.186 for parton showering. The A14 parameter set [106] was used together with the NNPDF2.3 [168] PDF set for tuning the shower. Furthermore, the PDF set used for generation was NNPDF3.0 [93]. The top quark spin correlations were obtained using MadSpin [200]. The predicted $t\bar{t}$ production cross-section is 832^{+20}_{-30} (scale) ± 35 (PDF + α_{S}) pb as calculated with Top++2.0 [201] to NNLO in perturbative QCD, including soft-gluon resummation to NNLO. The top quark mass was expected to be $m_t = 172.5\,\mathrm{GeV}$. The scale uncertainty arises from independent variations of the factorization and renormalization scales, while the second uncertainty is associated with variations of the PDF set and α_{S}, following the PDF4LHC [202] prescription using the MSTW2008 68% CL NNLO [92], CT10 NNLO [203], and NNPDF2.3 PDF sets.

Single-top quark events produced in Wt final states were generated by Powheg-Box v2 with the CT10 PDF set. Such events in other final states were generated by Powheg-Box v1. Powheg-Box uses the four-flavour scheme for the NLO QCD matrix element calculations together with the fixed four-flavour PDF set CT10f4. The parton shower, hadronization, and underlying event were simulated with Pythia 6.428 [188] using the CTEQ6L1 PDF set and

the corresponding Perugia 2012 tune (P2012) [189]. The NLO cross-sections used to normalize these MC samples are summarized in Ref. [187].

The $t\bar{t}W$, $t\bar{t}Z$, and $t\bar{t}H$ processes were generated at LO with MADGRAPH v2.2.2 [204] and MADGRAPH v2.3.2 using the NNPDF2.3 PDF set. PYTHIA 8.186 was used for parton showering with the A14 tune [106]. The contributions were normalized using theoretical cross-sections summarised in Ref. [191].

Diboson processes leading to pure leptonic final states were generated with SHERPA 2.2.1, using matrix elements containing all diagrams with four electroweak vertices. They were calculated for up to three partons at LO accuracy, and up to one (4ℓ, 2ℓ+2ν) or zero partons (3ℓ+1ν) at NLO QCD using Comix and OpenLoops. The merging with the SHERPA parton shower [198] follows the ME+PS@NLO prescription. The NNPDF3.0NNLO [93] PDF set was used together with a parton shower tuning by the SHERPA authors.

Diboson processes with one boson decaying hadronically and the other one decaying leptonically were generated with SHERPA 2.1.1 [102]. They were calculated for up to three additional partons at LO accuracy and up to one (ZZ) or zero (WW, WZ) additional partons at NLO using Comix and OpenLoops matrix element generators. The merging with the SHERPA parton shower [198] follows the ME+PS@NLO prescription. The CT10 PDF set was used with a dedicated parton shower tuning. The SHERPA 2.1.1 diboson prediction was scaled by 0.91 to account for differences between the internal electroweak scheme used in this SHERPA version and the G_μ scheme which is the common default. Loop-induced diboson production with both bosons decaying fully leptonically was simulated with SHERPA 2.1.1 at LO, while up to one additional jet is merged with the matrix element.

Additional diboson samples for WZ and ZZ production were generated with POWHEG-BOX v2 to estimate theoretical uncertainties, using PYTHIA 8.186 for the parton shower. The CT10 PDF set was used for the matrix element calculation, and the parton shower was configured with the CTEQL1 PDF set. The non-perturbative effects were modelled using the AZNLO [185] tune.

All simulated samples except those generated with SHERPA used the EvtGen v1.2.0 program [205] to model b- and c-hadron decays. The effect of the pile-up was included by overlaying minimum-bias events simulated with PYTHIA 8.186 on each simulated event. The pile-up simulation is described in more detail in Ref. [206]. As described in Section 5.3, the response of the ATLAS was simulated using the GEANT4 toolkit, all events were reconstructed with the default ATLAS software, and correction factors were applied to simulated events to better match the performance of the detectors.

8.2 EVENT RECONSTRUCTION AND SELECTION

8.2.1 *Event reconstruction*

In this search, the signature is the final state of a same-charge lepton pair: $e^\pm e^\pm$, $e^\pm \mu^\pm$, $\mu^\pm \mu^\pm$. The objects are reconstructed as described in Section 5.5, and only further selection cuts are described here. The aim of further criteria is to reduce the prompt, fake and misreconstructed backgrounds, and therefore to increase sensitivity to new phenomena.

All selected events are required to have at least one reconstructed primary vertex with at least two associated tracks with $p_{\mathrm{T}} > 400\,\mathrm{MeV}$. Furthermore, all events pass the data quality requirements and specific event-level vetos to reject bad and corrupted events.

Charged leptons are classified in two exclusive categories called *tight* and *loose*, defined specifically for each lepton flavour. Leptons selected in the tight category are selected in the

signal region and are mostly prompt leptons. Loose leptons are mostly fakes, and are used for the fake-background estimation.

8.2.1.1 *Electrons*

Electrons used in the search are reconstructed by matching energy deposits from the EM calorimeter to a track in the ID, as described in Section 5.5.3. They are required to pass certain selection criteria: the electron identification working points chosen are called `LHLoose` and `LHMedium`, having electron identification efficiencies of 90% and 95%, respectively. All electrons are required to pass at least the `LHLoose` identification level, while analysis electrons entering the signal region have tighter identification requirements to reduce fakes arising from QCD jets.

To further suppress the jet background, a requirement on isolation is applied both on calorimeter clusters and tracks in the inner detector. The main motivation for the selection of `loose` isolation working point was to have the largest possible efficiency still feasible for the analysis.

Electrons are required to have $|\eta| < 2.47$. Electron candidates within the transition region between the barrel and endcap electromagnetic calorimeters ($1.37 < |\eta| < 1.52$) are vetoed because their reconstruction quality is worse in this gap region. The p_{T} cut of 30 GeV is applied to have clean, high-momenta electrons and to reject softer background. Moreover, cuts on the transverse and longitudinal impact parameters are used to ensure that the electron originates from a primary vertex, i.e. the electron is prompt. All these cuts summarized in Table 7 together improve the sensitivity to new physics.

Table 7: A summary of the electron definitions in the analysis.

Requirement	Signal electrons (tight)	Background electrons (loose)
Identification	`LHMedium`	`LHLoose` `OR`
Isolation	`loose`	fail `loose`
p_{T} cut	$p_{\mathrm{T}} > 30\,\mathrm{GeV}$	$p_{\mathrm{T}} > 30\,\mathrm{GeV}$
η cut	$\lvert\eta\rvert < 2.47$ and veto $1.37 < \lvert\eta\rvert < 1.52$	$\lvert\eta\rvert < 2.47$ and veto $1.37 < \lvert\eta\rvert < 1.52$
$\lvert d_0\rvert/\sigma_{d_0}$ cut	$\lvert d_0\rvert/\sigma_{d_0} < 5.0$	$\lvert d_0\rvert/\sigma_{d_0} < 5.0$
$\lvert z_0 \sin(\theta)\rvert$ cut	$\lvert z_0 \sin(\theta)\rvert < 0.5\,\mathrm{mm}$	$\lvert z_0 \sin(\theta)\rvert < 0.5\,\mathrm{mm}$

8.2.1.2 *Muons*

Muons are reconstructed by combining information from the Muon Spectrometer and the Inner Detector, as described in Section 5.5.4. Muons with $p_{\mathrm{T}} > 30\,\mathrm{GeV}$ and within the acceptance $|\eta| < 2.5$ are selected in the analysis, where the η range covers the effective range of the Muon Spectrometer and the Inner Detector. Muons are required to pass the `Medium` reconstruction working point. In order to reduce fake background from real muons embedded within a jet and produced by in-flight decays of mesons, the detector activity surrounding the muons is used to discriminate between prompt and background muons. The isolation

working point chosen is `FixedCutTightTrackOnly`. The motivation for choosing these working points is the same as for electrons: the idea is to have the largest possible efficiency and background rejection in order to have a good signal sensitivity. Muon selection criteria are shown in Table 8.

Table 8: A summary of the muon definitions in the analysis.

Requirement	Signal muons (tight)	Background muons (loose)
Quality	`Medium`	`Medium`
Isolation	`FixedCutTightTrackOnly`	fail `FixedCutTightTrackOnly`
p_{T} cut	$p_{\mathrm{T}} > 30\,\mathrm{GeV}$	$p_{\mathrm{T}} > 30\,\mathrm{GeV}$
η cut	$\lvert\eta\rvert < 2.5$	$\lvert\eta\rvert < 2.5$
$\lvert d_0\rvert/\sigma_{d_0}$ cut	$\lvert d_0\rvert/\sigma_{d_0} < 3.0$	$\lvert d_0\rvert/\sigma_{d_0} < 10.0$
$\lvert z_0 \sin(\theta)\rvert$ cut	$\lvert z_0 \sin(\theta)\rvert < 0.5\,\mathrm{mm}$	$\lvert z_0 \sin(\theta)\rvert < 0.5\,\mathrm{mm}$

8.2.1.3 *Jets*

Jets are reconstructed by the anti-k_t algorithm with a radius parameter $R = 0.4$, as described in Section 5.5.5. In this analysis, events containing b-jets are vetoed in order to reduce the fake background. Such jets are identified with a multivariate discriminant [207] that has a b-jet efficiency of 77% in simulated $t\bar{t}$ events, and a rejection factor of ≈ 40 for jets originating from gluons and ≈ 20 for jets originating from light quarks.

8.2.1.4 *Overlap removal*

It could happen that a physical object is reconstructed by several different algorithms: an electron can be reconstructed as an electron and as a muon. To account for this, ambiguous objects are removed using an overlap removal procedure.

After electron and muon identification, jet calibration, and pile-up jet removal, overlaps between reconstructed particles or jets are resolved in order to remove duplicates. Electrons are removed if they share a track with a muon. After that, ambiguities between electrons and jets are resolved. If a jet is within $\Delta R < 0.2$ of an electron, the jet is rejected. Electrons within $\Delta R < 0.4$ of the remaining jets are discarded. Finally, if a jet is within $\Delta R < 0.4$ of a muon, and the jet features less than 3 tracks, the jet is removed. Otherwise the muon is discarded.

8.2.1.5 *Used derivations*

As mentioned in Section 5.4, large data samples can be reduced to select only targeted events and store only the necessary information for each analysis. The search makes use of various derivations that have additional criteria for event selection:

- `EXOT12`: require at least two light leptons with p_{T} >20 GeV. Selected electrons have to pass at least the `LHLoose` identification criteria and muons have to be combined. This derivation is used for the main analysis in the $ee, e\mu$ and $\mu\mu$ channels.
- `EXOT19`: require at least one electron with p_{T} >20 GeV passing `LHLoose` identification criteria. This derivation is used for measuring the electron fake factors and electron charge misidentification probability.

- `EXOT22`: require at least one combined muon with $p_{\mathrm{T}} > 20\,\mathrm{GeV}$. Similarly to `EXOT19`, the muon fake factors are measured using this derivation.

8.2.2 *Event selection and analysis regions*

In the search for new physics, it is often not enough to look at all the observed final state particles without adding any additional requirements on the selection such as momenta, mass, isolation or identification criteria. Of course, the goal of the analysis is to have as many signal-like events as possible, and as low backgrounds as possible. In a successful analysis strategy, the signal efficiency is enhanced and backgrounds are suppressed but also well understood.

Events are classified in independent categories, called *analysis regions* optimized for specific purposes. Each of these regions is defined by a selection on the events and objects reconstructed in the events. The *control regions* are background-rich regions used to constrain free parameters in the statistical analysis described in detail in Section 8.6. The methods and scale factors for background estimation are validated against data in *validation regions*. These two types of regions are designed to reject signal events. Finally, a special selection targeting signal events defines the *signal regions*, which are the regions of interest to the analysis, dominated by signal-like events and preferably has only a low background contribution. All regions are orthogonal, which means regions are strictly separated and the same events should not fall into different regions.

As mentioned, doubly charged Higgs bosons decay into pairs of same-charge leptons. To enhance sensitivity, regions are further divided into *channels* depending on the flavour combination of the same-charge pair: $e^{\pm}e^{\pm}$, $e^{\pm}\mu^{\pm}$ ("mixed channel"), and $\mu^{\pm}\mu^{\pm}$.

The lepton multiplicity in the event is used to categorize the analysis regions in 2-, 3- and 4-lepton regions. This categorization is done in order to catch as much signal as possible despite possible detector acceptance or efficiency limitations which leave one or two leptons undetected. Events with two or three leptons are required to have exactly one same-charge lepton pair, with an exception of the Opposite-Charge Control Region (OCCR) which selects events with exactly two electrons of opposite charges. Events with four leptons are required to have two same-charge pairs with a zero total charge. The mixed channel in the three-lepton region makes a further distinction between the cases $\ell^{\pm}\ell^{\pm}\ell^{\mp}$ and $\ell^{\pm}\ell^{\pm}\ell'^{\mp}$ where the opposite-charge lepton has a different flavour.

The main discriminating variable to define the type of all regions is the invariant mass of the same-charge lepton pairs. The same-charge pairs are required to have the invariant masses above 200 GeV in the signal regions, and below 200 GeV in the control and validation regions. A lower bound of at least 60 GeV on the invariant mass is set in all regions to remove low-mass events, which would potentially bias the background estimation of the analysis while maximizing the available number of events. In all regions, events with at least one b-tagged jet are vetoed in order to suppress background events arising from top-quark decays. The b-veto does not affect the $H^{\pm\pm}$ signal yield but may make the analysis less sensitive to some BSM scenarios.

8.2.3 *Control and validation regions*

Table 9: Summary of all regions used in the analysis. The table is split into three blocks: the upper block indicates the final states for each region, the middle block indicates the mass range of the corresponding final state, and the lower block indicates the event selection criteria for the region. The application of a selection requirement is indicated by a check-mark (✓). The 2P4L regions include all lepton flavour combinations. In the three lepton regions, $\ell^{\pm}\ell^{\pm}\ell'^{\mp}$ indicates that same-charge leptons have the same flavour, while the opposite-sign lepton has a different flavour.

Region / Channel	Control Regions			Validation Regions			Signal Regions		
	OCCR	DBCR	4LCR	SCVR	3LVR	4LVR	1P2L	1P3L	2P4L
Electron channel	$e^{\pm}e^{\mp}$	$e^{\pm}e^{\pm}e^{\mp}$		$e^{\pm}e^{\pm}$	$e^{\pm}e^{\pm}e^{\mp}$		$e^{\pm}e^{\pm}$	$e^{\pm}e^{\pm}e^{\mp}$	
Mixed channel	-	$e^{\pm}\mu^{\pm}\ell^{\mp}$	$\ell^{\pm}\ell^{\pm}\ell^{\mp}\ell^{\mp}$	$e^{\pm}\mu^{\pm}$	$e^{\pm}\mu^{\pm}\ell^{\mp}$ $\ell^{\pm}\ell^{\pm}\ell'^{\mp}$	$\ell^{\pm}\ell^{\pm}\ell^{\mp}\ell^{\mp}$	$e^{\pm}\mu^{\pm}$	$e^{\pm}\mu^{\pm}\ell^{\mp}$ $\ell^{\pm}\ell^{\pm}\ell'^{\mp}$	$\ell^{\pm}\ell^{\pm}\ell^{\mp}\ell^{\mp}$
Muon channel	-	$\mu^{\pm}\mu^{\pm}\mu^{\mp}$		$\mu^{\pm}\mu^{\pm}$	$\mu^{\pm}\mu^{\pm}\mu^{\mp}$		$\mu^{\pm}\mu^{\pm}$	$\mu^{\pm}\mu^{\pm}\mu^{\mp}$	
$m(e^{\pm}e^{\pm})$ [GeV]	$[130, 2000]$	$[90, 200)$		$[130, 200)$	$[90, 200)$		$[200, \infty)$	$[200, \infty)$	
$m(\ell^{\pm}\ell^{\pm})$ [GeV]	-	$[90, 200)$	$[60, 150)$	$[130, 200)$	$[90, 200)$	$[150, 200)$	$[200, \infty)$	$[200, \infty)$	$[200, \infty)$
$m(\mu^{\pm}\mu^{\pm})$ [GeV]	-	$[60, 200)$		$[60, 200)$	$[60, 200)$		$[200, \infty)$	$[200, \infty)$	
b-jet veto	✓	✓	✓	✓	✓	✓	✓	✓	✓
Z veto	-	inverted	-	-	✓	-	-	✓	✓
$\Delta R(\ell^{\pm}, \ell^{\pm}) < 3.5$	-	-	-	-	-	-	✓	✓	-
$p_{\mathrm{T}}(\ell^{\pm}\ell^{\pm}) > 100$ GeV	-	-	-	-	-	-	✓	✓	-
$\sum \lvert p_{\mathrm{T}}(\ell) \rvert > 300$ GeV	-	-	-	-	-	-	✓	✓	-
$\Delta M / \bar{M}$ requirement	-	-	-	-	-	-	-	-	✓

Multiple control and validation regions are designed to constrain and validate specific backgrounds. The *fake lepton background* is present in all of the analysis regions, and is estimated with a fake factor method as described in Section 7.5.2. The fake background estimation is validated in two- and three-lepton validation regions. *Drell–Yan* background enters in regions which include electrons, and where one of the electrons has been reconstructed with a wrong charge. This background is constrained in the opposite-charge control region with exactly two electrons, and the obtained normalization factor is applied to all the regions where such events can enter. The electron charge misidentification is validated in same-charge lepton validation regions. Finally, the *diboson* background contributes to all analysis regions, and it is constrained in diboson control region where three leptons and at least one Z boson are required by requiring that the mass of the opposite-charge same-flavour lepton pair is $81.2\,\text{GeV} \leq m(\ell^+\ell^-) \leq 101.2\,\text{GeV}$. Control and validation regions with their specific selection cuts are summarized in Table 9, and the corresponding distributions are presented in Section 8.4.

- The *same-charge validation region* (SCVR) requiring exactly two same-charge leptons is used to validate the data-driven fake background estimation in all channels, and the electron charge misidentification in channels involving electrons.
- The *three-lepton validation region* (3LVR) is designed to validate the SM diboson background and fake events with three reconstructed leptons. The events are rejected if any opposite-charge same-flavour lepton pair is within 10 GeV of the Z boson mass ($81.2\,\text{GeV} < m(\ell^+\ell^-) < 101.2\,\text{GeV}$). This requirement is applied to reject diboson events in the final state.
- The *four-lepton validation region* (4LVR) is used to validate the diboson modelling in the four-lepton region.
- The *opposite-charge control region* (OCCR) with exactly two opposite-charge electrons is designed to constrain the $Z \to e^+e^-$ background, which contaminates the signal regions involving electrons due to the electron charge mis-identification.
- The *diboson control region* (DBCR) requiring exactly three leptons is used to constrain the diboson background yield. In this region, the Z veto is inverted: the events is required to have an opposite-charge same-flavour lepton pair is within 10 GeV of the Z boson mass.
- The *four-lepton control region* (4LCR) is used to constrain the yield of the diboson background in four-lepton regions. The Z boson veto is not applied in four-lepton control and validation regions in order to increase the available number of simulated diboson events.

In the electron and mixed channels the lower bound of the invariant mass of the same-charge pair is increased to 90 GeV in the three-lepton regions, and to 130 GeV in the two-lepton regions. The motivation for increasing the lower mass bound in regions containing electrons is the data-driven electron charge misidentification background estimation, where the $Z \to e^+e^-$ peak is used to measure the charge misidentification rates, as described in Section 8.3. In the two-lepton regions, this bound is set to 130 GeV to completely remove the Z peak region. In the three-lepton regions, where the misidentification rate is not as strong, the bound is relaxed to 90 GeV to reduce the statistical uncertainty of the sample. As the muon channels do not have the charge misidentification background, there is no need to increase the lower mass bound in the muon channels.

8.2.4 *Signal region optimization*

Multilepton final states with same-charge lepton pairs provide an impressive handle to search for the pair production of doubly charged Higgs bosons. It is necessary to define a set of selection cuts in the signal region to discriminate the rare signal from SM backgrounds in order to claim a discovery or set powerful exclusion limit.

The signal regions are categorized in two-, three- and four-lepton regions in order to measure as much signal as possible, and the regions are further divided into flavour categories to increase the sensitivity. Table 10 shows the lepton multiplicity in signal events for three benchmark $H^{\pm\pm}$ mass points of 200 GeV, 500 GeV and 1000 GeV. The selection efficiency to four tight leptons ranges from 40% to 60%. As expected from the pair-production of $H^{\pm\pm}$, the number of events containing exactly four leptons, i.e. two same-charge pairs, is higher than the events containing exactly 1 pair. For lower mass values of $H^{\pm\pm}$, lower lepton multiplicities are also obtained. Tightening the selection from loose to tight causes 6% of the events to loose one lepton and fall into the 3 lepton category. Therefore, selecting events with 3 leptons and exactly 1 same-sign pair is an efficient way to retrieve events where a fourth lepton is lost due to selection acceptance.

Table 10: Fraction of events as a function of lepton multiplicity in three different signal samples: m($H^{\pm\pm}$)=200 GeV, m($H^{\pm\pm}$)=500 GeV, and m($H^{\pm\pm}$)=1000 GeV. Tight and loose refer to the lepton definitions. Signal acceptance is the ratio between the number of events containing from zero up to five leptons and the number of all generated events. Events with two, three or four leptons always contain at least one same-charge lepton pair.

	Number of charged leptons					
m($H^{\pm\pm}$)=200 GeV	0	1	2	3	4	5
Loose	0.04%	1.3%	12.2%	35.3%	50.9%	0.2%
Tight	0.2%	2.8%	16.8%	40%	40%	0.2%
m($H^{\pm\pm}$)=500 GeV,	0	1	2	3	4	5
Loose	0.02%	0.5%	6.3%	31.1%	61.7%	0.4%
Tight	0.04%	0.9%	8.1%	33.7%	57.2%	0.5%
m($H^{\pm\pm}$)=1000 GeV,	0	1	2	3	4	5
Loose	0.01%	0.4%	5.2%	29.9%	64.4%	0.5%
Tight	0.03%	0.7%	6.6%	31.8%	60.8%	0.2%

In order to maximize the signal sensitivity, additional requirements are imposed on all same-charge lepton pairs. The variables exploited for the optimization are chosen based on the signal and background kinematic distributions, and they utilize both the boosted decay topology of the $H^{\pm\pm}$ resonance and the high energy of the decay products. The signal region selection is summarized in Table 9.

In the pair production, the $H^{\pm\pm}$ are expected to have the same mass and to be produced nearly back-to-back. Their decay product leptons are assumed to have high transverse momenta and to form a narrow high-mass resonance peak. The same-charge leptons from SM backgrounds, on the other hand, are expected to be more randomly located in the detector. The main backgrounds in signal regions with exactly two leptons and one same-charge pair (SR1P2L), and exactly three leptons and one same-charge pair (SR1P3L) depend on the lepton

flavour: electron channels have largest background contribution from Drell–Yan and diboson production as well as from fake leptons, while mixed ($e^+\mu^+$) and muon channels are mostly affected by diboson and fake backgrounds.

Figures 57a-57c show the $\Delta R(\ell^\pm, \ell^\pm)$ distribution without any requirement on the same-charge lepton separation in the 1P3L signal region. Based on these distributions, the same-charge lepton separation is required to be $\Delta R(\ell^\pm, \ell^\pm) < 3.5$ in two- and three-lepton signal regions in order to enhance the signal sensitivity. As mentioned, another powerful way to reduce backgrounds is to have requirements on the transverse momenta of the same-charge lepton pair. Figures 57d-57f show the unoptimized scalar sum of the leptons' transverse momenta, which clearly discriminates against the SM backgrounds above 300 GeV. In a similar manner, the combined vector sum of the leptons' transverse momenta is optimized to be $p_{\mathrm{T}}(\ell^\pm\ell^\pm) > 100$ GeV in the 1P2L and 1P3L signal regions.

In signal regions with three and four leptons, the major background arises from the diboson events. The ZZ contribution can be effectively reduced by removing events where the opposite-charge same-flavour lepton pair has an invariant mass is within 10 GeV of the Z boson mass, i.e. by applying a Z-veto. Additionally, the doubly charged Higgs bosons and therefore the two same-charge lepton pairs are expected to have exactly the same invariant mass. For this reason, a cut on the invariant mass difference can be applied, defined as $\Delta M/\bar{M}$, where $\bar{M} = (m^{++} + m^{--})/2$. The cut value is optimized for different flavour combinations, because the width of the same-charge pair invariant mass distribution grows with the increasing $H^{\pm\pm}$ mass and electrons and muons have different momentum resolutions. This effect becomes more evident at high masses. The $\Delta M/\bar{M}$ cut suppresses especially the ZZ background from the signal region event selection. The transverse momentum and lepton separation cuts are removed in the four-lepton region in order to maximize available statistics. In order to keep the analysis selection as inclusive as possible, no further requirement on jet multiplicity or missing transverse energy is added on the events with same-charge leptons.

The signal selection efficiency times the detector acceptance varies with the assumed branching ratio into light leptons. Given the $H^{\pm\pm}$ branching ratio of 100% to leptons, the signal region with exactly two same-charge leptons is the least sensitive, because the signal efficiency is low for events containing exactly two leptons and there is larger background contamination from Standard Model events passing such selection. The three lepton signal region has a lower Standard Model background and approximately 30% signal efficiency. Finally, in the four-lepton signal region the cuts provide roughly 50% signal efficiency across the $H^{\pm\pm}$ mass range. Figure 58 shows the selection efficiency for all three lepton flavour categories when combining all signal regions together. As can be seen, all flavour categories achieve similar efficiencies across all masses of the $H^{\pm\pm}$ boson.

8.3 BACKGROUND COMPOSITION AND ESTIMATION

8.3.1 *Prompt backgrounds*

Prompt SM backgrounds consist of leptons originating from Z, W, and H bosons, or leptons from leptonic τ decays where the τ originated from a prompt source (e.g. $Z \to \tau\tau$). Such backgrounds are estimated using simulated samples defined in Section 8.1 in all analysis regions. Simulated events which contain at least one non-prompt tight or loose lepton are removed in order to avoid overlap with the data-driven fake background estimation.

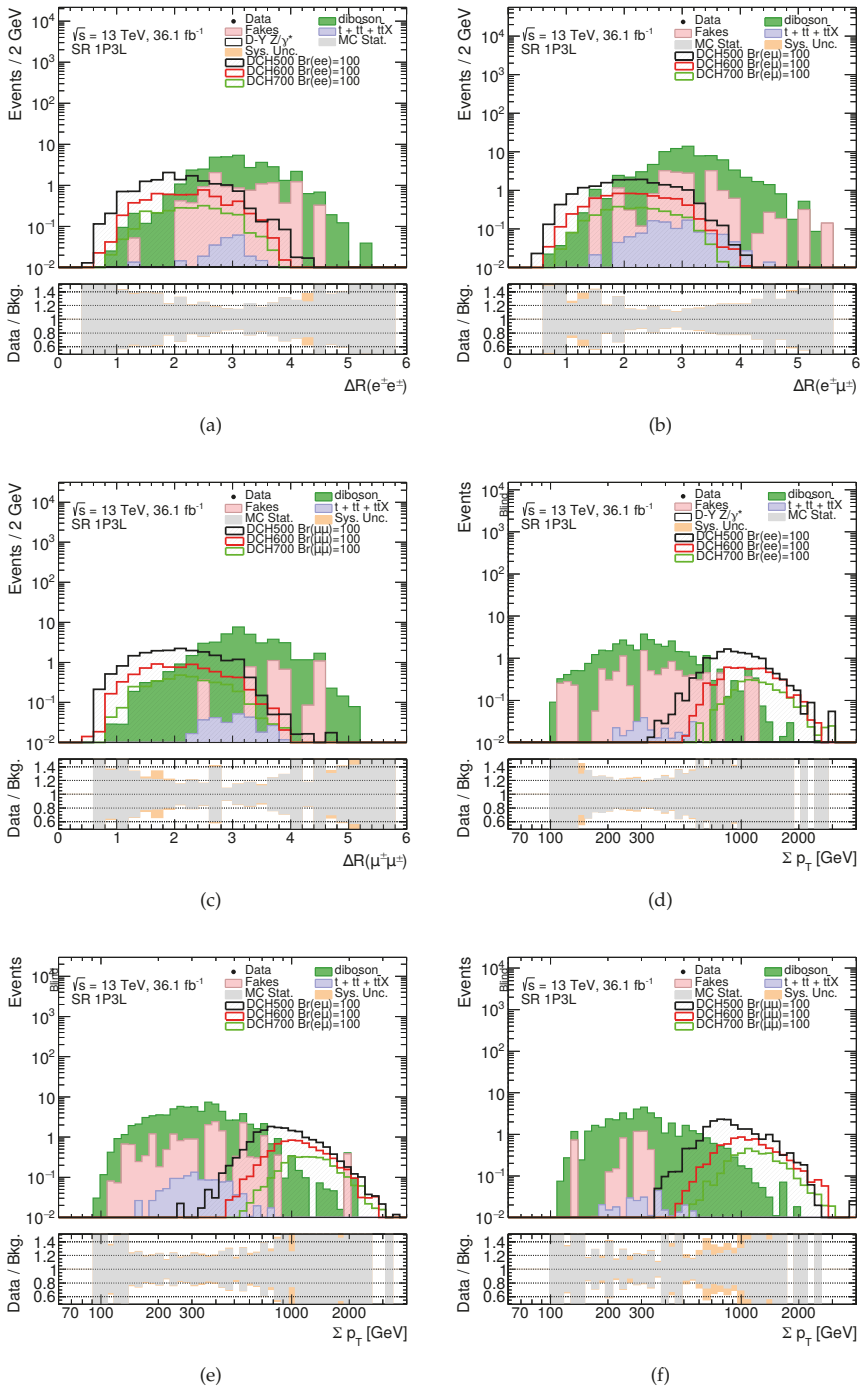

Figure 57: Distributions for signal region optimization, shown in the region with exactly three leptons and one same-charge pair before any optimization. The ΔR distribution for the (a) electron, (b) electron–muon, and (c) muon channels. The $\sum p_{\mathrm{T}}$ distribution for (d) electron, (e) electron–muon, and (f) muon channels, respectively.

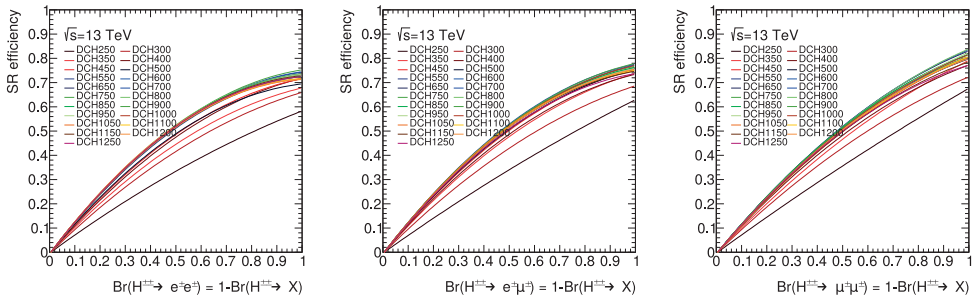

(a) (b) (c)

Figure 58: Combined signal region efficiency times acceptance as a function of the $H^{\pm\pm} \to \ell^{\pm}\ell^{\pm}$ branching ratio in (a) electron, (b) electron–muon, and (c) muon channels. [173]

8.3.2 *Electron charge misidentification background*

To correct electron charge misidentification caused predominantly by bremsstrahlung, the charge misidentification probability is measured in the data and compared to the charge misidentification probability in the simulation as described in Section 7.4.3. The main processes affecting the analysis through charge misidentification are Drell–Yan ($q\bar{q} \to Z/\gamma^* \to e^+e^-$ and $t\bar{t}$ production.

The charge misidentification probability is measured in a selected $Z/\gamma^* \to e^+e^-$ data sample with a likelihood fit, which takes the number of same-charge and opposite-charge electron pairs ($N^{ij} = N^{ij}_{\text{SC}} + N^{ij}_{\text{OC}}$) as an input. The invariant mass has to satisfy $|m_{\text{OC}}(ee) - m(Z)| < 14$ GeV in the opposite-charge (OC) selection and $|m_{\text{SC}}(ee) - m(Z)| < 15.8$ GeV in the same-charge (SC) selection. Other backgrounds are modelled using MC and their normalization is determined from data in a Z peak mass window defined as $14\,\text{GeV} < |m_{\text{OC}}(ee) - m(Z)| < 18\,\text{GeV}$ for OC and $15.8\,\text{GeV} < |m_{\text{SC}}(ee) - m(Z)| < 31.6\,\text{GeV}$ for SC, respectively. In such a selection all electrons are assumed to be real, because the Z boson cross-section clearly exceeds the one of W+jets production cross-section and therefore fakes from W+jets process are suppressed. Figure 59 shows the dielectron mass distribution in the Z region.

The charge misidentification probability $P(p_{\text{T}}, \eta) = f(\eta) \times \sigma(p_{\text{T}})$ is parametrized as a function of electron p_{T} and η, and the binned values of the charge misidentification probabilities ($f(\eta)$, $\sigma(p_{\text{T}})$) are used as free parameters in the likelihood fit. The sum of the $f(\eta)$ values is set to 1 to ensure the proper normalization of $P(p_{\text{T}}, \eta)$. The components of the charge misidentification probability $P(p_{\text{T}}, \eta) = \sigma(p_{\text{T}}) \times f(\eta)$, measured in data and in simulation, are shown in Figure 60.

Scale factors are applied to simulated prompt electrons to account for the different charge misidentification probabilities between data and simulation. The origin information of the simulated electron is obtained by using truth matching. The scale factors are defined as

- $P(p_{\text{T}}, \eta; \text{data}) / P(p_{\text{T}}, \eta; \text{MC})$ if the charge is misreconstructed, and
- $(1 - P(p_{\text{T}}, \eta; \text{data})) \,/\, (1 - P(p_{\text{T}}, \eta; \text{MC})$ if the charge is correctly reconstructed.

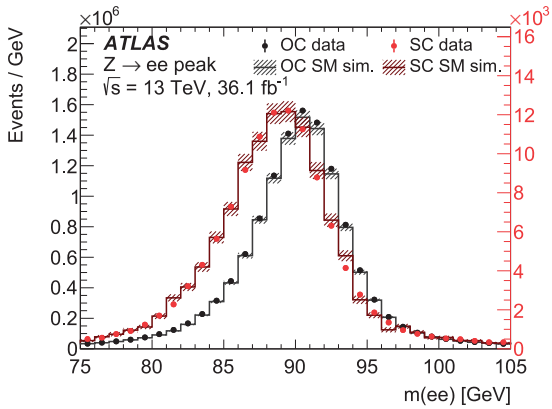

Figure 59: Dielectron mass distributions for opposite-charge (black) and same-charge (red) electron pairs for data (filled circles) and MC simulation (continuous line). The simulated events are corrected for charge misidentification. The hatched band indicates the statistical error and the luminosity uncertainty summed in quadrature applied to simulated events.

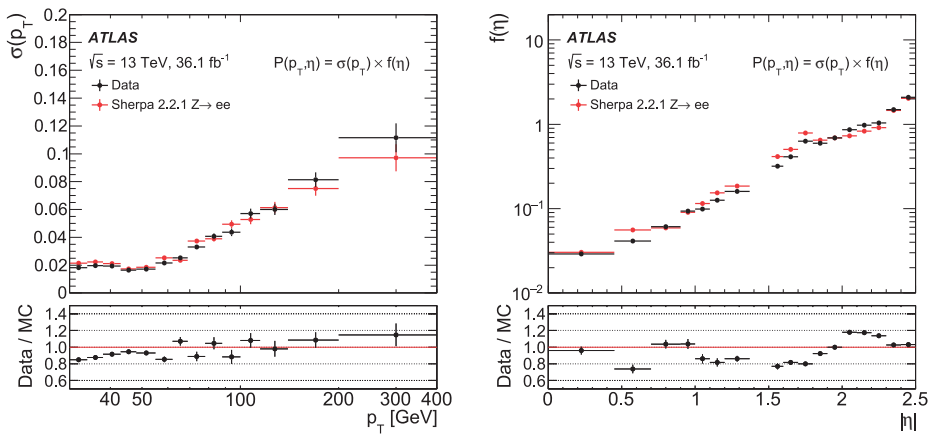

(a) (b)

Figure 60: The factors composing the charge misidentification probability $P(p_{\mathrm{T}}, \eta) = \sigma(p_{\mathrm{T}}) \times f(\eta)$ measured in data and in simulation using the likelihood fit: (a) the charge misidentification probability component as a function of p_{T}, and (b) the component as a function of $|\eta|$. Error bars correspond to the statistical uncertainties estimated with the likelihood fit.

8.3.3 *Fake backgrounds*

Fake leptons passing the analysis selection originate mostly from in-flight decays of mesons inside jets, jets misreconstructed as electrons, and conversions of initial- and final-state radiation photons. The b-jet veto significantly removes fake leptons from heavy-flavour decays. The fake background is estimated with a data-driven approach using the fake factor method, as described in Section 7.5.2, which gives an estimate of number of fake leptons entering the analysis regions. In this method, a control sample of events enriched with fakes is selected, and then a fake factor relating these events to the background in the signal region is determined. The fake factor $F(p_{\mathrm{T}}, \eta, \text{flavour})$ describes the probability for a fake lepton to be identified as a tight analysis lepton.

For fake factor measurements, events cannot be selected using the nominal dilepton triggers, because the leptons firing them are likely to originate from the interaction point and therefore are real. Instead, a specific set of single lepton triggers was used, as summarized in Table 11. They ensure a sufficiently loose identification requirement for both muons and electrons. However, these single lepton triggers are prescaled and therefore cannot be combined using a simple logical `OR`. Depending on the lepton p_{T}, each lepton is required to match a specific trigger.

Table 11: Single electron and single muon trigger schemes used for the fake enriched region.

Trigger name	p_{T} [GeV]	Trigger prescale
`HLT_e26_lhvloose_nod0_L1EM20VH`	$30 - 65$	112.4
`HLT_e60_lhvloose_nod0`	$65 - 125$	25.6
`HLT_e120_lhloose_nod0`	$125 - 145$	6.69
`HLT_e140_lhloose_nod0`	$145 - \infty$	1
`HLT_mu24`	$30 - 50$	≈ 45
`HLT_mu50`	$50 - \infty$	1

For electron fake factor measurements, a region with mostly fake electrons is designed. This is challenging, because fake electrons can mimic the characteristics of prompt electrons and the contribution of prompt leptons cannot be completely suppressed. To select such a region, basic event selection requirements are applied and several event selection criteria are required to discard events with real prompt electrons.

Events with two or more tight electrons are removed, but events with more than one loose electron can still pass the selection. Any events with a pair of tight or loose electrons with invariant mass within 20.0 GeV of the Z mass window (71.2 GeV $< m_{ee} <$ 111.2 GeV) are discarded to remove $Z \to ee$ events. In order to remove prompt electrons from $W \to e\nu$ events, any events with $E_{\mathrm{T}}^{\mathrm{miss}}$ greater than 25 GeV are discarded. Finally, a b-jet veto is applied to suppress the fake contribution from $t\bar{t}$ events.

Most of these events still contain some prompt electrons after all selection requirements are applied. These remaining prompt electrons are subtracted from data using W+jets, Drell–Yan, $t\bar{t}$, diboson, and single top simulated samples. The fake-enriched region corresponds to a dijet event selection.

The electron fake factors together with various systematic uncertainties are shown in Figure 61. The main sources of the systematic uncertainties come from Monte Carlo modelling

of the subtracted prompt leptons, from the normalization of Monte Carlo samples in the fake-enriched region, and from the different composition of fake electrons in the fake-enriched region compared to the signal region. The electron fake factor was measured independently for many variations. The nominal $E_{\mathrm{T}}^{\mathrm{miss}}$ cut for the fake enriched region was loosened to 60.0 GeV in order to probe the modelling of the W+jets process. All simulated samples were varied by $\pm 10\%$ to account for cross-section and luminosity uncertainties. Finally, in order to measure the fake factor for a different composition of fake leptons, an additional requirement of the *away side jet* ($\Delta\phi(\mathrm{jet}, \mathrm{electron}) > 2.4$) with $p_{\mathrm{T}} > 30$ GeV for each electron in the event is added. The combined systematic uncertainty of the electron fake factors was calculated by adding all variations and the statistical uncertainty in quadrature. The largest contributions to the uncertainty are the $E_{\mathrm{T}}^{\mathrm{miss}} < 60.0$ GeV requirement and the 10% MC variation in the first η slice of $0 < |\eta| < 1.37$. The measurement is relatively stable up to very high electron p_{T}, being at most 20%.

The muon fake factors are measured using the *tag-and-probe* method[1] targeting dijet events as they provide high statistics.

Events are selected by requiring exactly one jet in the event, the *tag*, and a reconstructed muon, the *probe*. The tag and probe are required to be back-to-back in the transverse plane, $\Delta\phi(\mu, \mathrm{jet}) > 2.7$, and have transverse momenta of $p_{\mathrm{T}}(\mu) > 25$ GeV and $p_{\mathrm{T}}(\mathrm{jet}) > 35$ GeV. Furthermore, $W \to \mu\nu +$ jets events are rejected by requiring $E_{\mathrm{T}}^{\mathrm{miss}} < 40$ GeV. Finally, events with at least one b-jet are rejected to avoid fakes from heavy flavour decays.

The systematic uncertainties on the measurement of the muon fake factors are estimated by altering the selection in the fake-enriched region. The requirement on the missing transverse energy $E_{\mathrm{T}}^{\mathrm{miss}}$ is varied by ± 10 GeV, affecting the fraction of W+jets events contaminating the selection and hence the largest fraction of prompt muons to be subtracted from data using simulation. To account for the different muon fake origin between the fake-enriched region and signal regions, the definition of the tight muons is altered by varying up and down the selection on $|d_0|/\sigma_{d_0}$ by one unit. Similarly, the isolation distribution of the fake muon might differ between regions. This effect is addressed by varying the transverse momentum of the recoiling jet in the event up to p_{T} (jet)> 40 GeV, affecting the collimation of the fake jet. The kinematic balance of the muon and the recoiling jet, which affects the isolation, is also varied up and down the back-to-back requirement $\Delta\phi(\mu, \mathrm{jet})$ by 0.1.

The effect of each systematic alteration on the nominal measurement and the total uncertainty on muon fake factors are shown in Figure 62. The total uncertainty is obtained by comparing the statistical uncertainty on the nominal measurement with the maximum deviation between the nominal fake factor and each systematically altered measurement. The largest signed deviation is taken to be the total uncertainty, ranging between 10% and 20% across the muon p_{T}.

8.4 DISTRIBUTIONS IN CONTROL AND VALIDATION REGIONS

As explained in Section 8.2.3, several control regions are designed to extract the normalization of the Drell–Yan and the diboson backgrounds. The diboson control region (DBCR) requiring exactly three charged leptons is used to constrain the diboson contribution, and the opposite-charge electron control region (OCCR) is used to constrain the $Z \to e^+e^-$ background, where one of the electrons has a misidentified charge. In the four-lepton control region, all lepton

1 The tag-and-probe method is a data-driven way to measure efficiencies. The basic idea is to select a "tag" object which passes a set of tight selection criteria (such as isolation and identification), and a "probe" object which passes a looser selection and is paired with the tag object within a resonance mass window. The efficiency is then a ratio between tagged objects and tagged+probe objects.

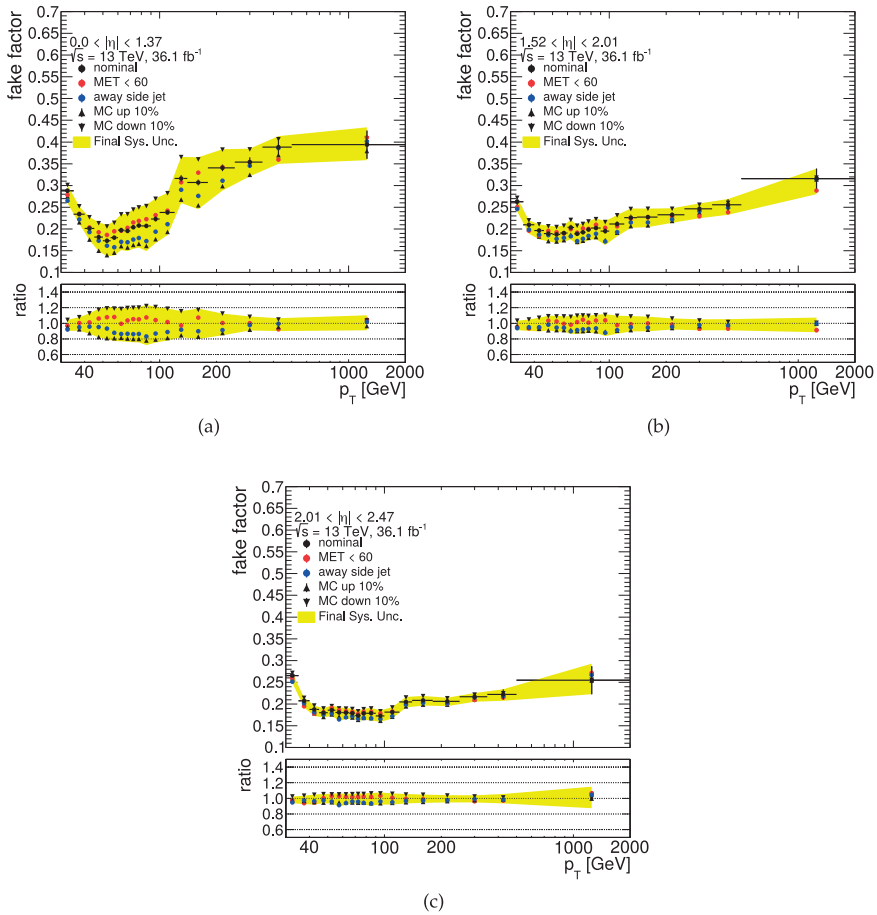

Figure 61: Electron fake factors as a function of the electron p_{T} in η bins: (a) $0 < |\eta| < 1.37$, (a) $1.52 < |\eta| < 2.01$, and (a) $2.01 < |\eta| < 2.47$. Each systematic variation accounted for in the measurement of the fake factor is also shown together with the total systematic band (yellow).

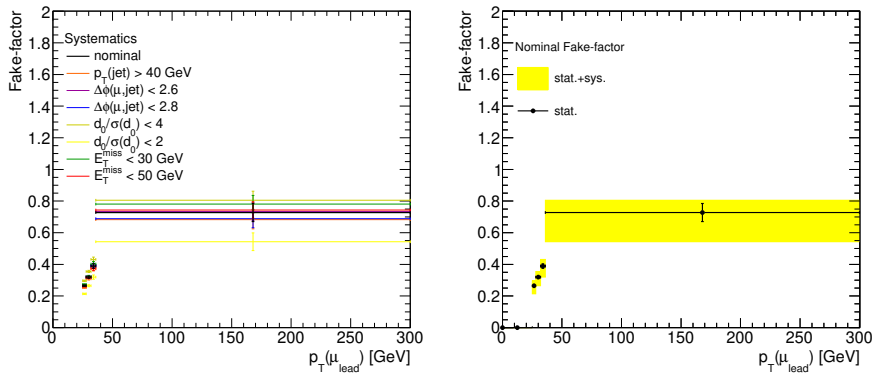

(a) (b)

Figure 62: Muon fake factors as a function of the muon p_T: (a) the nominal value (black points) with each systematic variation separately, and (b) the total uncertainty of the muon fake factor measurement.

flavours are merged together in order to increase statistics. Each background is normalized separately for different flavour combinations and lepton multiplicities. Representative invariant mass distributions after the fit are shown in Figure 63. All distributions show a good agreement between MC predictions and observed data.

The two-lepton and three-lepton validation regions, defined in Table 9, are used to validate the data-driven fakes, electron charge misidentification probability, and diboson modelling estimation in regions that are as similar to the signal regions as possible with a minimal signal event contamination. Signal and validation regions are orthogonal, which is ensured by requiring the invariant mass of the same-charge lepton pair $m(\ell^{\pm}\ell^{\pm})$ to be less than 200 GeV in the validation regions.

In Figures 64 and 65, validation regions sensitive to different background sources are presented: same-charge two-lepton validation regions (SCVR) validate the charge misidentification estimate and fake-background predictions, and three-lepton and four-lepton validation regions (3LVR and 4LVR) are designed to test the diboson modelling. Good background modelling is observed in all these regions.

8.5 SYSTEMATIC UNCERTAINTIES

Several sources of both experimental and theoretical systematic uncertainties affecting the background and signal predictions are taken into account in the analysis. They are summarized in Table 12. All considered sources of systematic uncertainties affect the total event yield, and all except the uncertainties on the luminosity and cross section also affect the shape of the distributions used in the fit.

8.5.1 *Experimental systematic uncertainties*

The experimental uncertainty on the electron charge misidentification probability arises from the statistical uncertainty on the $Z/\gamma^* \to ee$ sample in the selected kinematic region, and is between 10% and 20% depending on the electron p_T and η. The systematic effects have been

studied by varying the selection criteria on the invariant mass window used to select $Z/\gamma^* \to ee$ events. The systematic uncertainty is negligible compared to the statistical uncertainty.

The systematic uncertainties in the data-driven fake lepton background estimation are evaluated by varying the nominal fake factor to account for different effects, as described in Section 8.3. The resulting uncertainty in the fake factors ranges between 10% and 20% across all p_T and η bins.

The analysis is affected by the finite number of simulated and data events. Analysis regions have a very restrictive selection, and only a small fraction of all the generated MC events passes the final selection. The uncertainty due to finite statistics varies from 5% to 40% in the signal regions.

Experimental systematic uncertainties related to different reconstruction, identification, isolation, and trigger efficiencies of leptons in data compared to the simulation are at most 3%. Lepton energy and momentum calibration lead to similar uncertainties. Therefore these uncertainties are less significant when compared with the other systematic uncertainties and MC statistical uncertainties. All the mentioned experimental systematic uncertainties affect both the signal and the background samples.

8.5.2 *Theoretical uncertainties*

The cross-sections used to normalize the simulated samples are altered to account for the scale and PDF uncertainties in the cross-section calculation. The variation is 6% for diboson production [208], 13% for $t\bar{t}W$ production, 12% for $t\bar{t}Z$ production, and 8% for $t\bar{t}H$ production [191].

The theoretical uncertainty on the Drell–Yan background is evaluated by varying PDF eigenvectors of the nominal PDF set, PDF scale, α_S, electroweak corrections, and photon-induced corrections. The effect of the PDF choice is estimated by comparing the nominal PDF set to CT10NNLO [203], MMHT14 [209], NNPDF3.0 [93], ABM12 [210], HERAPDF2.0 [211, 212], and JR14 [213], and taking into account the largest deviations from the nominal PDF choice. The diboson production process is assigned an additional theoretical uncertainty by comparing the nominal SHERPA 2.2.1 prediction with the POWHEG prediction, giving the uncertainty ranging from 5% to 10%.

Furthermore, the theoretical uncertainty of the signal process was estimated. The theoretical uncertainty in the NLO cross-section for $pp \to H^{++}H^{--}$ is reported to be about 15% [35]. It includes the renormalization and factorization scale dependence and the uncertainty in the parton densities.

The uncertainty in the simulated $pp \to H^{++}H^{--}$ events is assessed by varying the tuned parameter sets in PYTHIA 8.186 and choosing alternative PDFs CTEQ6L1 and CT09MC1 [214], as will be discussed more in detail in Appendix A. The impact on the signal acceptance is found to be negligible.

8.5.3 *Total uncertainty*

Correlations between uncertainty sources are evaluated and used to estimate the total uncertainty in the SM background prediction. Individual uncertainties can be correlated, and do not necessarily add in quadrature to the total background uncertainty. The total relative systematic uncertainty after the fit and its components in all analysis regions are shown in Figure 66.

Table 12: Summary of systematic effects considered in the analysis. The systematic type and effect of the source (experimental/theoretical and normalization/shape) together with MC samples affected by the systematic effect are shown. "DY" denotes Drell–Yan process.

Systematic effect	Systematic type	Effect	Affected MC Samples
Luminosity	exp.	norm.	all
Expected yield fit	exp.	norm.	DY, diboson
Lepton efficiencies	exp.	shape + norm.	all
Lepton scale & resolution	exp.	shape + norm.	all
MC statistics	exp.	shape + norm.	all
Charge misidentification method	exp.	shape + norm.	-
Fake background method	exp.	shape	-
PDF choice	th.	shape + norm.	DY
PDF variation	th.	shape + norm.	DY
MC modelling	th.	shape + norm.	DY

The final estimate of the systematic uncertainties as determined by the fit is shown in the pull plot in Figure 67, which shows the relative difference compared to the nominal prediction. As mentioned, the uncertainties are constrained using data in the control regions during the fit. Most of the systematic uncertainties are obtained as $\pm 1\sigma$ variation from the nominal value. All post-fit systematic uncertainties, obtained with the best-fit values of nuisance parameters and using the fitted yields of diboson and Drell–Yan backgrounds, are shown in Figure 67, All systematic uncertainties are within $\pm 1\sigma$ when compared to the pre-fit values.

8.6 STATISTICAL ANALYSIS AND RESULTS

The statistical framework HistFitter [178] is used in the search for doubly charged Higgs bosons to perform a maximum-likelihood fit of the invariant mass distribution of the same-charge leptons in all control and signal regions, and the $\bar{M}$ distribution in four-lepton regions to obtain the numbers of signal and background events. The main goal is to determine 95% CL upper limits on the $pp \to H^{++}H^{--}$ production cross-section as a function of the $H^{\pm\pm}$ mass hypothesis for various branching ratio assumptions, using the CL_s method [177], as described in Section 7.6.

The likelihood is constructed as the product of a Poissonian probability density function describing the observed number of events, and Gaussian distributions to constrain the nuisance parameters related to the systematic uncertainties. Five additional free parameters are added for the Drell–Yan and the diboson background contributions to fit their yields in the analysis regions. These fits of the dominant backgrounds reduce the systematic uncertainty in the predicted background yield. All the fitted normalizations are found to be compatible with the SM predictions within the uncertainties.

The observed and expected yields in all control, validation, and signal regions used in the analysis after the fit are presented in Figure 68 and summarized in Tables 13, 14, and 15.

No significant excess is observed. The same-charge invariant mass distributions in the two- and four-lepton signal regions are shown in Figure 69, and in the three-lepton signal regions in Figure 70. In the four-lepton signal region, only one data event is observed: an $e^+\mu^+e^-\mu^-$ event with invariant masses of 228 GeV and 207 GeV for the same-charge lepton pairs, and its event display is shown in Figure 71.

Table 13: The number of predicted background events in **control regions** after the fit, compared to the data. Uncertainties correspond to the total uncertainties in the predicted event yields, and are smaller for the total than the sum of the components in quadrature due to correlations between these components. Due to rounding the totals can differ from the sums of components. Background processes with a negligible yield are marked with the en dash (–).

	OCCR $e^{\pm}e^{\mp}$	DBCR $e^{\pm}e^{\pm}e^{\mp}$	DBCR $e^{\pm}\mu^{\pm}\ell^{\mp}$	DBCR $\mu^{\pm}\mu^{\pm}\mu^{\mp}$	4LCR $\ell^{\pm}\ell^{\pm}\ell^{\mp}\ell^{\mp}$
Observed events	184 569	576	1025	797	140
Total background	184 570 ± 430	574 ± 24	1025 ± 32	797 ± 28	140 ± 12
Drell–Yan	169 980 ± 990	–	–	–	–
Diboson	5060 ± 900	449 ± 28	909 ± 35	775 ± 29	138 ± 12
Fakes	2340 ± 300	123 ± 15	113 ± 14	19.9 ± 6.5	1.31 ± 0.16
Top	7200 ± 250	1.58 ± 0.06	2.90 ± 0.11	2.04 ± 0.08	0.37 ± 0.01

As this search targets only decays of the $H^{\pm\pm}$ into light leptons, other final states X that fall outside of the scope of this search (such as τ leptons or W bosons) can be taken into account by reducing the lepton multiplicity of the final state. Furthermore, some models predict different branching ratio combinations to target specific neutrino mass models to distinguish the normal hierarchy, the inverted hierarchy, and the degenerate scenario. For these reasons, the final result of the fit is a lower limit on the two-dimensional grid of the $H^{\pm\pm}$ boson mass for any combination of light lepton branching ratios that sum to a certain value. The fit was performed for values of $B(H^{\pm\pm} \to \ell^{\pm}\ell^{\pm})$ from 1% to 5% in 1% intervals, and from 10% to 100% in 10% intervals. The total assumed branching ratio of $H^{\pm\pm}$ is therefore $B(H^{\pm\pm} \to e^{\pm}e^{\pm}) + B(H^{\pm\pm} \to e^{\pm}\mu^{\pm}) + B(H^{\pm\pm} \to \mu^{\pm}\mu^{\pm}) + B(H^{\pm\pm} \to X) = B(H^{\pm\pm} \to \ell^{\pm}\ell^{\pm}) + B(H^{\pm\pm} \to X) = 100\%$.

For $B(H^{\pm\pm} \to \ell^{\pm}\ell^{\pm}) = 100\%$ the production cross-section is excluded down to 0.1 fb. This exclusion corresponds to 3-4 signal events, which is the theoretical limit of a 95% CL exclusion at 36.1 fb^{-1} as ($\mathcal{L}_{\text{poiss}}(0|3) \simeq 0.05$) [173]. Representative cross-section upper limits as a function of the $H^{\pm\pm}$ boson mass are shown in Figure 72 for different branching ratio combinations. The wide one standard deviation discrepancy from 600 to 900 GeV, shown in Figure 72a, is caused by the two observed events in the same mass range in the electron channel of the three-lepton signal region.

Expected and observed limits for all $H^{\pm\pm} \to \ell^{\pm}\ell^{\pm}$ branching ratio combinations that sum to 100% are shown in Figure 73 for $H_L^{\pm\pm}$, and in Figure 74 for $H_R^{\pm\pm}$. Figures 76 and 77 present the results of the fit for $H_L^{\pm\pm}$ and $H_R^{\pm\pm}$, respectively. In these plots, only decays into $e^{\pm}e^{\pm}$, $\mu^{\pm}\mu^{\pm}$, and $e^{\pm}\mu^{\pm}$ final states are considered. The minimum limit for each value of $B(H^{\pm\pm} \to \ell^{\pm}\ell^{\pm})$ is shown. The minimum limit is obtained by taking the least stringent limit for any combination of branching ratios that sum to $B(H^{\pm\pm} \to \ell^{\pm}\ell^{\pm})$. The lower mass limits for all the lepton flavour combinations are similar, which indicates that the analysis is almost equally sensitive to each decay channel. Representative results for the $B(H^{\pm\pm} \to \ell^{\pm}\ell^{\pm}) < 100\%$ scans are presented in Figure 75. All scan results are shown in Ref. [2].

The observed lower mass limits are between 770 GeV and 870 GeV for $H_L^{\pm\pm}$ with $B(H^{\pm\pm} \to \ell^{\pm}\ell^{\pm}) = 100\%$ and are above 450 GeV for $B(H^{\pm\pm} \to \ell^{\pm}\ell^{\pm}) \geq 10\%$. The lower mass limits of

Table 14: The number of predicted background events in two-lepton and four-lepton **validation regions** (top) and three-lepton validation regions (bottom) after the fit, compared to the data. Uncertainties correspond to the total uncertainties in the predicted event yields, and are smaller for the total than the sum of the components in quadrature due to correlations between these components. Due to rounding the totals can differ from the sums of components. Background processes with a negligible yield are marked with the en dash (–).

	SCVR $e^{\pm}e^{\pm}$	SCVR $e^{\pm}\mu^{\pm}$	SCVR $\mu^{\pm}\mu^{\pm}$	4LVR $\ell^{\pm}\ell^{\pm}\ell^{\mp}\ell^{\mp}$
Observed events	3237	1162	1006	3
Total background	3330 ± 210	1119 ± 51	975 ± 50	4.62 ± 0.40
Drell–Yan	2300 ± 190	–	–	–
Diboson	319 ± 25	547 ± 23	719 ± 30	4.59 ± 0.4
Fakes	640 ± 65	502 ± 54	249 ± 47	–
Top	71.5 ± 6.8	70.5 ± 2.6	6.93 ± 0.27	0.033 ± 0.001

	3LVR $e^{\pm}e^{\pm}e^{\mp}$	3LVR $e^{\pm}\mu^{\pm}\ell^{\mp}$	3LVR $\mu^{\pm}\mu^{\pm}\mu^{\mp}$	3LVR $\mu^{\pm}\mu^{\pm}e^{\mp}, e^{\pm}e^{\pm}\mu^{\mp}$
Observed events	108	180	126	16
Total background	88.1 ± 5.8	192.9 ± 9.9	107.0 ± 5.1	27.0 ± 3.9
Diboson	64.4 ± 5.8	147.3 ± 9.0	100.9 ± 5.0	4.72 ± 0.79
Fakes	23.3 ± 3.0	43.9 ± 4.9	5.3 ± 1.2	21.3 ± 3.4
Top	0.50 ± 0.03	1.73 ± 0.09	0.82 ± 0.05	1.01 ± 0.15

$H_R^{\pm\pm}$ vary from 660 GeV to 760 GeV for $B(H^{\pm\pm} \to \ell^{\pm}\ell^{\pm}) = 100\%$ and are above 320 GeV for $B(H^{\pm\pm} \to \ell^{\pm}\ell^{\pm}) \geq 10\%$. The observed limits are consistent with the expected limits.

8.7 CONCLUSION AND SUMMARY

The search for doubly charged Higgs bosons in the same-charge dilepton invariant mass spectrum using $e^{\pm}e^{\pm}$, $e^{\pm}\mu^{\pm}$ and $\mu^{\pm}\mu^{\pm}$ final states was performed with 36.1 fb^{-1} of data from proton–proton collisions at $\sqrt{s} = 13$ TeV, recorded during the 2015 and 2016 data-taking periods by the ATLAS detector. No significant excess above the Standard Model prediction was found, and consequently lower limits are set on the mass of doubly charged Higgs bosons. The observed lower limits vary between 770 GeV and 870 GeV for the $H_L^{\pm\pm}$ mass assuming $B(H^{\pm\pm} \to \ell^{\pm}\ell^{\pm}) = 100\%$, and are above 450 GeV for $B(H^{\pm\pm} \to \ell^{\pm}\ell^{\pm}) \geq 10\%$ for any combination of partial branching ratios. The observed lower limits on the $H_R^{\pm\pm}$ mass range from 660 GeV to 760 GeV for $B(H^{\pm\pm} \to \ell^{\pm}\ell^{\pm}) = 100\%$ and are above 320 GeV for $B(H^{\pm\pm} \to \ell^{\pm}\ell^{\pm}) \geq 10\%$. The obtained lower limits on the $H_L^{\pm\pm}$ and $H_R^{\pm\pm}$ masses obtained in this search, assuming $B(H^{\pm\pm} \to \ell^{\pm}\ell^{\pm}) = 100\%$, are 300 GeV higher than those from the previous ATLAS analysis [215].

Table 15: The number of predicted background events in two-lepton and four-lepton **signal regions** (top) and three-lepton signal regions (bottom) after the fit, compared to the data. Uncertainties correspond to the total uncertainties in the predicted event yields, and are smaller for the total than the sum of the components in quadrature due to correlations between these components. Due to rounding the totals can differ from the sums of components. Background processes with a negligible yield are marked with the en dash (–).

	SR1P2L $e^{\pm}e^{\pm}$	SR1P2L $e^{\pm}\mu^{\pm}$	SR1P2L $\mu^{\pm}\mu^{\pm}$	SR2P4L $\ell^{\pm}\ell^{\pm}\ell^{\mp}\ell^{\mp}$
Observed events	132	106	26	1
Total background	160 ± 14	97.1 ± 7.7	22.6 ± 2.0	0.33 ± 0.23
Drell–Yan	70 ± 10	–	–	–
Diboson	30.5 ± 3.0	40.4 ± 4.5	20.3 ± 1.8	0.11 ± 0.06
Fakes	52.2 ± 5.0	53.1 ± 5.8	1.94 ± 0.47	0.22 ± 0.19
Top	7.20 ± 0.97	3.62 ± 0.53	0.42 ± 0.03	0.007 ± 0.002

	SR1P3L $e^{\pm}e^{\pm}e^{\mp}$	SR1P3L $e^{\pm}\mu^{\pm}\ell^{\mp}$	SR1P3L $\mu^{\pm}\mu^{\pm}\mu^{\mp}$	SR1P3L $\mu^{\pm}\mu^{\pm}e^{\mp}, e^{\pm}e^{\pm}\mu^{\mp}$
Observed events	11	23	13	2
Total background	13.0 ± 1.6	34.2 ± 3.6	13.2 ± 1.3	3.1 ± 1.4
Diboson	9.5 ± 1.3	23.1 ± 2.9	13.1 ± 1.3	0.27 ± 0.14
Fakes	3.3 ± 0.67	10.7 ± 1.7	–	2.6 ± 1.2
Top	0.14 ± 0.02	0.45 ± 0.04	0.12 ± 0.01	0.19 ± 0.08

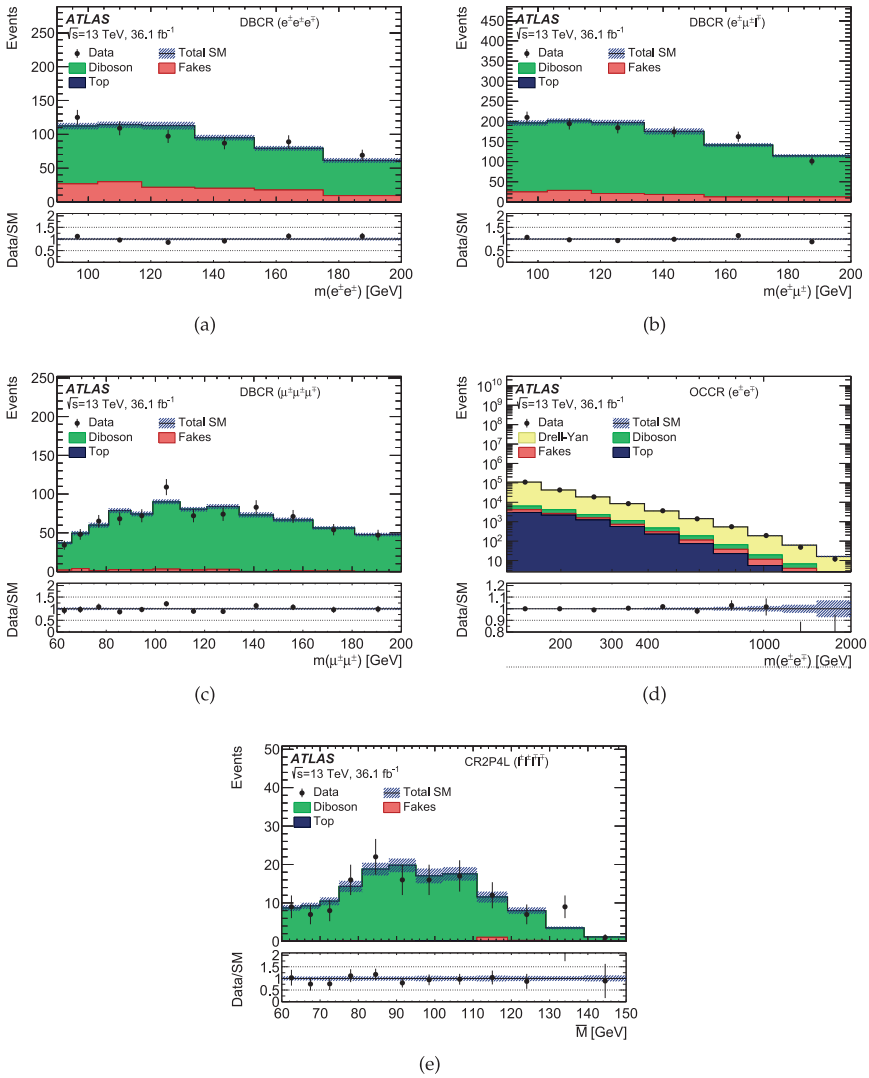

Figure 63: Post-fit distributions of $m(\ell^{\pm}\ell^{\pm})$ in control regions: (a) the electron–electron channel in diboson control region (DBCR), (b) the electron–muon channel in diboson control region (DBCR) (c) the muon–muon in diboson control region (DBCR), (d) the opposite-charge dielectron region (OCCR), and (e) the inclusive channel in four-lepton control region (4LCR). The hatched bands include all systematic uncertainties post-fit with the correlations between various sources taken into account.

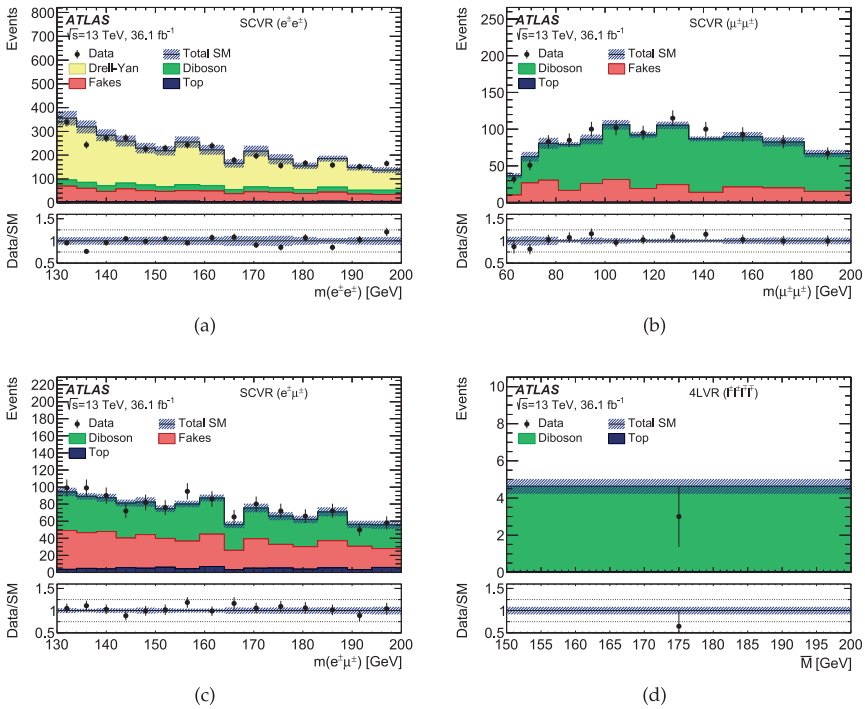

Figure 64: Post-fit distributions of $m(\ell^{\pm}\ell^{\pm})$ in two- and four-lepton validation regions: (a) the electron–electron, (b) the muon–muon, and (c) the electron–muon two-lepton validation regions, and (d) the four-lepton validation region. The hatched bands include all systematic uncertainties post-fit with the correlations between various sources taken into account.

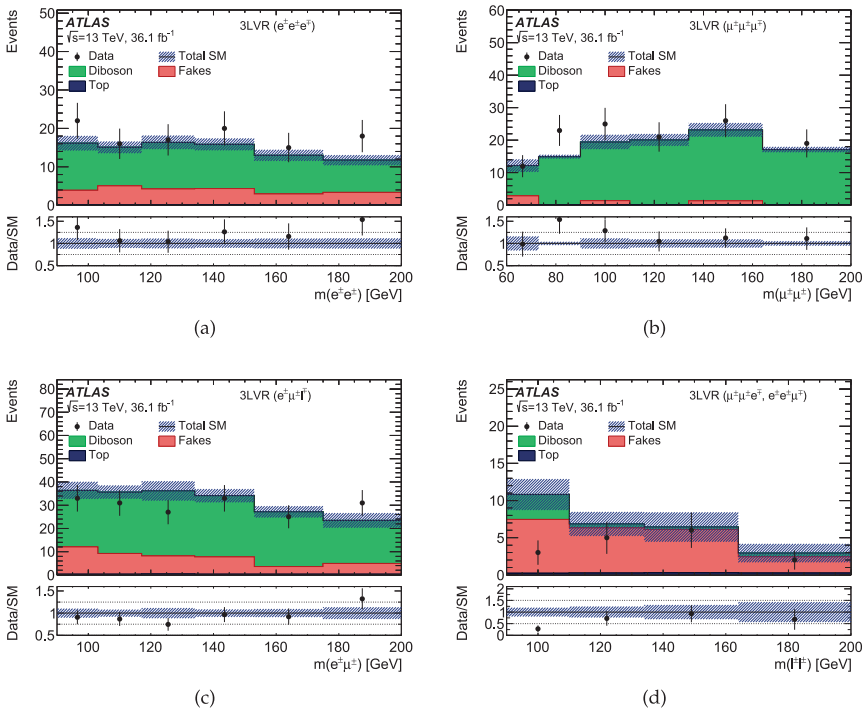

Figure 65: Post-fit distributions of $m(\ell^{\pm}\ell^{\pm})$ in three-lepton validation regions: (a) the three-electron validation region, (b) the three-muon validation region, (c) the 3LVR with an electron–muon same-charge pair ($e^{\pm}\mu^{\pm}\ell^{\mp}$), and (d) the 3LVR with a same-flavour same-charge pair ($e^{\pm}e^{\pm}\mu^{\mp}$ or $\mu^{\pm}\mu^{\pm}e^{\mp}$). The hatched bands include all systematic uncertainties post-fit with the correlations between various sources taken into account.

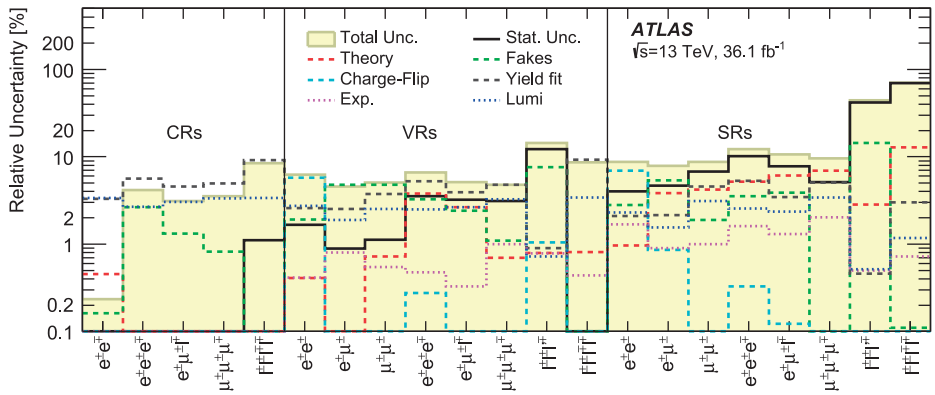

Figure 66: Relative uncertainties in the total background yield estimation after the fit. *Stat. Unc.* corresponds to reducible and irreducible background statistical uncertainties. *Yield fit* comes from the uncertainty arising from fitting the yield of diboson and Drell–Yan backgrounds. *Lumi* corresponds to the uncertainty in the luminosity. *Theory* indicates the theoretical uncertainties. Correspondingly, *Exp* indicates the experimental uncertainties (e.g. related to reconstruction efficiencies). *Fakes* is the uncertainty associated with the model of the fake background. The total background uncertainty is shown as *Total Unc.*.

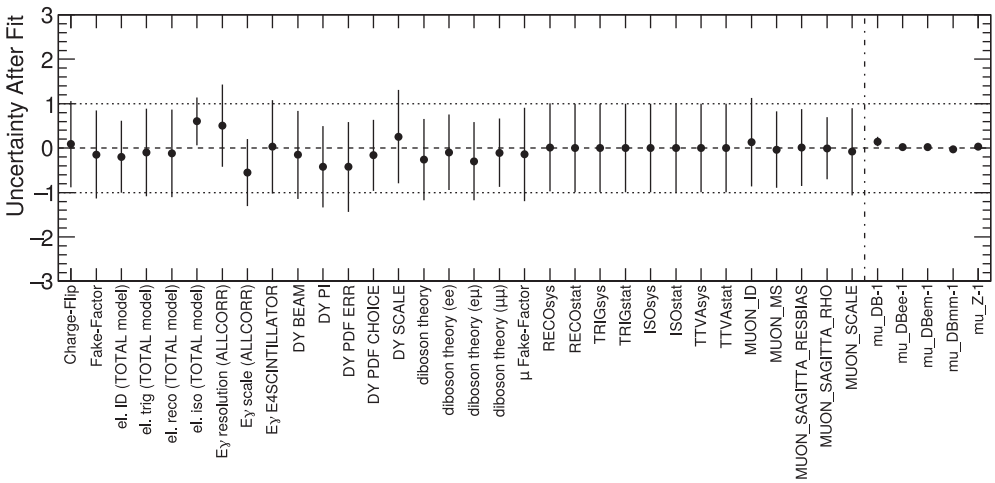

Figure 67: Systematic pulls in the fit showing the relative difference compared to the nominal prediction. The right side of the plot shows the fitted yields of the largest SM contributions: diboson and Drell–Yan processes. Values between -1 and 1 indicate the one standard deviation band of the uncertainty.

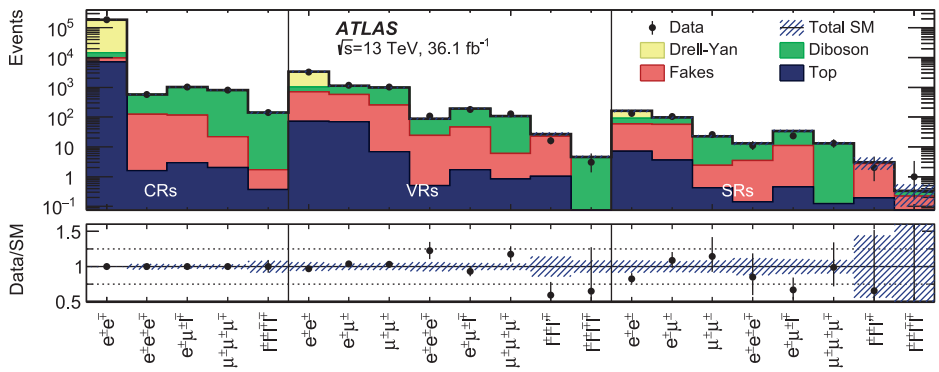

Figure 68: Number of observed and expected events in the control, validation, and signal regions for all channels considered. The background expectation is the result of the fit described in the text. The hatched bands include all systematic uncertainties post-fit with the correlations between various sources taken into account. The notation $\ell^{\pm}\ell'^{\pm}\ell^{\mp}$ indicates that the same-charge leptons have different flavours and $\ell^{\pm}\ell^{\pm}\ell'^{\mp}$ indicates that same-charge leptons have the same flavour, while the opposite-charge lepton has a different flavour.

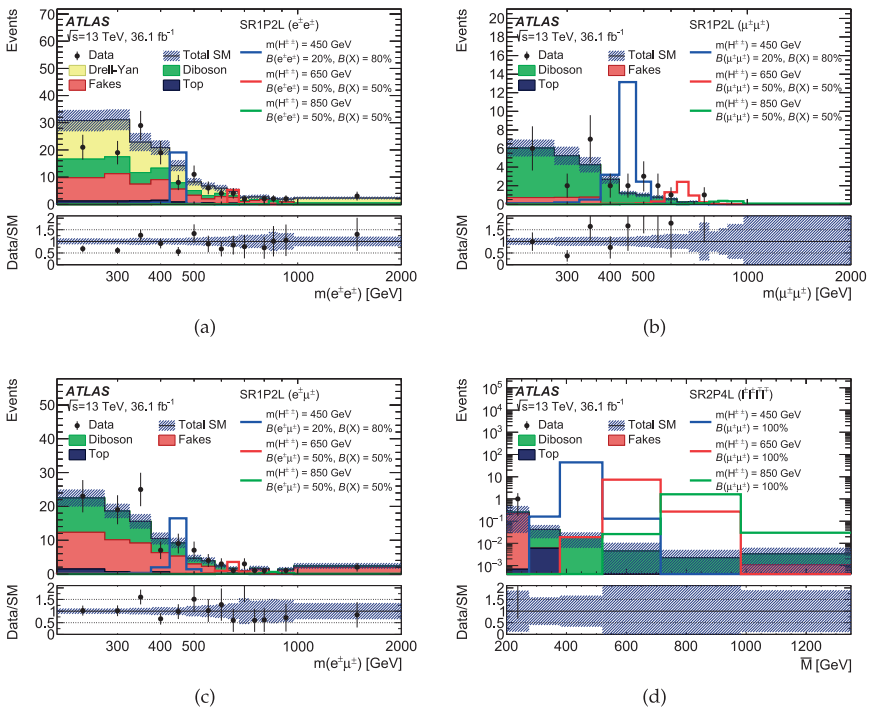

Figure 69: Distributions of $m(\ell^{\pm}\ell^{\pm})$ in representative signal regions, namely (a) the electron–electron two-lepton signal region (SR1P2L), (b) the muon–muon two-lepton signal region (SR1P2L), (c) the electron–muon two-lepton signal region (SR1P2L), and (d) the four-lepton signal region (SR2P4L). The hatched bands include all systematic uncertainties post-fit with the correlations between various sources taken into account. The solid coloured lines correspond to signal samples, normalized using the theory cross-section, with the $H^{\pm\pm}$ mass and decay modes marked in the legend.

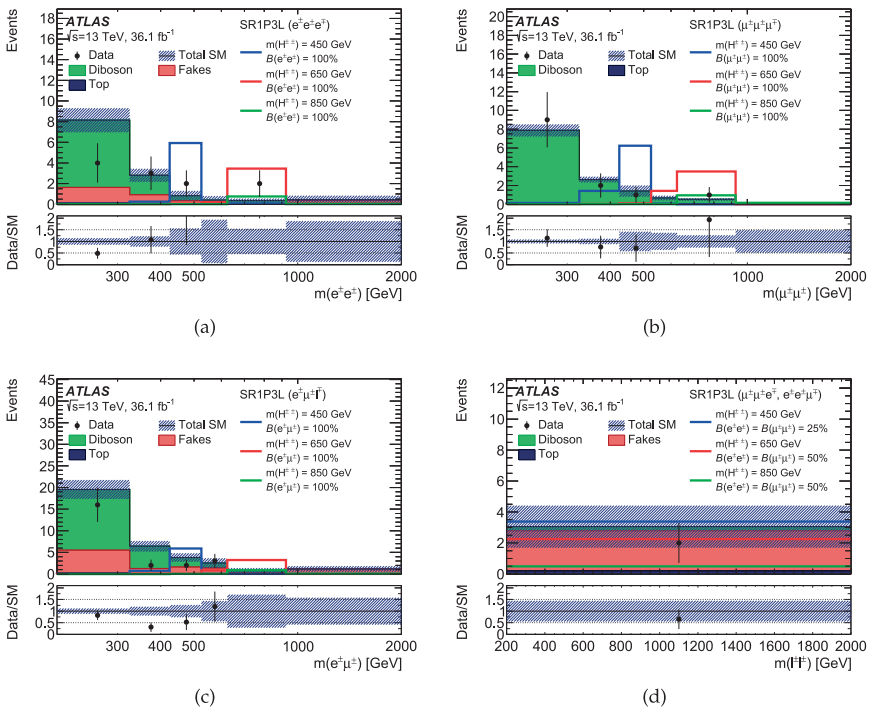

Figure 70: Distributions of $m(\ell^{\pm}\ell^{\pm})$ in three-lepton signal regions, in (a) the three-electron SR (SR1P3L), (b) the three-muon SR (SR1P3L), (c) the SR1P3L with an electron–muon same-charge pair ($e^{\pm}\mu^{\pm}\ell^{\mp}$), and (d) the SR1P3L with a same-flavour same-charge pair ($e^{\pm}e^{\pm}\mu^{\mp}$ or $\mu^{\pm}\mu^{\pm}e^{\mp}$). The hatched bands include all systematic uncertainties post-fit with the correlations between various sources taken into account. The solid coloured lines correspond to signal samples, normalized using the theory cross-section, with the $H^{\pm\pm}$ mass and decay modes marked in the legend.

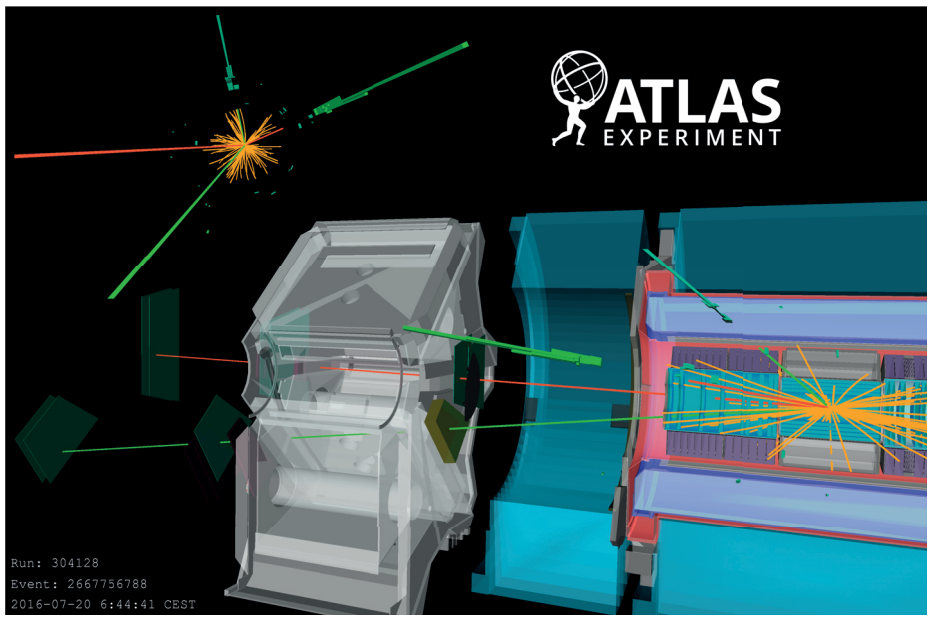

Figure 71: Event display of the single data event in the four lepton signal region (SR 2P4L). It is an $e^+\mu^+e^-\mu^-$ event with the same-charge invariant masses of 228 GeV and 207 GeV.

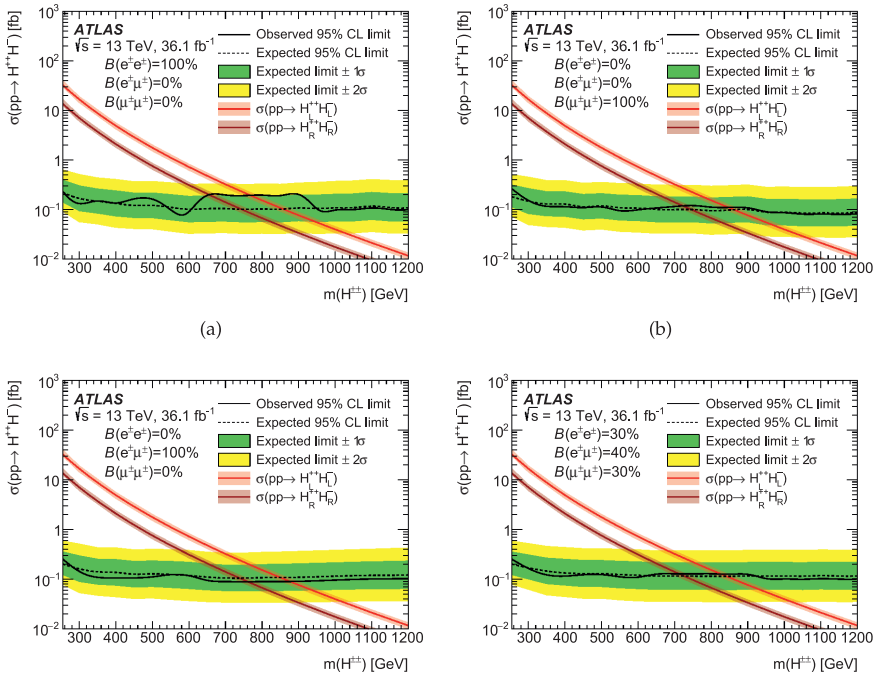

Figure 72: Upper limit on the cross-section for $pp \to H^{++}H^{--}$ for several branching ratio values presented as $B(ee)/B(e\mu)/B(\mu\mu)$: (a) 100%/0%/0%, (b) 0%/0%/100%, (c) 0%/100%/0%, and (d) 30%/40%/30%. The theoretical uncertainty in the cross-section for $pp \to H^{++}H^{--}$ is presented with the shaded band around the central value.

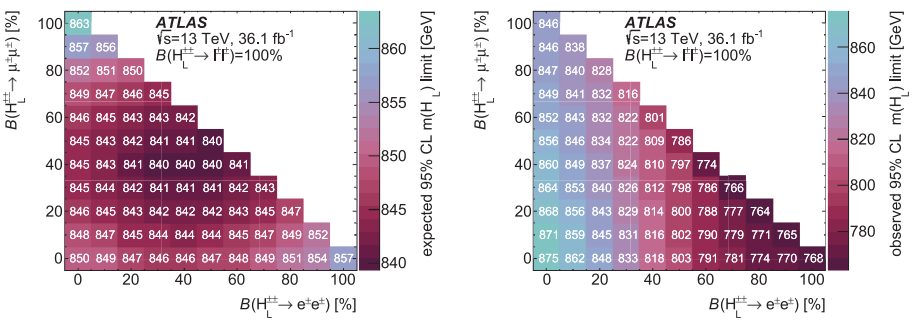

Figure 73: The (a) expected and (b) observed lower limits on the $H_L^{\pm\pm}$ boson mass for all branching ratio combinations that sum to 100%.

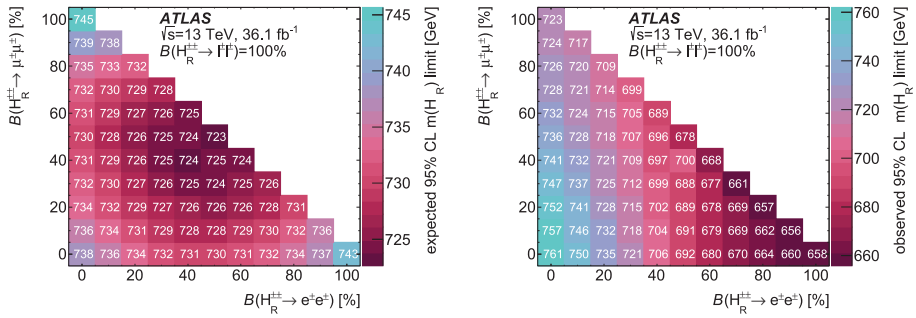

(a) (b)

Figure 74: The (a) expected and (b) observed lower limits on the $H_R^{\pm\pm}$ boson mass for all branching ratio combinations that sum to 100%.

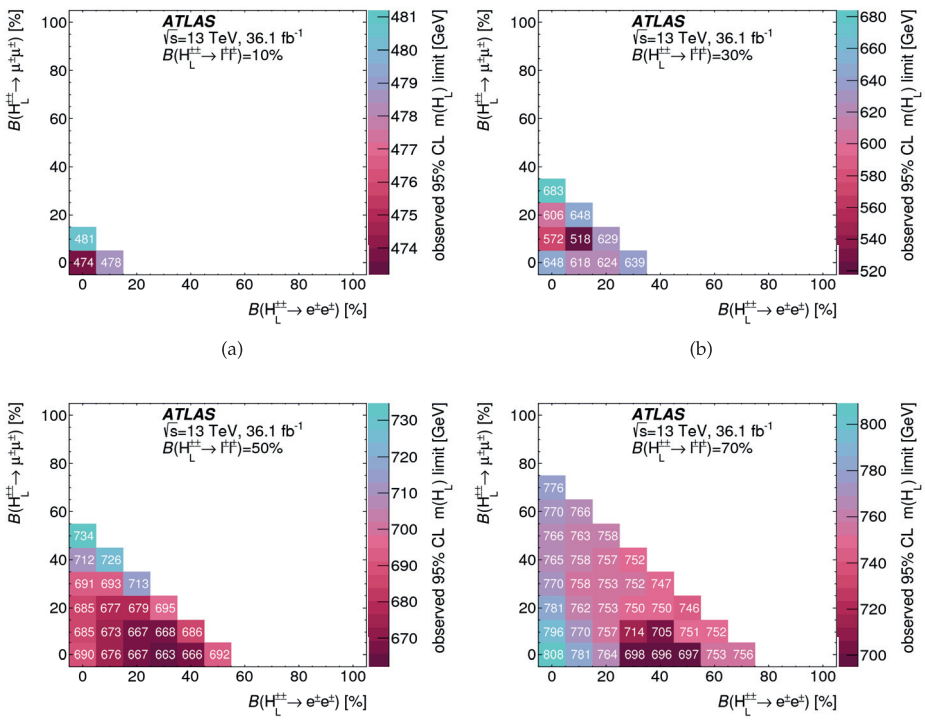

(a) (b)

(c) (d)

Figure 75: The observed lower limits on the $H_L^{\pm\pm}$ boson mass for all branching ratio combinations that sum to (a) 10%, (b) 30%, (c) 50%, and (d) 70%.

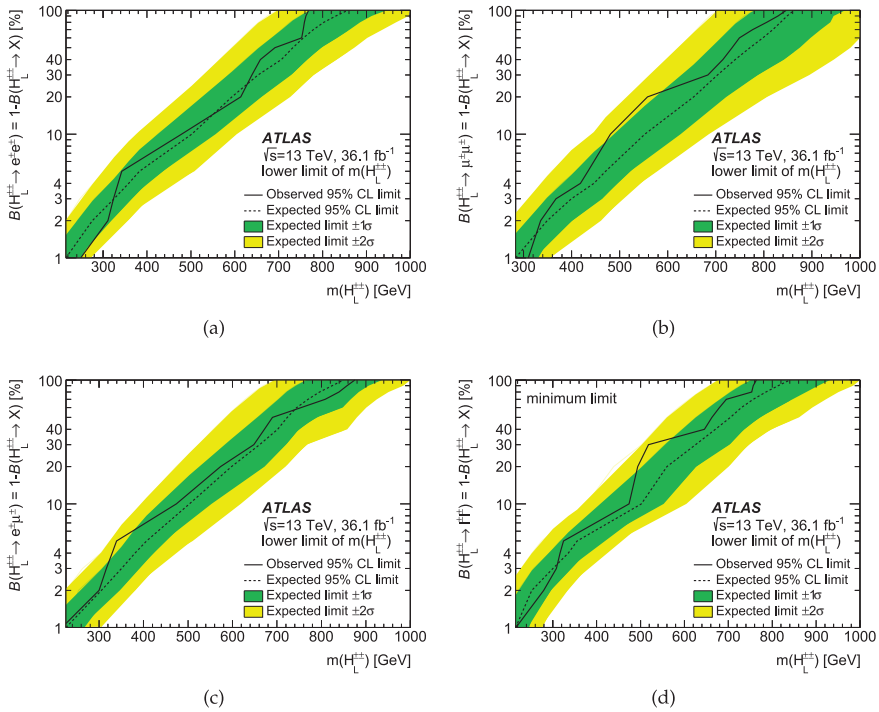

Figure 76: Lower limit on the $H_L^{\pm\pm}$ boson mass as a function of the branching ratio $B(H_L^{\pm\pm} \to \ell^{\pm}\ell^{\pm})$, for (a) $H_L^{\pm\pm}$ decays only into electrons and "X", (b) $H_L^{\pm\pm}$ decays only into muons and "X", and (c) $H_L^{\pm\pm}$ decays only into electron–muon pairs and "X", with "X" not entering any of the signal regions. Finally, (d) shows the minimum observed and expected limit as a function of $B(H_L^{\pm\pm} \to \ell^{\pm}\ell^{\pm})$.

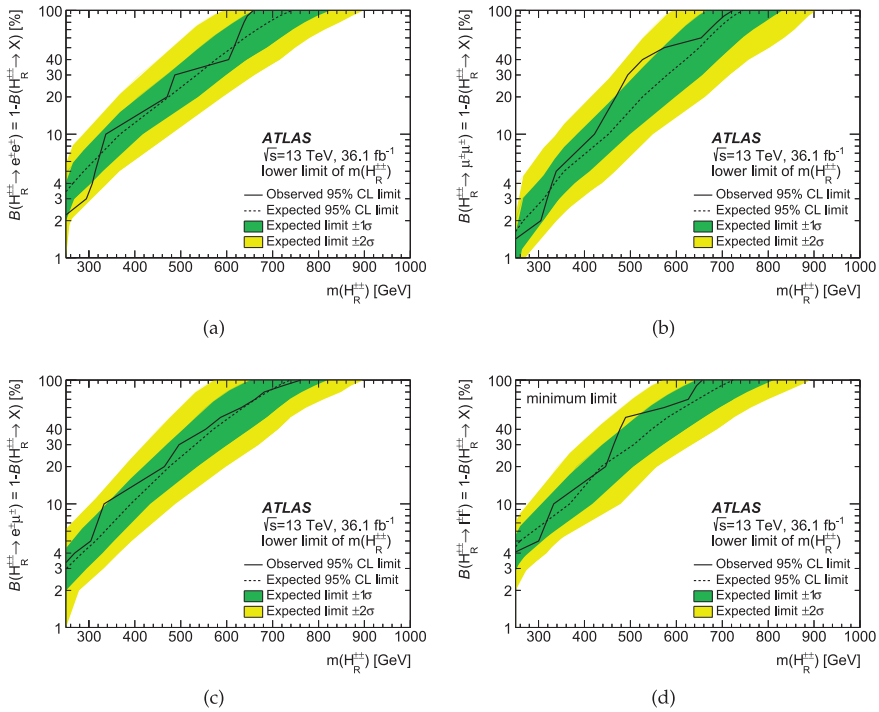

Figure 77: Lower limit on the $H_R^{\pm\pm}$ boson mass as a function of the branching ratio $B(H_R^{\pm\pm} \to \ell^{\pm}\ell^{\pm})$, for (a) $H_R^{\pm\pm}$ decays only into electrons and "X", (b) $H_R^{\pm\pm}$ decays only into muons and "X", and (c) $H_R^{\pm\pm}$ decays only into electron–muon pairs and "X", with "X" not entering any of the signal regions. Finally, (d) shows the minimum observed and expected limit as a function of $B(H_R^{\pm\pm} \to \ell^{\pm}\ell^{\pm})$.

9 SEARCH FOR DOUBLY CHARGED HIGGS BOSONS WITH 139 FB^{-1}

The second search for doubly charged Higgs bosons covered in this thesis uses the full Run 2 dataset collected in 2015-2018 corresponding to the integrated luminosity of 139 fb^{-1}. This search adds hadronically decaying taus into the analysis, hence covering all lepton flavour combinations of the $H^{\pm\pm}$ boson decays: $H^{\pm\pm} \to \ell^{\pm}\ell^{\pm}$, $H^{\pm\pm} \to \ell^{\pm}\tau^{\pm}_{\text{had}}$, and $H^{\pm\pm} \to \tau^{\pm}_{\text{had}}\tau^{\pm}_{\text{had}}$, where ℓ denotes electrons and muons, which can also originate from leptonic tau decays. Throughout this Chapter, τ denotes a hadronically decaying tau. With adding taus into the search, the analysis can probe if the doubly charged Higgs bosons have larger, mass-dependent couplings to the third-generation leptons, which would lead to an enhancement of decays into tau leptons. Furthermore, tau-inclusive final states form a majority of all possible final state combinations and therefore significantly more phase-space can be utilized in the search. The analysis regions including final states with electrons and muons are further optimized with respect to the search presented in Chapter 8, increasing the sensitivity to find new physics. In the absence of evidence for a signal, lower limits on the mass of the $H^{\pm\pm}$ boson are set at the 95% confidence level.

Section 9.1 describes the datasets used. Event and physics object selection are presented in Section 9.2. Section 9.3 describes how different backgrounds are estimated in order to reach very good agreement between the SM predictions and the observed data. The distributions in the control and validation regions are presented in Section 9.4, and the systematic uncertainties in Section 9.5. Finally, the statistical analysis and results are presented in Section 9.6.

9.1 DATASET AND SIMULATED EVENT SAMPLES

9.1.1 *Data sample*

The data were collected at $\sqrt{s} = 13\,\text{TeV}$ during the LHC Run 2 in 2015–2018, corresponding to an integrated luminosity of 139 fb^{-1}. The average number of pp interactions per bunch crossing in the dataset is $\langle\mu\rangle = 33.7$. The uncertainty in the combined 2015–2018 integrated luminosity is 1.7% [88], obtained using the LUCID-2 detector [216] for the primary luminosity measurements.

9.1.2 *Triggers*

Different triggers were used in different channels. In the electron and muon channels, di-electron and dilepton triggers are used. Combined electron–muon triggers are used in the mixed channel containing both electrons and muons. Similarly, in the channels containing both light leptons and taus, combined electron–tau and muon–tau triggers are used together with a single–tau trigger. Trigger requirements are specific and unprescaled for each year of the Run 2 data taking, and are summarized in Tables 16 and 17.

The electron triggers require electrons to have at least `lhloose` (loose) and `lhvloose` (very loose) offline reconstruction level without additional isolation requirements. Additionally, for the 2016, 2017 and 2018 triggers no information on the impact parameter d_0 was used, as stated by `"nod0"` in the trigger name. The muon triggers require muons to satisfy the `Medium`

Table 16: A summary of the used triggers in 2015 and 2016.

	2015	2016
ee	HLT_2e12_lhloose_L12EM10VH	HLT_2e17_lhvloose_nod0
$e\mu$	HLT_e17_lhloose_mu14	HLT_e17_lhloose_nod0_mu14
$\mu\mu$	HLT_mu18_mu8noL1	HLT_mu22_mu8noL1
$e\tau$	HLT_e17_lhmedium_tau80_medium1_tracktwo	HLT_e17_lhmedium_nod0_tau80_medium1_tracktwo
$\mu\tau$	HLT_mu14_tau35_medium1_tracktwo	HLT_mu14_ivarloose_tau35_medium1_tracktwo
$\tau\tau/\tau\ell$	HLT_tau160_medium1_tracktwo	HLT_tau160_medium1_tracktwo

Table 17: A summary of the used triggers in 2017 and 2018.

	2017+2018
ee	HLT_2e24_lhvloose_nod0
$e\mu$	HLT_e17_lhloose_nod0_mu14
$\mu\mu$	HLT_mu22_mu8noL1
$e\tau$	HLT_e17_lhmedium_nod0_tau80_medium1_tracktwo
$\mu\tau$	HLT_mu14_ivarloose_tau35_medium1_tracktwo
$\tau\tau/\tau\ell$	HLT_tau160_medium1_tracktwo

working point at the trigger level, requiring $p_{\mathrm{T}}^{\mathrm{varcone30}}/p_{\mathrm{T}}(\mu) < 0.07$ isolation criteria. In the mixed channel, the trigger selects events with one electron and one muon with a p_{T} threshold of 17 GeV and 14 GeV, respectively. In the tau-inclusive triggers, specific p_{T} criteria are applied for both the light lepton and hadronic tau, requiring to have at least one but at most three tracks in the Inner Detector, as indicated by `"tracktwo"`.

9.1.3 *Simulated samples*

Prompt, irreducible background from the SM processes is formed of pairs of same-charge leptons, caused mainly by diboson ($W^{\pm}W^{\pm}$ / ZZ / WZ) and $t\bar{t}X$ processes ($t\bar{t}W$, $t\bar{t}Z$, and $t\bar{t}H$). Prompt background predictions were obtained using simulated events, summarized in Table 18. There are only a few differences with respect to the previous search when considering prompt background simulation. The Drell–Yan process is generated using SHERPA instead of POWHEG-BOX, and the single top cross-sections are derived up to NNLO. Furthermore, three- and four-top samples are added to the analysis. Finally, the diboson samples are updated with a newer version of SHERPA. As further details on the parton showers, PDF sets and tunes are shown in Table 18 and were described earlier in Section 8.1, they will not be repeated here. The MC samples are normalized using theoretical cross-sections in most of the cases. However, the yields of Drell–Yan and diboson samples are taken as free parameters in the final likelihood fit.

The signal samples were generated at LO using PYTHIA 8.186, which uses the left-right-symmetry model scenario of $H^{\pm\pm}$ production. As the search targets both at the light lepton and hadronic tau final states, two sets of signal samples are used. The first set is the same as

in the previous analysis, containing only light leptons, and the second set contains at least one hadronic tau in the final state, as described in detail in Section 7.3.

Table 18: Simulated signal and background event samples: the corresponding event generator, parton shower, cross-section normalization, PDF set used for the matrix element and set of tuned parameters are shown for each sample.

Physics process	Event generator	ME PDF set	Cross-section normalization	Parton shower	Parton shower tune
Signal $H^{\pm\pm}$	Pythia 8.186	NNPDF2.3NLO [168]	NLO	Pythia 8.186	A14
Drell-Yan					
$Z/\gamma^* \to ee/\mu\mu/\tau\tau$	Sherpa 2.2.1	NNPDF3.0NNLO [93]	NLO [184]	Pythia 8.212	Sherpa default
Top					
$t\bar{t}$	Powheg-Box v2	NNPDF3.0NNLO	NNLO [186]	Pythia 8.212	A14
Single t	Powheg-Box v2	NNPDF3.0NNLO	NNLO [186]	Pythia 8.212	A14
$3t$, $4t$	MadGraph5_aMC@NLO	NNPDF2.3LO	LO	Pythia 8.212	A14
$t\bar{t} + W/Z$	MadGraph5_aMC@NLO	MEN30NLO	NNLO	Pythia 8.212	A14
Diboson					
ZZ, WZ	Sherpa 2.2.1 & 2.2.2 [102]	NNPDF3.0NNLO	NLO [217]	Pythia 8.212	Sherpa default
Multiboson					
WWW, WWZ, WZZ, ZZZ	Sherpa 2.2.1 & 2.2.2	NNPDF3.0NNLO	NNLO	Pythia 8.212	Sherpa default

9.2 EVENT RECONSTRUCTION AND SELECTION

9.2.1 *Event reconstruction*

The doubly charged Higgs search targets final states with same-charge lepton pairs: $\ell^\pm\ell^\pm$, $\ell^\pm\tau^\pm$, $\tau^\pm\tau^\pm$, where $\ell = e, \mu$. All physics objects are reconstructed as described earlier in Section 5.5. Additional selection criteria are applied to reduce the backgrounds and to increase the sensitivity of the search.

As earlier, all selected events have at least one reconstructed primary vertex with at least two associated tracks with $p_T > 400\,\text{MeV}$, and pass the data quality requirements and specific event-level vetos to reject bad and corrupted events. Selected charged leptons are classified in the *tight* category containing signal-like leptons, and and the *loose* category containing mostly fake leptons used for the fake-background estimation.

9.2.2 *Electrons*

Electron selection in the full Run 2 analysis is summarized in Table 19. The electron identification and isolation selection was further optimized after the first analysis presented earlier. There is an interplay between signal and background yields. Even if some signal events are lost by requiring a specific working point, tighter cuts and working points may be used if large amounts of background can be rejected at the same time. The figure of merit chosen for the optimization is significance Z [176], defined as

$$Z = \sqrt{2[(s+b)\ln(1+\frac{s}{b}) - s]} \tag{69}$$

where s is the signal yield and b is the background.

For example in the two-electron signal region, tightening the tight electron identification criteria from the previously used `LHMedium` working point to `LHTight` working point decreased the estimated background yield by 12%, but the loss in sensitivity is only about 1.2% across various $H^{\pm\pm}$ mass points. Two isolation working points `FCLoose` and `FCTight` were also compared. While `FCTight` isolation working point would both decrease background and increase sensitivity to doubly charged Higgs signal by a few percent, it significantly decreased signal yields in other analyses using the same derived dataset. Therefore, the tight electrons used in the analysis are chosen to pass `LHTight` identification level and `FCLoose` isolation requirements in order to further suppress the jet background. All electrons are required to pass at least the `LHLooseBL` identification level, where at least one pixel hit in the B-layer is required in addition to `LHLoose` criteria.

Furthermore, the electron p_{T} cut was increased by 10 GeV in order to reduce the number of fake and background electrons. This selection has a negligible impact on the signal yield because the electrons from the doubly charged Higgs boson decays are expected to have high momenta. Other selection cuts were kept consistent with the previous analysis, selecting only isolated, prompt electrons originating from the primary vertex.

Table 19: A summary of the baseline electron definitions in the full Run 2 analysis.

Requirement	Signal electrons (tight)	Background electrons (loose)
Identification	`LHTight`	`LHLooseBL` `OR`
Isolation	`FCLoose`	fail `FCLoose`
p_{T} cut	$p_{\mathrm{T}} > 40\,\mathrm{GeV}$	$p_{\mathrm{T}} > 40\,\mathrm{GeV}$
η cut	$\lvert\eta\rvert < 2.47$ and veto $1.37 < \lvert\eta\rvert < 1.52$	$\lvert\eta\rvert < 2.47$ and veto $1.37 < \lvert\eta\rvert < 1.52$
$\lvert d_0\rvert/\sigma_{d_0}$ cut	$\lvert d_0\rvert/\sigma_{d_0} < 5.0$	$\lvert d_0\rvert/\sigma_{d_0} < 5.0$
$\lvert z_0 \sin(\theta)\rvert$ cut	$\lvert z_0 \sin(\theta)\rvert < 0.5\,\mathrm{mm}$	$\lvert z_0 \sin(\theta)\rvert < 0.5\,\mathrm{mm}$

9.2.3 *Muon selection*

Muon selection in the full Run 2 analysis is summarized in Table 20. As for electrons, the muon identification and isolation selection was further optimized after the first analysis. After careful comparions of various working points, the muon quality and isolation working point were chosen to remain unchanged, selecting signal muons to satisfy `Medium` quality with `FixedCutTightTrackOnly` isolation. Other improvements include increasing the muon p_{T} threshold to 40 GeV to further reject background muons, and applying a tighter criterion on the impact parameter $\lvert d_0\rvert/\sigma_{d_0}$ to select tracks compatible with a primary vertex.

9.2.4 *Tau selection*

As described in Section 5.5.6, the reconstruction of the visible decay products of hadronic tau decays starts with a jet reconstruction, clustered using the anti-k_t algorithm. The three-dimensional topological clusters of calorimeter cells are used as seeds of the hadronic tau candidates. As the hadronic decays are characterized by the presence of one or three charged

Table 20: Summary of the baseline muon definitions in the full Run 2 analysis.

Requirement	Signal muons (tight)	Background muons (loose)
Quality	`Medium`	`Medium`
Isolation	`FixedCutTightTrackOnly`	fail `FixedCutTightTrackOnly`
p_{T} cut	$p_{\mathrm{T}} > 40\,\mathrm{GeV}$	$p_{\mathrm{T}} > 40\,\mathrm{GeV}$
η cut	$\lvert\eta\rvert < 2.5$	$\lvert\eta\rvert < 2.5$
$\lvert d_0\rvert/\sigma_{d_0}$ cut	$\lvert d_0\rvert/\sigma_{d_0} < 3.0$	$\lvert d_0\rvert/\sigma_{d_0} < 3.0$
$\lvert z_0 \sin(\theta)\rvert$ cut	$\lvert z_0 \sin(\theta)\rvert < 0.5\,\mathrm{mm}$	$\lvert z_0 \sin(\theta)\rvert < 0.5\,\mathrm{mm}$

tracks, tracks are associated to the $\tau_{\mathrm{had-vis}}$ candidate. In this search, the number of associated tracks has to be exactly one or three, and the total sum of charges has to be ± 1. The $\tau_{\mathrm{had-vis}}$ candidate must have the transverse momentum greater than 20 GeV, and it must be within the pseudorapidity range $|\eta| < 2.5$, excluding the transition region between the barrel and endap calorimeters.

The tau identification is performed using a multivariate boosted decision tree (BDT) algorithm to discriminate against quark- and gluon-initiated jets, requiring all taus passing the `AtLeastVeryLoose` working point based on the jet BDT score. The signal taus are required to pass `Medium` jet BDT score, leading to higher rejection of jets misidentified as taus. An additional likelihood-based electron veto, `EleBDTLoose`, is used to reduce the number of electrons misidentified as hadronic taus. No separate discriminant for muons is applied, but they are mostly rejected by the overlap removal process. All the selection criteria are summarized in Table 21.

Table 21: Summary of the baseline hadronic tau definitions in the full Run 2 analysis.

Requirement	Signal taus (tight)	Background taus (loose)
Identification	`Medium`	`AtLeastVeryLoose`
p_{T} cut	$p_{\mathrm{T}} > 20\,\mathrm{GeV}$	$p_{\mathrm{T}} > 20\,\mathrm{GeV}$
η cut	$\lvert\eta\rvert < 2.5$ and veto $1.37 < \lvert\eta\rvert < 1.52$	$\lvert\eta\rvert < 2.47$ and veto $1.37 < \lvert\eta\rvert < 1.52$
Track selection	1 or 3 tracks	1 or 3 tracks
Charge	$\lvert Q\rvert = 1$	$\lvert Q\rvert = 1$
Electron rejection	`EleBDTLoose`	`EleBDTLoose`

9.2.5 *Jet selection*

The analysis tries to be as inclusive as possible by selecting events with any number of jets reconstructed using the anti-k_t algorithm with a radius parameter $R = 0.4$. The only exception comes from the b-jet veto, which is implemented in order to reduce the fake background. The b-jets are identified with a multivariate discriminant, and the working point used in this search has an efficiency of 77% for b-jet tagging.

9.2.5.1 *Missing Transverse Momentum*

The missing transverse energy $E_{\mathrm{T}}^{\mathrm{miss}}$ arises from any undetected energy in the event, either from neutrinos escaping detection or other particles falling outside the acceptance, or any event misreconstruction. The $E_{\mathrm{T}}^{\mathrm{miss}}$ is computed as the imbalance of the total visible p_{T} in the event with contributions from all visible objects in the event which are selected, reconstructed and fully calibrated. Furthermore, the so-called soft-term, accounting for all tracks in the event which are not associated with any visible object but are associated with the identified hard-scatter vertex, are included. This is motivated by an improved performance in $E_{\mathrm{T}}^{\mathrm{miss}}$ reconstruction against pile-up.

9.2.5.2 *Overlap removal*

In order to prevent reconstruction of one object as two different objects, and to help in isolation, overlap removal procedure is applied. Geometrically overlapping objects are removed in the following order: first, $\tau_{\mathrm{had-vis}}$ candidates within $\Delta R < 0.2$ of electrons and muons are excluded. Second, electron candidates sharing a track with any muon candidates are removed. After that, possible overlaps between electrons and jets are resolved. If a jet is within $\Delta R < 0.2$ of an electron, the jet is rejected. Electrons within $\Delta R < 0.4$ of the remaining jets are discarded. If a jet is within $\Delta R < 0.4$ of a muon, and the jet features less than 3 tracks, the jet is removed. Otherwise the muon is discarded. Finally, jets within $\Delta R < 0.2$ of a hadronic tau are excluded.

9.2.5.3 *Used derivations*

As earlier, the search makes use of various data sample derivations that have additional criteria for event selection. As described in Section 8.2.1.5, the `EXOT12` derivation is used for the main analysis involving only light lepton final states, `EXOT19` for electron fake factor estimation, and `EXOT22` for muon fake factor estimation. In addition to those three derivations, two additional derivations are used in order to study events involving hadronic taus:

- `SUSY3`: select events containing at least one `Loose` 1- or 3-prong hadronic tau with $p_{\mathrm{T}} > 15\,\mathrm{GeV}$ after the final calibration. This is the main derivation used in channels including taus.
- `SUSY11`: require events with a single-jet trigger. Selected hadronic taus must be 1- or 3-prong and have $p_{\mathrm{T}} > 15\,\mathrm{GeV}$ after the final calibration. The tau fake factors are measured using this derivation.

9.2.6 *Event selection and analysis regions*

Events are categorized in several analysis regions defined by a selection on the events and objects reconstructed in the events. Control regions constrain free parameters in the statistical analysis, validation regions are used to validate methods and scale factors for background estimation, and signal regions are designed to target at signal events of doubly charged Higgs decaying into same-charge lepton pairs. The analysis regions are further divided into channels depending on the flavour combination of the same-charge pair in order to enhance sensitivity: $e^{\pm}e^{\pm}$, $e^{\pm}\mu^{\pm}$, $\mu^{\pm}\mu^{\pm}$, $e^{\pm}\tau^{\pm}$, $\mu^{\pm}\tau^{\pm}$, and $\tau^{\pm}\tau^{\pm}$. All regions are strictly orthogonal, which is ensured by requiring exact lepton multiplicity, meaning that for example dielectron regions do not have any hadronic taus.

The lepton multiplicity in the event is used to categorize the analysis regions in 2-, 3- and 4-lepton regions. This categorization tries to maximize the signal yield despite possible detector acceptance or event reconstruction efficiency limitations which leave one or two leptons

undetected. The main discriminating variable to define the type of all regions is the invariant mass of the same-charge lepton pairs. The same-charge lepton pairs are required to have the invariant masses above 200 GeV in the signal regions, and below 200 GeV in the control and validation regions. In all regions, events with at least one b-tagged jet are vetoed in order to suppress background events arising from top-quark decays. In the following, precise descriptions of each of the analysis regions are given.

9.2.7 *Control and validation regions*

The search uses multiple control and validation regions are designed to constrain and validate specific backgrounds. Fake background is present in all of the analysis regions and is estimated for each lepton flavour separately using the data-driven fake factor method, as will be described in Section 9.3.4. Background from prompt leptons is estimated using simulated events.

The control and validation region definitions including *only light leptons* are almost identical compared to the previous search presented in Section 8.2.3 and summarized in Table 9. Only difference with respect to the previous analysis in the light lepton regions is in the two- and three-lepton signal regions, where the $p_{\mathrm{T}}(\ell^{\pm}\ell^{\pm})$ requirement was increased to 300 GeV in order to reject more background. The distributions in the control and validation regions are presented in Section 9.4. All validation and control regions have only negligible signal contamination: mostly less than 3%, with an exception of the four-lepton validation region with light leptons where the signal contamination is approximately 7.5% for the already excluded mass point of 300 GeV.

The analysis regions including *hadronically decaying taus* are different from those with light leptons only mostly due to different background composition and the fact that events have additional missing transverse energy from neutrinos. The tau-inclusive signal regions are defined in Table 22 and will be further discussed in Section 9.2.8. Various control and validation regions were tested by inverting each of the signal region cuts one at a time to validate the tau fake estimation, which will be presented in Section 9.3.4.3. Tau-inclusive control and validation regions are divided into different groups depending on the lepton flavour combination and lepton multiplicity. Two control regions are defined, and they require exactly

- Two same-charge hadronic taus and zero light leptons, or
- One same-charge lepton pair, and three leptons of which at least one is a hadronic tau and at least one is a light lepton.

Similarly, four orthogonal validation regions are designed to validate the fake background estimation in different lepton flavour combinations and multiplicities, requiring exactly

- One same-charge lepton pair with a hadronic tau and a light lepton,
- One same-charge tau pair with exactly three taus,
- Two same-charge tau pairs ($\tau^{+}\tau^{+}\tau^{-}\tau^{-}$), or
- Two same-charge lepton pairs with at least one tau and one light lepton.

In the tau-inclusive control and validation regions, a Z veto and a b-jet veto are applied. If the mass of the opposite-charge lepton pair is within 10 GeV from the Z boson mass ($81.2\,\mathrm{GeV} < m(\ell^{+}\ell^{-}) < 101.2\,\mathrm{GeV}$), the event is rejected, discarding mainly diboson events. The b-jet veto is applied in all regions to reduce fake background. Furthermore, the total transverse mass of the same-charge pair and missing transverse energy is required to be less than 300 GeV in order to not select events from the signal region.

Table 22: Summary of the tau-inclusive signal regions used in the analysis. Hadronic taus are denoted τ while light leptons are denoted $\ell = e, \mu$.

Selection \ Region	SR1SF2L	SR1DF2L	SR1P3τ	SR1P3L-$\ell\tau$	SR2P4τ	SR2P4L-$\ell\tau$
channel	$\tau^{\pm}\tau^{\pm}$	$e^{\pm}\tau^{\pm}$ $\mu^{\pm}\tau^{\pm}$	$\tau^{\pm}\tau^{\pm}\tau^{\mp}$	$\tau^{\pm}\tau^{\pm}\ell^{\mp}$ $\ell^{\pm}\ell^{\pm}\tau^{\mp}$ $\ell^{\pm}\tau^{\pm}\ell^{\mp}$ $\ell^{\pm}\tau^{\pm}\tau^{\mp}$	$\tau^{\pm}\tau^{\pm}\tau^{\mp}\tau^{\mp}$	$\ell^{\pm}\ell^{\pm}\tau^{\mp}\tau^{\mp}$ $\ell^{\pm}\tau^{\pm}\ell^{\mp}\tau^{\mp}$ $\ell^{\pm}\ell^{\pm}\ell^{\mp}\tau^{\mp}$ $\tau^{\pm}\tau^{\pm}\ell^{\mp}\tau^{\mp}$
Z veto	✓	✓	✓	✓	✓	✓
b-jet veto	✓	✓	✓	✓	✓	✓
$\Delta R(\ell^{\pm}, \ell^{\pm}) < 3.5$	✓	✓	✓	✓		
$M_{\mathrm{T}}^{\mathrm{tot}}(\ell^{\pm}\ell^{\pm} + E_{\mathrm{T}}^{\mathrm{miss}}) > 300\,\mathrm{GeV}$	✓	✓	✓	✓	✓	✓
$\sum \lvert p_{\mathrm{T}}(\ell)\rvert > 400\,\mathrm{GeV}$	✓	✓	✓	✓		

9.2.8 *Signal region optimization*

The signal regions are categorized in two-, three- and four-lepton regions in order to measure as much signal as possible, and the regions are further divided into flavour categories to increase the sensitivity. The variables exploited for the sensitivity optimization are chosen based on the signal and background kinematic distributions in a similar manner as in the previous search. The selections make use of the boosted decay topology of the $H^{\pm\pm}$ resonance and the high energy of the decay products.

Optimizations were done to increase the signal significance defined based on the MC simulation studies for a given set of selection requirements. To increase the sensitivity in the light lepton channels, additional cuts on the $p_{\mathrm{T}}(\ell^{\pm}\ell^{\pm})$, $\sum |p_{\mathrm{T}}(\ell)|$, and $\Delta R(\ell^{\pm}, \ell^{\pm})$ are required with respect to the baseline selection. While previously defined analysis regions presented in Section 8.2.4 were found to be very good at rejecting backgrounds and having a large sensitivity to signal events, the $p_{\mathrm{T}}(\ell^{\pm}\ell^{\pm})$ requirement was increased to 300 GeV. This requirement eliminates some background event yield mainly from Drell–Yan and diboson processes in all light lepton channels without causing a loss in the signal yield. Otherwise the signal region selection for final states with light leptons, as summarized in Table 9, stays the same.

As mentioned, the main discriminant variable for light lepton channels is the same-charge dilepton invariant mass. However, it is not fully adequate for studying the final states with hadronically decaying taus. As neutrinos are always present in tau decays, reconstructing only the visible decay products of taus underestimates the real mass resonance. Furthermore, the mass resolution of the visible decay products is rather poor. Other ways to reconstruct the invariant mass of final states with at least one hadronic tau were studied. A couple of often used methods, the Missing Mass Calculator (MMC) [218] and Matrix Oriented Sampling Calculator (MOSAIC) [219], are typically more computationally heavy and optimized especially around the Higgs mass at 125 GeV, and are therefore not suitable for searching for the doubly charged Higgs bosons at high masses.

The collinear mass approximation can be used to reconstruct invariant masses of hadronically decaying taus. The approximation assumes that the neutrinos are collinear, i.e. going to the same direction, as the visible decay products of the tau. It also assumes that all the missing energy in the event comes only from neutrinos from tau decays. However, the ap-

proximation does not perform well if the two taus are produced back-to-back, and the mass resolution is limited by missing transverse energy. More details on applying a collinear mass approximation in the search for doubly charged Higgs bosons can be found in Ref. [170].

In this search, the total transverse mass is chosen as the final variable to be used in the likelihood fit in the two- and three-lepton tau-inclusive channels. It is defined as

$$M_{\mathrm{T}}^{\mathrm{tot}} = \sqrt{M_{\mathrm{T}}^2(\tau_1,\tau_2) + M_{\mathrm{T}}^2(\tau_1, E_{\mathrm{T}}^{\mathrm{miss}}) + M_{\mathrm{T}}^2(\tau_2, E_{\mathrm{T}}^{\mathrm{miss}})} \tag{70}$$

where

$$M_{\mathrm{T}} = \sqrt{2 p_{\mathrm{T}} E_{\mathrm{T}}^{\mathrm{miss}} (1 - \cos\Delta\phi)} \tag{71}$$

with $\Delta\phi$ being the angle between the lepton and $E_{\mathrm{T}}^{\mathrm{miss}}$ in the transverse plane. It allows reconstructing the mass in presence of neutrinos, is quick to compute, and can provide some discriminating power for the signal against backgrounds even in the regions where the number of selected events is relatively low. Similarly as for the light leptons, in the four-lepton tau-inclusive regions the final discriminating variable is the average invariant mass distribution of the two same-charge pairs, $\bar{M} = (m^{++} + m^{--})/2$.

In order to have a good background rejection to separate a small signal amongst a large background, various sets of selection criteria were studied also in the tau-inclusive channels. As the tau decays involve neutrinos, it was studied if adding a cut on the $E_{\mathrm{T}}^{\mathrm{miss}}$ significance (as defined in Section 5.5.7) could help to distinguish the signal from the large fake backgrounds. Figure 78 shows the $E_{\mathrm{T}}^{\mathrm{miss}}$ significance distributions in various unoptimized tau-inclusive regions, without any other cuts than the initial object selection. In these plots, data-driven fake estimation were used. A high value of the $E_{\mathrm{T}}^{\mathrm{miss}}$ significance indicates that the event is likely to contain undetected objects. As can be seen, especially the region with two hadronic taus could benefit from adding a cut on the $E_{\mathrm{T}}^{\mathrm{miss}}$ significance as the fake backgrounds tend to have smaller $E_{\mathrm{T}}^{\mathrm{miss}}$ significance values than the expected signal. However, no cut was assigned in the final signal region selection due to the low expected signal yield across all the $E_{\mathrm{T}}^{\mathrm{miss}}$ significance bins.

Figure 79 shows the leading lepton p_{T} distribution in the unoptimized regions, where either exactly two hadronic taus or exactly one hadronic tau and one lepton are required. It confirms that the decay products of the $H^{\pm\pm}$ are expected to have high transverse momenta, and cuts related to the momenta provide a powerful way to reduce backgrounds.

The optimized signal region selection for final states including hadronically decaying taus is presented in Table 22. As mentioned earlier, the tau-inclusive signal regions are divided into different groups depending on the lepton flavour combination and lepton multiplicity. Regions are distinct for fully hadronic final states with two, three and four hadronic taus, and for final states that also include light leptons. This categorization is done in order to get the first estimates of the sensitivity of fully hadronic final states.

The largest background in the signal regions with hadronic taus comes from QCD jets misidentified as taus. Smaller background contributions originate from Z/W+jets, $t\bar{t}$, and diboson events. The QCD jet background is challenging to cut away using the usual kinematic selection cuts without causing significant losses in the signal sensitivity. In signal regions with less than four leptons, the Z veto and b-jet veto are applied in order to reduce background from diboson and fake events. The same-charge lepton separation is required to be $\Delta R < 3.5$ in order to enhance the signal sensitivity. Last, $\sum |p_{\mathrm{T}}|$ of the leptons is required to be larger than 400 GeV, which effectively eliminates the background but not have a significant impact on signal. In the four-lepton signal regions, the selection cuts are loosened in order to have more events passing the selection. Only the b-jet veto is applied together with the $M_{\mathrm{T}}^{\mathrm{tot}}$ requirement. The total transverse mass $M_{\mathrm{T}}^{\mathrm{tot}}(\ell^{\pm}\ell^{\pm} + E_{\mathrm{T}}^{\mathrm{miss}})$ is required to be greater than

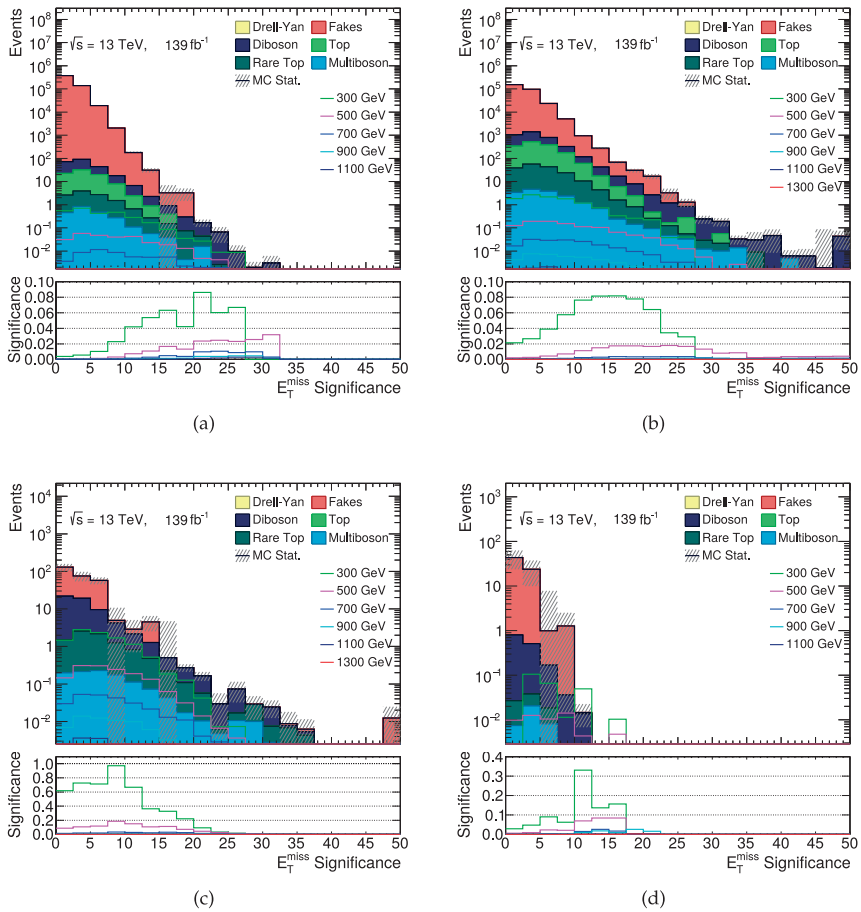

Figure 78: The $E_{\mathrm{T}}^{\mathrm{miss}}$ significance distributions for the tau-inclusive signal region optimization, shown in the region where exactly (a) two hadronic taus, (b) one hadronic tau and one lepton, (c) three leptons with at least one hadronic tau and one lepton, and (d) four hadronic taus are required.

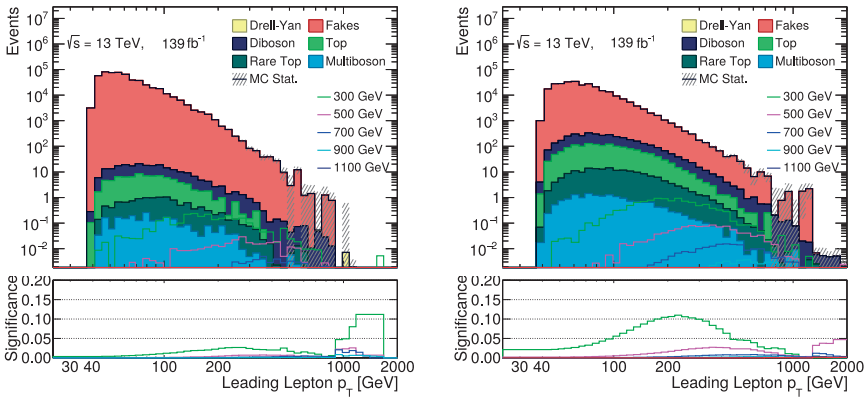

(a) (b)

Figure 79: The leading lepton p_T distributions for the tau-inclusive signal region optimization, shown in the region where exactly (a) two hadronic taus, and (b) one hadronic tau and one lepton are required.

300 GeV in all the signal regions in a similar manner as the visible mass has to be greater than 200 GeV in the light lepton regions. This choice is justified because the doubly charged Higgs boson is expected to be heavy and decay into high-energetic particles, and the total transverse mass takes into account E_T^{miss} from neutrinos.

9.3 BACKGROUND COMPOSITION AND ESTIMATION

9.3.1 *Prompt backgrounds*

The prompt SM backgrounds consist of leptons originating from diboson and $t\bar{t}$ processes. Such backgrounds are estimated using the simulated samples summarized in Table 18 in all analysis regions. Simulated events which contain at least one non-prompt tight or loose lepton are removed in order to avoid overlap with the data-driven fake background estimation.

9.3.2 *Electron charge misidentification background*

The main processes affecting the analysis through electron charge misidentification are Drell-Yan ($q\bar{q} \to Z/\gamma^* \to e^+e^-$) and $t\bar{t}$ production. In the previous search, electron charge misidentification probability was measured in the data and compared to the charge misidentification probability in the simulation. The approach used in the previous search was adapted by the ATLAS EGamma group [220]. The group produces a centrally derived set of charge reconstruction scale factors, which are applied to the corresponding simulated samples to account for the different charge misidentification probabilities between data and simulation.

A closure test was performed to verify that the derived scale factors work as expected. Same-charge electron pairs with an invariant mass of $|m(ee) - m(Z)| < 15.8\,\text{GeV}$ are selected from the data and compared to the prediction by applying the charge reconstruction scale factors to the simulated same-charge events.

Resulting invariant mass distribution is shown in Figure 80a after applying the scale factors. The distributions show a much better agreement compared to the initial distributions of the same-charge $Z \to ee$ region shown in Figure 80b.

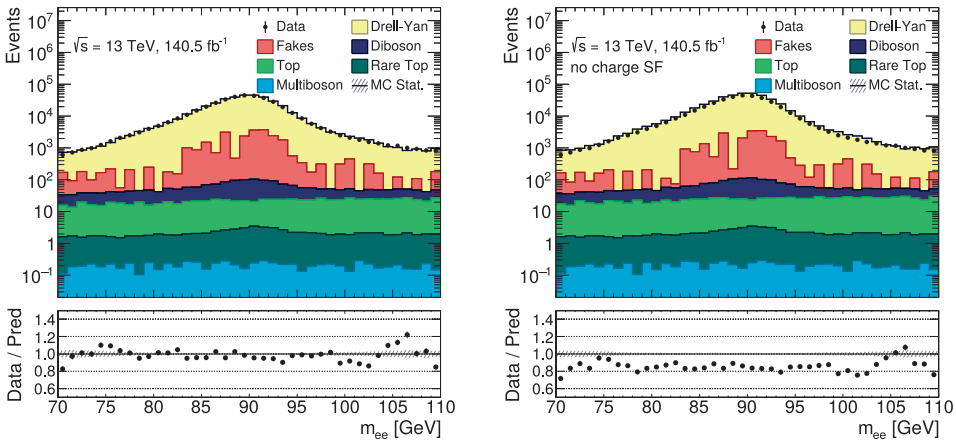

Figure 80: The electron charge misidentification closure test. Only systematics on the charge misidentification are applied. Invariant mass distribution of the same-charge electron pair (a) after applying the scale factors, and (b) before applying the scale factors.

9.3.3 *Tau charge misidentification background*

As hadronically decaying tau leptons are added to the analysis, and the correct charge measurement is essential when searching for new physics in the same-charge lepton final states, the uncertainty in the tau charge misidentification was studied. The tau charge misidentification is not the dominant background, instead that comes from misidentification of jets. Only a brief summary of the method and preliminary results are given below, and more details can be found in Ref. [172].

The tau charge misidentification probability was studied both in data and Monte Carlo. Both data-driven likelihood and tag-and-probe methods were used in a similar manner as is done for electrons. The data samples are contaminated by fake taus, and therefore it is important to extract a region in data which contains only true taus in order to measure the charge misidentification probability. This is achieved by using a template fit method, where opposite-charge (OC) and same-charge (SC) data events are divided into signal and background (bkg):

$$N^{\mathrm{OC}}_{\mathrm{data}}(\eta_i) = N^{\mathrm{OC}}_{\mathrm{signal}}(\eta_i) + N^{\mathrm{OC}}_{\mathrm{bkg}}(\eta_i) \tag{72}$$

$$N^{\mathrm{SC}}_{\mathrm{data}}(\eta_i) = N^{\mathrm{SC}}_{\mathrm{signal}}(\eta_i) + N^{\mathrm{SC}}_{\mathrm{bkg}}(\eta_i). \tag{73}$$

The charge misidentification rate is assumed to depend strongly only on η. In total four templates are required to describe the total shape. A template for $N^{\mathrm{OC}}_{\mathrm{signal}}$ is composed of MC events where the tau is truth matched to its origin, and a template for $N^{\mathrm{OC}}_{\mathrm{bkg}}$ is composed of all MC events where the tau is not truth matched. Similarly, templates for $N^{\mathrm{SC}}_{\mathrm{signal}}$ and $N^{\mathrm{SC}}_{\mathrm{bkg}}$ can be

derived using the truth match information on simulated taus. After finding such templates, they are fitted to data in order to find the optimal scaling parameters.

The template fit is performed in the $t\bar{t}$ control region, where $t\bar{t}$ decays into two taus with one tau decaying into a muon, and another decaying hadronically. This region has the highest same-charge truth matched signal to background ratio when compared to the $Z \to \tau\tau$ and the $t\bar{t} \to b\bar{b}\tau\tau \to b\bar{b}\tau_{had}\tau_{had}$ regions. The selection criteria in the $t\bar{t}$ control region are presented in Table 23. At least one b-tagged jet is required instead of exactly two b-tagged jets, because requiring exactly two b-jets significantly reduces the number of simulated events, causing the same-charge signal template to fluctuate too much.

Table 23: Selection criteria in the template fit method for estimating the tau charge misidentification.

Type	Selections
Baseline	Single muon trigger: `HLT_mu20_iloose + HLT_mu50 (2015)` `HLT_muon26_ivarmedium + HLT_mu50 (2016-2017)` Exactly one muon and one tau. Electron veto Muon: $p_{\mathrm{T}} > 30\,\mathrm{GeV}$, `Medium` working point, isolated, $\lvert z_0 \sin(\theta)\rvert < 0.5\,\mathrm{mm}$ $\lvert d_0\rvert/\sigma_{d_0} < 3.0$ Tau: $p_{\mathrm{T}} > 30\,\mathrm{GeV}$, `JetBDTMedium` working point
$t\bar{t}$ control region	Muon: $p_{\mathrm{T}} > 50\,\mathrm{GeV}$, Tau: $p_{\mathrm{T}} > 50\,\mathrm{GeV}$ At least one b-tagged jet

The fit of the templates to the data is performed using `RooFit`. The yields from diboson, Drell–Yan, single top and ttX processes are fixed, and only the $t\bar{t}$ templates are allowed to float in order for the fit to be more stable. In addition, the tag-and-probe method was used in the $t\bar{t}$ control region to derive estimate for the tau charge misidentification rate using only Monte Carlo. In Figure 81, the preliminary results of the charge misidentification rate are shown derived both in MC and data. As can be seen, the tau charge misidentification rate ranges from 0.4% up to 3.8%, giving an estimate of an additional uncertainty to be assigned.

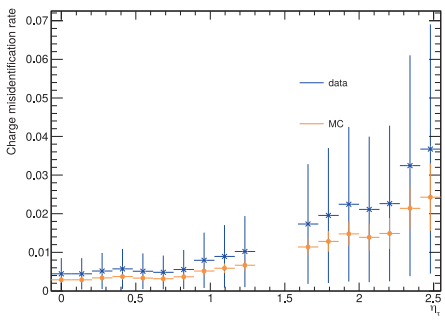

Figure 81: Charge misidentification rate of hadronic taus for data and MC estimated using template fit and tag-and-probe method, respectively. [172]

9.3.4 *Fake backgrounds*

The fake background composition can be studied in the fake enriched-regions by looking at the origin of the fake leptons in Monte Carlo simulation. In the fake-enriched region, the fake electrons consist mostly of hadrons reconstructed as electrons, final state radiation electrons, photon conversions and non-prompt heavy flavour decay products. In the signal region, fake electrons come almost entirely from jets misidentified as electrons, mostly from $W \to \ell\nu$ and top processes. Muon fakes are mainly heavy flavour non-prompt muons from top processes.

For tau fakes, the fake background composition has a huge impact on the fakes estimation. The tau fake rate depends on the fake origin, and is different for gluon- and quark-initiated jets. Therefore, a precise knowledge of the tau fake composition in all regions is essential, because the quark/gluon fraction and therefore the fake composition and the fake rate differ depending on specific object and event selections. A more detailed study on the fake tau composition in various processes is shown in Appendix C using simulated samples to analyse the truth information of the fake origin.

The fake background for all charged lepton flavours is estimated with a data-driven approach using the fake factor method, as described in Section 7.5.2. The method gives an estimate of the number of fake leptons entering the analysis regions. In this method, a control sample of events enriched with fakes is selected, and then a fake factor relating these events to the background in the signal region is determined. The fake factor $F(p_{\mathrm{T}}, \eta, \text{flavour})$ describes the probability for a fake lepton to be identified as a tight analysis lepton.

For fake factor measurements, events cannot be selected using the nominal dilepton triggers, because the leptons firing them are likely to originate from the interaction point and therefore are real. Instead, a specific set of single lepton and single jet triggers was used, as summarized in Table 24. Single electron and single muon triggers are used for fake electron and muon estimation, respectively, whereas single jet triggers are used for estimating the fake taus. These single lepton and single jet triggers are mostly prescaled, and are selected to have as low isolation as possible.

9.3.4.1 *Electron fake factor*

To select a region with a large number of fake electrons, a special single electron region is defined. Several requirements are implemented in order to discard any real prompt electrons while keeping the selection kinematically compatible enough with the signal region selection:

- Require exactly one electron and zero muons.
- $W \to e\nu$ + jets constraint: select events with $25\,\mathrm{GeV} < E_{\mathrm{T}}^{\mathrm{miss}}$ and $25\,\mathrm{GeV} \geq E_{\mathrm{T}}^{\mathrm{miss}}$ separately to get a good description of fakes across the whole phase-space.
- The b-jet veto is applied to suppress fakes from $t\bar{t}$ events, but no other cuts on jet multiplicity are set.

This fake-enriched region corresponds to a dijet event selection, and may still contain some prompt electrons. The remaining prompt electrons are subtracted from data using simulated samples. In order to estimate the systematic uncertainty on the fake factor, it was analysed independently for many variations. The nominal $E_{\mathrm{T}}^{\mathrm{miss}}$ cut for the fake-enriched region was removed in order to probe the effect of fake composition. For the same reason, another variation with at least two jets was measured. All Monte Carlo samples were varied by $\pm 10\,\%$ to account for cross-section and luminosity uncertainties as well as the modelling of the simulated events used in the prompt lepton subtraction procedure. Figure 82 shows the measured

Table 24: Summary of electron, muon, and jet trigger schemes used for the fake enriched region. Jet prescales are calculated using data 2018 only, unless the trigger was not used in runs in 2018 in which the last year of usage has been used. The dash ("–") in the minimum p_T implies that the threshold for turn-ons for each the triggers at 99% efficiency is not centrally given.

Trigger name	Average prescale	periods	min. p_T [GeV]	max. p_T [GeV]
HLT_mu24	48.928	2015–2018	30	53
HLT_mu50	/	2015–2018	53	∞
HLT_e26_lhvloose_nod0_L1EM20VH	111	2015–2016	30	65
HLT_e28_lhvloose_nod0_L1EM20VH	368	2017	30	65
HLT_e28_lhvloose_nod0_L1EM22VH	385	2018	30	65
HLT_e60_lhvloose_nod0	33	2015–2018	65	315
HLT_e200_etcut	1	2015	315	∞
HLT_e300_etcut	1	2016-2018	315	∞
HLT_j25	4841923	2015–2018	34	∞
HLT_j35	868709	2015–2018	48	∞
HLT_j45	89117	2015–2018	57	∞
HLT_j55	5573	2015	-	∞
HLT_j60	42065	2015–2018	72	∞
HLT_j110	2886	2015–2018	125	∞
HLT_j175	395	2015–2018	194	∞
HLT_j260	62	2015–2018	283	∞
HLT_j380	1	2016	-	∞
HLT_j400	1–1.5	2017–2018	-	∞
HLT_j420	1	2017–2018	464	∞

nominal fake factors for different $E_{\mathrm{T}}^{\mathrm{miss}}$ bins, and the measured fake factor in different pseudorapidity bins for each systematic variation requiring $E_{\mathrm{T}}^{\mathrm{miss}} < 25\,\mathrm{GeV}$. The combined systematic uncertainty of the electron fake factors was calculated by adding all variations and the statistical uncertainty in quadrature. The largest contribution to the uncertainty comes from the MC scaling. The measurement is relatively stable up to very high electron p_{T}. However, the maximum uncertainty can get very high, up to 100 %.

9.3.4.2 *Muon fake factor*

The muon fake factor measurement is performed in the same way as described in previously in Section 8.3.3, and is therefore not repeated here. The tag-and-probe method was used to select a fake-enriched sample corresponding to a dijet selection.

The effect of each systematic alteration, again performed in a similar manner as previously, can be seen in Figure 83 in different pseudorapidity bins. Each variation tries to account for different systematic effects, such as the effect of different fake composition in the fake-enriched regions compared to the signal region, and MC modelling and normalization in the fake-enriched region. The total uncertainty is estimated by comparing the statistical uncertainty on the nominal measurement with the maximum deviation between the nominal fake-factor and systematically varied measurement. An uncertainty varies between $\approx$ 10 % and $\approx$ 50 % across p_{T} intervals.

9.3.4.3 *Tau fake factor*

Taus are not the only objects producing hadronic signatures. Quarks and gluons are produced in the initial hard scatter. Since they cannot exist alone, they form sprays of hadrons, called jets, in the showering and hadronization process. It is challenging to understand which kind of a particle initiated a jet based on signature it left in trackers and calorimeters: the hadronic decays of taus can closely resemble usual quark- and gluon-initiated jets. They look similar with a couple of different characteristics: a typical tau has 1 or 3 charged tracks (causing taus to be called 1- and 3-prong taus, respectively) and it is rather collimated, whereas a typical jet contains all sorts of hadrons and is usually wider. Furthermore, the tau lepton travels a short distance before it decays leading to a larger transverse impact parameter of the tracks, which can be used for tau identification. However, light leptons can also be misidentified as taus. Electrons faking taus are mostly rejected by a likelihood based discriminant, and muons misidentified as taus are usually resolved during the overlap removal process.

There is a large fraction of fake taus present in all of the tau-inclusive analysis regions. Tau fake factors are measured using events in control regions, which have similar topology and quark/gluon composition to the signal regions of the analysis. Having similar quark/gluon composition is essential as it defines the fake composition and therefore the fake rate. Indeed, the main challenge does not come from the difficulty to find a fake-enriched region but from making sure that the fake composition is similar between the measurement region and the signal region.

Different control regions are defined to measure the tau fake factor in different topologies. To measure fake factors suitable to be used in the two and three lepton signal regions where the leptons in the same-charge pair have different flavours, two regions are defined. These regions are called 1DF2L and 1DF3L, respectively, where DF refers to the different flavour in a pair, and 2/3 to the lepton multiplicity. They are chosen so that they have almost identical selection with the signal region, except the Z veto is inverted and the requirements on the total transverse mass and the separation between particles are dropped, making sure that the regions are orthogonal with respect to the main signal regions. In this region, the fakes come

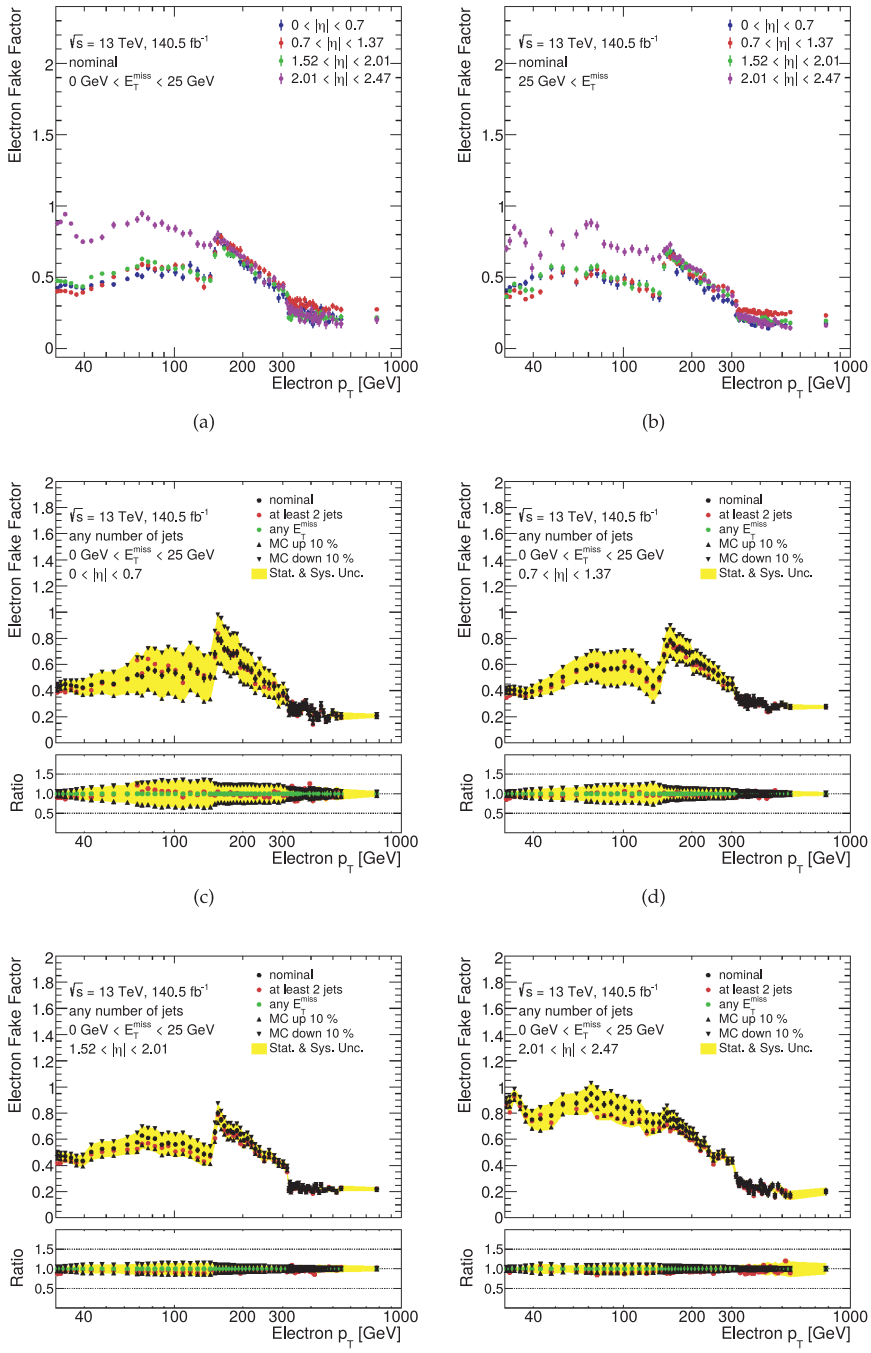

Figure 82: Electron fake factors measured as a function of p_{T} for different $E_{\mathrm{T}}^{\mathrm{miss}}$ bins: (a) $E_{\mathrm{T}}^{\mathrm{miss}} < 25\,\mathrm{GeV}$, (b) $E_{\mathrm{T}}^{\mathrm{miss}} > 25\,\mathrm{GeV}$. The measured fake factor in different pseudorapidity bins for each systematic variation requiring $E_{\mathrm{T}}^{\mathrm{miss}} < 25\,\mathrm{GeV}$: (c) $0 < |\eta| < 0.7$ (d) $0.7 < |\eta| < 1.37$ (e) $1.52 < |\eta| < 2.01$, and (f) $2.01 < |\eta| < 2.47$.

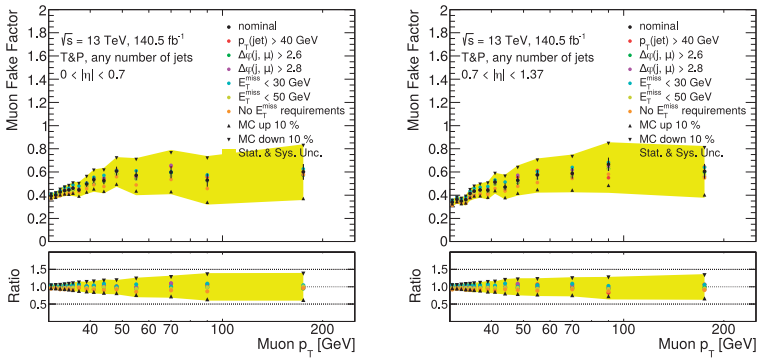

Figure 83: The measured muon fake factors for each systematics variation in various pseudorapidity bins: (a) $0 < |\eta| < 0.7$, (b) $0.7 < |\eta| < 1.37$, (c) $1.37 < |\eta| < 1.52$, (d) $1.52 < |\eta| < 2.01$, and (e) $2.01 < |\eta| < 2.5$.

mostly from V+jets events instead of QCD multijet events. Contributions from electron and muon fakes are subtracted after estimating them with the fake factor method. Contamination from real leptons is also subtracted and estimated using simulated events in a similar way as for electron and muon fake factors.

Measuring a fake factor suitable to be used in the case where the same-charge pair consists of two hadronic taus is more difficult to define due to the ambiguity in selecting the probe tau. For this region, a multijet selection is used to measure fake-factors in such regions because the di-tau pair events are contaminated by a higher fraction of multijet events with respect to regions with different flavour same-charge pairs. Events are selected with single jet triggers. Exactly one tau and at least one jet with a $p_{\mathrm{T}}(\mathrm{jet}) > 20\,\mathrm{GeV}$ are required in the event, and events with muons and electrons are rejected. Furthermore, the tau is required to be the third leading object in the event to to enhance the gluon-initiated fake component. Real tau contamination is estimated with simulated events and subtracted from this control region. These fake factors measured using a multijet topology are also used to estimate fake taus in all regions featuring four leptons, because they are expected to be mostly contaminated by this kind of events.

Differences between fake factors measured in all these regions are found to be largely mitigated by the requirement for all taus to satisfy at least the `VeryLoose` tau identification working point in the denominator region. This requirement increases the level of confidence for the fake factors to be less sensitive to any fake composition and topological differences.

Fake factors are measured independently for tau leptons featuring one or three associated tracks. Tau fake factors are shown in Figure 84 for all the described control regions.

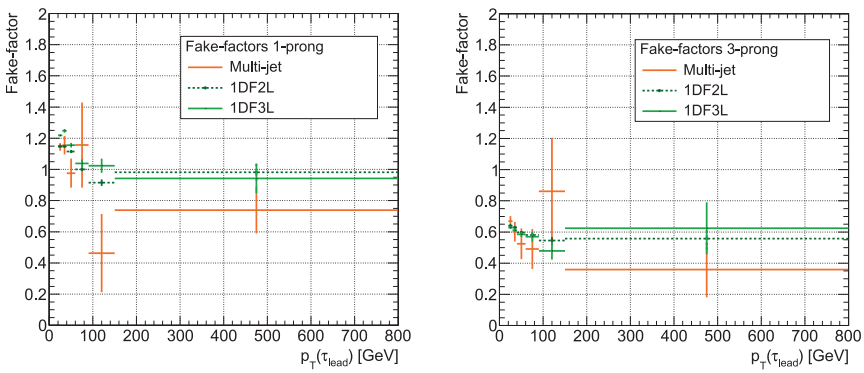

(a) (b)

Figure 84: Tau fake factors as a function of the tau transverse momentum measured in the multi-jet, and two and three lepton control regions having exactly one different-flavour same-charge pair, denoted 1DF2L and 1DF3L. (a) 1-prong fake factors (b) 3-prong fake factors.

9.4 DISTRIBUTIONS IN CONTROL AND VALIDATION REGIONS

Several control regions are designed to extract the normalization of the largest background contributions in different lepton multiplicities and flavour compositions, as defined in Section 9.2.7. Figure 85 presents diboson and opposite-charge light lepton control regions used to constrain diboson and Drell–Yan background compositions, showing very good agreement be-

tween the Standard Model predictions and observed data. Figure 86 shows two tau-inclusive control regions constraining the large fake tau contribution.

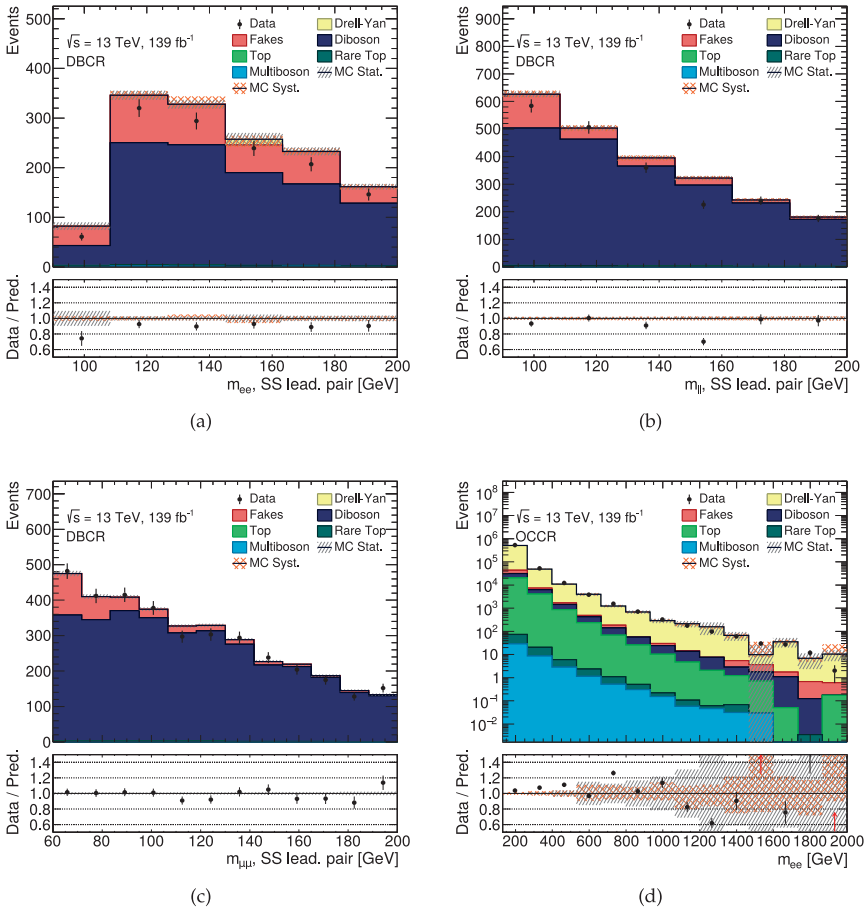

Figure 85: Pre-fit distributions of $m(\ell^{\pm}\ell^{\pm}), \ell = e, \mu$ in the control regions: (a) the electron–electron channel in diboson control region (DBCR), (b) the electron–muon channel in diboson validation region (DBCR), (c) the muon–muon in diboson control region (DBCR), and (d) the opposite-charge di-electron region (OCCR). The hatched bands include all systematic uncertainties.

Validation regions sensitive to fake background predictions and diboson modelling are presented in Figures 87 and 88 for light lepton channels. Similarly, representative validation regions for the tau-inclusive channels are shown in Figure 89. Good background modelling is observed in all of these regions with various lepton flavour combinations and multiplicities.

9.5 SYSTEMATIC UNCERTAINTIES

Several sources of both experimental and theoretical systematic uncertainties affecting both the background and signal predictions are considered in the analysis. All considered sources

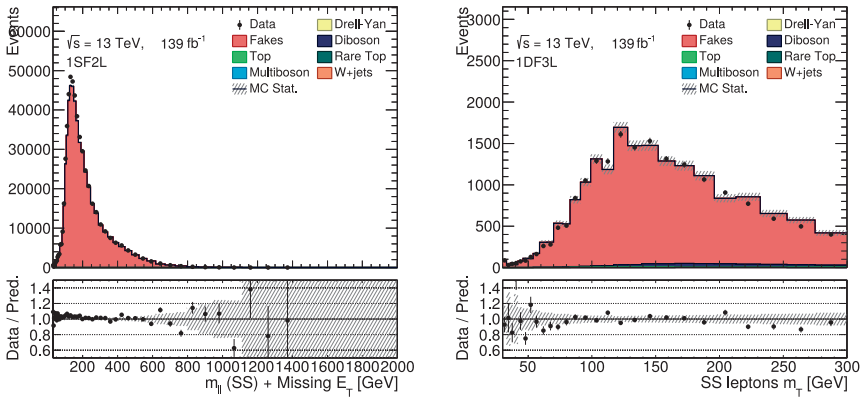

(a) (b)

Figure 86: Pre-fit distributions of the tau-inclusive control regions: (a) with exactly two hadronic taus, and (b) with exactly three leptons of which one is a hadronic tau. Only statistical uncertainties are considered. "SS" refers to a same-charge pair.

of systematic uncertainties have an effect on the total event yield. Apart from the uncertainties on the luminosity and cross-section, all sources also affect the shape of the distributions used in the fit. The plots and results including hadronic taus show only the statistical uncertainties, because the full systematics are not available at the time of writing.

The major experimental uncertainties come from the estimation of fake lepton backgrounds. The systematic uncertainties are evaluated by varying the nominal fake factor to account for various effects, such as the MC modelling used to subtract the contamination from real prompt leptons. The resulting uncertainty in the fake factors typically ranges between 10% and 50% across all p_T and η bins, as described in Section 9.3.4.

The analysis is affected by the finite number of both simulated and data events. Analysis regions have a very restrictive selection optimized for finding a doubly charged Higgs boson, and only a small fraction of all the generated MC events passes the final selection. The uncertainty arising from the finite statistic varies between different regions, and is between 3% and 50%.

Experimental systematic uncertainties associated to different reconstruction, identification, isolation, and trigger efficiencies of leptons as well as lepton energy and momentum calibration are taken into account, and vary between 0.6% and 6%. Furthermore, systematic uncertainties related to jet energy scale and resolution calibration as well as jet efficiency and missing transverse energy are taken into account, each having a small uncertainty of less than 1%. All the mentioned experimental systematic uncertainties affect both the signal and the background samples.

Theoretical uncertainties are estimated in a similar way as described previously in Section 8.5: samples are altered to account for the scale and PDF uncertainties in the cross-section calculation, and therefore the details will not be repeated here. The largest theoretical uncertainty coming from the diboson uncertainty is up to 25% in the light lepton signal regions. However, no theoretical uncertainty on the signal is applied at the time of writing. The uncertainty related to luminosity is $2.1 - 3.6\%$.

Events including tau leptons will be assigned with additional systematic uncertainties associated with the tau identification, reconstruction efficiency, energy scale, and a likelihood-

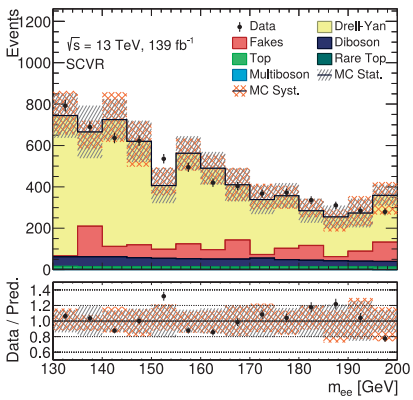

(a)

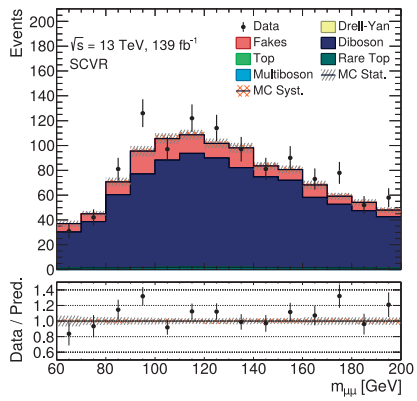

(b)

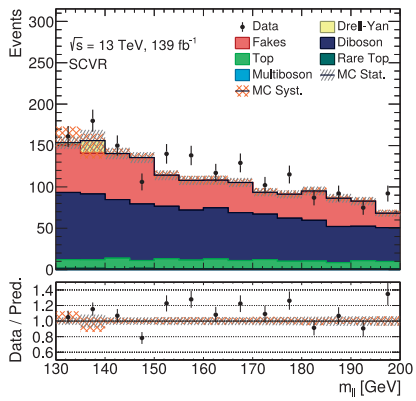

(c)

Figure 87: Pre-fit distributions of $m(\ell^{\pm}\ell^{\pm}), \ell = e, \mu$ in the two same-charge lepton validation regions: (a) the electron–electron, (c) the electron–muon, and (b) the muon–muon channels. The hatched bands include all systematic uncertainties.

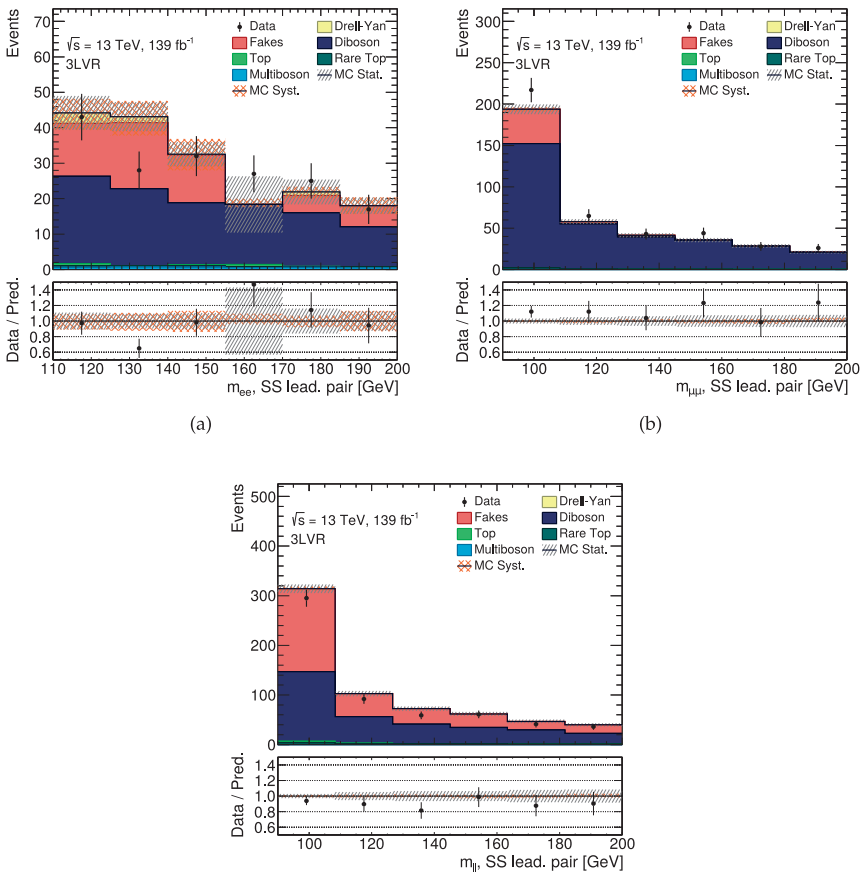

(a) (b)

(c)

Figure 88: Pre-fit distributions of $m(\ell^{\pm}\ell^{\pm})$ in the three-lepton validation regions: (a) the three-electron validation region, (b) the three-muon validation region, (c) the 3LVR mixed electron–muon region. The hatched bands include all systematic uncertainties.

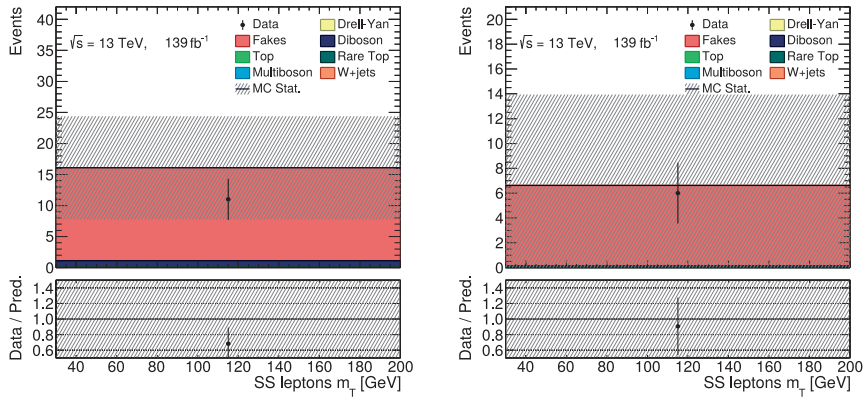

(a) (b)

Figure 89: Pre-fit distributions of the tau-inclusive validation regions showing the total transverse mass distribution in regions with exactly (a) four leptons of which at least one is a tau, and (b) with exactly four hadronic taus. Only statistical uncertainties are considered. "SS" refers to a same-charge pair.

based electron veto. The largest uncertainty is however expected to be caused by the fake factor method and limited statistics, especially in the channels with fully hadronic final states.

9.6 STATISTICAL ANALYSIS AND RESULTS

The statistical framework HistFitter [178] is used in the search for doubly charged Higgs bosons to perform a binned maximum-likelihood fit. For final states involving only light leptons, the invariant mass distribution of the same-charge leptons in all control and signal regions, and the $\bar{M}$ distribution in four-lepton regions is used to obtain the numbers of signal and background events. For the tau-inclusive final states, the total transverse mass distribution is used in all two- and three-lepton control and signal regions to account for the presence of neutrinos from tau decays. In the four-lepton tau-inclusive regions, the $\bar{M}$ distribution is used. In the absence of signal, the main goal is to determine 95% CL upper limits on the $pp \to H^{++}H^{--}$ production cross-section as a function of the $H^{\pm\pm}$ mass hypothesis, using the CL_s method [177].

In the likelihood fit, a Poissonian probability density function describes the observed number of events, and Gaussian distributions are used to constrain the nuisance parameters related to the systematic uncertainties. Additional free parameters are added for constraining the major background contributions to fit their yields in the analysis regions. All the fitted normalizations are found to be compatible with the SM predictions within the uncertainties.

No significant excess is observed. For light lepton channels, the pre-fit same-charge invariant mass distributions in the two- and four-lepton signal regions before the fit are shown in Figure 90, and in the three-lepton signal regions in Figure 91. For tau-inclusive channels, the representative pre-fit distributions in the two-, three- and four-lepton signal regions are shown in Figure 92. In these figures, the solid coloured lines correspond to signal samples, normalized using the theory cross-section, with the $H^{\pm\pm}$ mass.

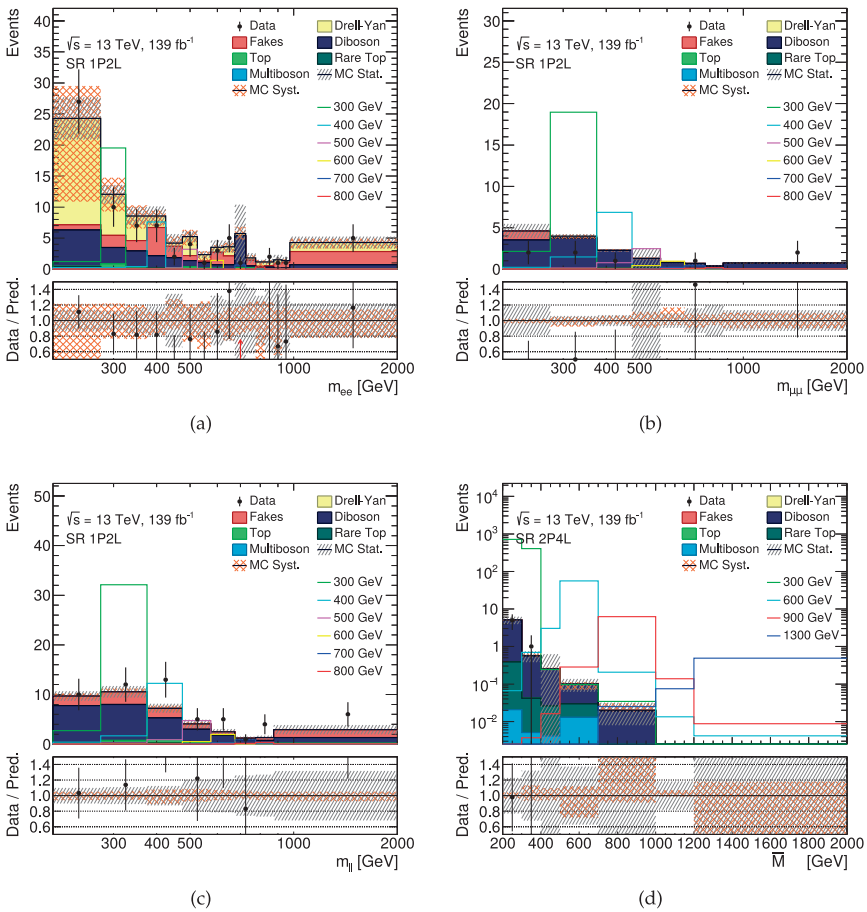

Figure 90: Pre-fit distributions of $m(\ell^{\pm}\ell^{\pm})$ in the representative signal regions: (a) the electron–electron two-lepton signal region (SR1P2L), (b) the muon–muon two-lepton signal region (SR1P2L), (c) the electron–muon two-lepton signal region (SR1P2L), and (d) the four-lepton signal region (SR2P4L). The hatched bands include all systematic uncertainties.

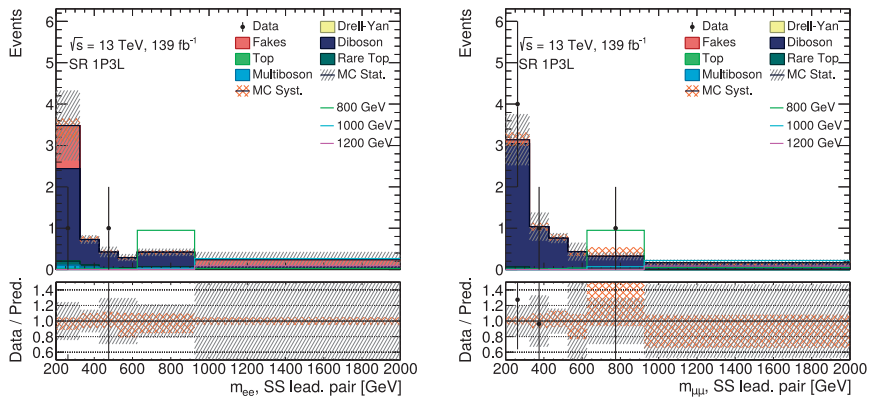

(a) (b)

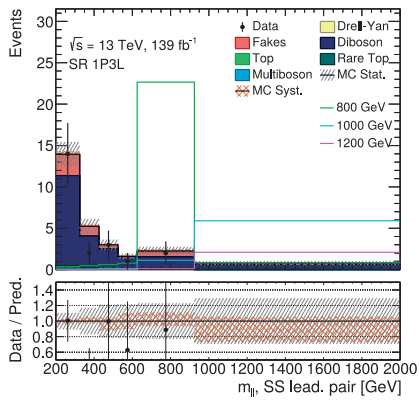

(c)

Figure 91: Pre-fit distributions of $m(\ell^{\pm}\ell^{\pm})$ in three-lepton signal regions, in (a) the three-electron SR (SR1P3L), (b) the three-muon SR (SR1P3L), and (c) the electron–muon SR (SR1P3L). The hatched bands include all systematic uncertainties.

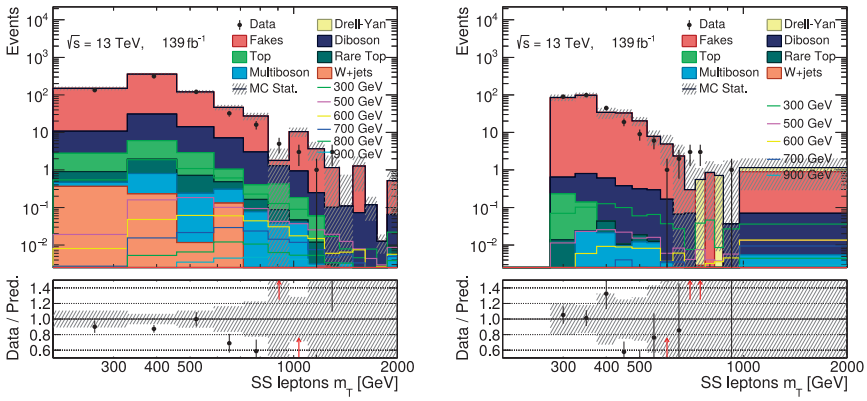

(a) (b)

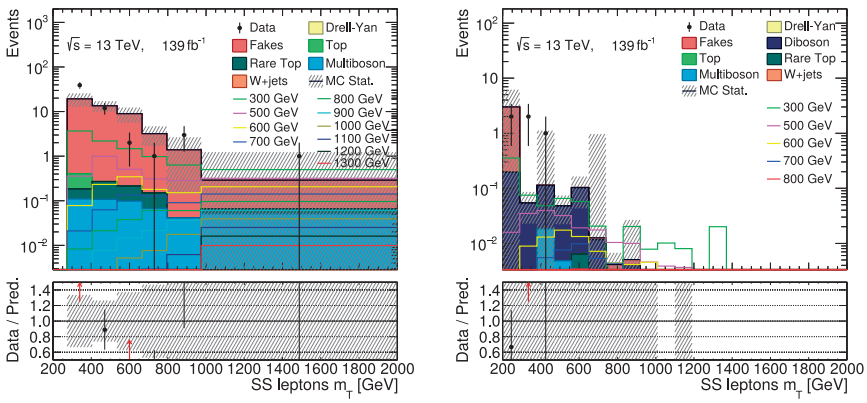

(c) (d)

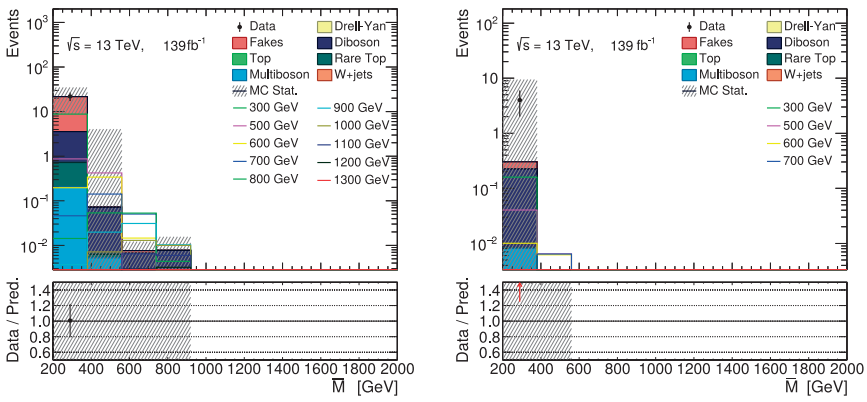

(e) (f)

Figure 92: Pre-fit distributions of the total transverse mass in two- and three-lepton tau-inclusive signal regions, requiring exactly (a) one tau and one light lepton, (b) two hadronic taus, (c) three leptons of which at least one is a tau, and (d) three taus. Similarly, the average invariant mass distribution in four-lepton tau-inclusive regions, requiring exactly (e) four leptons of which at least one is a tau, (f) four hadronic taus. Only statistical uncertainties are shown. "SS" refers to a same-charge pair.

For $B(H^{\pm\pm} \to \ell^{\pm}\ell^{\pm}) = 100\%$ where $\ell = e, \mu$, the production cross-section is excluded down to more than 0.1 fb. The expected and observed upper limits on the production cross-section as a function of the $H^{\pm\pm}$ boson mass are shown in Figure 93 for $e^{\pm}e^{\pm}$, $e^{\pm}\mu^{\pm}$, and $\mu^{\pm}\mu^{\pm}$ final states. The observed lower limit on the mass of the $H_L^{\pm\pm}$ is 1065 GeV (1020^{+88}_{-100} GeV expected) using only final states with electrons, while it is 1053 GeV (1014^{+92}_{-92} GeV expected) using only final states with muons. For the mixed final states, the observed limit on the mass of the $H_L^{\pm\pm}$ is 1045 GeV (1010^{+102}_{-40} GeV expected). The observed limits on the mass of the $H_R^{\pm\pm}$ are above 850 GeV for all light lepton flavours. All the observed limits are consistent with the expected limits. The resulting exclusion limits are similar across all light lepton channels, and therefore the search is equally sensitive in these channels.

As expected from the pair production mechanism, the four-lepton signal region provides the highest potential for a discovery of the doubly charged Higgs. In fact, including only the four-lepton signal regions in the fit leads to very similar expected limits on the cross-section and $H^{\pm\pm}$ mass. Using only the two- and three-lepton signal regions alone result in the lower limit on the $H_L^{\pm\pm}$ mass between 300 GeV and 400 GeV. However, these regions may still be sensitive to other types of new physics.

For channels involving hadronically decaying taus, the expected limits are weaker due to large fake backgrounds that are challenging to eliminate without rejecting a lot of signal. Even without adding strict cuts, the fully hadronic channel has relatively low statistics. The observed $H_L^{\pm\pm}$ lower mass limits are found to be 494 GeV (468^{+55}_{-41} GeV expected) for the tau-inclusive channels, when only statistical uncertainties are taken into account. Using only the channel with four hadronically decaying taus, the observed lower limit on the $H_L^{\pm\pm}$ mass is found to be 292.7 GeV (289^{+33}_{-38} GeV expected). As the expected limits are so different between tau-inclusive regions and light lepton regions, combining them does not affect the strongly the light lepton channels.

9.7 FUTURE WORK

The presented analysis can be further improved to increase the sensitivity to new physics. These improvements include many aspects from improving analysis methods to using other signal hypotheses to estimate sensitivity to other physics models or making the analysis fully model-independent.

First, moving from a cut-based analysis to using multivariate analysis techniques, such as boosted decision trees or neural networks, could enhance the sensitivity to new physics by improving the discrimination between the background and the same-charge signal events. Such multivariate techniques use more variables than invariant mass only, such as other kinematic variables including p_{T} of the particles, and missing transverse energy. Especially channels involving hadronically decaying taus, $\ell^{\pm}\tau^{\pm}$ and $\tau^{\pm}\tau^{\pm}$, could benefit from the multivariate approach due to the more challenging detector signature of hadronic taus. The multivariate approach was not utilized yet in this search mainly for two reasons. First, the aim of the analysis is to avoid selecting events mainly oriented to a very specific model, but to be sensitive to various models involving two same-charge leptons in the final state, having the doubly charged Higgs boson production as the main benchmark. Optimizing a classifier to select only events with a certain signal hypothesis can limit the generalizability of the search. Second, the aim is to have a full understanding of hadronically decaying taus in the same-charge final states and get the first impression of the achievable mass reach before using more complex methods.

The channels involving hadronically decaying taus can also be further optimized in many ways. The search would greatly benefit from using the new recurrent neural network (RNN)

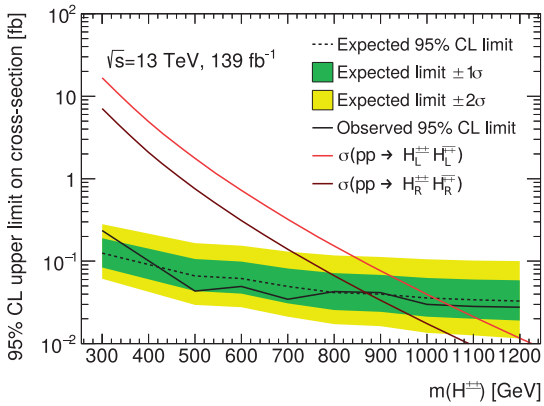

(a)

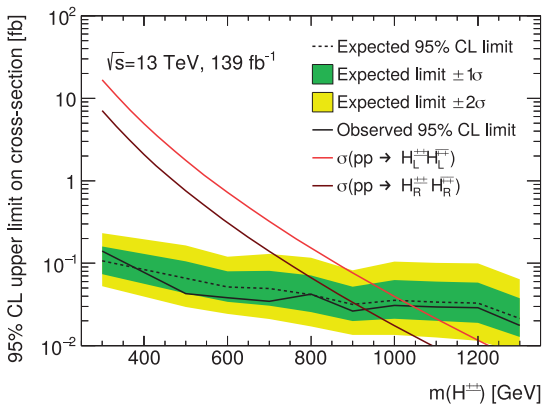

(b)

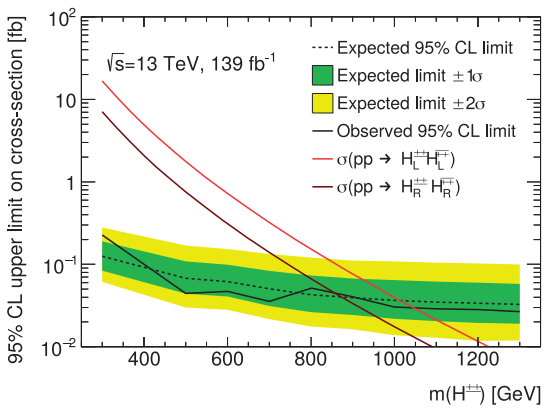

(c)

Figure 93: The observed and expected upper limits on the production cross-section as a function of the $H^{\pm\pm}$ boson mass using (a) only electron final states, (b) electron–muon final states, and (c) only muon final states. In all of the cases, it is assumed that the $H^{\pm\pm}$ boson decays only into light lepton final states. No theoretical uncertainty on the signal is applied.

tau identification algorithm [221]. The RNN algorithm uses information from tracks and energy clusters associated to $\tau_{\text{had-vis}}$ candidates together with various high-level discriminating variables. Figure 94 shows the rejection power for fake taus using both the RNN-based and BDT-based classifiers, illustrating the much greater fake rejection for the new algorithm when comparing to the currently used BDT-based algorithm. As the channels with hadronic taus have very large background coming from misidentified jets, using the new identification algorithm is expected to increase sensitivity remarkably.

Just as the Standard Model Higgs searches and measurements, the doubly charged Higgs search could make use of other variables and more optimized methods to reconstruct the invariant mass of the same-charge hadronic taus. The di-tau mass reconstruction is challenging because of the presence of neutrinos from the tau decays. The existing methods taking into account the missing energy from neutrinos, such as the Missing Mass Calculator (MMC) [218] and Matrix Oriented Sampling Calculator (MOSAIC) [219], are typically optimized especially for the Higgs mass at 125 GeV, therefore being too low for the needs of the $H^{\pm\pm}$ search. The collinear approximation still serves as an interesting alternative to other variables to be used in future.

In addition to further optimized object selection or adding other variables, background estimation and rejection methods may be improved in Run 3. Such improvements include for example an implementation of a new BDT-based tool to decrease the electron charge misidentification rate. By improving the background modelling, smaller associated systematic uncertainties can be achieved especially in terms of fake backgrounds.

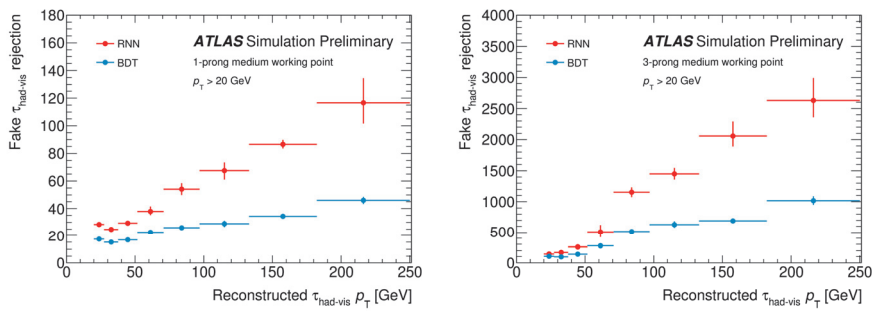

(a) (b)

Figure 94: Rejection power for quark and gluon jets misidentified as $\tau_{\text{had-vis}}$ for (a) 1-prong and (b) 3-prong $\tau_{\text{had-vis}}$ candidates using the `Medium` working point as the function of the transverse momentum p_T. The rejection power is shown both for the RNN-based (red) and BDT-based (blue) classifiers. From [221].

The search for the pair-production of doubly charged Higgs bosons can be extended to take into account other production mechanisms or even other models than the left-right symmetric model. The associated production of a singly charged Higgs boson and a doubly charged Higgs ($pp \to W^{\pm *} \to H^{\mp}H^{\pm\pm}$) may result in similar or higher production cross-sections compared to the pair production mechanism. Probing such production mechanism in three- and four-lepton final states, as the CMS experiment does [65], would therefore increase the sensitivity for discoveries. Furthermore, new NLO cross-section calculations on the doubly charged Higgs boson production will be useful considering both the pair and associated production of doubly charged Higgs bosons. As outlined in Section 2.2.4, the 3-3-1 model predicts the production of bilepton $Y^{\pm\pm}$ leading to same-charge lepton final states. The current search will

be extended to asses if the search is equally sensitive to a spin-0 and spin-1 doubly charged bosons, assuming no lepton flavour violating modes. Being both theoretically well motivated and experimentally feasible, this analysis will be a great addition to the current one. In addition, the properties of tau leptons, such as tau polarization revealing the chiral properties of its parent particle, might further be used to discriminate different models describing neutrino mass mechanisms [222, 223].

As no observations of new physics has been observed neither by CMS nor ATLAS yet, and the SM predictions are becoming more and more precise, the search using same-charge final states could be converted to be more model-independent, targeting general Beyond Standard Model scenarios. The advantage of performing a strictly model-dependent search is that the search can be very precisely optimized to maximize the sensitivity to a particular model. However, at the same time there may be more general models with the same collider signature that the search is not sensitivite to due to too strict selection. In addition, model-independent searches may be easier to reinterpret in terms of other signal hypotheses.

9.8 CONCLUSIONS AND SUMMARY

The search for doubly charged Higgs bosons in the same-charge dilepton invariant mass spectrum using $e^{\pm}e^{\pm}$, $e^{\pm}\mu^{\pm}$, $\mu^{\pm}\mu^{\pm}$, $e\tau_{\text{had}}$, $\mu\tau_{\text{had}}$ and $\tau_{\text{had}}\tau_{\text{had}}$ final states was performed with 139 fb^{-1} of data from proton–proton collisions at $\sqrt{s} = 13$ TeV, recorded during the LHC full Run 2 in 2015–2018 by the ATLAS detector. In addition to adding hadronically decaying taus and utilizing the much larger full Run 2 dataset, the physics object selection and analysis regions were optimized such that more background was rejected without losses in the signal sensitivity. All regions show very good agreement between the Standard Model predictions and observed data. No significant excess above the Standard Model prediction was found in any of the signal regions, and consequently the limits are set on the production cross-section and the mass of doubly charged Higgs bosons.

The observed lower limits on the $H^{\pm\pm}$ mass in regions involving only light leptons vary between 1045 GeV and 1065 GeV for the $H_L^{\pm\pm}$ mass assuming $B(H^{\pm\pm} \to \ell^{\pm}\ell^{\pm}) = 100\%$, while the expected limits are between 1010 GeV and 1020 GeV. This showcases that all light lepton channels have equal sensitivity to find new physics in the same-charge lepton final states. These limits extend the previous search described in this thesis by approximately 200 GeV, providing the most stringent limits up-to-date and excluding a remarkable part of the reachable phase-space at the LHC.

This analysis also studied a combination of all tau-inclusive final states for the first time in the $H^{\pm\pm}$ searches in ATLAS. The full systematic uncertainties affecting the tau-inclusive regions are missing at the time of writing, and the lower limits on the doubly charged Higgs boson mass were determined using statistical uncertainties only. The tau-inclusive final states have shown to provide weaker exclusion limits on the doubly charged Higgs boson mass of approximately 500 GeV mostly due to difficulties in restricting the large fake background entering the signal region. The fake background arising mainly from multijet events has very similar properties as the signal if the doubly charged Higgs decays into hadronic taus. However, even the fully hadronic final state of $\tau_{\text{had}}^{\pm}\tau_{\text{had}}^{\pm}$ was shown to provide some discrimination power between the doubly charged Higgs signal and the background events. The presented studies provide a good and promising starting point for more optimized studies in future using larger datasets.

10

SUMMARY

By studying the invariant mass distributions of the same-charge lepton pairs with the ATLAS detector, this thesis has searched for doubly charged Higgs bosons which, if found, could reveal the mechanism for generating small neutrino masses and open a window into new physics. Final states of same-charge leptons can be efficiently triggered and measured, and have low backgrounds from the Standard Model processes, providing a distinct and powerful signature towards discoveries.

In order to find a clear peak in the invariant mass distribution of the same-charge lepton pairs above a smooth background, an excellent tracking performance, good momentum resolution, and a wide detector coverage to reach the maximal signal acceptance are required. This thesis work started by determining the drift time and the spatial hit accuracy with the outermost tracking detector, the Transition Radiation Tracker (TRT). Multiple drift time calibrations were performed in various gas configurations using xenon and argon-based gas mixtures in order to ensure the best possible momentum reconstruction and position resolution in the TRT. The calibrations were done using both simulated and real data from proton–proton and heavy ion collisions. In all of these cases, good position resolutions and data quality is achieved, which shows that the argon-based gas mixture is adequate for tracking. The TRT detector performed very well for tracking during the full Run 2 despite the gas leaks and challenging environment due to large pile-up and high occupancy.

The search for doubly charged Higgs bosons $H_{L,R}^{\pm\pm}$ using 36.1 fb^{-1} of data from proton–proton collisions at $\sqrt{s} = 13$ TeV utilized the same-charge final states $e^{\pm}e^{\pm}$, $e^{\pm}\mu^{\pm}$ and $\mu^{\pm}\mu^{\pm}$ final states as well as final states with three or four light leptons. After careful design of analysis regions, and selecting events with isolated, prompt leptons, the background predictions from the Standard Model and data agree well, representing excellent understanding of the detector, and particle and event reconstruction. The absence of deviations from the Standard Model predictions was used to constrain the production cross-section and the lower mass of the doubly charged Higgs bosons. The observed lower limits on the the $H_L^{\pm\pm}$ mass are between 770 GeV and 870 GeV for $B(H^{\pm\pm} \to \ell^{\pm}\ell^{\pm}) = 100\%$, and are above 450 GeV for $B(H^{\pm\pm} \to \ell^{\pm}\ell^{\pm}) \geq 10\%$ for any combination of partial branching ratios. The observed lower limits on the $H_R^{\pm\pm}$ mass range from 660 GeV to 760 GeV for $B(H^{\pm\pm} \to \ell^{\pm}\ell^{\pm}) = 100\%$ and are above 320 GeV for $B(H^{\pm\pm} \to \ell^{\pm}\ell^{\pm}) \geq 10\%$. The obtained lower limits on the $H_L^{\pm\pm}$ and $H_R^{\pm\pm}$ masses obtained in this search for $B(H^{\pm\pm} \to \ell^{\pm}\ell^{\pm}) = 100\%$ are 300 GeV higher than those from the previous ATLAS analysis. This search is really close to reach the maximum sensitivity of the experiment with the given luminosity, and all the observed limits agree well with the expected ones.

After the first search made during the first years of data taking in Run 2, the search was extended by including final states with hadronically decaying taus, and the full Run 2 data corresponding to 139 fb^{-1}, recorded during the 2015–2018 data taking periods. Tau-inclusive final states are particularly interesting as they allow the analysis to probe if the doubly charged Higgs bosons have larger, mass-dependent couplings to the third-generation leptons, which would enhance the decays into tau leptons. Furthermore, complementing the search with taus, all possible final state combinations of charged leptons and therefore a plenty of previously uncovered phase-space can be utilized. The electron and muon selection as well as the analysis regions were further optimized to enhance the sensitivity to new physics. In all

analysis channels, very good agreement with the observed data and expected backgrounds are obtained. No excess of signal events was found in any of the signal regions, and the upper limits on the production cross-section and the lower limits on the mass of the doubly charged Higgs bosons were set. With the full Run 2 dataset, the search can exclude the doubly charged Higgs masses up to 1 TeV using light lepton final states. These limits extend the previous search described in this thesis by approximately 200 GeV, and provide the most stringent exclusion limits up-to-date.

The analysis covered a combination of all tau-inclusive final states for the first time in the $H^{\pm\pm}$ searches in ATLAS. While full systematic uncertainties are missing at the time of writing, the tau-inclusive final states have shown to provide exclusion limits on the doubly charged Higgs boson of approximately 500 GeV. Even the fully hadronic final state of $\tau^{\pm}_{\text{had}}\tau^{\pm}_{\text{had}}$ was shown to provide some discrimination power between the doubly charged Higgs signal and the background events despite lower sensitivity when comparing with light lepton channels, providing a good and promising starting point for more optimized studies in future. All in all, the presented searches cover a very interesting signature with multiple same-charge lepton final states, allowing a wide spectrum of theoretical interpretations.

As the Run 3 will provide a dataset corresponding to a total integrated luminosity of over $300\,\text{fb}^{-1}$, and the High Luminosity LHC has the goal of reaching up to $3000\,\text{fb}^{-1}$, the statistical reach of the searches will be greatly increased. The search for doubly charged Higgs bosons can be further improved by introducing multivariate analysis techniques, using other signal hypotheses to estimate sensitivity to other physics models, as well as using all the latest improvements in reconstruction performance and event selection. Together with all experimental improvements including the new all-silicon tracking system in ATLAS, and better analysis methods and tools, new physics may still be observed in the final states with same-charge leptons.

Part IV

APPENDICES

A

DOUBLY CHARGED HIGGS BOSON SIGNAL UNCERTAINTY

The search for doubly charged Higgs bosons implements uncertainties in the background sources, as described in Section 8.5. In addition, the statistical analysis also needs to account for both experimental and theoretical systematic uncertanties of the signal source. The theory uncertainty in the NLO K-factors for $pp \to H^{++}H^{--}$ cross-sections is about 15% [35]. It includes the QCD renormalization and factorization scale dependence and the uncertainty of the parton density functions. The theoretical uncertainties due to the used set of tuning parameters in Pythia 8 could also affect the signal efficiency as they may change the modelling of initial state radiation and MPI interactions. For this reason, the signal acceptance was studied in many tests by varying the showering parameters in Pythia 8, and checking the signal efficiency.

In this study, Pythia 8 was used to generate eight sets of 100000 new events for a single $H^{\pm\pm}$ mass point of 600 GeV, which is in the middle of the searched $H^{\pm\pm}$ mass range. Either the tune or parton density function was altered in each of these sets. The tunes mainly effet the modelling of initial and final state radiation, and multiparton interactions. The used tunes [106] and PDFs are the following:

- Nominal: ATLAS A14 central tune with NNPDF2.3LO.
- Tune 23: ATLAS A14 variation 1+ of the nominal, where values of variables related to multiparton interactions (MPI α_S) and beam remnants (colour reconnection strength) are varied. These variations affect underlying event activity and jet shapes.
- Tune 25: ATLAS A14 variation 2+ of the nominal, where values of variables related to space and time showers are varied, affecting jet shapes and substructure. These variables are the ISR p_T cutoff and factorization/renormalization scale damping, and FSR α_S.
- Tune 27: ATLAS A14 variation 3a+ of the nominal, where values of MPI α_S, ISR p_T cutoff and factorization/renormalization scale damping as well as factor on maximum ISR evolution scale and FSR α_S are varied. Therefore ISR and FSR distributions are most sensitive to such variations.
- Tune 31: ATLAS A14 variation 3c+ of the nominal alters the ISR α_S from the nominal NNPDF value of 0.127 to 0.140.
- Tune 32: ATLAS A14 variation 3c- of the nominal alters the ISR α_S from the nominal NNPDF value of 0.127 to 0.114.
- Alternative PDF set CTEQ6L1, LO
- Alternative PDF set CT09MC1, LO.

After generating events, the signal efficiency was determined in truth-level, i.e. not taking into any reconstruction and detector effects into account. Events containing exactly four electrons ($e^+e^+e^-e^-$) were selected, because the four-lepton electron channel provides very good sensitivity. Further preselection cuts such as the invariant mass cuts were applied to mimic the signal region defined after reconstruction, and finally the signal efficiency (ratio between number of selected events and all generated events) was measured. Figure 95 shows the obtained signal efficiencies for various tunes and parton density functions. The first point shows

the signal efficiency obtained with the nominal setting, whereas other points represent other variations as listed above.

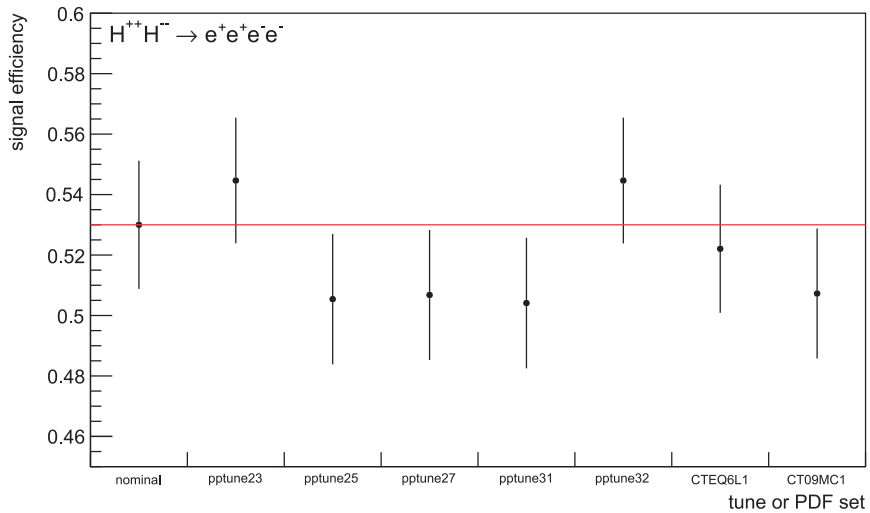

Figure 95: Signal efficiency for various tunes and parton density functions. Red line represents the nominal value.

Each of the variations differs less than 5% of the nominal value, and all points agree with the statistical uncertainties within a few percent. The nominal choice is in between of the extreme values of variations. Therefore, the effect of the additional systematic variations on the signal acceptance is ignored in the final fit, and no additional signal uncertainties were considered. This is motivated by several reasons. First, the search is primarily model independent and not targeting to exclude specific parameter values for a specific model. Second, the signal uncertainties are not available for the doubly charged Higgs boson models quoted in these searches. Furthermore, the signal samples are normalized to cross-sections provided by theorists [35] and are not obtained directly from Pythia 8. To summarize, the signal uncertainties were found to be negligible for this search.

B

STUDY OF THE $H^{\pm\pm} \to WW$ DECAY ON RESULTS

Results of the doubly charged Higgs search reported in Chapter 8 are presented in a general way where the sum of branching ratios of the $H^{\pm\pm}$ boson to light leptons (e and μ) does not necessarily add to 100%, as shown in Figures 75,76, and 77.

Therefore, it is important to verify that the other decay modes that could accommodate final states with X do not have a significant impact on obtained results. The decay modes with X could be for example W bosons or other particles that escape detection. This appendix presents such studies for $X = WW$, which is the most critical decay mode and possible for the case where the vacuum expectation value of the Higgs triplet is non-zero ($v_\Delta \neq 0$), as illustrated in Figure 9.

The study is performed by generating a set of new truth-level signal MC samples for one mass point of $m(H^{\pm\pm}) = 600\,\text{GeV}$, and a few values of v_Δ that cover branching ratios of $H^{\pm\pm} \to WW$ in various orders of magnitude. For the lowest values of v_Δ, the branching ratio to WW is negligible and for $v_\Delta = 10$ the branching ratio is 75% for this mass point. For each value of v_Δ the likelihood fit is performed for two cases:

- "X" = WW: true leptons originating directly from the $H^{\pm\pm}$ boson decay are combined with the true leptons originating from W bosons.
- "X" = invisible: leptons originating from W bosons are removed from the MC sample to mimic the way the results are presented in the analysis.

For each of the two cases, signal histograms are derived and the signal strength parameter (μ_{SIG}) is fitted with the nominal background prediction as described in Section 8.6. Results of the fit are presented in Figure 96. For low values of v_Δ the results for the two cases are identical and for higher values of v_Δ the case where leptons from W bosons are included in the signal histograms are becoming more stringent. This is expected, because the signal yield increases. However, leptons originating from W decays do not form a peak in the invariant mass distribution. Since the differences are small and limits are more stringent in the "X" = WW case, it is correct to assume that the results, presented in Section 8.6, are valid and conservative for this assumption.

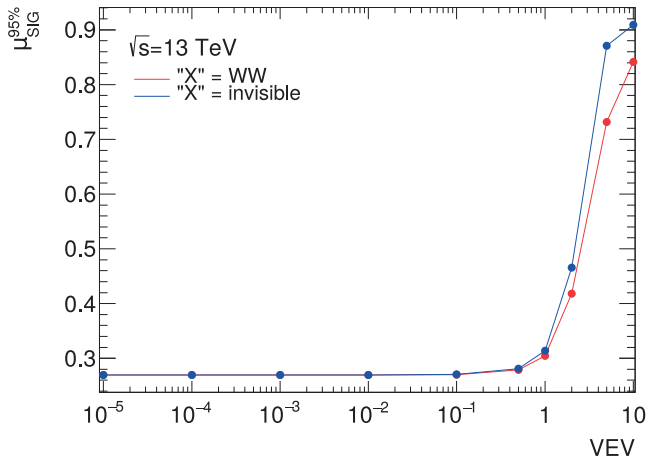

(a)

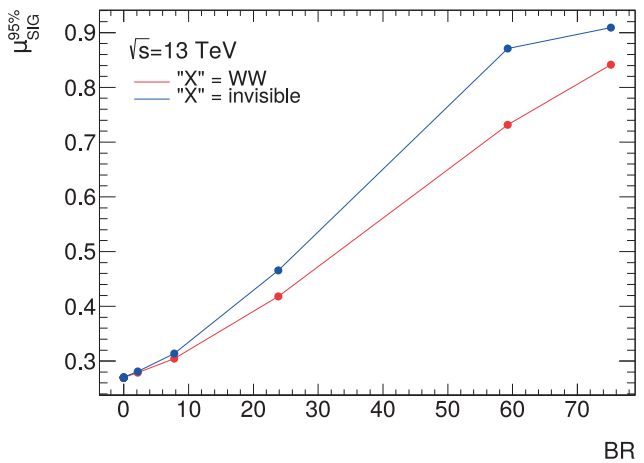

(b)

Figure 96: Impact of the $H^{\pm\pm} \to WW$ decay on the fitted $\mu^{95\%\text{SIG}}$ for $m(H^{\pm\pm}) = 600\,\text{GeV}$. The red curve represents the case where leptons from W bosons are removed from the sample. The blue curve represents the case where leptons from W bosons are treated the same as leptons originating directly from the $H^{\pm\pm}$ boson. Dependence of $\mu^{95\%}_{\text{SIG}}$ is shown for correlated variables: (a) the vacuum expectation value v_Δ (VEV) and (b) the branching ratio (BR) of $H^{\pm\pm}$ to WW.

C

FAKE TAUS IN SIMULATION

Final states involving τ-leptons are very common in searches for new physics and Standard Model measurements. Because τ-leptons decay leptonically (via $\tau \to \ell\nu_\ell\nu_\tau$, where ℓ is an electron or muon) only in about 35% of the cases, it is important to understand their hadronic decays (referred to as τ_{had}) very well. In the following, only consider hadronic taus are considered, unless otherwise stated. All hadronic tau candidates recorded by ATLAS undergo a sophisticated procedure for the reconstruction, calibration and identification, as described in detail in Section 5.5.6.2. Nevertheless, even after the whole identification process, some contamination of the jets that are misidentified as taus can still remain. These jets are referred to as *fake taus*.

The simulation of misidentified taus is usually not reliable enough to be used as the only way for background estimation: first because the comparison between data and Monte Carlo has shown to be rather poor without additional, data-driven background estimation, and second because the simulated samples have low statistics to estimate the corresponding fake-tau background with small enough statistical uncertainties.

However, it is important to improve and understand the simulated data samples to pinpoint possible differences in data and MC, and to understand origin and nature of the fake taus. This appendix is dedicated to two studies. First, the origin of the fake taus is studied in different simulated samples to understand how fake composition differs depending on specific object and event selections, as such study is difficult to perform using collision data only. Second, the simulated fake taus are compared between fast and full simulation. If no difference is observed between the fast and full simulated samples, fast simulation can be used to obtain large datasets faster and in a more CPU-efficient way.

C.1 BASELINE SAMPLE SELECTION

The samples used in the following studies are derived from centrally produced simulated samples: $Z \to \mu\mu$+jets samples are simulated using Powheg +Pythia 8, AZ tune and NLOCTEQ6L1 PDF set, and QCD dijet samples are simulated using Pythia 8, A14 tune and NNPDF23LO PDF set. The derived samples use specific reconstruction and identification algorithms for hadronically decaying taus. Therefore, these samples do not have any bias caused by initial offline selection used in derivations (e.g. in `SUSY` derivation samples used in the doubly charged Higgs searches). Such selection could be for example JetBDTScore cuts, and jet or lepton veto. Furthermore, in order to have as pure comparisons as possible and minimize the effect of pile-up, no pile-up reweighting, trigger scale factors, or further calibration were applied.

The baseline selection is very loose: the transverse momentum of the tau candidate is $p_{\text{T}}(\tau_{\text{had}}) > 20\,\text{GeV}$, and the pseudorapidity is $0 < |\eta| < 1.37, 1.5 < |\eta| < 2.5$ to exclude the crack region. Number of charged tracks is required to be exactly 1 or 3, and the total charge has to be ± 1. Tau identification has to pass the very loose `JetBDTScoreSigTrans`> 0.005 cut, and no additional BDT cuts on the tau identification are applied. Electron overlap tool is used to remove possible duplicates.

C.2 ORIGIN OF THE FAKE TAUS

Several processes at the LHC produce jets that arise from the hadronization and fragmentation of quarks and gluons, mimicking the signature of a hadronic tau decay. Consequently, a large amount of jets are misidentified as hadronic taus. The tau fake rate depends on the fake origin, and is different for gluon- and quark-initiated jets. Therefore, a precise knowledge of the tau fake composition is essential, as the quark/gluon fraction and therefore the fake composition and the fake rate differ depending on specific object and event selections.

Fake taus are selected from Monte Carlo using truth information, defined as reconstructed taus that are not truth-matched to real taus. Jets misreconstructed as taus are labelled using the attribute "`PartonTruthLabelID`" (PDG ID), corresponding to the particle data group identification number of the highest energy parton ghost-matched to the jet. In such ghost-matching, tracks are associated to jets by using a zero-energy copy of a track in the jet clustering algorithm. In some cases even a majority of the particles in an event can come from the pile-up jets, and in this case they will be labelled as unmatched fake taus. Unmatched means that truth matching algorithm failed or no link to original vertex was not found: these unmatched particles are most likely pile-up jets, because there is no primary vertex associated to them. More unmatched fake taus were found in MC16d (corresponding to 2018 data taking period) than in MC16a (corresponding to 2015 data taking period) most likely due to increased pile-up.

The fake tau origin in different processes is illustrated in Figure 97. In $Z \to \mu\mu$ + jets events, majority of the fake taus originate from quark jets, whereas in QCD dijet events the gluon-initiated fakes dominate. For this reason, it is important to understand which processes dominate in the analysis signal regions, and to derive different fake rates using V+jets samples and QCD multijet samples.

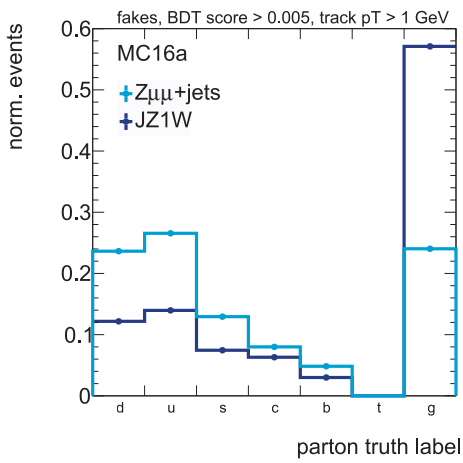

Figure 97: Fake tau origin in $Z \to \mu\mu$ + jets events and in dijet events (JZ1W) where p_{T} (jet)=20 – 60 GeV. Parton truth label refers to the origin of the fake tau: either a quark (d, u, s, c, b, t) or a gluon (g).

It is essential to have a good estimation on how many fake taus enter to the signal region in different analyses. Such estimation can be obtained using fake factors, as described in Section 7.5.2. As mentioned, two regions with different quark/gluon jet faking tau fractions lead to different fake factors, and therefore the quark/gluon fraction has to be accurately

understood. To get the fraction, a template fit of specific distributions sensitive to different gluon and quark properties can be performed.

As gluons carry both a colour and anti-colour while quarks carry only a single colour charge, on average gluon jets have more constituents than quark jets, i.e. gluon jets are broader than quark jets. In order to distinguish if the jets originate from quarks or gluons, ATLAS has developed specific tools ("taggers") that utilize various properties such as jet width, jet track width, charged particle multiplicity or convolutional neural networks with jet images to discriminate quarks from gluons [224, 225]. Since hadronic tau decays mostly have 1 or 3 charged tracks and since physics analyses introduce hard cuts on the number of core and isolation tracks, the number of tracks is less helpful in studying the origin of fake taus.

Before getting a definite choice about the variable to be used for the final template fit, many variables were checked by ATLAS Fake-Tau Task Force. Because of observed mismodelling of jet width when comparing simulation to data, it was decided to use the jet track width as a discriminating variable between quarks and gluons when deriving the templates. The jet track width was seen to be better modelled than the jet width because width is more sensitive to any mismodelling of pile-up clusters. Therefore, the final variable for templates is chosen to be the track width, defined as

$$w = \frac{\sum_i p_{\mathrm{T},i} \times \Delta R(i, \mathrm{jet})}{\sum_i p_{\mathrm{T},i}} \tag{74}$$

where the p_{T} cut is at 500 MeV. Increasing p_{T} may lead to even better modelling because of the reduced sensitivity to soft physics.

Figure 98 illustrates the jet track width shape for quark- and gluon-initiated 1-prong fake taus in QCD dijet events where p_{T} (jet)=$20 - 60$ GeV, confirming that gluon-initiated fakes are in general wider than quark-initiated fakes. The shape difference in jet track width therefore works as a handle to differentiate quark and gluon fraction in data sample, and to derive different fake rates corresponding to the fraction in the analysis regions.

Furthermore, it is important to understand if tau fakes are modelled in the same way in the ATLAS full and fast simulation. As presented earlier in Table 2, using Atlfast-II fast simulation can significantly reduce computing time, which comes even more crucial in future when datasets become larger with increasing luminosity and pile-up. Figure 99 shows the comparison between full and fast simulation in dijet events for fakes arising from quarks and gluons. The agreement between full and fast simulation is generally really good, which means that it is safe to use fast simulation instead of relying the full simulation when deriving the templates for the final fakes estimation. To make sure agreement also holds for jets with much higher p_{T}, other p_{T} slices in dijet sample were scanned. An example is shown in Figure 100, where the jet track width is plotted for the high p_{T} slice of $1300 - 1800$ GeV. The results of the comparison are consistent with lower p_{T} slices: no significant discrepancies are found.

It is also essential to make sure that other processes, and samples with different parton density functions and tunes will lead to the same conclusions. The jet track width distributions, as shown in Figure 101, indicate that there is no difference in full and fast simulation in the $Z \to \mu\mu$ + jets samples. Other kinematic variables, such as transverse momentum or pseudo-rapidity, do not have any discrepancies either. This study confirms that the fast simulation chain can be used when deriving fakes estimation for taus.

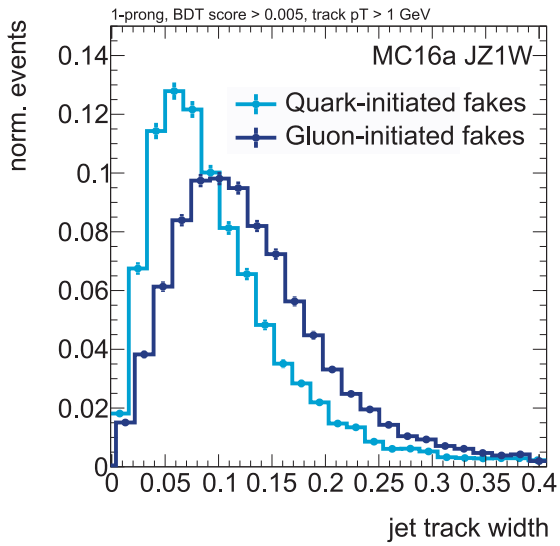

Figure 98: Jet track width shape for quark- and gluon-initiated 1-prong fake taus in dijet events where p_{T} (jet)=20 − 60 GeV, using MC16a pile-up profile matching the 2015+2016 data taking conditions, trigger menu and μ profile.

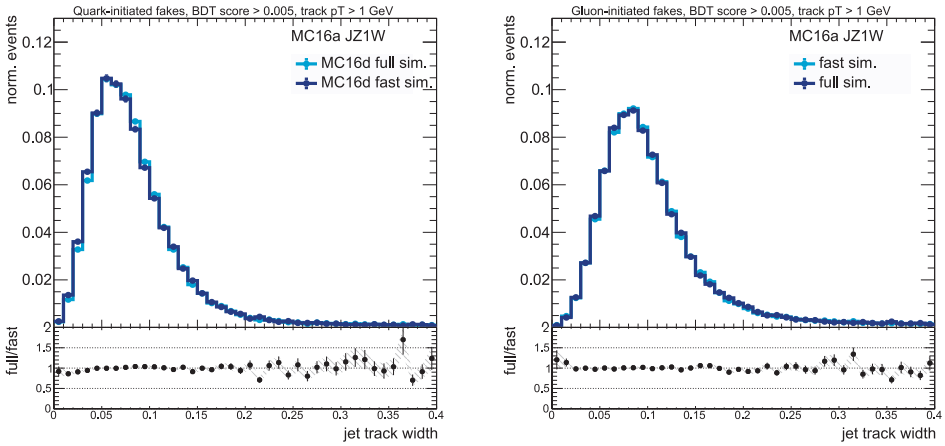

(a) (b)

(c) (d)

Figure 99: Jet track width shape in dijet events where p_{T} (jet)=20 – 60 GeV, for (a) quark-initiated fakes in MC16a, (b) gluon-initiated fakes in MC16a, (c) quark-initiated fakes in MC16d, and (d) gluon-initiated fakes in MC16d.

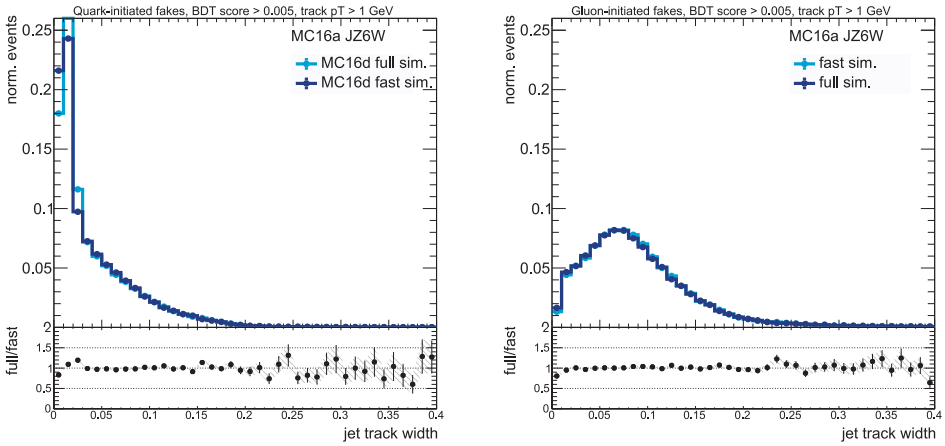

(a) (b)

(c) (d)

Figure 100: Jet track width shape in dijet events where p_{T} (jet)=1300 – 1800 GeV, for (a) quark-initiated fakes in MC16a, (b) gluon-initiated fakes in MC16a, (c) quark-initiated fakes in MC16d, and (d) gluon-initiated fakes in MC16d.

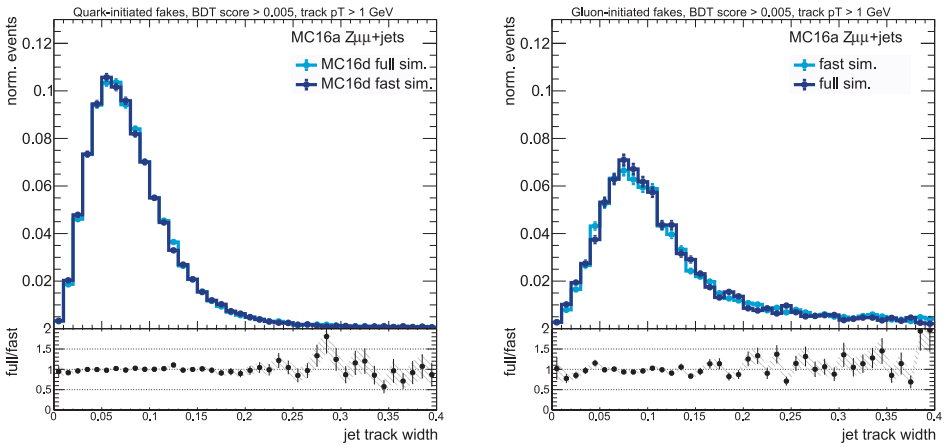

(a) (b)

Figure 101: Jet track width shape in $Z \to \mu\mu$ + jets events, for (a) quark-initiated fakes in MC16a, and (b) gluon-initiated fakes in MC16a.

D

FAKE-TAU FILTER DEVELOPMENT

Main aim of the ATLAS Fake-Tau Task Force (FTTF) is to harmonise the estimation of backgrounds with fake-tau objects and compute the associated systematic uncertainties. As a part of FTTF, a fake-tau filter based on Quentin Buat's original work was developed to generate simulated data samples enriched with fake-tau objects. In this appendix, the filtering algorithm together with the obtained results are shown.

D.1 FAKE-TAU FILTER ALGORITHM

The Monte Carlo simulation is usually not reliable enough to account for the misidentification of hadronic tau candidates, as the visible signature of hadronically decaying taus closely mimics that of QCD jets. Furthermore, the existing simulated samples have low statistics to estimate the corresponding fake-tau background with small enough statistical uncertainties. Therefore, data-driven fake background estimation methods are used to estimate the misidentification rate of hadronic tau candidates.

However, simulated samples can help in validating data-driven estimations of fake-tau background and in estimating systematic uncertainties. The idea of the fake-tau filter is to enrich simulated data samples with jets misidentified as hadronic taus to increase the statistical power of the existing simulated data. To generate such a data sample, a fake-tau filter is implemented in the event generation level before simulating the detector response. The main algorithm of the filter is as follows:

1. Loop over all particles in the event and build up the truth jets:
   - Remove unstable particles
   - Remove muons and neutrinos, because muons are only rarely misidentified as hadronic taus
2. Cluster selected particles together in anti-*kt* jets using FastJet package [134]
   - Classify charged particles with $p_{\mathrm{T}} > 1\,\mathrm{GeV}$:
     - core tracks ($\Delta R < 0.2$): used to compute charge multiplicity
     - isolation tracks ($0.2 < \Delta R < 0.4$)
   - tau candidate is formed from the sum the 4-vectors of the particles within the core cone
3. Check that the selected particle makes a good track candidate, and apply kinematic cuts and track selection on the truth reconstructed taus.

D.2 FILTER EFFICIENCY

The fake-tau filter studies are performed using different ATLAS Athena releases corresponding the MC16a (2015+2016 data taking period) simulated data processing. All the used Monte Carlo samples, listed in Table 25, are generated at a centre-of-mass energy of 13 TeV using the centrally generated default job options together with the fake-tau filter. Produced events were

simulated using both ATLAS fast simulation and full simulation, where the response of the ATLAS detector is simulated using GEANT4. Physics lists consists of numerical models that describe both electromagnetic and hadronic particle interactions in GEANT4 simulation. In the presented studies, `FTFP_BERT_ATL_VALIDATION` physics list was used. It includes the Fritiof parton model (`FTF`), Bertini cascade model (`BERT`) and Precompound models (`P`) as a part of the hadronic physics package.

Table 25: Simulated event samples. Cross-sections are obtained from the centrally derived samples, i.e. before applying the filter.

Physics process	Event generator	Tune and PDF set	Cross-section [nb]
V+jets:			
$Z \to \mu\mu$ + jets	POWHEG + PYTHIA 8 (v8.186)	AZNLOCTEQ6L1	1.9
$W^+ \to \mu^+\nu$ + jets	POWHEG + PYTHIA 8 (v8.186)	AZNLOCTEQ6L1	11.3
$W^- \to \mu^-\nu$ + jets	POWHEG + PYTHIA 8 (v8.186)	AZNLOCTEQ6L1	8.3
Dijet:			
p_T 0 − 20 GeV	PYTHIA 8	A14NNPDF23LO	-
p_T 20 − 60 GeV	PYTHIA 8	A14NNPDF23LO	$7.8 \cdot 10^7$
p_T 60 − 160 GeV	PYTHIA 8	A14NNPDF23LO	$2.4 \cdot 10^6$

The baseline selection criteria are defined as

- FastJet cone size $\Delta R \leq 0.4$
- FastJet $p_T > 17$ GeV
- FastJet $|\eta| < 2.8$
- Track $p_T > 1$ GeV
- Core track $p_T > 17$ GeV
- 0-6 core tracks are required, but there is no isolation track criteria
- Core cone size $\Delta R \leq 0.2$
- Isolation cone size $\Delta R \leq 0.4$.

These requirements are chosen to have as many fake objects passing the analysis selection criteria as possible. Loosening some of the requirements, particularly the transverse momentum cut, would increase the number of fake taus. However, such low-p_T fake objects would not satisfy any real analysis selection criteria, and therefore generating them would not increase our knowledge on fake taus affecting physics analyses.

The hadronically decaying taus are classified according to the number of charged tracks in the core cone, most of the taus decays having one or three charged tracks (or prongs). However, the requirement of the number of core tracks in the filter is loosened to be at most six. This very loose requirement is added for several reasons. First, there is some track reconstruction inefficiency for charged hadrons, so it can happen that 2 tracks with generated $p_T > 1$ GeV will either fail the track reconstruction threshold due to p_T resolution, or not be

Table 26: Number of all events, events with at least one fake tau, real taus, and fake taus in the simulated dijet samples where jet p_T = 0-20 GeV. "Fast" refers to ATLAS fast simulation, and "full" to ATLAS full simulation. "Fil." denotes the sample generated using the filter, and "off." the centrally derived official sample.

	process	#all events	#fake events	#real taus	# fakes
MC16a fast	JZoW fil.	1000	306	0	404
MC16a full	JZoW fil.	1000	313	0	397
MC16a fast	JZoW off.	10000	1481	0	1859
MC16a full	JZoW off.	10000	1530	0	1932
MC16d fast	JZoW fil.	1000	559	0	791
MC16d full	JZoW fil.	1000	549	0	803
MC16d fast	JZoW off.	10000	2748	0	3994
MC16d full	JZoW off.	10000	2778	0	3940

reconstructed at all. Second, the criteria is applied already at the truth level, and a specific η/ϕ smearing is applied between the truth and reconstruction level especially in the calorimeter-based reconstruction. Therefore, the η/ϕ of the reconstructed tau may be away from the η/ϕ of the truth jet, which leads to including different tracks at the reconstruction level than at the truth level. Last, the track classification at reconstruction level uses multivariate technique. Therefore a jet with initially 6 core tracks can end up having 3 good-quality tau tracks and be reconstructed as a tau.

As mentioned, the centrally generated default job options are extended with the fake-tau filter selection, and a set of new samples are generated. After event reconstruction, the number of events with at least one fake tau are compared between the new set of samples and the centrally derived samples without the filter. A fake tau is defined as a reconstructed tau which is not truth matched to a real tau (`TauJetsAuxDyn.truthMatchParticle_pdgID != 15` where a real tau has a particle ID 15).

Finally, the filter efficiency can be determined from the selection efficiency of the official centrally derived sample e_{off} without the filter, and the efficiency of the filtered sample. First, the selection efficiency of the official sample is simply a ratio between passed events and generated events: $e_{\text{off}} = N_{\text{off,pass}}/N_{\text{off,gen}}$. Similarly, efficiency in the filtered sample e_{own} is the ratio between passed events and generated events in the filtered sample: $e_{\text{own}} = N_{\text{fil,pass}}/N_{\text{fil,gen}} = e_{\text{off}} \times e_{\text{fil}}$. From that relation, the "pure" filter efficiency can be obtained as

$$e_{\text{fil}} = e_{\text{own}}/e_{\text{off}}. \tag{75}$$

Table 26 shows the number of all events, events with at least one fake tau, real taus, and fake taus in the simulated low-p_T dijet samples where jet p_T = 0-20 GeV. Similarly, Table 27 shows similar numbers in the simulated dijet sample where jet p_T = 20-60 GeV. Finally, Table 28 shows the corresponding numbers for a simulated sample consisting of $Z \to \mu\mu$+jets events obtained using MC16a fast simulation.

The filter efficiencies are computed in Table 29 for two dijet samples with two p_T slices covering a p_T range from 0 GeV up to 60 GeV, obtained both for MC16a and MC16d as well as for fast and full simulation. The $Z \to \mu\mu$+jets samples are obtained only for MC16a fast simulation due to technical challenges with available computing resources in the event generation

Table 27: Number of all events, events with at least one fake tau, real taus, and fake taus in the simulated dijet samples where jet p_T = 20-60 GeV. "Fast" refers to ATLAS fast simulation, and "full" to ATLAS full simulation. "Fil." denotes the sample generated using the filter, and "off." the centrally derived official sample.

	process	#all events	#fake events	#real taus	# fakes
MC16a fast	JZ1W fil.	1000	605	0	887
MC16a full	JZ1W fil.	1000	585	0	876
MC16a fast	JZ1W off.	10000	5822	6	8569
MC16a full	JZ1W off.	10000	5807	7	8484
MC16d fast	JZ1W fil.	1000	691	0	1265
MC16d full	JZ1W fil.	1000	687	0	1238
MC16d fast	JZ1W off.	10000	6523	7	10858
MC16d full	JZ1W off.	10000	6610	6	11060

Table 28: Number of all events, events with at least one fake tau, real taus, and fake taus in the simulated $Z \to \mu\mu$+jets samples. "Fast" refers to ATLAS fast simulation. "Fil." denotes the sample generated using the filter, and "off." the centrally derived official sample.

	process	#all events	#fake events	#real taus	# fakes
MC16a fast	$Z \to \mu\mu$+jets fil.	1000	368	1	513
MC16a fast	$Z \to \mu\mu$+jets off.	10000	2945	1	3855

Table 29: Fake-tau filter efficiencies for various samples in MC16a (corresponding to 2015+2016 data taking period) and M16d (corresponding to 2018 data taking period) in both full and fast simulation. $W \to \mu\nu$+jets samples were only studied at the truth level without detector simulation.

process	data period	sim. type	filter efficiency
dijet JZoW p_T0-20 GeV			
	MC16a	fast	$0.306/0.1481 = 2.066$
	MC16a	full	$0.313/0.1530 = 2.046$
	MC16d	fast	$0.559/0.2748 = 2.034$
	MC16d	full	$0.549/0.2778 = 1.976$
dijet JZ1W p_T20-60 GeV			
	MC16a	fast	$0.605/0.5822 = 1.039$
	MC16a	full	$0.585/0.5807 = 1.007$
	MC16d	fast	$0.691/0.6523 = 1.059$
	MC16d	full	$0.687/0.6610 = 1.039$
$Z \to \mu\mu$+jets			
	MC16a	fast	$0.368/0.2945 = 1.250$

Table 30: Fake-tau filter efficiencies obtained in the $W \to \mu\nu$+jets samples, which were only studied at the truth level without detector simulation.

process	truth jet p_{T} threshold	filter efficiency
$W \to \mu\nu$+jets		
	$p_{\mathrm{T}} > 15\,\mathrm{GeV}$	1.18
	$p_{\mathrm{T}} > 17\,\mathrm{GeV}$	1.13
	$p_{\mathrm{T}} > 20\,\mathrm{GeV}$	1.08
	$p_{\mathrm{T}} > 25\,\mathrm{GeV}$	1.05

level. As can be seen, the designed fake-tau filter increases the amount of fake-tau events in $Z \to \mu\mu$+jets events up to 25%, and in low-p_{T} dijet samples it can even double the number of fake events. However, for the dijet sample where the jet p_{T} is increased to $p_{\mathrm{T}} =$ 20-60 GeV, the impact of the filter is much less significant. There are only small differences, all within the statistical fluctuations, when comparing MC16a and MC16d conditions or full and fast simulation.

To fully understand the impact of varying the p_{T} threshold of the leading jet, a specific truth-level study was performed using the $W \to \mu\nu$+jets samples. Table 30 shows the filter efficiencies obtained using the $W \to \mu\nu$+jets samples at the truth level without detector simulation. The p_{T} threshold of the leading jet was varied from $p_{\mathrm{T}} > 15\,\mathrm{GeV}$ to $p_{\mathrm{T}} > 25\,\mathrm{GeV}$. The filter efficiency decreased from 1.18 at $p_{\mathrm{T}} > 15\,\mathrm{GeV}$ to 1.05 at $p_{\mathrm{T}} > 25\,\mathrm{GeV}$, clearly confirming that the most effective requirement in the filter is the p_{T} of the leading jet, and by loosening the requirement more fake taus can be generated. However, this will not help in the dijets case because the samples are sliced according to the jet p_{T} in order to have enough statistics in the high p_{T} regions. Another test with the $W \to \mu\nu$+jets truth-level samples was performed to study the impact on tuning the track selection. It turned out that requiring 0 or at least 1 core tracks does not affect the filter efficiency as expected, but adding the isolation track cut selecting $0 - 2$ isolation tracks decreases the filter efficiency up to 30%.

All in all, extending the centrally derived samples with the filter does not cause a significant gain. However, further studies and adding additional information to the filter may help increasing the performance. Selecting additional variables could be inspired by the variables used in the multivariate tau identification, such as cluster-level variables, momentum fraction of the tracks, electromagnetic energy fraction of charged pions, and number of hits in specific Inner Detector layers. However, these variables require information from the detector simulation and therefore cannot be simply implemented in the event-generation level.

BIBLIOGRAPHY

[1] ATLAS collaboration. "Search for heavy Majorana or Dirac neutrinos and right-handed W gauge bosons in final states with two charged leptons and two jets at $\sqrt{s} = 13$TeV with the ATLAS detector." In: *Journal of High Energy Physics* 2019.1 (2019), p. 16. ISSN: 1029-8479. DOI: 10.1007/JHEP01(2019)016. URL: https://doi.org/10.1007/JHEP01(2019)016.

[2] ATLAS Collaboration. "Search for doubly charged Higgs boson production in multi-lepton final states with the ATLAS detector using proton–proton collisions at $\sqrt{s} = 13$ TeV." In: *Eur. Phys. J. C* 78 (2018), p. 199. DOI: 10.1140/epjc/s10052-018-5661-z. arXiv: 1710.09748 [hep-ex].

[3] ATLAS Collaboration. *Search for type-III seesaw heavy leptons in proton-proton collisions at $\sqrt{s} = 13$ TeV with the ATLAS detector*. Tech. rep. ATLAS-CONF-2018-020. Geneva: CERN, 2018. URL: http://cds.cern.ch/record/2621484.

[4] ATLAS Collaboration. *Search for doubly-charged Higgs boson production in multi-lepton final states with the ATLAS detector using proton–proton collisions at $\sqrt{s} = 13$ TeV*. ATLAS-CONF-2017-053. 2017. URL: https://cds.cern.ch/record/2273869.

[5] T. Whyntie and O. Pugh. *Introducing Particle Physics: A Graphic Guide*. Introducing (Thriplow, England). Icon Books, 2013. ISBN: 9781848315891.

[6] Carsten Burgard. *Example: Standard model of physics*. 2016. URL: http://www.texample.net/tikz/examples/model-physics/ (visited on 06/04/2019).

[7] M. Tanabashi et al. "Review of Particle Physics." In: *Phys. Rev.* D98.3 (2018), p. 030001. DOI: 10.1103/PhysRevD.98.030001.

[8] R.L. Weber. *More Random Walks in Science*. CRC Press, 2017. ISBN: 9781351430135.

[9] Bo Andersson, G. Gustafson, G. Ingelman, and T. Sjostrand. "Parton Fragmentation and String Dynamics." In: *Phys. Rept.* 97 (1983), pp. 31–145. DOI: 10.1016/0370-1573(83)90080-7.

[10] John Campbell, Joey Huston, and Frank Krauss. *The black book of quantum chromodynamics: a primer for the LHC era*. Oxford: Oxford University Press, 2018. DOI: 10.1093/oso/9780199652747.001.0001. URL: https://cds.cern.ch/record/2286381.

[11] A Zee. *Quantum Field Theory in a Nutshell*. Nutshell handbook. Princeton, NJ: Princeton Univ. Press, 2003. URL: https://cds.cern.ch/record/706825.

[12] David Griffiths. *Introduction to elementary particles*. 2008. ISBN: 9783527406012.

[13] Jakob Schwichtenberg. *Physics from Symmetry*. Undergraduate Lecture Notes in Physics. Cham: Springer International Publishing, 2018. ISBN: 9783319666303, 9783319666310. DOI: 10.1007/978-3-319-66631-0. URL: http://www.springer.com/de/book/9783319666303.

[14] CMS Collaboration. "Observation of a new boson at a mass of 125 GeV with the CMS experiment at the LHC." In: *Physics Letters B* 716.1 (2012), 30–61. ISSN: 0370-2693. DOI: 10.1016/j.physletb.2012.08.021. URL: http://dx.doi.org/10.1016/j.physletb.2012.08.021.

[15] ATLAS Collaboration. "Observation of a new particle in the search for the Standard Model Higgs boson with the ATLAS detector at the LHC." In: *Physics Letters B* 716.1 (2012), 1–29. ISSN: 0370-2693. DOI: 10.1016/j.physletb.2012.08.020. URL: http://dx.doi.org/10.1016/j.physletb.2012.08.020.

[16] David Miller. "Politics, solid state and the Higgs." In: *Physics World* 6.9 (1993), pp. 27–27. DOI: 10.1088/2058-7058/6/9/26. URL: https://doi.org/10.1088%2F2058-7058%2F6%2F9%2F26.

[17] P. A. R. Ade et al. "Planck2015 results." In: *Astronomy & Astrophysics* 594 (2016), A13. ISSN: 1432-0746. DOI: 10.1051/0004-6361/201525830. URL: http://dx.doi.org/10.1051/0004-6361/201525830.

[18] R.N. Mohapatra. "Neutrino mass - an overview." In: *Nuclear Physics B - Proceedings Supplements* 138 (2005), 257–266. ISSN: 0920-5632. DOI: 10.1016/j.nuclphysbps.2004.11.061. URL: http://dx.doi.org/10.1016/j.nuclphysbps.2004.11.061.

[19] Rabindra N Mohapatra. "Supersymmetry and R-parity: an overview." In: *Physica Scripta* 90.8 (2015), p. 088004. DOI: 10.1088/0031-8949/90/8/088004. URL: https://doi.org/10.1088%2F0031-8949%2F90%2F8%2F088004.

[20] ATLAS Collaboration. "Search for supersymmetry in final states with two same-sign or three leptons and jets using 36 fb^{-1} of $\sqrt{s} = 13$ TeV pp collision data with the ATLAS detector." In: *JHEP* 09 (2017), p. 084. DOI: 10.1007/JHEP09(2017)084. arXiv: 1706.03731 [hep-ex].

[21] G. Senjanovic. "Neutrino mass: From LHC to grand unification." In: *Riv. Nuovo Cim.* 34 (2011), pp. 1–68. DOI: 10.1393/ncr/i2011-10061-8.

[22] Wai-Yee Keung and Goran Senjanovic. "Majorana Neutrinos and the Production of the Right-Handed Charged Gauge Boson." In: *Phys. Rev. Lett.* 50 (19 1983), pp. 1427–1430. DOI: 10.1103/PhysRevLett.50.1427. URL: https://link.aps.org/doi/10.1103/PhysRevLett.50.1427.

[23] ATLAS Collaboration. "Search for heavy Majorana neutrinos with the ATLAS detector in pp collisions at $\sqrt{s} = 8$ TeV." In: *JHEP* 07 (2015), p. 162. DOI: 10.1007/JHEP07(2015)162. arXiv: 1506.06020 [hep-ex].

[24] Camilo Garcia-Cely and Julian Heeck. "Phenomenology of left-right symmetric dark matter." In: *Journal of Cosmology and Astroparticle Physics* 2016.03 (2016), 021–021. ISSN: 1475-7516. DOI: 10.1088/1475-7516/2016/03/021. URL: http://dx.doi.org/10.1088/1475-7516/2016/03/021.

[25] Jogesh C. Pati and Abdus Salam. "Lepton Number as the Fourth Color." In: *Phys. Rev. D* 10 (1974). Erratum: Phys. Rev. D11 (1975) 703, pp. 275–289. DOI: 10.1103/PhysRevD.10.275,10.1103/PhysRevD.11.703.2.

[26] Rabindra N. Mohapatra and Jogesh C. Pati. "Left-Right Gauge Symmetry and an Isoconjugate Model of CP Violation." In: *Phys. Rev. D* 11 (1975), pp. 566–571. DOI: 10.1103/PhysRevD.11.566.

[27] G. Senjanovic and Rabindra N. Mohapatra. "Exact Left-Right Symmetry and Spontaneous Violation of Parity." In: *Phys. Rev. D* 12 (1975), p. 1502. DOI: 10.1103/PhysRevD.12.1502.

[28] P.S. Bhupal Dev, Rabindra N. Mohapatra, and Yongchao Zhang. "Displaced photon signal from a possible light scalar in minimal left-right seesaw model." In: *Phys. Rev. D* 95.11 (2017), p. 115001. DOI: 10.1103/PhysRevD.95.115001. arXiv: 1612.09587 [hep-ph].

[29] Debasish Borah and Arnab Dasgupta. "Observable lepton number violation with predominantly Dirac nature of active neutrinos." In: *JHEP* 01 (2017), p. 072. DOI: 10.1007/JHEP01(2017)072. arXiv: 1609.04236 [hep-ph].

[30] Rabindra N. Mohapatra and Goran Senjanovic. "Neutrino Mass and Spontaneous Parity Nonconservation." In: *Phys. Rev. Lett.* 44 (14 1980), pp. 912–915. DOI: 10.1103/PhysRevLett.44.912. URL: https://link.aps.org/doi/10.1103/PhysRevLett.44.912.

[31] P. H. Frampton. "Chiral dilepton model and the flavor question." In: *Phys. Rev. Lett.* 69 (20 1992), pp. 2889–2891. DOI: 10.1103/PhysRevLett.69.2889. URL: https://link.aps.org/doi/10.1103/PhysRevLett.69.2889.

[32] Gennaro Corcella, Claudio Coriano, Antonio Costantini, and Paul H. Frampton. "Bilepton Signatures at the LHC." In: *Phys. Lett.* B773 (2017), pp. 544–552. DOI: 10.1016/j.physletb.2017.09.015. arXiv: 1707.01381 [hep-ph].

[33] Gennaro Corcella, Claudio Corianò, Antonio Costantini, and Paul H. Frampton. "Exploring Scalar and Vector Bileptons at the LHC in a 331 Model." In: *Phys. Lett.* B785 (2018), pp. 73–83. DOI: 10.1016/j.physletb.2018.08.015. arXiv: 1806.04536 [hep-ph].

[34] Stephen L. Adler. "Axial-Vector Vertex in Spinor Electrodynamics." In: *Phys. Rev.* 177 (5 1969), pp. 2426–2438. DOI: 10.1103/PhysRev.177.2426. URL: https://link.aps.org/doi/10.1103/PhysRev.177.2426.

[35] Margarete Muhlleitner and Michael Spira. "Note on doubly charged Higgs pair production at hadron colliders." In: *Phys. Rev. D* 68 (2003), p. 117701. DOI: 10.1103/PhysRevD.68.117701. arXiv: hep-ph/0305288.

[36] A. G. Akeroyd and Mayumi Aoki. "Single and pair production of doubly charged Higgs bosons at hadron colliders." In: *Phys. Rev. D* 72 (2005), p. 035011. DOI: 10.1103/PhysRevD.72.035011. arXiv: hep-ph/0506176.

[37] A. Hektor, M. Kadastik, M. Muntel, M. Raidal, and L. Rebane. "Testing neutrino masses in little Higgs models via discovery of doubly charged Higgs at LHC." In: *Nucl. Phys. B* 787 (2007), pp. 198–210. DOI: 10.1016/j.nuclphysb.2007.07.014. arXiv: 0705.1495 [hep-ph].

[38] Pavel Fileviez Perez, Tao Han, Gui-Yu Huang, Tong Li, and Kai Wang. "Testing a neutrino mass generation mechanism at the Large Hadron Collider." In: *Phys. Rev. D* 78 (2008), p. 071301. DOI: 10.1103/PhysRevD.78.071301. arXiv: 0803.3450 [hep-ph].

[39] Wei Chao, Zong-Guo Si, Zhi-zhong Xing, and Shun Zhou. "Correlative signatures of heavy Majorana neutrinos and doubly-charged Higgs bosons at the Large Hadron Collider." In: *Phys. Lett. B* 666 (2008), pp. 451–454. DOI: 10.1016/j.physletb.2008.08.003. arXiv: 0804.1265 [hep-ph].

[40] J. E. Cieza Montalvo, Nelson V. Cortez, J. Sa Borges, and Mauro D. Tonasse. "Searching for doubly charged Higgs bosons at the LHC in a 3-3-1 model." In: *Nucl. Phys. B* 756 (2006). Erratum: Nucl. Phys. B 796 (2008) 422, pp. 1–15. DOI: 10.1016/j.nuclphysb.2006.08.013,10.1016/j.nuclphysb.2008.01.003. arXiv: hep-ph/0606243.

[41] J. F. Gunion, R. Vega, and J. Wudka. "Higgs triplets in the standard model." In: *Phys. Rev. D* 42 (1990), pp. 1673–1691. DOI: 10.1103/PhysRevD.42.1673.

[42] N. Arkani-Hamed, A. G. Cohen, E. Katz, A. E. Nelson, T. Gregoire, and Jay G. Wacker. "The Minimal Moose for a Little Higgs." In: *JHEP* 08 (2002), p. 021. DOI: 10.1088/1126-6708/2002/08/021. arXiv: hep-ph/0206020.

[43] Howard Georgi and Marie Machacek. "Doubly Charged Higgs Bosons." In: *Nucl. Phys. B* 262 (1985), pp. 463–477. DOI: 10.1016/0550-3213(85)90325-6.

[44] Subhaditya Bhattacharya, Sudip Jana, and S. Nandi. "Neutrino masses and scalar singlet dark matter." In: *Phys. Rev. D* 95.5 (2017), p. 055003. DOI: 10.1103/PhysRevD.95.055003. arXiv: 1609.03274 [hep-ph].

[45] A. Zee. "Quantum Numbers of Majorana Neutrino Masses." In: *Nucl. Phys. B* 264 (1986), pp. 99–110. DOI: 10.1016/0550-3213(86)90475-X.

[46] K. S. Babu. "Model of 'Calculable' Majorana Neutrino Masses." In: *Phys. Lett. B* 203 (1988), pp. 132–136. DOI: 10.1016/0370-2693(88)91584-5.

[47] Miguel Nebot, Josep F. Oliver, David Palao, and Arcadi Santamaria. "Prospects for the Zee-Babu Model at the CERN LHC and low energy experiments." In: *Phys. Rev. D* 77 (2008), p. 093013. DOI: 10.1103/PhysRevD.77.093013. arXiv: 0711.0483 [hep-ph].

[48] J. F. Gunion, J. Grifols, A. Mendez, Boris Kayser, and Fredrick I. Olness. "Higgs bosons in left-right symmetric models." In: *Phys. Rev. D* 40 (1989), p. 1546. DOI: 10.1103/PhysRevD.40.1546.

[49] N. G. Deshpande, J. F. Gunion, Boris Kayser, and Fredrick I. Olness. "Left-right symmetric electroweak models with triplet Higgs." In: *Phys. Rev. D* 44 (1991), pp. 837–858. DOI: 10.1103/PhysRevD.44.837.

[50] K. S. Babu and Sudip Jana. "Probing doubly charged Higgs bosons at the LHC through photon initiated processes." In: *Phys. Rev. D* 95.5 (2017), p. 055020. DOI: 10.1103/PhysRevD.95.055020. arXiv: 1612.09224 [hep-ph].

[51] K. Huitu, J. Maalampi, A. Pietila, and M. Raidal. "Doubly charged Higgs at LHC." In: *Nucl. Phys. B* 487 (1997), pp. 27–42. DOI: 10.1016/S0550-3213(97)87466-4. arXiv: hep-ph/9606311.

[52] A. G. Akeroyd, Cheng-Wei Chiang, and Naveen Gaur. "Leptonic signatures of doubly charged Higgs boson production at the LHC." In: *Journal of High Energy Physics* 2010.11 (2010). ISSN: 1029-8479. DOI: 10.1007/jhep11(2010)005. URL: http://dx.doi.org/10.1007/JHEP11(2010)005.

[53] Vikram Rentala, William Shepherd, and Shufang Su. "Simplified model approach to same-sign dilepton resonances." In: *Phys. Rev. D* 84 (3 2011), p. 035004. DOI: 10.1103/PhysRevD.84.035004. URL: https://link.aps.org/doi/10.1103/PhysRevD.84.035004.

[54] Bhaskar Dutta, Ricardo Eusebi, Yu Gao, Tathagata Ghosh, and Teruki Kamon. "Exploring the doubly charged Higgs boson of the left-right symmetric model using vector boson fusion-like events at the LHC." In: *Phys. Rev. D* 90 (2014), p. 055015. DOI: 10.1103/PhysRevD.90.055015. arXiv: 1404.0685 [hep-ph].

[55] Pavel Fileviez Pérez, Tao Han, Guiyu Huang, Tong Li, and Kai Wang. "Neutrino masses and the CERN LHC: Testing the type II seesaw mechanism." In: *Phys. Rev. D* 78 (1 2008), p. 015018. DOI: 10.1103/PhysRevD.78.015018. URL: https://link.aps.org/doi/10.1103/PhysRevD.78.015018.

[56] Morris L. Swartz. "Limits on doubly charged Higgs bosons and lepton-flavor violation." In: *Phys. Rev. D* 40 (5 1989), pp. 1521–1528. DOI: 10.1103/PhysRevD.40.1521. URL: https://link.aps.org/doi/10.1103/PhysRevD.40.1521.

[57] L3 Collaboration. "Search for doubly-charged Higgs bosons at LEP." In: *Phys. Lett. B* 576.1 (2003), pp. 18 –28. ISSN: 0370-2693. DOI: https://doi.org/10.1016/j.physletb.2003.09.082. URL: http://www.sciencedirect.com/science/article/pii/S0370269303015107.

[58] Do Collaboration. "Search for Doubly Charged Higgs Boson Pair Production in $p\overline{p}$ Collisions at $\sqrt{s} = 1.96$ TeV." In: *Phys. Rev. Lett.* 108 (2 2012), p. 021801. DOI: 10.1103/PhysRevLett.108.021801. URL: https://link.aps.org/doi/10.1103/PhysRevLett.108.021801.

[59] DCF Collaboration. "Search for Doubly Charged Higgs Bosons with Lepton-Flavor-Violating Decays Involving τ Leptons." In: *Phys. Rev. Lett.* 101 (12 2008), p. 121801. DOI: 10.1103/PhysRevLett.101.121801. URL: https://link.aps.org/doi/10.1103/PhysRevLett.101.121801.

[60] H1 Collaboration. "Search for doubly-charged Higgs boson production at HERA." In: *Physics Letters B* 638.5 (2006), pp. 432 –440. ISSN: 0370-2693. DOI: https://doi.org/10.1016/j.physletb.2006.05.061. URL: http://www.sciencedirect.com/science/article/pii/S0370269306006551.

[61] ATLAS Collaboration. "Search for doubly charged Higgs bosons in like-sign dilepton final states at $\sqrt{s} = 7$ TeV with the ATLAS detector." In: *The European Physical Journal C* 72.12 (2012). ISSN: 1434-6052. DOI: 10.1140/epjc/s10052-012-2244-2. URL: http://dx.doi.org/10.1140/epjc/s10052-012-2244-2.

[62] ATLAS Collaboration. "Search for anomalous production of prompt like-sign lepton pairs at $\sqrt{s} = 7$ TeV with the ATLAS detector." In: *Journal of High Energy Physics* 2012.12 (2012). ISSN: 1029-8479. DOI: 10.1007/jhep12(2012)007. URL: http://dx.doi.org/10.1007/JHEP12(2012)007.

[63] ATLAS Collaboration. "Search for new phenomena in events with three or more charged leptons in pp collisions at $\sqrt{s} = 8$ TeV with the ATLAS detector." In: *Journal of High Energy Physics* 2015.8 (2015). ISSN: 1029-8479. DOI: 10.1007/jhep08(2015)138. URL: http://dx.doi.org/10.1007/JHEP08(2015)138.

[64] CMS Collaboration. *Search for a doubly-charged Higgs boson with $\sqrt{s} = 8$ TeV pp collisions at the CMS experiment*. Tech. rep. CMS-PAS-HIG-14-039. Geneva: CERN, 2016. URL: https://cds.cern.ch/record/2127498.

[65] CMS Collaboration. *A search for doubly-charged Higgs boson production in three and four lepton final states at $\sqrt{s} = 13$ TeV*. Tech. rep. CMS-PAS-HIG-16-036. Geneva: CERN, 2017. URL: https://cds.cern.ch/record/2242956.

[66] CMS Collaboration. "Study of Vector Boson Scattering and Search for New Physics in Events with Two Same-Sign Leptons and Two Jets." In: *Phys. Rev. Lett.* 114 (5 2015), p. 051801. DOI: 10.1103/PhysRevLett.114.051801. URL: https://link.aps.org/doi/10.1103/PhysRevLett.114.051801.

[67] ATLAS Collaboration. "Search for doubly charged scalar bosons decaying into same-sign W boson pairs with the ATLAS detector." In: *Eur. Phys. J.* C79.1 (2019), p. 58. DOI: 10.1140/epjc/s10052-018-6500-y. arXiv: 1808.01899 [hep-ex].

[68] OPAL Collaboration. "Search for the single production of doubly-charged Higgs bosons and constraints on their couplings from Bhabha scattering." In: *Physics Letters B* 577.3 (2003), pp. 93 –108. ISSN: 0370-2693. DOI: https://doi.org/10.1016/j.physletb.2003.10.034. URL: http://www.sciencedirect.com/science/article/pii/S0370269303015867.

[69] G. W. Bennett et al. "Final report of the E821 muon anomalous magnetic moment measurement at BNL." In: *Physical Review D* 73.7 (2006). ISSN: 1550-2368. DOI: 10.1103/physrevd.73.072003. URL: http://dx.doi.org/10.1103/PhysRevD.73.072003.

[70] Oliver Sim Bruening et al. *LHC Design Report*. CERN Yellow Reports: Monographs. Geneva: CERN, 2004. DOI: 10.5170/CERN-2004-003-V-1. URL: https://cds.cern.ch/record/782076.

[71] Esma Mobs. "The CERN accelerator complex. Complexe des accélérateurs du CERN." In: (2016). General Photo. URL: https://cds.cern.ch/record/2197559.

[72] ATLAS Collaboration. "The ATLAS Experiment at the CERN Large Hadron Collider." In: *JINST* 3 (2008), S08003. DOI: 10.1088/1748-0221/3/08/S08003.

[73] CMS Collaboration. "The CMS Experiment at the CERN LHC." In: *JINST* 3 (2008), S08004. DOI: 10.1088/1748-0221/3/08/S08004.

[74] ALICE Collaboration. "The ALICE experiment at the CERN LHC." In: *JINST* 3 (2008), S08002. DOI: 10.1088/1748-0221/3/08/S08002.

[75] LHCb Collaboration. "The LHCb Detector at the LHC." In: *JINST* 3 (2008), S08005. DOI: 10.1088/1748-0221/3/08/S08005.

[76] LHCb Collaboration. *The LHCb Public results*. 2019. URL: http://lhcbproject.web.cern.ch/lhcbproject/Publications/LHCbProjectPublic/Summary_all.html (visited on 09/20/2019).

[77] Lyndon Evans and Philip Bryant. "LHC Machine." In: *Journal of Instrumentation* 3.08 (2008), S08001–S08001. DOI: 10.1088/1748-0221/3/08/s08001. URL: https://doi.org/10.1088%2F1748-0221%2F3%2F08%2Fs08001.

[78] James Stirling. *Standard Model cross sections as a function of collider energy, with 125 GeV Higgs and including 33 TeV HE LHC*. Private communication. URL: http://www.hep.ph.ic.ac.uk/~wstirlin/plots/plots.html (visited on 10/29/2019).

[79] ATLAS Collaboration. *ATLAS luminosity measurements in Run 2*. 2019. URL: https://twiki.cern.ch/twiki/bin/view/AtlasPublic/LuminosityPublicResultsRun2 (visited on 10/10/2019).

[80] R. B. Palmer et al. "Muon colliders." In: *AIP Conference Proceedings* 372.1 (1996), pp. 3–30. DOI: 10.1063/1.50922. URL: http://dx.doi.org/10.1063/1.50922.

[81] ATLAS Collaboration. *Letter of Intent for the Phase-II Upgrade of the ATLAS Experiment*. Tech. rep. CERN-LHCC-2012-022. LHCC-I-023. Draft version for comments. Geneva: CERN, 2012. URL: https://cds.cern.ch/record/1502664.

[82] T G Cornelissen et al. *Updates of the ATLAS Tracking Event Data Model (Release 13)*. Tech. rep. ATL-SOFT-PUB-2007-003. ATL-COM-SOFT-2007-008. Geneva: CERN, 2007. URL: http://cds.cern.ch/record/1038095.

[83] Walter Blum, Werner Riegler, and Luigi Rolandi. *Particle detection with drift chambers; 2nd ed.* Berlin: Springer, 2008. DOI: 10.1007/978-3-540-76684-1. URL: https://cds.cern.ch/record/1105920.

[84] R.L. Gluckstern. "Uncertainties in track momentum and direction, due to multiple scattering and measurement errors." In: *Nuclear Instruments and Methods* 24 (1963), pp. 381 –389. ISSN: 0029-554X. DOI: https://doi.org/10.1016/0029-554X(63)90347-1. URL: http://www.sciencedirect.com/science/article/pii/0029554X63903471.

[85] ATLAS Collaboration. *Track Reconstruction Performance of the ATLAS Inner Detector at* $\sqrt{s} = 13$ *TeV*. ATL-PHYS-PUB-2015-018. 2015. URL: https://cds.cern.ch/record/2037683.

[86] ATLAS Collaboration. *ATLAS Insertable B-Layer Technical Design Report*. Tech. rep. CERN-LHCC-2010-013. ATLAS-TDR-19. 2010. URL: http://cds.cern.ch/record/1291633.

[87] Ian Connelly. "Performance and calibration of b-tagging with the ATLAS experiment at LHC Run-2." In: *EPJ Web Conf.* 164 (2017), p. 07025. DOI: 10.1051/epjconf/201716407025.

[88] ATLAS Collaboration. *Luminosity determination in pp collisions at* $\sqrt{s} = 13$ *TeV using the ATLAS detector at the LHC*. Tech. rep. ATLAS-CONF-2019-021. Geneva: CERN, 2019. URL: https://cds.cern.ch/record/2677054.

[89] ATLAS Collaboration. *The Run-2 ATLAS Trigger System*. Tech. rep. ATL-DAQ-PROC-2016-003. Geneva: CERN, 2016. DOI: 10.1088/1742-6596/762/1/012003. URL: https://cds.cern.ch/record/2133909.

[90] S. Agostinelli et al. "GEANT4 - a simulation toolkit." In: *Nucl. Instrum. Meth. A* 506 (2003), pp. 250–303. DOI: 10.1016/S0168-9002(03)01368-8.

[91] J. Pumplin et al. "New Generation of Parton Distributions with Uncertainties from Global QCD Analysis." In: *JHEP* 07 (2002), p. 012. DOI: 10.1088/1126-6708/2002/07/012. arXiv: hep-ph/0201195.

[92] A. D. Martin, W. J. Stirling, R. S. Thorne, and G. Watt. "Uncertainties on α_S in global PDF analyses and implications for predicted hadronic cross sections." In: *Eur. Phys. J. C* 64 (2009), pp. 653–680. DOI: 10.1140/epjc/s10052-009-1164-2. arXiv: 0905.3531 [hep-ph].

[93] Richard D. Ball et al. "Parton distributions for the LHC Run II." In: *JHEP* 04 (2015), p. 040. DOI: 10.1007/JHEP04(2015)040. arXiv: 1410.8849 [hep-ph].

[94] B.R. Webber. "A QCD model for jet fragmentation including soft gluon interference." In: *Nuclear Physics B* 238.3 (1984), pp. 492 –528. ISSN: 0550-3213. DOI: https://doi.org/10.1016/0550-3213(84)90333-X. URL: http://www.sciencedirect.com/science/article/pii/055032138490333X.

[95] B. R. Webber. *Fragmentation and Hadronization*. 1999. arXiv: hep-ph/9912292 [hep-ph].

[96] Frank Siegert. "Monte-Carlo event generation for the LHC." PhD thesis. Durham U., 2010.

[97] Torbjörn Sjöstrand. "Monte Carlo event generation for LHC." In: CERN-TH-6275-91 (1991), 25 p. DOI: 10.5170/CERN-1992-002.227. URL: https://cds.cern.ch/record/226013.

[98] Andy Buckley et al. "General-purpose event generators for LHC physics." In: *Phys. Rept.* 504 (2011), pp. 145–233. DOI: 10.1016/j.physrep.2011.03.005. arXiv: 1101.2599 [hep-ph].

[99] Torbjorn Sjostrand. "Status and developments of event generators." In: *Proceedings of Fourth Annual Large Hadron Collider Physics — PoS(LHCP2016)* (2016). DOI: 10.22323/1.276.0007. URL: http://dx.doi.org/10.22323/1.276.0007.

[100] Torbjorn Sjöstrand, Stephen Mrenna, and Peter Skands. "A brief introduction to PYTHIA 8.1." In: *Comput. Phys. Commun.* 178 (2008), pp. 852–867. DOI: 10.1016/j.cpc.2008.01.036. arXiv: 0710.3820 [hep-ph].

[101] G. Corcella et al. "HERWIG 6: an event generator for hadron emission reactions with interfering gluons (including supersymmetric processes)." In: *JHEP* 01 (2001), p. 010. DOI: 10.1088/1126-6708/2001/01/010. arXiv: hep-ph/0011363.

[102] T. Gleisberg et al. "Event generation with SHERPA 1.1." In: *JHEP* 02 (2009), p. 007. DOI: 10.1088/1126-6708/2009/02/007. arXiv: 0811.4622 [hep-ph].

[103] Johan Alwall, Michel Herquet, Fabio Maltoni, Olivier Mattelaer, and Tim Stelzer. "MadGraph 5 : going beyond." In: *JHEP* 06 (2011), p. 128. DOI: 10.1007/JHEP06(2011)128. arXiv: 1106.0522 [hep-ph].

[104] Stefano Frixione, Paolo Nason, and Carlo Oleari. "Matching NLO QCD computations with parton shower simulations: the POWHEG method." In: *JHEP* 11 (2007), p. 070. DOI: 10.1088/1126-6708/2007/11/070. arXiv: 0709.2092 [hep-ph].

[105] Michelangelo L. Mangano, Mauro Moretti, Fulvio Piccinini, Roberto Pittau, and Antonio D. Polosa. "ALPGEN, a generator for hard multiparton processes in hadronic collisions." In: *JHEP* 07 (2003), p. 001. DOI: 10.1088/1126-6708/2003/07/001. arXiv: hep-ph/0206293 [hep-ph].

[106] ATLAS Collaboration. *ATLAS Pythia 8 tunes to 7 TeV data*. ATL-PHYS-PUB-2014-021. 2014. URL: https://cds.cern.ch/record/1966419.

[107] Andy Buckley and Holger Schulz. "Tuning of MC generator MPI models." In: *Adv. Ser. Direct. High Energy Phys.* 29 (2018), pp. 281–301. DOI: 10.1142/9789813227767_0013. arXiv: 1806.11182 [hep-ph].

[108] J. Allison et al. "Recent developments in Geant4." In: *Nuclear Instruments and Methods in Physics Research Section A: Accelerators, Spectrometers, Detectors and Associated Equipment* 835 (2016), pp. 186 –225. ISSN: 0168-9002. DOI: https://doi.org/10.1016/j.nima.2016.06.125. URL: http://www.sciencedirect.com/science/article/pii/S0168900216306957.

[109] J Schaarschmidt. "The new ATLAS Fast Calorimeter Simulation." In: *Journal of Physics: Conference Series* 898 (2017), p. 042006. DOI: 10.1088/1742-6596/898/4/042006. URL: https://doi.org/10.1088%2F1742-6596%2F898%2F4%2F042006.

[110] ATLAS Collaboration. "The ATLAS Simulation Infrastructure." In: *The European Physical Journal C* 70.3 (2010), pp. 823–874. ISSN: 1434-6052. DOI: 10.1140/epjc/s10052-010-1429-9. URL: https://doi.org/10.1140/epjc/s10052-010-1429-9.

[111] G. Duckeck et al. "ATLAS computing: Technical design report." In: (2005).

[112] Lorenzo Rinaldi et al. "Collecting conditions usage metadata to optimize current and future ATLAS software and processing." In: *Journal of Physics: Conference Series* 898 (Oct. 2017), p. 042028. DOI: 10.1088/1742-6596/898/4/042028.

[113] I. Antcheva et al. "ROOT — A C++ framework for petabyte data storage, statistical analysis and visualization." In: *Computer Physics Communications* 180.12 (2009). 40 YEARS OF CPC: A celebratory issue focused on quality software for high performance, grid and novel computing architectures, pp. 2499 –2512. ISSN: 0010-4655. DOI: https://doi.org/10.1016/j.cpc.2009.08.005. URL: http://www.sciencedirect.com/science/article/pii/S0010465509002550.

[114] P. Calafiura, W. Lavrijsen, C. Leggett, M. Marino, and D. Quarrie. "The Athena control framework in production, new developments and lessons learned." In: *Computing in high energy physics and nuclear physics. Proceedings, Conference, CHEP'04, Interlaken, Switzerland, September 27-October 1, 2004*. 2005, pp. 456–458.

[115] T. Cornelissen, M. Elsing, I. Gavrilenko, W. Liebig, E. Moyse, and A. Salzburger. "The new ATLAS track reconstruction (NEWT)." In: *J. Phys. Conf. Ser.* 119 (2008), p. 032014. DOI: 10.1088/1742-6596/119/3/032014.

[116] R Mankel. "Pattern recognition and event reconstruction in particle physics experiments." In: *Reports on Progress in Physics* 67.4 (2004), 553–622. ISSN: 1361-6633. DOI: 10.1088/0034-4885/67/4/r03. URL: http://dx.doi.org/10.1088/0034-4885/67/4/R03.

[117] ATLAS Collaboration. "Performance of the ATLAS track reconstruction algorithms in dense environments in LHC Run 2." In: *The European Physical Journal C* 77.10 (2017), p. 673. ISSN: 1434-6052. DOI: 10.1140/epjc/s10052-017-5225-7. URL: https://doi.org/10.1140/epjc/s10052-017-5225-7.

[118] Andreas Salzburger. *Optimisation of the ATLAS Track Reconstruction Software for Run-2*. Tech. rep. ATL-SOFT-PROC-2015-056. 7. Geneva: CERN, 2015. DOI: 10.1088/1742-6596/664/7/072042. URL: https://cds.cern.ch/record/2018442.

[119] ATLAS Collaboration. *Early Inner Detector Tracking Performance in the 2015 Data at $\sqrt{s} =$ 13 TeV*. ATL-PHYS-PUB-2015-051. 2015. URL: https://cds.cern.ch/record/2110140.

[120] ATLAS Collaboration. *Performance of electron and photon triggers in ATLAS during LHC Run 2*. Tech. rep. 2019. arXiv: 1909.00761 [hep-ex].

[121] ATLAS Collaboration. "Electron efficiency measurements with the ATLAS detector using 2012 LHC proton–proton collision data." In: *EPJ C* C77.3 (2017), p. 195. DOI: 10.1140/epjc/s10052-017-4756-2. arXiv: 1612.01456 [hep-ex].

[122] ATLAS Collaboration. "Electron reconstruction and identification in the ATLAS experiment using the 2015 and 2016 LHC proton–proton collision data at $\sqrt{s}$=13 TeV." In: *The European Physical Journal C* 79.8 (2019), p. 639. ISSN: 1434-6052. DOI: 10.1140/epjc/s10052-019-7140-6. URL: https://doi.org/10.1140/epjc/s10052-019-7140-6.

[123] ATLAS Collaboration. "Electron reconstruction and identification in the ATLAS experiment using the 2015 and 2016 LHC proton-proton collision data at $\sqrt{s}$ = 13 TeV." In: *Eur. Phys. J.* C79.8 (2019), p. 639. DOI: 10.1140/epjc/s10052-019-7140-6. arXiv: 1902.04655 [physics.ins-det].

[124] J. Illingworth and J. Kittler. "A survey of the Hough transform." In: *Computer Vision, Graphics, and Image Processing* 44.1 (1988), pp. 87 –116. ISSN: 0734-189X. DOI: https://doi.org/10.1016/S0734-189X(88)80033-1. URL: http://www.sciencedirect.com/science/article/pii/S0734189X88800331.

[125] ATLAS Collaboration. "Muon reconstruction performance of the ATLAS detector in proton–proton collision data at $\sqrt{s}$ =13 TeV." In: *The European Physical Journal C* 76.5 (2016). ISSN: 1434-6052. DOI: 10.1140/epjc/s10052-016-4120-y. URL: http://dx.doi.org/10.1140/epjc/s10052-016-4120-y.

[126] Morad Aaboud et al. "Jet reconstruction and performance using particle flow with the ATLAS Detector." In: *Eur. Phys. J.* C77.7 (2017), p. 466. DOI: 10.1140/epjc/s10052-017-5031-2. arXiv: 1703.10485 [hep-ex].

[127] M. Aaboud et al. "Jet energy scale measurements and their systematic uncertainties in proton-proton collisions at $\sqrt{s} = 13$ TeV with the ATLAS detector." In: *Phys. Rev.* D96.7 (2017), p. 072002. DOI: 10.1103/PhysRevD.96.072002. arXiv: 1703.09665 [hep-ex].

[128] Ryan Atkin. "Review of jet reconstruction algorithms." In: *Journal of Physics: Conference Series* 645 (2015), p. 012008. DOI: 10.1088/1742-6596/645/1/012008. URL: https://doi.org/10.1088%2F1742-6596%2F645%2F1%2F012008.

[129] Gavin P. Salam. "Towards Jetography." In: *Eur. Phys. J.* C67 (2010), pp. 637–686. DOI: 10.1140/epjc/s10052-010-1314-6. arXiv: 0906.1833 [hep-ph].

[130] David Krohn, Jesse Thaler, and Lian-Tao Wang. "Jet trimming." In: *Journal of High Energy Physics* 2010.2 (2010). ISSN: 1029-8479. DOI: 10.1007/jhep02(2010)084. URL: http://dx.doi.org/10.1007/JHEP02(2010)084.

[131] ATLAS Collaboration. "Measurements of b-jet tagging efficiency with the ATLAS detector using t events at $\sqrt{s} = 13$ TeV." In: *JHEP* 08 (2018), p. 089. DOI: 10.1007/JHEP08(2018)089. arXiv: 1805.01845 [hep-ex].

[132] ATLAS Collaboration. "Reconstruction of hadronic decay products of tau leptons with the ATLAS experiment." In: *The European Physical Journal C* 76.5 (2016). ISSN: 1434-6052. DOI: 10.1140/epjc/s10052-016-4110-0. URL: http://dx.doi.org/10.1140/epjc/s10052-016-4110-0.

[133] Matteo Cacciari, Gavin P. Salam, and Gregory Soyez. "The anti-k_t jet clustering algorithm." In: *JHEP* 04 (2008), p. 063. DOI: 10.1088/1126-6708/2008/04/063. arXiv: 0802.1189 [hep-ph].

[134] Matteo Cacciari, Gavin P. Salam, and Gregory Soyez. "FastJet User Manual." In: *Eur. Phys. J. C* 72 (2012), p. 1896. DOI: 10.1140/epjc/s10052-012-1896-2. arXiv: 1111.6097 [hep-ph].

[135] ATLAS Collaboration. *Reconstruction, Energy Calibration, and Identification of Hadronically Decaying Tau Leptons in the ATLAS Experiment for Run-2 of the LHC*. ATL-PHYS-PUB-2015-045. 2015. URL: https://atlas.web.cern.ch/Atlas/GROUPS/PHYSICS/PUBNOTES/ATL-PHYS-PUB-2015-045.

[136] ATLAS Collaboration. *Object-based missing transverse momentum significance in the ATLAS detector*. Tech. rep. ATLAS-CONF-2018-038. Geneva: CERN, 2018. URL: https://cds.cern.ch/record/2630948.

[137] ATLAS TRT Collaboration. "The ATLAS Transition Radiation Tracker (TRT) proportional drift tube: Design and performance." In: *JINST* 3 (2008), P02013. DOI: 10.1088/1748-0221/3/02/P02013.

[138] ATLAS TRT collaboration. "The ATLAS TRT Barrel Detector." In: *Journal of Instrumentation* 3.02 (2008), P02014–P02014. DOI: 10.1088/1748-0221/3/02/p02014. URL: https://doi.org/10.1088%2F1748-0221%2F3%2F02%2Fp02014.

[139] ATLAS TRT collaboration. "The ATLAS TRT end-cap detectors." In: *Journal of Instrumentation* 3.10 (2008), P10003–P10003. DOI: 10.1088/1748-0221/3/10/p10003. URL: https://doi.org/10.1088%2F1748-0221%2F3%2F10%2Fp10003.

[140] ATLAS Collaboration. "Performance of the ATLAS Transition Radiation Tracker in Run 1 of the LHC: tracker properties." In: *Journal of Instrumentation* 12.05 (2017), P05002–P05002. ISSN: 1748-0221. DOI: 10.1088/1748-0221/12/05/p05002. URL: http://dx.doi.org/10.1088/1748-0221/12/05/P05002.

[141] ATLAS Collaboration. "ATLAS inner detector: Technical design report. Vol. 1." In: (1997).

[142] Claus Grupen and Boris Schwartz. *Particle detectors*. Vol. 26. Cambridge, UK: Cambridge Univ. Pr., 2008. URL: http://www.cambridge.org/zw/academic/subjects/physics/particle-physics-and-nuclear-physics/particle-detectors-2nd-edition?format=PB.

[143] Boris Dolgoshein. "Transition radiation detectors." In: *Nuclear Instruments and Methods in Physics Research Section A: Accelerators, Spectrometers, Detectors and Associated Equipment* 326.3 (1993), pp. 434 –469. ISSN: 0168-9002. DOI: https://doi.org/10.1016/0168-9002(93)90846-A. URL: http://www.sciencedirect.com/science/article/pii/016890029390846A.

[144] Oliver Ricken. *Studies of the ATLAS TRT Geometry Running with* $ArCO_2O_2$. Tech. rep. ATL-COM-INDET-2018-048. Geneva: CERN, 2015. URL: https://cds.cern.ch/record/2631585.

[145] ATLAS TRT collaboration. "The ATLAS Transition Radiation Tracker (TRT) proportional drift tube: design and performance." In: *Journal of Instrumentation* 3.02 (2008), P02013–P02013. DOI: 10.1088/1748-0221/3/02/p02013. URL: https://doi.org/10.1088%2F1748-0221%2F3%2F02%2Fp02013.

[146] Oleksandr Viazlo. "Search for beyond Standard Model physics with high-pt leptons." Presented 17 Feb 2017. PhD thesis. 2017. URL: https://cds.cern.ch/record/2255033.

[147] Fabio Sauli. "Principles of operation of multiwire proportional and drift chambers." In: *Experimental Techniques in High Energy Physics*. CERN, Geneva, 1975 - 1976. CERN. Geneva: CERN, 1977, 92 p. DOI: 10.5170/CERN-1977-009. URL: https://cds.cern.ch/record/117989.

[148] T Akesson et al. "Straw tube drift-time properties and electronics parameters for the ATLAS TRT detector." In: *Nucl. Instrum. Meth.* A449 (2000), pp. 446–460. DOI: 10.1016/S0168-9002(99)01470-9.

[149] A Alonso et al. *Impact of Operating the TRT with Argon-Based Gas Mixtures in ATLAS Performance and Physics Analyses*. Tech. rep. ATL-INDET-INT-2013-010. Geneva: CERN, 2013. URL: https://cds.cern.ch/record/1614495.

[150] ATLAS Collaboration. *ATLAS inner detector: Technical Design Report. Vol. 2*. Technical Design Report ATLAS. Geneva: CERN, 1997. URL: https://cds.cern.ch/record/331064.

[151] Christophe Pol A Roland. *Optimizing simulation of the argon-based active gas mixture in the Transition Radiation Tracker (TRT)*. Tech. rep. ATL-COM-INDET-2017-048. Geneva: CERN, 2017. URL: https://cds.cern.ch/record/2287404.

[152] ATLAS TRT Collaboration. "The ATLAS TRT electronics." In: *Journal of Instrumentation* 3.06 (June 2008), P06007–P06007. DOI: 10.1088/1748-0221/3/06/p06007. URL: https://doi.org/10.1088%2F1748-0221%2F3%2F06%2Fp06007.

[153] S Mehlhase and T C Petersen. *A probability based approach to PID in the TRT detector of ATLAS*. Tech. rep. ATL-COM-INDET-2006-017. Geneva: CERN, 2006. URL: https://cds.cern.ch/record/988085.

[154] ATLAS Collaboration. *Particle Identification Performance of the ATLAS Transition Radiation Tracker*. ATLAS-CONF-2011-128. 2011. URL: https://cds.cern.ch/record/1383793.

[155] Daniel Richter. "Energy Loss Measurements with the ATLAS Transition Radiation Tracker Using Test Beam Data." Diplom Thesis. Humboldt Universität zu Berlin, 2008. URL: http://atlas-archiv.desy.de/theses/Richter_dipl.pdf.

[156] Alejandro Alonso. "Transition Radiation Tracker calibration, searches beyond the Standard Model and multiparticle correlations in ATLAS." Presented 20 May 2012. 2012. URL: https://cds.cern.ch/record/1452211.

[157] Andreas Salzburger. "Track Simulation and Reconstruction in the ATLAS experiment." PhD thesis. Innsbruck U., 2008. URL: http://physik.uibk.ac.at/hephy/theses/diss_as.pdf.

[158] ATLAS Collaboration. *Performance of the reconstruction of large impact parameter tracks in the inner detector of ATLAS*. ATL-PHYS-PUB-2017-014. 2017. URL: https://atlas.web.cern.ch/Atlas/GROUPS/PHYSICS/PUBNOTES/ATL-PHYS-PUB-2017-014/.

[159] ATLAS Collaboration. *Calibration of the ATLAS Transition Radiation Tracker*. ATLAS-CONF-2011-006. 2011. URL: https://cds.cern.ch/record/1330712.

[160] Katja Mankinen. *Validation of r-t and to calibration procedure in Monte Carlo for 2016 gas geometry in the TRT*. Tech. rep. ATL-COM-INDET-2017-014. Geneva: CERN, 2017. URL: https://cds.cern.ch/record/2258403.

[161] R. Veenhof. "Garfield, a drift chamber simulation program." In: *Conf. Proc.* C9306149 (1993). [,66(1993)], pp. 66–71.

[162] Spencer R. Klein, Joakim Nystrand, Janet Seger, Yuri Gorbunov, and Joey Butterworth. "STARlight: A Monte Carlo simulation program for ultra-peripheral collisions of relativistic ions." In: *Comput. Phys. Commun.* 212 (2017), pp. 258–268. DOI: 10.1016/j.cpc.2016.10.016. arXiv: 1607.03838 [hep-ph].

[163] ATLAS Collaboration. "Performance of the ATLAS track reconstruction algorithms in dense environments in LHC Run 2." In: *Eur. Phys. J. C* 77 (2017), p. 673. DOI: 10.1140/epjc/s10052-017-5225-7. arXiv: 1704.07983 [hep-ex].

[164] ATLAS Collaboration. *ATLAS data quality operations and performance for 2015-2018 data-taking*. 2019. arXiv: 1911.04632 [physics.ins-det].

[165] ATLAS Collaboration. "Observation of Light-by-Light Scattering in Ultraperipheral Pb+Pb Collisions with the ATLAS Detector." In: *Phys. Rev. Lett.* 123 (5 2019), p. 052001. DOI: 10.1103/PhysRevLett.123.052001. URL: https://link.aps.org/doi/10.1103/PhysRevLett.123.052001.

[166] M. Kadastik, M. Raidal, and L. Rebane. "Direct determination of neutrino mass parameters at future colliders." In: *Phys. Rev. D* 77 (2008), p. 115023. DOI: 10.1103/PhysRevD.77.115023. arXiv: 0712.3912 [hep-ph].

[167] Pavel Fileviez Perez, Tao Han, Gui-yu Huang, Tong Li, and Kai Wang. "Neutrino masses and the CERN LHC: Testing type II seesaw." In: *Phys. Rev. D* 78 (2008), p. 015018. DOI: 10.1103/PhysRevD.78.015018. arXiv: 0805.3536 [hep-ph].

[168] Richard D. Ball et al. "Parton distributions with LHC data." In: *Nucl. Phys. B* 867 (2013), pp. 244–289. DOI: 10.1016/j.nuclphysb.2012.10.003. arXiv: 1207.1303 [hep-ph].

[169] Pavel M. Nadolsky et al. "Implications of CTEQ global analysis for collider observables." In: *Phys. Rev. D* 78 (2008), p. 013004. DOI: 10.1103/PhysRevD.78.013004. arXiv: 0802.0007 [hep-ph].

[170] Simon Arnling Bååth. "Doubly Charged Higgs Signal with Same-Sign Tau-inclusive Dilepton Final States." eng. Master's thesis. 2018. URL: http://lup.lub.lu.se/student-papers/record/8958257.

[171] ATLAS Collaboration. *Standard Model Summary Plots Summer 2019*. Tech. rep. ATL-PHYS-PUB-2019-024. CERN, 2019. URL: http://cds.cern.ch/record/2682186.

[172] Shi Qiu. "Searching for doubly charged Higgs bosons using same-sign hadronic tau final states - A focused study on the charge-flip background of hadronic taus." eng. Master's thesis. 2019. URL: http://lup.lub.lu.se/student-papers/record/8991933.

[173] Miha Muskinja. "Search for new physics processes with same charge leptons in the final state with the ATLAS detector using proton–proton collisions at $\sqrt{s} = 13$ TeV." Presented 20 Sep 2018. PhD thesis. 2018. URL: https://cds.cern.ch/record/2643902.

[174] Carsten Hensel and Kevin Kröninger. "Statistical Methods Commonly Used in High Energy Physics." In: *Data Analysis in High Energy Physics*. John Wiley & Sons, Ltd, 2013. Chap. 10, pp. 329–356. ISBN: 9783527653416. DOI: 10.1002/9783527653416.ch10. eprint: https://onlinelibrary.wiley.com/doi/pdf/10.1002/9783527653416.ch10. URL: https://onlinelibrary.wiley.com/doi/abs/10.1002/9783527653416.ch10.

[175] Luca Lista. "Statistical Methods for Data Analysis in Particle Physics." In: *Lect. Notes Phys.* 941 (2017), pp. 1–257. DOI: 10.1007/978-3-319-62840-0.

[176] Glen Cowan, Kyle Cranmer, Eilam Gross, and Ofer Vitells. "Asymptotic formulae for likelihood-based tests of new physics." In: *The European Physical Journal C* 71.2 (2011). ISSN: 1434-6052. DOI: 10.1140/epjc/s10052-011-1554-0. URL: http://dx.doi.org/10.1140/epjc/s10052-011-1554-0.

[177] Alexander L. Read. "Presentation of search results: the CL_S technique." In: *J. Phys. G* 28 (2002), pp. 2693–2704. DOI: 10.1088/0954-3899/28/10/313.

[178] M. Baak, G. J. Besjes, D. Côte, A. Koutsman, J. Lorenz, and D. Short. "HistFitter software framework for statistical data analysis." In: *Eur. Phys. J. C* 75 (2015), p. 153. DOI: 10.1140/epjc/s10052-015-3327-7. arXiv: 1410.1280 [hep-ex].

[179] ATLAS Collaboration. "Luminosity determination in pp collisions at $\sqrt{s} = 8$ TeV using the ATLAS detector at the LHC." In: *Eur. Phys. J. C* 76 (2016), p. 653. DOI: 10.1140/epjc/s10052-016-4466-1. arXiv: 1608.03953 [hep-ex].

[180] ATLAS Collaboration. "Muon reconstruction performance of the ATLAS detector in proton–proton collision data at $\sqrt{s} = 13$ TeV." In: *Eur. Phys. J. C* 76 (2016), p. 292. DOI: 10.1140/epjc/s10052-016-4120-y. arXiv: 1603.05598 [hep-ex].

[181] Simone Alioli, Paolo Nason, Carlo Oleari, and Emanuele Re. "A general framework for implementing NLO calculations in shower Monte Carlo programs: the POWHEG BOX." In: *JHEP* 06 (2010), p. 043. DOI: 10.1007/JHEP06(2010)043. arXiv: 1002.2581 [hep-ph].

[182] Paolo Nason. "A new method for combining NLO QCD with shower Monte Carlo algorithms." In: *JHEP* 11 (2004), p. 040. DOI: 10.1088/1126-6708/2004/11/040. arXiv: hep-ph/0409146.

[183] Hung-Liang Lai et al. "New parton distributions for collider physics." In: *Phys. Rev. D* 82 (2010), p. 074024. DOI: 10.1103/PhysRevD.82.074024. arXiv: 1007.2241 [hep-ph].

[184] Sayipjamal Dulat et al. "New parton distribution functions from a global analysis of quantum chromodynamics." In: *Phys. Rev. D* 93.3 (2016), p. 033006. DOI: 10.1103/PhysRevD.93.033006. arXiv: 1506.07443 [hep-ph].

[185] ATLAS Collaboration. "Measurement of the Z/γ^* boson transverse momentum distribution in pp collisions at $\sqrt{s} = 7$ TeV with the ATLAS detector." In: *JHEP* 09 (2014), p. 145. DOI: 10.1007/JHEP09(2014)145. arXiv: 1406.3660 [hep-ex].

[186] Michal Czakon and Alexander Mitov. "Top++: A program for the calculation of the top-pair cross-section at hadron colliders." In: *Comput. Phys. Commun.* 185 (2014), p. 2930. DOI: 10.1016/j.cpc.2014.06.021. arXiv: 1112.5675 [hep-ph].

[187] Nikolaos Kidonakis. *Theoretical results for electroweak-boson and single-top production*. 2015. arXiv: 1506.04072 [hep-ph].

[188] Torbjörn Sjöstrand, Stephen Mrenna, and Peter Z. Skands. "PYTHIA 6.4 physics and manual." In: *JHEP* 05 (2006), p. 026. DOI: 10.1088/1126-6708/2006/05/026. arXiv: hep-ph/0603175.

[189] Peter Zeiler Skands. "Tuning Monte Carlo generators: The Perugia tunes." In: *Phys. Rev. D* 82 (2010), p. 074018. DOI: 10.1103/PhysRevD.82.074018. arXiv: 1005.3457 [hep-ph].

[190] J. Alwall et al. "The automated computation of tree-level and next-to-leading order differential cross sections, and their matching to parton shower simulations." In: *JHEP* 07 (2014), p. 079. DOI: 10.1007/JHEP07(2014)079. arXiv: 1405.0301 [hep-ph].

[191] D. de Florian et al. "Handbook of LHC Higgs cross sections: 4. Deciphering the nature of the Higgs sector." In: (2016). arXiv: 1610.07922 [hep-ph].

[192] J. Pumplin, D. R. Stump, J. Huston, H. L. Lai, Pavel M. Nadolsky, and W. K. Tung. "New generation of parton distributions with uncertainties from global QCD analysis." In: *JHEP* 07 (2002), p. 012. DOI: 10.1088/1126-6708/2002/07/012. arXiv: hep-ph/0201195.

[193] N. Davidson, T. Przedzinski, and Z. Was. *PHOTOS Interface in C++: Technical and Physics Documentation*. 2010. arXiv: 1011.0937 [hep-ph].

[194] Charalampos Anastasiou, Lance J. Dixon, Kirill Melnikov, and Frank Petriello. "High precision QCD at hadron colliders: Electroweak gauge boson rapidity distributions at NNLO." In: *Phys. Rev. D* 69 (2004), p. 094008. DOI: 10.1103/PhysRevD.69.094008. arXiv: hep-ph/0312266.

[195] Sergey G. Bondarenko and Andrey A. Sapronov. "NLO EW and QCD proton-proton cross section calculations with mcsanc-v1.01." In: *Comput. Phys. Commun.* 184 (2013), pp. 2343–2350. DOI: 10.1016/j.cpc.2013.05.010. arXiv: 1301.3687 [hep-ph].

[196] Tanju Gleisberg and Stefan Höche. "Comix, a new matrix element generator." In: *JHEP* 12 (2008), p. 039. DOI: 10.1088/1126-6708/2008/12/039. arXiv: 0808.3674 [hep-ph].

[197] Fabio Cascioli, Philipp Maierhofer, and Stefano Pozzorini. "Scattering Amplitudes with Open Loops." In: *Phys. Rev. Lett.* 108 (2012), p. 111601. DOI: 10.1103/PhysRevLett.108.111601. arXiv: 1111.5206 [hep-ph].

[198] Steffen Schumann and Frank Krauss. "A Parton shower algorithm based on Catani-Seymour dipole factorisation." In: *JHEP* 03 (2008), p. 038. DOI: 10.1088/1126-6708/2008/03/038. arXiv: 0709.1027 [hep-ph].

[199] Stefan Höche, Frank Krauss, Marek Schönherr, and Frank Siegert. "QCD matrix elements + parton showers: The NLO case." In: *JHEP* 04 (2013), p. 027. DOI: 10.1007/JHEP04(2013)027. arXiv: 1207.5030 [hep-ph].

[200] Pierre Artoisenet, Rikkert Frederix, Olivier Mattelaer, and Robbert Rietkerk. "Automatic spin-entangled decays of heavy resonances in Monte Carlo simulations." In: *JHEP* 03 (2013), p. 015. DOI: 10.1007/JHEP03(2013)015. arXiv: 1212.3460 [hep-ph].

[201] Michal Czakon and Alexander Mitov. "Top++: A program for the calculation of the top-pair cross-section at hadron colliders." In: *Comput. Phys. Commun.* 185 (2014), p. 2930. DOI: 10.1016/j.cpc.2014.06.021. arXiv: 1112.5675 [hep-ph].

[202] Michiel Botje et al. *The PDF4LHC Working Group Interim Recommendations*. 2011. arXiv: 1101.0538 [hep-ph].

[203] Jun Gao et al. "CT10 next-to-next-to-leading order global analysis of QCD." In: *Phys. Rev. D* 89.3 (2014), p. 033009. DOI: 10.1103/PhysRevD.89.033009. arXiv: 1302.6246 [hep-ph].

[204] Johan Alwall, Michel Herquet, Fabio Maltoni, Olivier Mattelaer, and Tim Stelzer. "MadGraph5: going beyond." In: *JHEP* 06 (2011), p. 128. DOI: 10.1007/JHEP06(2011)128. arXiv: 1106.0522 [hep-ph].

[205] D. J. Lange. "The EvtGen particle decay simulation package." In: *Nucl. Instrum. Meth. A* 462 (2001), p. 152. DOI: 10.1016/S0168-9002(01)00089-4.

[206] ATLAS Collaboration. "Simulation of Pile-up in the ATLAS Experiment." In: *J.Phys.Conf.Ser.* 513 (2014), p. 022024. DOI: 10.1088/1742-6596/513/2/022024.

[207] ATLAS Collaboration. "Jet energy scale measurements and their systematic uncertainties in proton–proton collisions at $\sqrt{s} = 13$ TeV with the ATLAS detector." In: *Phys. Rev. D* 96 (2017), p. 072002. DOI: 10.1103/PhysRevD.96.072002. arXiv: 1703.09665 [hep-ex].

[208] ATLAS Collaboration. *Multi-Boson Simulation for 13 TeV ATLAS Analyses*. ATL-PHYS-PUB-2017-005. 2017. URL: https://cds.cern.ch/record/2261933.

[209] Patrick Motylinski, Lucian Harland-Lang, Alan D. Martin, and Robert S. Thorne. *Updates of PDFs for the 2nd LHC run*. 2016. arXiv: 1411.2560.

[210] S. Alekhin, J. Blumlein, and S. Moch. "The ABM parton distributions tuned to LHC data." In: *Phys. Rev. D* 89.5 (2014), p. 054028. DOI: 10.1103/PhysRevD.89.054028. arXiv: 1310.3059 [hep-ph].

[211] A. M. Cooper-Sarkar. *PDF Fits at HERA*. 2011. arXiv: 1112.2107 [hep-ph].

[212] Zhiqing Zhang. *HERA Inclusive Neutral and Charged Current Cross Sections and a New PDF Fit, HERAPDF 2.0*. 2015. arXiv: 1511.05402 [hep-ex].

[213] Pedro Jimenez-Delgado and Ewald Reya. "Delineating parton distributions and the strong coupling." In: *Phys. Rev. D* 89.7 (2014), p. 074049. DOI: 10.1103/PhysRevD.89.074049. arXiv: 1403.1852 [hep-ph].

[214] Hung-Liang Lai et al. "Parton Distributions for Event Generators." In: *JHEP* 04 (2010), p. 035. DOI: 10.1007/JHEP04(2010)035. arXiv: 0910.4183 [hep-ph].

[215] ATLAS Collaboration. "Search for anomalous production of prompt same-sign lepton pairs and pair-produced doubly charged Higgs bosons with $\sqrt{s} = 8$ TeV pp collisions using the ATLAS detector." In: *JHEP* 03 (2015), p. 041. DOI: 10.1007/JHEP03(2015)041. arXiv: 1412.0237 [hep-ex].

[216] ATLAS Collaboration. "The new LUCID-2 detector for luminosity measurement and monitoring in ATLAS." In: *JINST* 13.07 (2018), P07017. DOI: 10.1088/1748-0221/13/07/P07017.

[217] ATLAS Collaboration. *Multi-boson simulation for 13 TeV ATLAS analyses*. ATL-PHYS-PUB-2016-002. 2016. URL: https://cds.cern.ch/record/2119986.

[218] A. Elagin, P. Murat, A. Pranko, and A. Safonov. "A new mass reconstruction technique for resonances decaying to di-tau." In: *Nuclear Instruments and Methods in Physics Research Section A: Accelerators, Spectrometers, Detectors and Associated Equipment* 654.1 (2011), 481–489. ISSN: 0168-9002. DOI: 10.1016/j.nima.2011.07.009. URL: http://dx.doi.org/10.1016/j.nima.2011.07.009.

[219] ATLAS Collaboration. *Search for Neutral Minimal Supersymmetric Standard Model Higgs Bosons $H/A \to \tau\tau$ produced in pp collisions at $\sqrt{s} = 18$ TeV with the ATLAS Detector*. ATLAS-CONF-2015-061. 2015. URL: https://cds.cern.ch/record/2114827.

[220] ATLAS Collaboration. *Electron identification and efficiency measurements in 2017 data*. Tech. rep. ATL-COM-PHYS-2018-1727. Geneva: CERN, 2019. URL: https://cds.cern.ch/record/2652163.

[221] ATLAS Collaboration. *Identification of hadronic tau lepton decays using neural networks in the ATLAS experiment*. Tech. rep. ATL-PHYS-PUB-2019-033. Geneva: CERN, 2019. URL: http://cds.cern.ch/record/2688062.

[222] B. K. Bullock, Kaoru Hagiwara, and Alan D. Martin. "Tau polarization and its correlations as a probe of new physics." In: *Nucl. Phys.* B395 (1993), pp. 499–533. DOI: 10.1016/0550-3213(93)90045-Q.

[223] Tong Li. "Type II Seesaw and tau lepton at the HL-LHC, HE-LHC and FCC-hh." In: *Journal of High Energy Physics* 2018.9 (2018), p. 79. ISSN: 1029-8479. DOI: 10.1007/JHEP09(2018)079. URL: https://doi.org/10.1007/JHEP09(2018)079.

[224] ATLAS Collaboration. *Quark versus Gluon Jet Tagging Using Charged-Particle Constituent Multiplicity with the ATLAS Detector*. ATL-PHYS-PUB-2017-009. 2017. URL: https://cds.cern.ch/record/2263679.

[225] ATLAS Collaboration. *Quark versus Gluon Jet Tagging Using Jet Images with the ATLAS Detector*. ATL-PHYS-PUB-2017-017. 2017. URL: https://cds.cern.ch/record/2275641.